

Coupling light into thin silicon layers for high-efficiency solar cells

THÈSE N° 5714 (2013)

PRÉSENTÉE LE 19 AVRIL 2013

À LA FACULTÉ DES SCIENCES ET TECHNIQUES DE L'INGÉNIEUR
LABORATOIRE DE PHOTOVOLTAÏQUE ET COUCHES MINCES ÉLECTRONIQUES
PROGRAMME DOCTORAL EN SCIENCE ET GÉNIE DES MATÉRIAUX

ÉCOLE POLYTECHNIQUE FÉDÉRALE DE LAUSANNE

POUR L'OBTENTION DU GRADE DE DOCTEUR ÈS SCIENCES

PAR

Karin SÖDERSTRÖM

acceptée sur proposition du jury:

Prof. A. Fontcuberta i Morral, présidente du jury
Prof. C. Ballif, Dr F.-J. Haug, directeurs de thèse
Dr S. Guha, rapporteur
Prof. A. Polman, rapporteur
Prof. A. N. Tiwari, rapporteur



ÉCOLE POLYTECHNIQUE
FÉDÉRALE DE LAUSANNE

Suisse
2013

Résumé

Pour garantir le transport des porteurs photo-générés dans les cellules solaires en couches minces à base de silicium amorphe (a-Si :H) et microcristallin, de fines couches photo-actives sont nécessaires. Cela limite la consommation de matière première mais réduit l'absorption de la lumière de grandes longueurs d'onde. Pour piéger la lumière dans les couches de silicium et augmenter le courant de court-circuit de la cellule solaire, la texturation de substrats pour diffuser la lumière est la technique la plus utilisée. Cependant celle-ci entraîne l'apparition de défauts dans les couches de silicium lors de leur croissance qui limitent la tension de circuit ouvert (V_{oc}) et le facteur de forme (FF) de la cellule solaire. La réalisation de substrats qui permettent un bon couplage de lumière tout en garantissant une croissance des couches de silicium sans défauts est ainsi un défi majeur de cette technologie.

Dans un premier temps, une meilleure compréhension du mécanisme du couplage de lumière par la texturation d'interface a été obtenue : la résolution en angle et en polarisation de l'efficacité quantique d'une cellule solaire déposée sur une texture périodique unidimensionnelle a permis de démontrer que le piégeage de lumière peut être interprété comme étant dû à l'excitation de modes guidés dans les couches de silicium. Cette interprétation très intuitive permet de mieux comprendre quelles sont les caractéristiques nécessaires aux substrats pour obtenir un piégeage de lumière efficace par la texturation des interfaces de la cellule solaire.

Afin d'émanciper la technologie en couches minces de silicium des textures d'interfaces conventionnelles, il était nécessaire de trouver de nouvelles façons de texturer les interfaces pour améliorer les schémas de couplage de lumière dans les cellules solaires. Dans cette optique, la réplication de textures par nanoimpression UV a été étudiée et développée. Grâce à l'utilisation d'un tampon non ductile, une haute fidélité de réplication a pu être obtenue de sorte que la texture originale ne puisse être distinguée de celle reproduite par microscopie à force atomique ou par microscopie électronique. L'utilisation de ces répliques pour texturer des électrodes sur supports plastiques et verres a conduit à la croissance de cellules solaires avec des rendements aussi hauts que ceux de cellules déposées sur des électrodes conventionnelles. Le processus de nanoimpression a en outre permis le développement d'un nouvel outil de nanomoulage permettant un large choix dans la nanotexturation de la surface des électrodes en oxyde de zinc ou d'autres matériaux. Il est aussi démontré que l'ajout de répliques contenant des structures de tailles micrométriques sur le devant des dispositifs solaires permet d'augmenter la densité de courant de plus de 4% par un effet antireflet. Les applications multiples de la technique de nanoimpression UV qui sont présentées dans cette thèse démontrent son extraordinaire polyvalence et la présente comme une plate-forme

expérimentale appropriée au domaine des couches minces de silicium.

Pour augmenter le courant photogénéré il est aussi important de réduire les sources d'absorptions parasites. Celles qui existent à l'arrière des cellules solaires déposées sur des réflecteurs métalliques ont été étudiées. Il est démontré qu'une fine couche d'épaisseur optimale d'oxyde de zinc entre la couche métallique et les couches de silicium permet non seulement d'atténuer l'absorption dans le métal, mais aussi dans la couche de silicium dopée adjacente. Aussi, les absorptions parasites liées à la qualité des couches d'argent déposées sur des substrats nanotexturés ont été identifiées et un moyen pour les réduire est proposé. Grâce à la combinaison de la texturation du plastique par nanoimpression UV avec un réflecteur d'argent amélioré de haute qualité, un rendement initial de 11,1% et stable de 9,2% a été obtenu en utilisant un dispositif a-Si:H/a-Si:H contenant moins de la moitié d'un micron de silicium sur substrat plastique. Cette efficacité stable est, à la connaissance de l'auteur, la plus haute jamais démontrée pour des cellules solaires à base de matériaux a-Si:H sur substrat flexible en plastique.

Finalement, pour résoudre le problème de défauts apparaissant lors de la croissance des couches de silicium sur substrats texturés qui limitent le V_{oc} et le FF de la cellule solaire, un nouveau type de substrat découplant l'interface diffusant la lumière de la surface sur laquelle le silicium croît a été étudié et réalisé. Il est démontré qu'un substrat unique peut combiner les exigences supposément opposées du substrat idéal qui doit posséder une interface optiquement rugueuse —pour augmenter l'absorption de lumière dans la couche photo-sensible de la cellule solaire— et une interface morphologiquement plane pour obtenir une croissance optimale de silicium sans défauts. Ce type de substrat est extrêmement prometteur pour encore améliorer l'efficacité des cellules solaires en couches minces de silicium. Un rendement record stable de 13% a été obtenu grâce à la croissance d'une cellule à triple jonction sur ce diffuseur plat de lumière. Il s'agit du plus haut rendement stable obtenu jusqu'à présent dans notre laboratoire pour une cellule solaire en couches minces de silicium.

Pour conclure, ce travail a apporté des améliorations à la fois dans la compréhension et dans l'efficacité des dispositifs : une meilleure compréhension du couplage de lumière a été obtenue en montrant que celui-ci est relié à l'excitation de modes guidés dans les couches de silicium. La technique de nanoimpression UV a ensuite permis l'introduction de nouvelles textures diffusantes sur différents supports pour obtenir des cellules solaires à hauts rendements. Finalement, le développement d'un nouveau type de substrat qui découple l'interface rugueuse diffusant la lumière de la surface plane utilisée pour la croissance du silicium a conduit à une efficacité record stable de 13% en cellule solaire à triple jonction, proche du record du monde de 13.4% communiqué fin 2012 par LG Solar.

Mots clés :

Cellule solaire, photovoltaïque, couches minces, silicium amorphe, silicium microcristallin, piégeage de lumière, nanoimpression UV, substrat, texturation d'interfaces, modes guidés, pertes par absorptions parasites, diffuseur plat de lumière, haute efficacité, triple jonction.

Abstract

Thin-film solar cells based on amorphous and microcrystalline silicon require thin photo-active layers to ensure a satisfactory collection of the photogenerated carriers. The small thickness is advantageous in terms of raw material consumption and industrial throughput but results in poor light absorption at long wavelengths. Most of the time, textured substrates are used for the deposition of solar cells inducing scattering of light and increased light absorption in the silicon layer which enhance the short-circuit current density (J_{sc}) but also inducing the growth of silicon layers with defects that limit the open-circuit voltage (V_{oc}) and the fill factor (FF). Therefore, a major challenge is the design and realisation of structures that allow proper growth of the material while providing efficient light coupling.

In a first part of this thesis a better understanding of the light in-coupling mechanism via interface textures is achieved. Angle- and polarisation-resolved analysis of the external quantum efficiency of a cell grown on a one-dimensional grating structure demonstrates that light management can be viewed as the excitation of guided modes that are supported by the silicon layers. Defined peaks of enhanced photocurrent in the weakly absorbing region were observed for this cell, and these absorption phenomena were related to dispersion curves calculated for guided-modes in an equivalent flat multilayer system. This allows an intuitive understanding of photocurrent enhancement via interface texturing and provides new insights into the features that are required for efficient light trapping.

Then, a novel means of substrate texturing was required in order to emancipate the thin-film silicon solar cells from the standard textures used for light management, and open the road for the implementation of novel photonic designs that improve light trapping in high-efficiency devices. To achieve both of these goals, the replication of textures by UV nano-imprinting was investigated and developed. The remarkable replication fidelity obtained is such that the original texture cannot be distinguished from the replicated one by measurements such as atomic force microscopy and scanning electron microscopy. Solar cell efficiencies as high as on standard electrodes were demonstrated by texturing both plastic substrates for the *n-i-p* configuration and glass substrates for both the *n-i-p* and *p-i-n* configurations. In addition, the nano-imprinting process enabled the development of a novel tool called nanomoulding which permits the selected shaping of the surface of zinc oxide layers. Furthermore, it was observed that nano-imprinting of micro-metric features at the front of *n-i-p* and *p-i-n* devices boosts the J_{sc} by more than 4% by providing an anti-reflection effect. The manifold applications which use UV nano-imprinting in this thesis show its extraordinary versatility and demonstrate that it is a suitable experimental platform for thin-film silicon solar cells.

The reduction of parasitic absorption in inactive layers is another means to enhance J_{sc} and solar cell efficiency. Therefore, parasitic absorption that takes place in rough metallic back reflectors which are commonly used in the $n-i-p$ configuration is investigated and reduced. It is shown that the addition of a zinc oxide buffer layer of optimal thickness between the metallic layer and the silicon layers helps to mitigate parasitic absorption both in the metal and in the adjacent doped layer. Then, parasitic absorption related to the quality of the silver back reflector when deposited on rough nano-textures was reduced using a thermal annealing at low temperature. The combination of texturing on plastic by UV nano-imprinting with the deposition of a high-quality silver reflector led to a flexible a-Si:H/a-Si:H device with remarkable initial and stable efficiencies of 11.1% and 9.2%, respectively, using less than half a micron of silicon.

Eventually, to circumvent the strong limitation of V_{oc} and FF due to the defective growth of silicon on textured substrates, a novel type of substrate was realised and studied. This substrate decouples the optically rough interface that allows high J_{sc} , from the growth surface which is made flat to allow the growth of devices with good-quality silicon and high V_{oc} and FF . Triple-junction $n-i-p$ a-Si:H/ μc -Si:H/ μc -Si:H solar cells were realised on this substrate, and a stable efficiency of 13% was obtained, which is the highest stable efficiency reported so far for thin-film silicon solar cells by our laboratory. This novel approach is very promising as it demonstrates that the usual morphology trade-off can be overcome through the use of a single flat light-scattering substrate that fulfills all the requirements to push even further thin-film silicon solar cell efficiencies.

To conclude, this thesis brought improvements both in understanding and in devices. A better understanding of the features required for efficient light coupling was first found by showing that light coupling via interface texturing is due to the excitation of guided modes. Then it was demonstrated that UV nano-imprinting allows the introduction of novel photonic designs for better light management in high-efficiency solar cells and also allows the introduction of textures suitable for efficient light management on different substrates. This is illustrated by the flexible a-Si:H/a-Si:H device exhibiting 9.2% stable efficiency on a plastic which is, to the knowledge of the author, the highest reported efficiency for a-Si:H on plastic substrate. Also, novel flat light-scattering substrates which allow the growth of excellent material quality were developed and introduced in solar cells. This led to the realisation triple-junction $n-i-p$ solar cell with a record stable efficiency of 13% that is close to the current world record of 13.4% reported in 2012 by LG Solar using the $p-i-n$ configuration.

Key words:

Solar cell, photovoltaics, thin films, amorphous silicon, microcrystalline silicon, light trapping, UV nano-imprinting, substrates, texturing of interfaces, guided modes, parasitic absorption losses, flat light-scattering, high-efficiency, triple-junction.

List of abbreviations and symbols

ADF	Angular distribution function
AFM	Atomic force microscopy
Ag	Silver
Al	Aluminium
AM1.5G	Air mass 1.5 global
Ar	Argon
a-Si:H	Hydrogenated amorphous silicon
Cr	Chromium
DC	Direct current
DR	Diffuse reflectance
EQE	External quantum efficiency
FF	Fill factor
Hot Ag	Silver sputtered on a glass held at high temperature
μ c-Si:H	Hydrogenated microcrystalline silicon
In ₂ O ₃ :H	Hydrogenated indium oxide
ITO	Indium tin oxide
J_{sc}	Short-circuit current density
LED	Light-emitting diode
LP-CVD	Low-pressure chemical vapor deposition
n	Refractive index
PE-CVD	Plasma-enhanced chemical vapor deposition
PEN	Polyethylene-naphtalate
RF	Radio frequency
rpm	Revolution per minute
SEM	Scanning electron microscopy
σ_{rms}	Root mean square roughness
Si / SiO _x	Silicon / Sub-stoichiometric silicon oxide
TCO	Transparent conductive oxide
TA / TR	Total absorption / Total reflectance
UV-NIL	UV nano-imprint lithography
V_{oc}	Open-circuit voltage
ZnO / ZnO:Al / ZnO:B	Zinc oxide / Aluminium-doped zinc oxide / Boron-doped zinc oxide
Z2 / Z5	2- μ m-thick LP-CVD ZnO / 5- μ m-thick LP-CVD ZnO

Contents

Abstract (Français/English)	v
List of abbreviations	vii
1 Introduction	1
1.1 Ecological and economical context	1
1.2 Solar energy: A quasi-infinite source for energy production	2
1.3 Thin-film silicon solar cells	5
1.4 Status of the field: Light trapping in thin-film silicon solar cells	7
1.5 Goals and structure of the thesis	10
1.6 Contribution of this thesis to the research field	13
2 Deposition systems, tools and characterisation techniques	15
2.1 UV nano-imprint lithography for the texturing of solar cell interfaces	15
2.1.1 UV nano-imprint lithography	16
2.1.2 Stamp fabrication	18
2.1.3 Specific issues	22
2.2 Deposition systems	24
2.2.1 Physical vapour deposition	24
2.2.2 Chemical vapour deposition	25
2.3 Post-fabrication modification of substrates	28
2.3.1 Argon plasma treatment	28
2.3.2 Chemical mechanical polishing	28
2.4 Characterisation techniques	29
2.4.1 Substrate characterisations	29
2.4.2 Solar cell characterisations	32
3 UV nano-imprint lithography	39
3.1 Introduction	40
3.2 Characterisation of the replication quality	41
3.2.1 Characterisation of replicated texture using soft PDMS stamp	41
3.2.2 Comparison of replication between soft and solid stamps: Towards high fidelity replication	46
3.3 Cell results in the <i>n-i-p</i> configuration	50

3.3.1	Single-junction <i>n-i-p</i> a-Si:H solar cells grown on a master substrate and on a solid-stamp replicated substrate	50
3.3.2	Single-junction <i>n-i-p</i> a-Si:H solar cells grown on master substrate and on a soft-stamp replicated substrate	51
3.3.3	Tandem a-Si:H/a-Si:H cells: Comparison of best master texture and soft-stamp replicated texture	53
3.4	Cell results in the <i>p-i-n</i> configuration	56
3.4.1	Proof of concept with micromorph solar cells	56
3.4.2	New photonic designs: Multi-scale substrates	58
3.5	Nanomoulding of LP-CVD ZnO surfaces	60
3.5.1	Characterisation of nanomoulded substrates	60
3.5.2	a-Si:H <i>p-i-n</i> solar cells on nanomoulded substrates	62
3.6	Anti-reflective coating	64
3.7	Conclusions	67
4	Experimental observation of guided mode excitation in a-Si:H solar cells	69
4.1	Introduction	69
4.2	Flat interface waveguide model	71
4.3	Coupling of incident light	74
4.4	Experimental observation of guided mode excitation via grating coupling in a-Si:H solar cells	76
4.5	Conclusions	80
5	Back reflector materials in a-Si:H solar cells	83
5.1	Introduction	83
5.2	ZnO:Al buffer layer	85
5.3	Aluminium vs silver as metallic back reflector	89
5.4	Improvement of silver by thermal annealing at low temperature	91
5.4.1	Experimental details	93
5.4.2	Optical properties and morphology analysis of bare substrates	94
5.4.3	Cell results	98
5.4.4	Towards industrialisation	99
5.5	Comparison of rough random textures in plasmonic or dielectric materials . .	100
5.6	Conclusions	105
6	Experimental study of flat light-scattering back reflectors in thick μc-Si:H solar cells	107
6.1	Introduction	107
6.2	Experimental details	109
6.3	Effect of dummy a-Si:H layer and its polishing	110
6.4	Potential of polished substrates: Comparison with a reference textured cell . .	114
6.4.1	Light-trapping performance of the polished substrates	114
6.4.2	Cell electrical performance on polished substrates	115
6.5	Perspectives	116

6.6	Conclusions	118
7	Texture optimisation: Towards high efficiencies in the <i>n-i-p</i> configuration	119
7.1	Introduction	120
7.2	Single-junction a-Si:H solar cells	121
7.2.1	Study of various back reflectors with low roughnesses	122
7.2.2	Study of various back reflectors with larger roughnesses	124
7.2.3	Optimised cell on glass substrate: 10.4% initial efficiency, 8.1% after degradation	129
7.3	Single-junction $\mu\text{c-Si:H}$ solar cells	131
7.3.1	Study of various back reflectors	131
7.3.2	Optimised cell on glass substrate: 10.1% initial efficiency	133
7.4	Tandem a-Si:H/a-Si:H solar cells	135
7.4.1	Comparison of front contacts: Sputtered ITO vs LP-CVD ZnO:B	135
7.4.2	Optimised cell on plastic substrate: 11.1% initial efficiency, 9.2% after degradation	137
7.5	Thin micromorph a-Si:H/ $\mu\text{c-Si:H}$ solar cells with fabrication processes compatible with plastic substrates	139
7.5.1	Study of various back reflectors	139
7.5.2	Optimised cell on a glass substrate with a process fully compatible with plastic substrates: 11.7% initial efficiency, 10.4% after degradation	141
7.6	Triple-junction a-Si:H/ $\mu\text{c-Si:H}$ / $\mu\text{c-Si:H}$ solar cells	142
7.6.1	Study of various back reflectors	143
7.6.2	Optimised cell on flat light-scattering substrate with a 13.0% stable efficiency	145
7.7	Conclusions	147
8	Conclusions and perspectives	149
8.1	General conclusions	149
8.1.1	Applications of the nano-imprint lithography technique	149
8.1.2	Experimental evidence of light trapping by guided mode excitation	150
8.1.3	Investigation of textured back reflector materials in a-Si:H solar cells	150
8.1.4	Study of innovative flat light-scattering substrates	151
8.1.5	High-efficiency devices	151
8.2	Perspectives	152
8.2.1	Application of UV nano-imprinting	152
8.2.2	Minimising absorption losses in textured back reflectors	153
8.2.3	On the road to the philosopher's stone texture for light management	154
8.2.4	Improvement of flat light-scattering substrates	154
8.2.5	Towards 15% stable efficiency and higher	155
	Bibliography	156

Contents

Acknowledgements	183
Curriculum Vitae	185
List of publications	187

1 Introduction

1.1 Ecological and economical context

For two hundred years, the availability of cheap sources for energy production such as coal and oil allowed Western economies to develop fast and reach a high quality of living. However, recent years have shown that easy and cheap access to energy is not without consequences, and that this is probably going to change in the near future because of political, economical and environmental concerns. At the same time, the energy demand increases every year both in the countries of the Organisation for Economic Co-operation and Development as well as in developing countries. According to the International Energy Agency (IEA) energy demand is likely to grow by 30% between 2012 and 2035, and, because part of the population in developing countries just started to have access to energy, 60% of this demand increase will come from China, India and the Middle East [IEA 12b]. The total final world energy consumption was 10^5 Tera Watt hours (TWh) in 2010 according to the IEA [IEA 12a], and 78% of that was supplied by fossil fuels such as oil, coal and natural gas (the rest being predominantly from nuclear, hydropower and biofuels). These fossil sources of fuels are becoming more difficult to exploit as demand increases and hence their prices will probably increase as well. The price increase may momentarily be halted by accessing untapped reservoirs as observed recently with the exploitation of shale gas in the United States of America. However, because fossil fuels were created by processes that took millions of years, their use cannot be sustainable and it is of little importance whether we run out of them in 50 years or in 300 years; replacements should be found. Prices and shortage are not the only concerns: It is now accepted and well documented that fossil fuel consumption has led to large greenhouse gas emissions which have likely led to major changes in the planet's climate, creating global warming [IPCC 12]. Major negative consequences that will probably affect the whole world's population and fauna and flora include an elevation of the sea level, more frequent cyclones, more frequent heat and cold waves and more frequent heavy rain [IPCC 07]. Hence, it is necessary to reduce the world emissions of greenhouse gases in order to limit global warming. Unfortunately, politicians are slow to find solutions and to act in a common global manner as we observed in the non-constraining agreements that were reached in the

conferences on climate change from Kyoto in 1992 to Doha in 2012. This is basically because developed countries do not want to modify their way of living and developing countries do not want to reduce their economic growth rate. In this phase of indecision, it is the role of scientists to propose fast new solutions for the production of energy and to perform research in many directions. There is probably room for many different technologies which will share the common trait of producing energy with as little greenhouse gas emissions as possible. Nevertheless, there are some paths that should be taken only carefully, including those that include unacceptable risks like nuclear power based on fission, and others like some biofuels which are grown on large land areas that should be dedicated to agriculture, considering that more than 850 million people suffer from hunger in the world [FAO 12]. To conclude, modification of our energy production should not be seen as a barrier to growth, but rather as a fantastic opportunity to create new jobs, new knowledge and a new economy that is more sustainable.

1.2 Solar energy: A quasi-infinite source for energy production

Direct proof of the power of solar energy is given by the amazingly diverse forms of life that exist on Earth that were predominantly created from using solar fuel. Solar can be said to have an extremely high potential to play an important role in the production of mankind's future energy as *"in just an hour, the solar energy intercepted by the Earth exceeds the world's energy consumption for the entire year"* [IPCC 12]. Solar resources can be exploited indirectly through wind, hydropower and biomass, or by transforming sunbeams directly into another form of energy such as heat or electricity. The direct production of electricity from solar is extremely interesting because it is easily transportable and can be converted, depending on the needs, into thermal, chemical and mechanical energy through the use of heat pumps, batteries or dams, respectively. Direct electricity generation is achieved either by concentrated solar power (CSP) or by transforming the sunbeams directly into electricity using photovoltaics (PV). CSP uses sets of mirrors to concentrate sunbeams to heat a material which, coupled with a heat engine produces electricity. Short-term storage which mitigates the effect of clouding on the amount of electricity delivered to the grid is an advantage of this technology, but its main disadvantage, as with any concentrator, is that it uses only the direct part of the sun's radiation and it is therefore most efficient in extremely sunny places. Except for concentrated PV, PV technologies use indirect as well as direct sunlight to produce electricity, allowing energy production throughout the whole world. Also, the sizes of the systems can be varied to take into account local needs. Systems can be installed which produce a few watts for lighting or tens of MW to provide electricity to tens of thousands of homes.

The common outdated and erroneous arguments against the installation of PV can be separated into three categories. First, it is argued that the sun does not deliver enough energy to the Earth. This argument is overthrown at once by calculating that if 5% of the surface of the Sahara were covered with solar modules that convert 10% of the sunlight into electricity, the whole world's primary energy consumption would be covered. Of course, in this case, the

1.2. Solar energy: A quasi-infinite source for energy production

transport of this energy to the rest of the world would be an issue, but this simple example shows that there is much more power at our disposal than what we need. It is also remarkable that sunlight is distributed more or less equally throughout the whole world, and, in this sense, it is a rather socially equitable source of energy. The second argument against PV is that it is not ecologically friendly because of the amount of energy required and CO₂ emitted during module production. A recent study from Fthenakis et al. [Fthenakis 11] discusses the literature related to these claims, and it appears that most of these arguments are based on outdated data or invalid assumptions. By taking more recent data, it becomes clear that, depending on the technology and location of the module, it takes between less than a year to three years for a module to produce the amount of energy required for its production. In addition, the emission of CO₂ per equivalent kWh produced is between 20 and 100 g which is more than an order of magnitude lower than with natural-gas-fired power plants [IPCC 12]. Finally, the last argument that is brought against PV is its expensive price. As a matter of fact, the large-scale penetration of PV for the production of our electricity can occur only if it is cost-competitive with other electricity sources. Again, on this matter, up-to-date data are important and, because of increased production capacities, PV module prices have shrunk by a factor of 20 between 1980 and 2010. In 2012, the European Commission for Energy and Transport showed that grid parity was already a reality for sunny countries in Europe as well as in places where electricity is expensive [Ossenbrink 12]. Other studies forecast that grid parity will be reached for most countries in the world by 2020 [IRENA 12, Breyer 13].

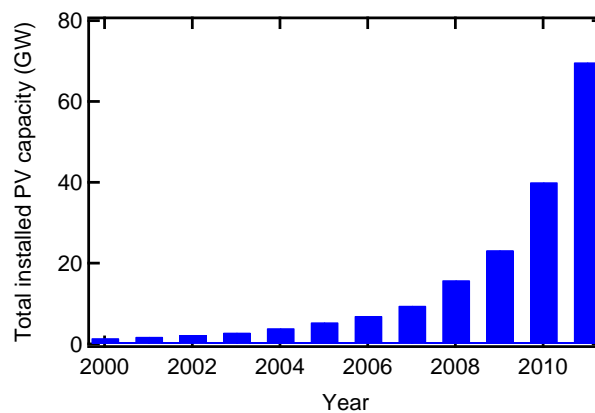


Figure 1.1: *Total installed PV capacity between 2000 and 2011. Source: European Photovoltaics Industry Association 2012.*

The previous discussion showed that electricity production with PV should not be considered as a futuristic dream, because this revolution is taking place right now. The PV market had an annual growth rate between 40% and 50% in recent years as shown in figure 1.1, which presents the worldwide total installed PV capacity between the year 2000 and 2011. It has to be noted that this tremendous growth led to new job opportunities in many different fields ranging from research to local installation. Currently, the market is strongly dominated (87% market share) by conventional crystalline silicon (c-Si) wafer-based technology [IRENA 12].

Chapter 1. Introduction

However, different technologies based on thin films of cadmium telluride (CdTe), amorphous silicon (a-Si:H), microcrystalline silicon ($\mu\text{c-Si:H}$) and copper-indium-gallium-selenide (CIGS) are beginning to penetrate the PV market as well. Thin-film products have several advantages such as the use of low amounts of raw materials and cell serial interconnection with laser scribing directly during the module production. Also, the realisation of flexible and lightweight modules of thin-film solar cells can decrease the cost of standard installations and allow easy integration into buildings. Figure 1.2 presents an example of a large rooftop PV system of 12 MW made with flexible a-Si:H modules which was installed in Spain.

The company First Solar is currently leading the thin-film market with modules based on CdTe, showing that this is a reliable technology and that low production costs are possible for large-scale production. However, further upscaling to the TW level might be prevented by the poor acceptance of Cd, which is a toxic material. CIGS is quickly emerging as a technology with high potential because high-efficiency solar cells were demonstrated, closing the gap between thin-film and c-Si efficiencies. Recently, a record efficiency of 20.4% was demonstrated on a flexible substrate by the Swiss Federal Laboratories for Materials Science and Technology. Compared to these two technologies, solar cells based on thin films of a-Si:H and $\mu\text{c-Si:H}$ suffer from their lower efficiency. The highest efficiency demonstrated yet for a thin-film silicon solar cell is 13.4% while it is 16.7% and 20.4% for CdTe and CIGS, respectively. The large advantage of thin-film silicon cells is that they are based on one of the most abundant materials on Earth and therefore their production growth will not be limited as with CdTe and CIGS technologies because of the current available resources of Te, In and Ga. Wadia et al. [Wadia 09] have shown that availability issues for CdTe and CIGS might not be short term, and that thin-film silicon is the technology with the highest long-term potential.



Figure 1.2: *Example of a large rooftop PV system of 12 MW made with a-Si:H modules installed in Spain. The picture is reproduced with permission from Guha et al. [Guha 11].*

The industrial fabrication of thin-film a-Si:H solar cells for electricity production for end-user applications started in the 1980s, but the real expansion of production to the MW level took place only in the 2004–2006. The pioneers of the production of rigid modules on glass substrates were Kaneka, Sharp and Mitsubishi Heavy Industries, whereas United Solar Ovonic Corporation and Fuji Electric have been pioneers in roll-to-roll processing of robust modules on flexible lightweight substrates. Since then, tens of companies have tried to penetrate the

PV market with thin-film silicon products, motivated by the exponential growth of installed capacity shown in figure 1.1 and low future production costs for thin-film silicon technologies. Unfortunately, the whole PV industry suffered from a hard collapse in 2010–2011 because of an overcapacity of modules. The overcapacity was due to the economical crisis and a brutal decrease in demand because the political incentive strategies for PV in Europe—one of the main market drivers in 2005–2010—were reduced. Thus, the PV industry is facing a phase of consolidation and many companies were forced to drastically reduce their PV production or to file for bankruptcy in 2011–2012. However, the long-term perspectives for the PV sector are heartening because demand will continue to grow as grid parity becomes more and more real in more countries. There will probably be room for many different technologies which may have different advantages depending on the application (e.g. end-user, residential, or utility scale) and on the location in which they are situated (e.g. warm or cold weather, direct or diffuse sunlight).

1.3 Thin-film silicon solar cells

Since the first evidence of photoconductivity in a-Si:H films deposited by glow discharge using SiH_4 gas [Chittick 69, Chittick 70], a-Si:H has drawn lots of attention. Substitutional doping was then demonstrated in this type of film [Spear 75], which allowed Carlson and Wronski to produce the first solar cell based on a-Si:H in the $p-i-n$ configuration [Carlson 76]. Figure 1.3 presents schematics of $n-i-p$ and $p-i-n$ devices whose main difference is the sequence of deposition. In the $n-i-p$ configuration, the n -doped layer is the first silicon layer to be deposited on the back contact, while in the $p-i-n$ configuration, it is the p -doped layer which is first deposited on the front contact. The doped layers create a field that extracts the carriers that are photogenerated in the intrinsic layer (i -layer) but they are too defective themselves to contribute to carrier generation. The front contact is made of a transparent conductive oxide (TCO) to let light enter the cell and to collect the carriers. The back contact can be made of a TCO or of a metallic layer. a-Si:H devices were seen to suffer from light-induced degradation of the material (often called the Staebler-Wronski effect) [Staebler 77] but it was then demonstrated that this degradation could be reduced by diluting the SiH_4 gas with hydrogen during film deposition [Guha 81] and by reducing the i -layer thickness [Hanak 82].

The deposition of a thin film of silicon by plasma discharge makes it possible to deposit silicon alloys and thus create films with different bandgap such as was shown by Chevallier et al. with germanium [Chevallier 77]. This triggered the design of multi-junction devices composed of a stack of solar cells of different bandgaps which can absorb light in a wider spectral range, allowing the reduction of the i -layer thicknesses, making these cells more efficient than single-junction cells [Marfaing 79]. Next, in 1994 IMT presented the first efficient solar cells using a $\mu\text{c-Si:H}$ i -layer which is a mixed-phase material composed of nanocrystals of silicon embedded in an a-Si:H matrix and which can be deposited in the same system as a-Si:H using the same gases [Meier 94]. $\mu\text{c-Si:H}$ has a lower bandgap than a-Si:H (1.1 eV for $\mu\text{c-Si:H}$ and around

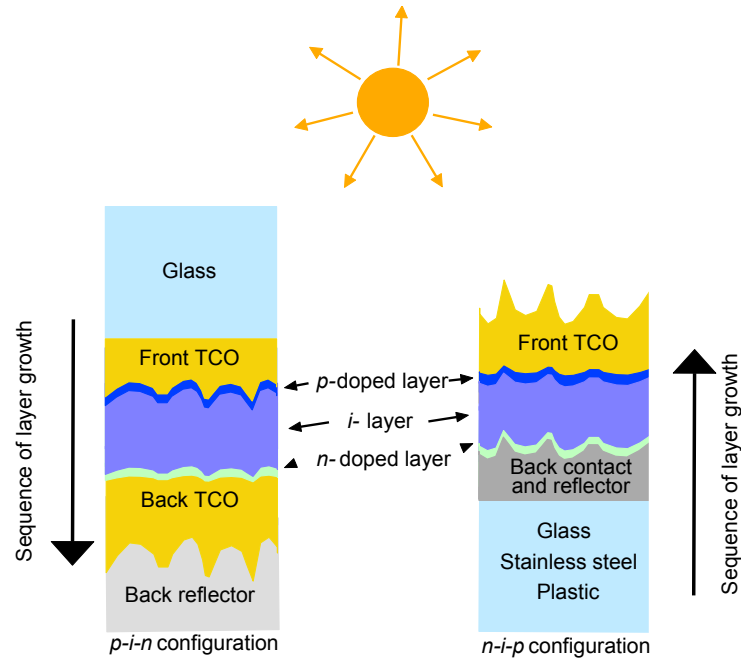


Figure 1.3: Schematics of thin-film silicon solar cells in the *p-i-n* and *n-i-p* configuration.

1.7 eV for a-Si:H) and is less susceptible to light-induced degradation. The combination of $\mu\text{c-Si:H}$ and a-Si:H into a tandem "Micromorph" device [Meier 96] could, in theory, lead to efficiencies of up to 30% because of their complementary bandgaps [Meillaud 06]. The major drawback of solar cells based a-Si:H and $\mu\text{c-Si:H}$ is that the light-induced degradation and the poor electronic transport of the materials limit the *i*-layer thicknesses to below the absorption lengths of light, which are of several μm in the red part of the solar spectrum for a-Si:H and tens of μm for $\mu\text{c-Si:H}$ material in the near infrared. This results in only partial absorption of the incident solar spectrum, which limits the solar cell efficiency if no strategy is implemented to increase absorption in the active part of the cell. Light-management schemes that confine and trap light in the cell absorber represent such a strategy. This topic has been intensively investigated in recent years, and it is the goal of this thesis to better understand these schemes in order to find novel approaches to increase the efficiencies of thin-film silicon solar cells via improved light trapping. Therefore, a review of prior and current studies on light trapping is given below.

1.4 Status of the field: Light trapping in thin-film silicon solar cells

Three different but interdependent approaches can be used to enhance absorption in the absorber layer and thereby increase J_{sc} :

1. Allow more light to enter the cell by reducing the primary reflection using an anti-reflection coating at the front of the device. This approach has been intensively studied and several methods are known to work efficiently, including rough nano-textures that induce a gradual change in the index of refraction between two layers [Bernhard 67], multi-layer stacks that produce destructive interference of the reflected beam for a selected range of wavelengths [Green 84] and large micro-metric features that cause multiple reflection of incoming light [Arndt 75]. Further research in this field is still required to produce low-cost anti-reflection coatings that are less sensitive to the wavelength, angle and polarisation of incident light.
2. To make better use of the light that is absorbed in the device, reduce all sources of parasitic absorption, i.e. absorption that does not occur in the active absorber layer. This is achieved by improving or modifying the materials that should be optically inactive in the solar cell. As an example, recent progress was made by alloying the doped layers with oxygen to render them more transparent [Cuony 10]. This is important because it was calculated that parasitic absorption remains one of the main limitations to reaching high J_{sc} values in thin-film silicon solar cells [Boccard 12c].
3. Decrease the amount of light that, after having been coupled into the solar cell, is coupled out of the cell. This is usually achieved by integrating so-called light-management or light-trapping schemes into the device. If the requirements for efficient light-trapping are better understood and if, in addition, novel processes to implement unconventional management schemes are made available, this is the most likely approach to provide new advances in solar cell efficiencies.

Light-management schemes are interesting not solely for a-Si:H and μc -Si:H thin-film solar cells. They can also be used in other technologies such as organic solar cells [Niggemann 04], in which the diffusion length of excitons is limited to a few tens of nanometers. Moreover, light management is extremely important in thin-film crystalline silicon solar cells that have thicknesses ranging from 3 μm up to 60 μm [Tiedje 84]. These cells are of interest because they resemble wafer-based devices with reduced silicon consumption. The main roads studied so far to obtain thin films of crystalline silicon are slicing thin wafers [Kray 09, Sakata 10], epitaxial growth on seed layers [Gall 06, Depauw 11, Branz 11, Petermann 12] or recrystallisation of thin amorphous films [Gall 09, Sontheimer 12]. In addition, CIGS technology could benefit from light trapping that would allow researchers to reduce the absorber thicknesses to hundreds of nanometers, which in turn would decrease the material consumption and the costs of the technology. Therefore, research on light-management schemes has attracted tremendous interest these last few years.

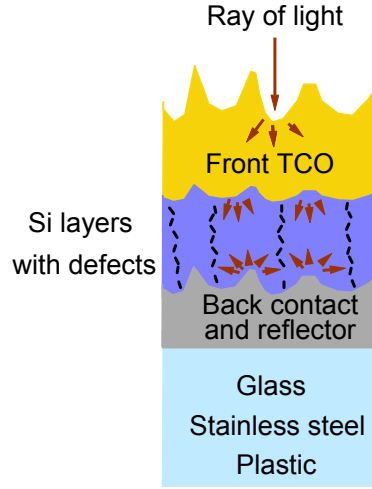


Figure 1.4: *Schematic of a thin-film silicon solar cell grown on a textured substrate. The light absorption in the silicon layer is increased because the light path is prolonged by light scattering but a textured substrate induces the growth of silicon layers with defects.*

The traditional light-trapping scheme relies on light scattering at textured interfaces between two media with different refractive indices n , as demonstrated in 1983 by several groups [Deckman 83, Tiedje 83, Iida 83]. This induces light scattering at each interface, thereby increasing the light path, and ultimately the absorption in the cell and the J_{sc} as schematically shown in figure 1.4. The most famous upper limit for the absorption enhancement that can be obtained by using a textured interface in thin films is the Yablonovitch limit, which is equal to $4n^2$ [Yablonovitch 82]. Several recent theoretical studies have investigated this limit because it relies on several assumptions that may not be valid in thin-film silicon solar cells. Most importantly, it assumes a continuous density of available photonic states in the film that are equivalently populated because of Lambertian scattering, and no parasitic absorption. Therefore, it was proposed that parasitic absorption and the discrete nature of the number of photonic modes available inside a thin silicon film leads to a more conservative limit for absorption enhancement in real solar cells [Stuart 97, Haug 11b]. Other studies proposed, to the contrary, that this $4n^2$ limit can be surpassed if a cell is well designed but in general the enhancement exceeds $4n^2$ only for a limited range of wavelengths [Sheng 83, Gee 02, Yu 10]. This thesis did not approach this subject in depth, and hence the author advises the interested reader to read the recent contribution of Mokkaapati et al. [Mokkaapati 12], which provides an excellent review on the upper limits that can be found depending on the assumptions and the analysis used.

To date, texturing of the interfaces is the most successful and widely implemented light-trapping scheme, and numerous studies have tried to optimise the feature sizes and shapes for optimal light trapping using random textures [Mizuhashi 88, Campbell 87, Banerjee 91, Kluth 99, Müller 04, Springer 05, Terrazzoni-Daudrix 06, Berginski 07, Faÿ 07, Franken 07],

1.4. Status of the field: Light trapping in thin-film silicon solar cells

[Söderström 09b, Sai 10, Boccard 10, Rockstuhl 10, Nicolay 11, Zhu 12, Bittkau 12, Yan 12a] and periodic textures [Heine 95, Eisele 01, Stiebig 06a, Isabella 08, Sai 09, Zhu 10, Madzharov 11, Owen 11, Hsu 12, Lal 12, Sontheimer 12, Sai 12]. Although theoretical studies indicate that periodic structures may enhance absorption more than random textures [Yu 10, Dewan 11], experiments have not yet succeeded in verifying this yet (see for instance Battaglia et al. [Battaglia 12b]), and the highest efficiencies reported so far for thin-film silicon solar cells have been achieved with random textures.

In order to further increase light absorption more exotic schemes have been proposed such as texturing of the absorber layer into three-dimensional photonic crystals that modify the density of available optical states [Duché 08, Chutinan 09, Meng 11], and decoupling the electrical path from the light path by using nanowires and nanorods [Zhu 09, Naughton 10, Vaneček 11, Jia 12]. Unfortunately, these two tactics may be extremely difficult to implement easily in thin-film silicon when the silicon layer is deposited from the vapour phase—as in this thesis—because the high aspect ratio of these textures prevents the growth of high-quality silicon. In a different approach, the enhancement provided by plasmon resonances was also intensively investigated [Catchpole 06, Pillai 07, Moulin 08, Atwater 10, Eminian 11]. The possibility to tune the energies at which plasmonic resonances take place and localise the electromagnetic field renders this approach promising. It is nevertheless still debatable whether these types of light-management schemes will beat traditional random textures because of the inevitable parasitic light absorption within the plasmonic material may be stronger than the absorption within the silicon layer itself [Atwater 10, Haug 11c, Schiff 11, Pahud 13].

To conclude, research on light management has been extremely abundant these last years, and novel ideas emerge every day. The main limitation of most of these schemes is that their implementation into solar cells is difficult and thus there is a lack of experimental evidence demonstrating the potential of each. Silicon film deposition from the vapour phase restricts for the moment the possible shapes and sizes of substrate texture that may be used for light management: In general, as schematically shown in figure 1.4, the growth of silicon on rough textures leads to layers that are more defective than those grown on a flat surface, thus limiting the V_{oc} and FF of devices with light-management schemes [Sakai 90, Nasuno 01, Python 08a, Hänni 13a]. For this reason, a compromise is usually made between rough textures that increase J_{sc} and smooth textures that promote high V_{oc} and FF . Hence, some light-management schemes try to circumvent this issue by decoupling the light-scattering interface from the growth surface [Sai 11a, Lee 11, Söderström 12c, Grandidier 12, Massiot 12]; this approach was shown to work efficiently but probably does not provide the ideal light management. For this reason, novel light-trapping schemes should be developed in combination with novel solar cell designs and deposition conditions that allow the solar cells to be tolerant of a wider range of textures.

1.5 Goals and structure of the thesis

The purpose of this thesis is to:

1. Provide a better understanding of the texture shapes and sizes needed for light trapping in thin-film silicon solar cells.
2. Realise better substrates for high-efficiency solar cells with an emphasis on obtaining better back reflectors for the *n-i-p* configuration.
3. Implement the most promising substrates in different types of devices to further improve the efficiencies of each. To reach these goals, research in optics, materials and processes was carried out. Summaries of the studies done in each chapter are described below.

Studying selected photonic textures directly in devices to assess their light-trapping properties required a novel means for substrate texturing. For this purpose a UV nano-imprint lithography (UV NIL) tool was further developed in collaboration with Dr. J. Escarré. The important technical details for replicating nano-textures are given in chapter 2. This chapter also gives an overview of the different machines used for layer deposition, and the characterisation tools that were used during this thesis.

Chapter 3 presents the results obtained with the replication process. First, the replication fidelity is quantified, and it is demonstrated that high-fidelity replication of the random nano-textures commonly used in PV devices can be obtained provided that the stamp material is well chosen. Then, the successful implementation of the replicated textures on the contacts of *n-i-p* and *p-i-n* devices. Efficiencies comparable to those on standard electrodes were achieved: A tandem a-Si:H/a-Si:H device with an 8.1% stable efficiency was obtained in the *n-i-p* configuration on a plastic substrate textured with UV-NIL, and a micromorph device with a 12% initial efficiency was obtained in the *p-i-n* configuration. UV NIL promises further efficiency increases in both cases by allowing the implementation of novel photonic textures for improved light management. This was done in collaboration with the *p-i-n* group at PV-Lab, and a micromorph device in the *p-i-n* configuration with a high initial efficiency of 14% was obtained by implementing a novel multi-scale textured electrode. It is then shown that the UV NIL technique can be used in more exotic applications such as moulding the surface of functional brittle materials with high fidelity at the nanoscale, and a first experimental demonstration with ZnO is shown. Finally, an application of the UV NIL tool which results in a further efficiency increase is shown. The replica of micro-metric textures at the front of devices can add, in a post-process step a broadband anti-reflection effect, boosting J_{sc} of *p-i-n* and *n-i-p* devices by more than 4%.

The UV NIL replication process allows the introduction into solar cells of textures that can be specifically designed for a special experiment. To better understand the light-trapping mechanism that occurs via textured interfaces, an electrode textured with a 1D periodic grating is of special interest because it contains a single spatial frequency and is a structure that is sensitive to light polarisation. Chapter 4 presents a study of an a-Si:H solar cell grown

on a 1D grating structure that allowed us to relate specific peaks in the EQE spectrum with the excitation of guided modes via grating coupling. This experiment thus validates the use of the waveguide framework for the description of solar cells, and provides new insights into the feature size requirements for efficient light trapping.

After gaining better understanding of the light-trapping mechanism in chapter 4, chapter 5 is dedicated to the experimental study of the back reflector that is generally used in the *n-i-p* configuration, i.e. a rough metallic layer covered with a thin dielectric buffer layer. In particular, the absorption losses that occur in the back reflector are discussed and possible means for their mitigation are investigated. In this regard, the buffer layer—which is commonly made of aluminium-doped zinc oxide (ZnO:Al)—is of particular importance and it is shown that this layer helps to mitigate parasitic absorption in the metallic back reflector and *n*-doped layer. However, the mitigation of the absorption in the metal by using an optimal thickness of ZnO:Al is not enough to make an aluminium reflector as lossless as a silver reflector. A silver back reflector parasitically absorbs part of the light, but to a lesser extent. When grown on a rough nano-texture however, a strong decrease in the silver reflectance is observed with the consequence that the efficiency of the solar cell grown on top decreases. In order to improve the reflectance of the silver layer, a thermal annealing step at low temperature is investigated and an increase in the silver grain size up to 40% is obtained. This results in a reflectance improvement and an absolute efficiency gain of up to 1% for solar cells grown on an annealed back reflector. Chapter 5 ends by comparing the light scattering that is provided by the same rough texture when it is made out of a dielectric or plasmonic material. The potential of light trapping provided by each type of material is evaluated and, although the light management provided by them is similar, the plasmonic back reflector provides higher total absorption which does not translate into higher J_{sc} but rather into more pronounced parasitic losses.

In thin-film silicon solar cells, a rough texture is desired to reach high J_{sc} while a smooth texture is preferred for the growth of high-quality silicon layers that promote high V_{oc} and FF values. Chapter 6 presents an experimental study of a newly developed substrate that fulfills both requirements. This substrate combines the advantage of being physically flat, allowing the growth of material of high quality and hence high V_{oc} and FF , while being optically rough to lead to remarkable light management and high J_{sc} . For these reasons, these substrates are highly promising for increased solar cell efficiencies, and a detailed study of the fabrication of these substrates and their effect in single-junction μc -Si:H solar cell is reported in chapter 6. A *p-i-n* μc -Si:H single-junction is shown to maintain a high V_{oc} of 520 mV on this substrate even for a 3.8- μm -thick *i*-layer, and a relative efficiency increase of 10% was demonstrated compared to an optimised cell on a textured substrate.

Chapter 7 provides a summary of the texture optimisation that was carried out for each type of investigated device. It also reports the highest-efficiency solar cells that were achieved by combining the knowledge acquired in the other chapters. It is first shown that with the processes that were used for silicon deposition, the substrate should be kept relatively smooth to achieve high-efficiency single-junction a-Si:H and μc -Si:H solar cells. These cells are the

basis of the multi-junction solar cells which were then optimised following two different roads:

1. Processes compatible with plastic substrates to obtain stable efficiencies between 9% and 11%: UV NIL combined with a high-quality silver reflector led to a flexible a-Si:H/a-Si:H device with a initial and stable efficiencies of 11.1% and 9.2% respectively, using less than half a micron of silicon. To the knowledge of the author, this is the highest efficiency reported for a device based on a-Si:H on a plastic substrate. Additionally, a micromorph a-Si:H/ μ c-Si:H device fabricated with processes fully compatible with plastic substrates with a initial and stable efficiencies of 11.7% and 10.4% respectively, was achieved. These efficiencies are not as high as what can be obtained on glass substrates, but the low material usage and high efficiencies for plastic substrates are very promising for the industrialisation of this technology.
2. High-efficiency devices on glass substrates with stable efficiencies above 12%: This was achieved by combining the flat light-scattering substrate investigated in chapter 6 with a triple-junction a-Si:H/ μ c-Si:H/ μ c-Si:H device and an anti-reflection coating made by UV NIL. A device with a stable efficiency of 13% is shown, which is the highest stable efficiency reported yet by our laboratory for thin-film silicon solar cells, and is close to the current thin-film silicon world record efficiency of 13.4% reported in 2012 by LG Solar.

Chapter 8 provides the conclusions of this thesis as well as the perspectives. It is shown that the goals of this thesis were fulfilled and that this thesis paves the way for further studies aimed at improving both the understanding of light trapping and the efficiencies of devices.

1.6 Contribution of this thesis to the research field

This thesis contributed to improvements in thin-film silicon solar cells in several ways. First, the excitation of guided modes in thin-film solar cells was demonstrated experimentally for the first time [Söderström 10c], providing new insights into the surface features required for efficient light trapping. This work was recognised by an invited talk at the 2010 OSA conference [Söderström 10b], and provided an experimental validation of the waveguide model used in studies on fundamental light-trapping limits [Haug 11b, Haug 11a, Naqavi 13]. A UV NIL technique was developed for the replication of textures with high fidelity [Söderström 10a, Escarré 11]. For the first time, cells grown on substrates textured by UV NIL were presented with high stable efficiencies and excellent yields on plastic [Söderström 11a], and record-high initial efficiencies above 14% on glass [Boccard 12b]. This work also contributed to a novel process to shape the surface of ZnO grown by low pressure chemical vapor deposition (LP-CVD ZnO) with high precision at the nanoscale [Battaglia 11b]. The quality of silver back reflectors was also improved, leading to a single-junction cell with a initial efficiency of 9.9% on plastic textured by UV NIL [Söderström 11b] and to a tandem a-Si:H/a-Si:H device with the highest reported stable efficiency of 9.2% on plastic substrates using less than half a micron of a-Si:H [Söderström 12b]. Finally, substrates that decouple the light-scattering interface from the growth interface were investigated and yielded efficiency gains in $\mu\text{c-Si:H}$ solar cells [Söderström 12c]. These substrates were then implemented in triple-junction solar cells to obtain a solar cell with a 12.5% stable efficiency [Söderström 12a]; this work was recognised by appearing in the highlights of the Journal of Applied Physics. A further efficiency gain was obtained by implementing an anti-reflective coating made by UV NIL at the front of the device, and a record stable efficiency of 13% was demonstrated. This is the highest stable efficiency reported so far by our laboratory and this value is also close to the current thin-film silicon world record of 13.4% reported in 2012 by LG solar. This result is highly promising to push further the efficiencies of thin-film silicon solar cells by using these types of substrates. This work has paved the road for the implementation of novel photonic textures for efficient light trapping in $n-i-p$ solar cells both on glass and plastic substrates. The high transparency of the resin also allows the implementation of novel photonic textures in the $p-i-n$ configuration.

2 Deposition systems, tools and characterisation techniques

This chapter reports the main tools used during this thesis. Section 2.1 describes the procedure of UV nano-imprint lithography (UV NIL) that was used by Dr. J. Escarré and myself to replicate textures for solar cell applications. Apart from the UV NIL set up, numerous deposition systems and techniques were used either for solar cell deposition or for the substrate production. The machines are described in section 2.2. The surfaces of some substrates were modified before use in solar cells. The two main modifications are described in section 2.3. Finally, the characterisation tools that were used for solar cell or for substrate analysis are described in section 2.4.

2.1 UV nano-imprint lithography for the texturing of solar cell interfaces

The nano-texture replication process by UV NIL is explained in detail in this section. The main steps of the process flow are depicted in figure 2.1 which captures the idea of UV NIL: First, the master texture is fabricated by any means. Second, the negative of the master texture is moulded to fabricate the stamp. Third, a substrate is covered with a UV-curable resin. Fourth, the substrate and the stamp are brought together and UV light is applied to cure the resin that will adopt the original master texture. Eventually, the sandwich made of the stamp and the substrate is separated to obtain the replica. The process consists of these five main steps but within each individual step small details may lead to successful or unsuccessful replication. Therefore, an extended description of the operating procedure is given in the following paragraphs.

In section 2.1.1, the machine used for the moulding process is first described. Then, the procedure for the replication of textures that was developed jointly by Dr. J. Escarré and myself is described. This development consisted in improving previous work done at IMT on UV NIL replication since 2002.

The stamps are one of the key points of the process and thus the details of their fabrication

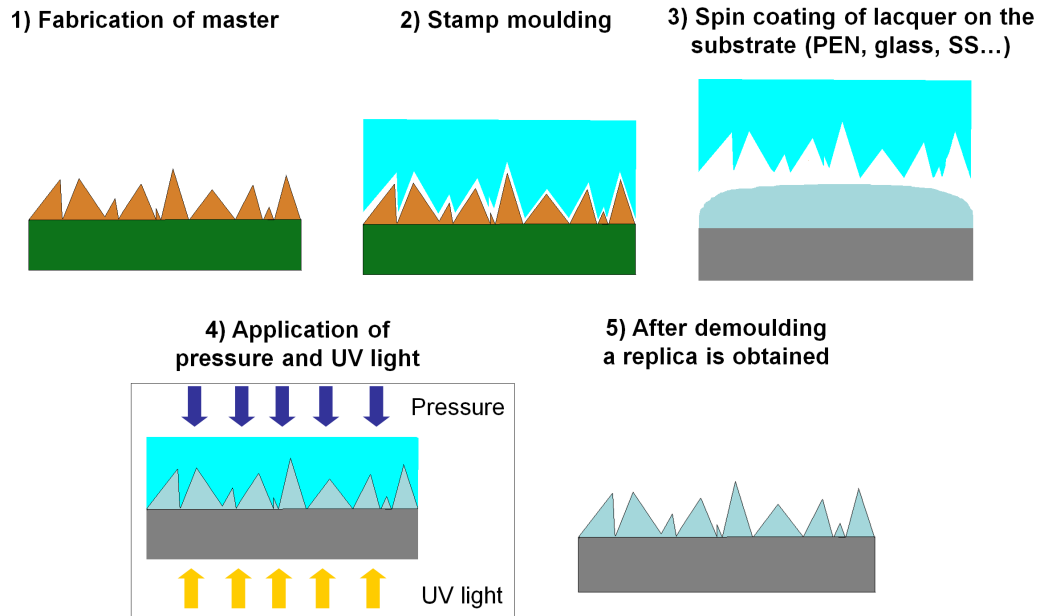


Figure 2.1: *Principle of UV nano-imprint lithography.*

are given in section 2.1.2. During this thesis the development of a solid stamp allowed very high-fidelity replication of nanotextures and also led to new ideas such as nanomoulding of boron-doped zinc oxide deposited by low pressure chemical vapour deposition (LP-CVD ZnO:B) and solar cell transfer from one substrate to another. Therefore, the modifications to the standard process that are needed for these new applications are also briefly described in section 2.1.2.

Section 2.1.3 discusses two specific issues that came up during the development of the UV NIL process. First, adhesion issues between the UV resin and PEN substrates are discussed and the solutions that were applied are described. Second, the intensity and the dose of UV light that were applied to the resin were seen to be important parameters in different regards: The dose was seen to impact the separation of the sandwich stamp-replica and the intensity was seen to impact the yield of solar cells when replications were used as substrates.

2.1.1 UV nano-imprint lithography

Machine description

Figure 2.2 shows a schematic of the replication machine¹. It consists of two chambers whose pressure can be independently tuned between atmospheric pressure and 40 mbar. The bottom part of chamber 1 is made of a soft malleable silicone membrane which serves to apply the

¹Designed and built by S. Pérregaux under a CTI grant in a collaboration with the company VHF technology (no. 8809.2)

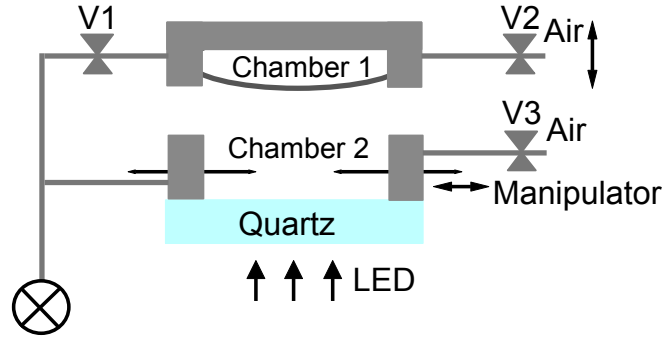


Figure 2.2: Schematic of the replication machine.

desired pressure in a controlled way during replication.

The control of the pressure is achieved as follows: A two-stage chemical diaphragm pump first pumps both chambers down to 40 mbar. Second, the valve V1 which connects both chambers is closed maintaining the pumping of chamber 2 while chamber 1 is isolated. The venting valve V2 of chamber 1 is then slowly opened, and the increase of chamber 1's pressure deforms the soft membrane which in turn applies a pressure in chamber 2. The release of the applied pressure is done by slowly venting chamber 2 with valve V3. As the membrane is opaque, the UV light is applied from the bottom as shown in figure 2.2. The process thus requires either a transparent substrate or a transparent stamp (or longer UV exposure time if the substrate is only partially transparent like PEN). Between 6 and 12 LED's from Roithner LaserTechnik GmbH (H2A1-H365) are used to shine the UV light.

Replication

Glass (0.5 mm thick, Schott AF45), stainless steel and flexible PEN (between 125 and 50 μm thick) with a size of 8.8 cm^2 or smaller were used as substrates for the UV-sensitive resin. The resins that were used in this thesis were Ormostamp andOrmocomp, which are hybrid polymers produced by the company Micro Resist Technology GmbH. The resin was applied by spin coating on the substrates. The Ormostamp product is specifically designed for stamp fabrication and, according to the company, sustains longer UV light exposure than Ormocomp before becoming brittle.

For most applications, the polymer layer thickness was chosen to be around 5 μm because thicker layers adhere less well to the substrate, and thinner layers did not lead to the full replication of the master features. Ormocomp diluted in solvent (OrmoThin ma-T 1050 from Micro Resist Technology GmbH) was first applied to obtain thicknesses between 28 μm (solvent free) and 500 nm (highly diluted) by spin coating at 3000 rpm for 30 s. In order to keep the process as simple as possible, Ormostamp was then used because layers with thicknesses of 5 μm are obtained when spin coated at 5000 rpm for 30 s without requiring solvent mixing.

A few particular experiments such as the replication of features with heights larger than 10 μm required thicker layers of resin and undilutedOrmocomp was used.

After spin coating, the substrate coated with the resin was thermally pre-baked to increase the homogeneity of the resin thickness and to increase the resin's adhesion to the substrate. This was done by placing the substrate on a hot plate (80–100 $^{\circ}\text{C}$) for 3–8 min. Then, the substrate and the stamp were brought into chamber 2 for moulding. They were kept apart by the manipulators until vacuum was achieved in both chambers. The separation between the stamp and the substrate avoids the formation of air bubbles which could occur if the stamp and the substrate were pressed together before the vacuum is established. Once a pressure of 40 mbar was reached in both chambers, the substrate and stamp were brought together and the pressure was applied on the sandwich with the soft membrane. After atmospheric pressure was reached slowly in chamber 1, the UV LEDs were switched on. The homogeneity of the light intensity is not perfect on the 8.8 cm^2 area: Intensities between 1.5 and 1.7 mW/cm^2 were measured under the middle of the substrate and of around 1 mW/cm^2 under the edge of the substrate. With these intensities a curing time of 1.5–3 min was used for glass substrates and an exposure time of 12–18 min was used for 125- μm -thick PEN substrates because their UV transmission is lower than glass. The LEDs were then switched off and chamber 2 was opened. In general, the substrate and the stamp were stuck together and were separated with care. The UV resin was not fully cured after this step and it was therefore placed under a UV light of an intensity of 3 mW/cm^2 for 20 min or longer. Subsequently, a thermal post-bake at 150 $^{\circ}\text{C}$ for three hours was needed to improve the film stability and to completely cure it.

2.1.2 Stamp fabrication

The master texture is moulded into the stamp (which hence contains the negative of the master texture) to obtain a replica which contains the original master texture as shown in figure 2.1. Two approaches were used for stamp fabrication: First, soft stamps using Polydimethylsiloxane (PDMS) were explored. Second, due to limitations in the fidelity of replication when PDMS was used, solid stamps were developed. These were made with high-fidelity of a direct replica in UV resin of the master. In the following paragraphs the processes used for stamp fabrication are explained. The stamp should possess efficient anti-sticking properties in order to allow for easy separation of the stamp-replica sandwich. The deposition of an additional anti-sticking layer was needed when solid stamps were used and this process is thus described. Finally, the process which led to the fabrication of the solid stamps allowed for the design of novel applications which are described as well.

Soft stamps

PDMS has been and is still widely used for the applications of moulding and replication of micro-textures (see in general [Xia 98, Qin 10] and references). PDMS provided by Dow Corning (Sylgard 184) was used in this thesis. It was prepared with a ratio of 10:1 between

the base and the curing agent and then degassed in vacuum. The PDMS was then slowly dispensed onto the master with a thickness of around 5 mm. The curing and hardening of the PDMS starts as soon as the two agents are mixed, but at a very slow rate at room temperature. In general, curing is carried out at 50 °C for 12 hours because curing at higher temperatures can reduce the replication fidelity because of higher PDMS shrinkage, and curing at lower temperatures was not seen to improve the replication quality.

The adhesion between PDMS and other materials is generally low and thus no anti-adhesion layer was added to the master prior to its moulding. After curing and demoulding the PDMS from the master substrate, a negative of the master texture was transferred to the surface of the PDMS which could then be used as a stamp.

Solid stamps

Other contributions have used ORMOCER[®] resins to produce solid stamps in a similar way as in this thesis [Klukowska 08, Klukowska 09, Mühlberger 09]. In this thesis, solid stamps were made by putting the master texture directly into contact with the UV-curable resin which was spin coated on a flexible PEN substrate. This resulted in a direct replica of the original texture and the presence of the negative texture into the UV resin. The use of the term "solid stamp" is slightly misleading. In the literature it generally refers to stamps made in quartz or other unyielding materials. In this thesis it is called "solid" in opposition to the soft PDMS stamp, as the UV-curable resin is much harder and less deformable than PDMS. The solid stamp was obtained following the procedure to replicate a texture on PEN as explained in section 2.1.1, but replacing the stamp by the master. Contrary to the PDMS stamp which had good anti-adhesion properties which allowed easy separation of the stamp from the master, the adherence between the master and the solid stamps is higher. Hence, it was necessary to deposit an anti-adhesion layer on the master prior to the stamp fabrication. Similarly, the use of a solid stamp in the replication process also required the deposition of an anti-adhesion layer on the stamp. The anti-adhesion treatment was done as follows: First, a thin layer of chromium (Cr) (5–15 nm) was deposited on the master or on the stamp. Second, a monolayer of fluoroalkylsilane(trichloro(tridecafluorooctyl)silane from United Chemical Technologies was deposited in the following way: A drop of the liquid was dispensed on a glass slide which was transferred with the substrate that required the anti-adhesion layer into a desiccator. The pumping of the desiccator led to the partial evaporation of the drop and the deposition of a monolayer on the substrate. The vacuum was then broken and the substrate was put for one hour in an oven set at 80 °C . After removing the stamp or the master from the oven they could be used after a rest of two hours. Depending on the imprinted texture, the anti-adhesion monolayer of fluoroalkylsilane was adjusted; the stamp or master was used several times before another layer of fluoroalkylsilane was added when the surfaces were smooth enough while, when aggressive textures were used, the deposition of fluoroalkylsilane was made prior to every use of the stamp or master. Examples of replicated textures using solid stamps can be found in figure 2.3.

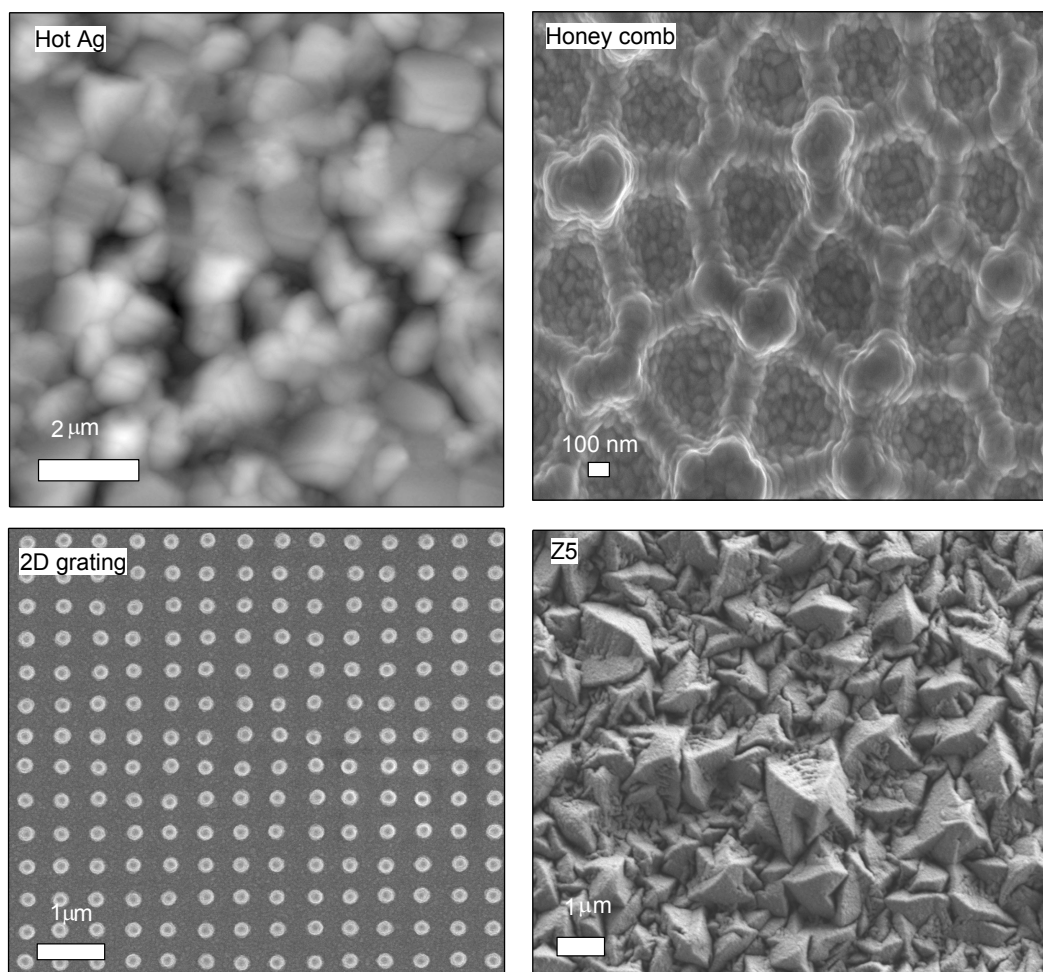


Figure 2.3: *Example of replicated textures using solid stamps.*

ZnO nanomoulding

The solid stamp fabrication and the use of the anti-adhesion layer inspired the development of a novel process to replicate arbitrary textures at the surface of LP-CVD ZnO layers. Figure 2.4 illustrates the process flow. First, a solid stamp containing the inverse of texture that the ZnO should adopt was processed as usual. Second, LP-CVD ZnO was grown on the solid stamp, adopting the desired texture on the growth nucleation side. Finally, the ZnO was detached from the stamp by anchoring it to a glass substrate using the UV resin. In order to be used as a substrate in solar cells, the nanomoulded ZnO was post baked in an oven for at least three hours at 150 °C .

The delicate step of this process was the adjustment of the solid stamp anti-adhesion layer, which should prevent spontaneous peeling of the ZnO while guaranteeing that controlled peeling during the anchoring remains possible. Most of the time, the anti-adhesion layer was

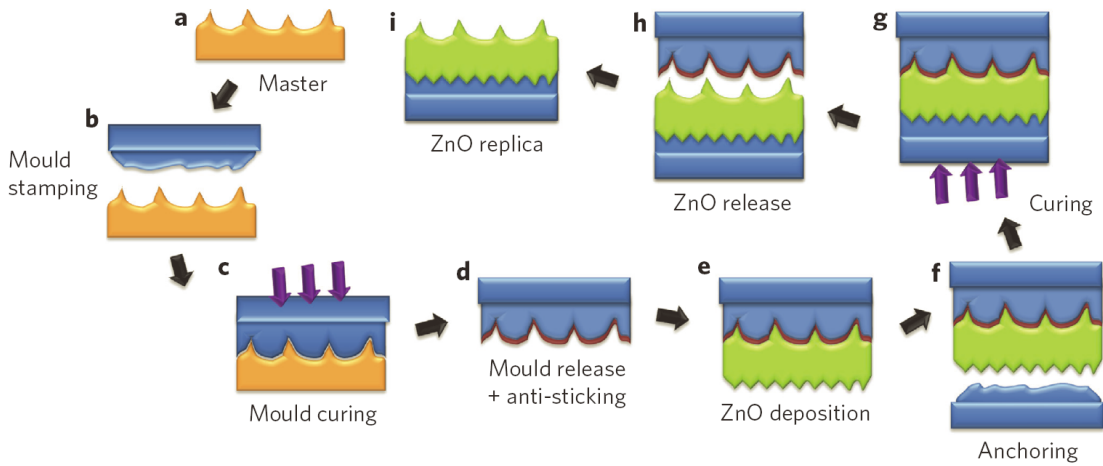


Figure 2.4: Schematic draw of the process flow for ZnO nanomoulding (reproduced from Battaglia et al. [Battaglia 11b]). The first steps a)–d) shows the fabrication of the solid stamp. In step e) is represented the deposition of LP-CVD ZnO on the solid stamp. Steps f) and g) present the anchoring of the nanomoulded ZnO by gluing it to glass with the standard UV resin and replication process. Finally, the nanomoulded ZnO replica is obtained in i) after careful peeling of the solid stamp as shown in h).

made as described previously but it was modified for the nanomoulding of smooth textures: To prevent spontaneous peeling either we used the deposition of the fluoroalkylsilane without adding the underlying Cr layer, or we used the Cr layer without depositing the monolayer of fluoroalkylsilane.

Whole or partial cell transfer and asymmetric intermediate reflectors

Once ZnO nanomoulding had been developed a wide range of transfer processes could be implemented. It was shown that the transference of a complete $p-i-n$ cell onto a flexible substrate could be done in a similar way as the ZnO nanomoulding [Escarré 12b]. One of the promising applications is the growth of advanced asymmetric LP-CVD ZnO intermediate reflectors for micromorph solar cells made of an a-Si:H $n-i-p$ cell and a $\mu\text{c-Si:H}$ $p-i-n$ cell. First, a stamp containing a negative of a texture suitable for the growth of an a-Si:H cell should be produced. Second, the asymmetric ZnO reflector should be deposited with feature sizes suitable for $\mu\text{c-Si:H}$ cell growth. Then the $\mu\text{c-Si:H}$ $p-i-n$ cell should be grown and LP-CVD ZnO should be deposited as a back contact. This stack should then be transferred onto a glass substrate by anchoring it with UV resin, and finally an a-Si:H top $n-i-p$ cell can be deposited prior to the final deposition of a LP-CVD ZnO front contact. This way, features on both sides of the intermediate reflector can be tuned independently.

2.1.3 Specific issues

Certain steps of the UV NIL process were more critical than others. In this section, the two main issues which came up during the development of the process are discussed.

Adhesion problems between resin and PEN substrates

The adhesion between the resin and the substrate can be critical when no adhesion promoter is added on the substrate prior to the resin spin coating. The company Micro Resist Technology GmbH sells a primer (OrmoPrime08) which is dedicated to increasing the adhesion of the ORMOCER[®] products to the substrate. The primer is very efficient when used with glass but it was not used for this purpose because there were no problems of adhesion with glass. Adhesion issues were critical with PEN substrates and, unfortunately, the provided primer does not adhere well to the PEN substrates. The primer could still be used effectively on PEN by depositing an SiO_x layer by PE-CVD before the primer spin coating, but this elongates the process of replication by a few hours. In order to reduce the time of processing, a second technique was used: The PEN substrates were covered with a thin Cr layer by sputtering (5–15 nm) and the adhesion of the resin to the PEN was increased sufficiently.

UV light intensity

The company Micro Resist Technology GmbH recommends an exposure dose between 500 and 6000 mJ/cm² for moulding applications, which is far above the dose described in section 2.1.1 when the stamp and the substrate are pressed together (100-300 mJ/cm²). This is because it was observed that when higher exposure dose was used during this step, the adhesion between the replica and the stamp was larger. This led to the resin transfer from the sample to the stamp during the separation of the stamp-replica sandwich when rough textures were replicated. This effect may be related to higher shrinkage of the polymer when exposed to higher UV dose, as shown by Geiser et al. [Geiser 10]. In this case, the polymer compress the mould, rendering the demoulding difficult due to high adhesion. Therefore, it was chosen to keep the UV exposure small before the sandwich separation, and additional UV and temperature curing can be done after demoulding.

There was another issue which could be partially controlled by UV light exposure: When replicas were used as substrates for the growth of solar cells, a degradation in yield was observed when LP-CVD ZnO was deposited after the silicon layers (as a front contact in *n-i-p* or back contact in *p-i-n* solar cells). Figure 2.5 presents *n-i-p* solar cells deposited on a glass/resin/Ag/ZnO:Al stack with a front contact made of LP-CVD ZnO. The image shown in figure 2.5a was recorded by lock-in thermography and an array of 16 cells (red squares) can be seen. The characteristic heating due to shunt paths can be recognised as the yellow lines which cross the cells. In general, shunt paths are due to point contacts between the front contact and the back contact and their origins can be diverse (dust, bad lift-off...). Accordingly, most

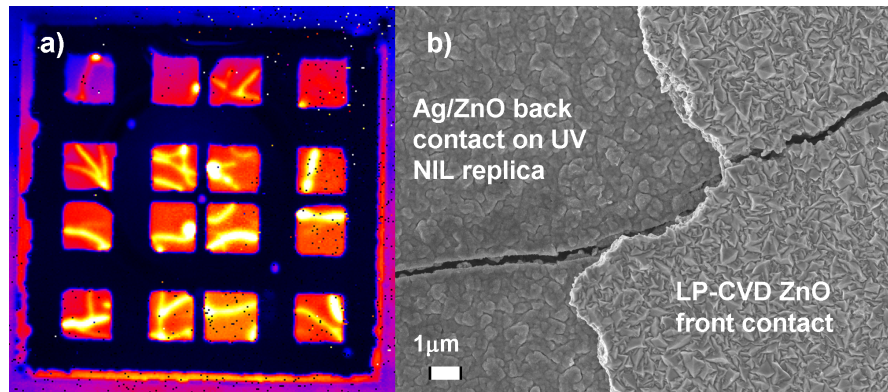


Figure 2.5: a) Lock-in thermography image of 16 solar cells. The cells can be recognised as the red squares and large yellow shunts of particular shapes appear on all cells. b) SEM image of a specific cell where both the back reflector and the front contact are visible. A large crack which is present in both the back and front contact is visible.

of the time, the specific yellow features are small points. The large lines that are observed in figure 2.5a indicate larger problems which are due to complete cracks in the solar cells. Large and spatially extended cracks could indeed be observed as shown in the SEM image of figure 2.5b. The replica shown in figure 2.5 was realised by curing the resin with twice the normal UV light intensity, the exposure dose was kept constant (i.e. the time of curing was reduced by a factor two), and no UV post-bake was done but the thermal post-bake was kept. As other cells made on replicas following the procedure described previously did not exhibit such large cracks, it was concluded that the curing procedure influences the mechanical properties of the resin. This is probably related to differences in the final conversion of the polymer as it was reported that the final conversion is not directly proportional to the exposure dose [Golaz 12]. Hence, the high intensity cure could possibly result in higher internal stress in the polymer [Schmidt 07].

This yield issue was not observed when an ITO front contact was used, and this can probably be related to the lower strain that the thin ITO film applies to the rest of the cell compared to a thick LP-CVD ZnO layer. Therefore, this issue could also depend on the deposition parameters of the LP-CVD ZnO contact, which can modify the internal stress in this layer [Addonizio 08].

In order to guarantee the best repeatability of the composite resin properties it is advisable to follow the procedure described in section 2.1.1 in which the polymerisation by UV and by thermal curing is kept long, thus ensuring reasonably stable properties. One should note that certainly other procedures in the process flow —thermal pre-bake, UV curing, UV post curing, thermal post bake— can be followed to obtain similar results. Also, the composition of the hybrid polymer may allow for different mechanical properties [Schmidt 07, Hussain 06] and thus the study and development of resins with specific properties will remain a busy field in the following years.

2.2 Deposition systems

At IMT, preparation of thin-film silicon solar cells begins with a bare glass (AF45 or AF32 supplied by Schott) or plastic substrate (PEN of 50 μm or 125 μm supplied by Goodfellow) onto which all other layers are deposited. For this purpose, several deposition techniques are used: Transparent conductive oxides (TCOs) were deposited either by sputtering (ITO, ZnO:Al) or by LP-CVD (ZnO), and metallic layers were deposited either by sputtering (Ag, Cr) or by evaporation (Al). Finally, all active or inactive silicon layers were deposited by plasma enhanced (PE) CVD. In this section, the different techniques and deposition systems are briefly presented.

2.2.1 Physical vapour deposition

Magnetron sputtering and evaporation were used to deposit metallic layers and TCOs by physical vapour deposition. The deposition systems and the typical conditions used are reported below.

Magnetron sputtering in Leybold Univex 450B

The Univex 450B is a Leybold system which is used to deposit metallic layers (Ag and Cr) and ZnO:Al buffer layers by magnetron sputtering with inert Ar gas. The targets have a disc shape with a diameter of 4 inches. The typical layer deposition conditions are listed in table 2.1. Some layers were used regularly in this thesis and thus their thicknesses and deposition temperature are also listed in table 2.1. Except for a few exceptions for which some help was provided, all the layers which were deposited in this machine and that are presented in this thesis were deposited by the author.

Table 2.1: *Typical sputtering parameters in Univex 450B with an Ar gas pressure of 5.5 μbar . The typical thicknesses of commonly used layers are also reported.*

	Power (W)	Excitation (DC or RF)	Deposition rate (nm/min)	Typical layer thickness (nm)
ZnO:Al	200	RF	5	
	As buffer between metal and Si in <i>n-i-p</i>			60–70
	As buffer between $\text{In}_2\text{O}_3\text{:H}$ and Si in <i>p-i-n</i>			20
Ag	250	DC	33–43	
	Standard Hot Ag for a-Si:H cell, glass substrate held at $\approx 200^\circ\text{C}$			500
	Standard Hot Ag for $\mu\text{c-Si:H}$ cell, glass substrate held at $\approx 300^\circ\text{C}$			700
Cr	500	DC	15	
	Standard adhesion layer			5–15

Reactive magnetron sputtering in MRC 603

The MRC 603 is a reactive magnetron sputtering tool that was used to deposit front contacts (ITO in the *n-i-p* configuration and hydrogenated indium oxide ($\text{In}_2\text{O}_3\text{:H}$) in the *p-i-n* configuration) using O_2 and water vapor as reactive gases and Ar as a carrier gas. The ITO and $\text{In}_2\text{O}_3\text{:H}$ targets had a size of 120 mm·378 mm.

For *n-i-p* solar cell front contacts, an ITO target composed of 90% In_2O_3 and 10% SnO_2 was used. Films with thicknesses between 55 and 75 nm were used to benefit from an anti-reflective effect to achieve maximum transmission into the cell around a wavelength of 550 nm [Cheek 79]. The film depositions were done at room temperature using a mixture of Ar and O_2 as gases. The addition of O_2 during sputtering allows the tuning of the electrical and optical properties [Kurdesau 06, Haug 12a]. The typical deposition parameters that were used are: A DC power of 1 kW, a pressure of 10 μbar with 6% of O_2 which led to a sheet resistance around 40 Ω_{\square} after annealing at 180 °C for 65-nm-thick films. All ITO layers presented in this thesis were deposited by the author except for those in the cells presented in section 3.3 and chapter 4 which were done by Dr. O. Cubéro.

For *p-i-n* front contacts, a target of indium oxide was used to deposit $\text{In}_2\text{O}_3\text{:H}$. In this case, the thickness of the film was less restricted by the anti-reflection condition as the highly textured resin already provides an anti-reflection effect due to the gradual effective index change at the $\text{In}_2\text{O}_3\text{:H}/\text{Si}$ interface. Also, low absorption can be reached even for thick films as the carrier density of this material is much lower than for standard ITO films. Hence, a thickness of 135 nm was used to obtain a sheet resistance of 26 Ω_{\square} after annealing at 200 °C. The deposition parameters were RF power of 0.8 kW, a pressure of 6 μbar with 0.2% of O_2 and a partial pressure of water vapor of $9 \cdot 10^{-2}$ μbar . More details on the fabrication of these film and on their properties can be found in the works of Koida et al. who first introduced these TCO films [Koida 07, Koida 10b, Koida 10a]. The $\text{In}_2\text{O}_3\text{:H}$ layers that are shown in section 3.4 were deposited by Dr. C. Battaglia and their optimisation layer was carried out by Dr. C. Battaglia and L. Erni.

Evaporation in Leybold Univex L560

Aluminium reflectors were made by using Joule effect evaporation of Al in a Leybold Univex system. The base pressure before evaporation was 5 μbar and the deposition rate was typically 6 Å/s. These evaporations were all made by X. Niquille.

2.2.2 Chemical vapour deposition

Chemical vapour deposition techniques were used to deposit ZnO contacts and all silicon layers in different systems that are described below.

LP-CVD ZnO

Front and back contacts in the laboratory are often based on boron-doped LP-CVD ZnO layers deposited using diethylzinc, water vapor and diborane as source gases. These layers are deposited in regimes for which the grain growth induces a natural pyramidally textured surface with pyramid sizes that can be tuned with deposition time and doping [Faÿ 05, Nicolay 09]. Common films are 2 μm thick (Z2) or 5 μm thick (Z5). The sheet resistance can be tuned by adjusting the doping. In this thesis the sheet resistance of the front contacts was between 8 Ω_{\square} and 40 Ω_{\square} . The ZnO pyramidal texture is known to lead to efficient light trapping in solar cells [Faÿ 07, Rockstuhl 10, Fahr 11]. The texture of the Z2 surface is optimised for a-Si:H single-junction solar cells while Z5 is more suitable for light trapping in $\mu\text{c-Si:H}$ single-junction solar cells. The deposition conditions of these films can lead to a multitude of different film properties which are widely covered in the literature [Faÿ 05, Steinhauser 07, Steinhauser 08, Nicolay 09, Faÿ 10, Nicolay 11, Ding 12]. Applications in thin-film silicon solar cells can be found in [Dominé 08, Python 08a, Boccad 12a] for the *p-i-n* configuration and in [Söderström 09a] for the *n-i-p* configuration. The LP-CVD ZnO layers that are shown in this thesis were deposited in a home-built system and only partially by the author.

PE-CVD for silicon

Silicon layers in this thesis were all deposited by PE-CVD and several systems were used for this purpose. All cells were deposited using mixtures of the following gases: silane (SiH_4), hydrogen (H_2), phosphine (PH_3), trimethyl boron (TMB), methane (CH_4) and carbon dioxide (CO_2). Mixture of SiH_4 and H_2 were used to deposit a-Si:H and $\mu\text{c-Si:H}$ *i*-layers. The doped layers were grown by adding PH_3 and TMB to mixtures of SiH_4 and H_2 to grow *n*- and *p*-doped layers, respectively. CH_4 can be added to the gas mixture to incorporate a small amount of carbon in the layer which increases its band gap. Finally, CO_2 can be added to the gas mixture to incorporate a small amount of oxygen to grow silicon oxide (SiO_x) layers. These last years, SiO_x doped layers have drawn a lot of interest: It was seen that the incorporation of these layers into cells leads to V_{oc} and FF values that are more tolerant to rough substrates and, at the same time, they are more transparent than standard doped layers and therefore lead to less parasitic absorption [Despeisse 10, Cuony 10]. Also, it was observed that they could play the dual role of electrical contact buffer layer in *n-i-p* solar cell back reflectors [Delli Veneri 10, Yan 11].

The silicon deposition systems and some details of the different solar cells that are shown in this thesis can be found below.

Small-area reactor system E for a-Si:H *n-i-p* Solar Cells

Except for the cells shown in section 3.3 and chapter 4, all solar cells which were deposited in system E and that are presented in this thesis were deposited by the author using a base recipe which was developed by T. Söderström, Dr. O. Cubéro, Dr. C. Pahud and R. Biron.

System E is a single-chamber "home-built" reactor which is used specifically for *n-i-p* a-Si:H solar cells. The active area for deposition is 8.8 cm² and the layers were deposited at a very high frequency (VHF) of 70 MHz, a temperature of 190 °C, with pressure around 300 μbar and power between 15 mW/cm² and 80 mW/cm². The *i*-layer was deposited with a dilution ratio $\frac{H_2}{SiH_4} = 2$. The *n*-doped layer was an amorphous silicon carbide layer deposited with a mixture of SiH₄, PH₃ and CH₄ as described in Söderström et al. [Söderström 08a]. The *p*-doped layer was deposited with a mixture of SiH₄, H₂ and TMB in the μc-Si:H regime in chapters 3 and 4. For the cells that are presented in the other chapters, CO₂ was added to the gas mixture during *p*-doped layer growth to incorporate oxygen as described in Biron et al. [Biron 11].

Large-area reactor: KAI-M for μc-Si:H *p-i-n* and μc-Si:H and a-Si:H *n-i-p* solar cells

The large-area KAI-M system is a double-chamber "home-built" reactor using plasma boxes and electrodes from the company Oerlikon. It was used to produce μc-Si:H solar cells in the *p-i-n* and *n-i-p* configurations as well as a-Si:H *n-i-p* solar cells on an homogeneous area of 25.25 cm².

μc-Si:H solar cells: The *n-i-p* μc-Si:H cells that are presented in this thesis were all deposited by the author and the *p-i-n* cells were deposited by G. Bugnon. The layers that were used for both *n-i-p* and *p-i-n* μc-Si:H solar cells were developed by Dr. A. Feltrin, Dr. G. Parascandolo and G. Bugnon. In all cases, the *i*-layer was deposited at a low deposition rate (approximately 3 Å/s), with pressure around 9 mbar, power around 150 mW/cm² at a temperature 180 °C to obtain high-quality μc-Si:H material. Small amounts of CO₂ were added to the precursor gases of the *n*- and *p*-doped layers. An extended study of the material qualities as a function of the growth conditions and oxygen content of the doped layers of *p-i-n* solar cells can be found in Bugnon et al. [Bugnon 12].

a-Si:H solar cells: The results shown in sections 5.2 and 5.3 required the deposition of co-deposited a-Si:H *n-i-p* solar cells on large areas. For this reason this solar cell structure was developed in the KAI-M reactor. This was done partially by the author but the layers that were used for this cell were transferred from previous work. All a-Si:H cells that were deposited in the KAI-M reactor and that are presented in this thesis were deposited by the author. The cell layers were deposited at a temperature of 180 °C at a high frequency of 40 MHz with a pressure around 0.3 mbar and a power around 50 mW/cm². The *n*-doped layer was grown in the μc-Si:H regime and the *p*-doped layer was also grown in the μc-Si:H regime but oxygen was incorporated into this layer to improve its transparency. The dilution ratio of the *i*-layer was around 2, similar as in the small-area reactor system E.

Large-area reactor: KAI-S for *p-i-n* a-Si:H solar cells

The *p-i-n* a-Si:H solar cells that are presented in sections 3.4, 3.5 and 3.6 were deposited in a large-area "home-built" KAI-S system using a plasma box and electrodes from the company Oerlikon. The homogeneous area of deposition is of 20·20 cm². The deposition and the solar cell development were done predominantly by M. Charrière. The silicon layers were deposited at a temperature of 200 °C at a high frequency of 40 MHz with a pressure around 0.5 mbar and a power around 40 mW/cm². The *n*-doped layer and *p*-doped layer were grown in the μ c-Si:H regime and oxygen was incorporated in these layers to improve their transparencies.

2.3 Post-fabrication modification of substrates

2.3.1 Argon plasma treatment

The pyramidal texture that develops during the standard LP-CVD ZnO deposition has proved to be a very good texture for light trapping. Millions of square meters were coated with LP-CVD ZnO by production lines sold by the company Oerlikon, enhancing the efficiencies of the produced modules. Other experimental and theoretical approaches found that this kind of texturing leads to excellent light trapping [Rockstuhl 10, Rockstuhl 11]. However, the sharp features of this pyramidal texture are detrimental for the growth of silicon material with high quality. Hence, the V_{oc} and FF of solar cells grown on pyramidal features are lower than those of a cell grown on a flat substrate. Therefore, the LP-CVD ZnO substrates are often treated by plasma using argon and oxygen as gases to reduce their roughness and to lead to more rounded features. The longer the LP-CVD ZnO layer is treated, the smoother it becomes. It was shown that a longer treatment leads to a decrease in the light trapping-properties of the substrate and an increase of the V_{oc} and FF values of solar cells grown [Bailat 06, Python 08b, Söderström 08a, Söderström 08b, Boccard 11, Boccard 12e]. Hence, the time of treatment is optimised to obtain the best compromise in the V_{oc} , FF and J_{sc} product to obtain the highest efficiency for the solar cell grown on top of the textured LP-CVD ZnO.

2.3.2 Chemical mechanical polishing

The chemical mechanical polishing (CMP) system was built by P. Cuony and S. Hänni [Cuony 11] and a sketch of this system is presented in figure 2.6. The sample to be polished is fixed on the bottom of a watertight aluminum receptacle. A solution of deionised water and silica particles with a diameter of 40 nm is poured into the receptacle. The actual polishing is performed by a felt disc which is mounted on a drill, rotated at 5000 rpm and pressed on the substrate with a homogeneous pressure. The aluminum receptacle is fixed on an X-Y moving table which has a step resolution of 20 μ m. The X-Y table is used to scan the sample below the rotating felt head in order to polish the sample in a homogeneous manner. The concentration of the silica particles in the solution, the number of polishing passes, as well as the distance of the X-Y table step can be used to control the final state of polishing. The polished sample has to

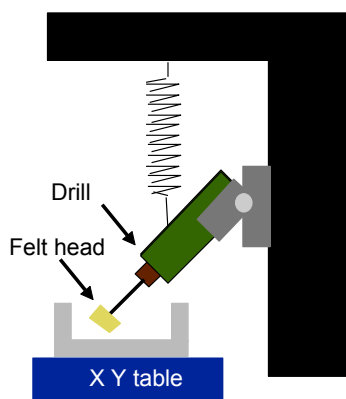


Figure 2.6: *Sketch of the chemical mechanical polishing system.*

be cleaned before further use as a lot of silica particles remain on the sample. The cleaning was done by scrubbing the sample with paper suitable for cleanroom activities below a water jet and finally blowing it dry using a nitrogen flow. In this thesis, the CMP was used to produce back reflectors of high quality for the growth of multi-junction solar cells as shown in chapter 6 and section 7.6.

2.4 Characterisation techniques

2.4.1 Substrate characterisations

Substrate characterisation was of high importance during this thesis. At first, we characterised the fidelity of replication technique. In the second part of the thesis, we related the substrate roughness with the electrical properties of a cell grown on the substrate. Except for some measurements shown in chapter 3 all substrate characterisation presented in this thesis was carried out by the author.

Spectrophotometer: Lambda 900 Perkin Elmer

Total (TR) and diffuse reflectance (DR) of back-reflector substrates and of complete solar cell devices were measured using a Lambda 900 Perkin Elmer dual-beam spectrometer equipped with an integrating sphere. A grating monochromator allows one to scan a wavelength range between 320 nm and 2000 nm that is produced by deuterium and halogen light sources. Figure 2.7 presents a sketch of the integrating sphere and of the sample position for TR measurements: The monochromatic probe beam enters the integrating sphere through a port and hits the sample with an angle of 7° . The reflected specular beam hits a port that is removable in order to allow the measurement of DR. A calibration is performed before the measurement by placing a highly reflective calibration sample made of SpectralongTM in the place of the

sample. The monochromatic reference beam is used to correct the background, which is

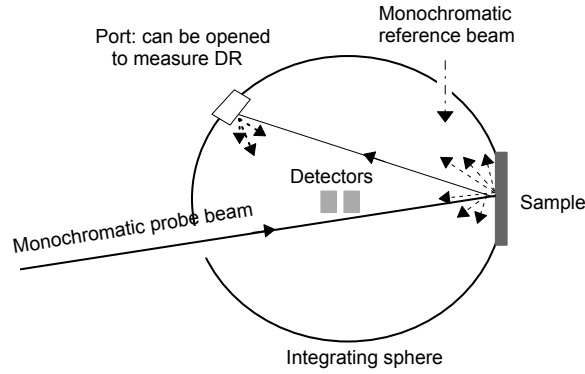


Figure 2.7: Sketch of the integrating sphere and position of the sample during TR measurement.

modified when the sample to be measured is placed at the position of the calibration sample and the port to measure DR is open. The haze value $\text{haze}(\lambda) = \text{DR}(\lambda) / \text{TR}(\lambda)$ is the percentage of scattered light for each wavelength and is very useful to probe the roughness of the sample.

Angular resolved scattering

The angular resolved scattering (ARS) measurement serves to quantify the angular distribution of the scattered light. Figure 2.8 presents a schematic of the measurement setup in reflection mode. The probe beam is a laser with a wavelength of 543 nm and is chopped and sent to the sample which is placed perpendicular to the laser beam. The intensity of the scattered light is measured with a silicon photodetector which is mounted on a goniometric arm that rotates in the plane that is perpendicular to the substrate with a step of 1.4° from an angle θ of -90° to $+90^\circ$. A lock-in system is used to amplify and measure the signal detected by the photodetector. When the light is isotropically scattered around the azimuthal angle ϕ , such as with random textures, the sine-weighted ARS gives to the total intensity which is scattered at each angle. Hence, in this thesis we compare the sine-weighted quantity defines as: $\text{sine-weighted ADF}(\theta) = \text{ARS}(\theta) * \sin(\theta)$. In reality, the integration of the sine-weighted ADF is equal to the haze value at the wavelength of measurement. But, as the ARS is measured in an air environment, and as the haze value is different in air and in silicon, in this thesis the sine-weighted ADF was arbitrarily normalised such that its maximum value is equal to one. This allows for the qualitative comparison of the angle of scattering in air.

Scanning electron microscope

If not stated otherwise, all images obtained with a scanning electron microscope (SEM) were taken by myself on a JSM-7500, which is a field-emission SEM of JEOL which is own by the Optic group of Prof. H.P. Herzig.

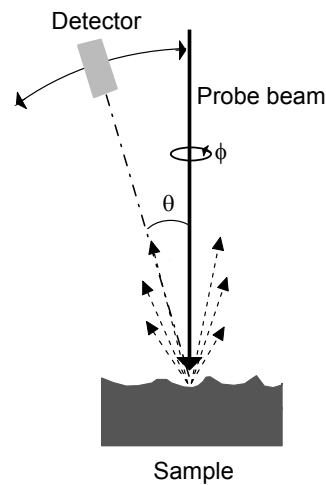


Figure 2.8: Sketch of the ARS measurement set-up.

SEM uses the high energy of an electron beam to resolve much smaller details than what a classical optical microscope can do. The beam of electron scans the sample and different detectors detect the electrons that are emitted from the surface due to the interaction of the probe beam and the atoms at the sample surface. The SEM that was used is equipped with two different detectors that rely on the detection of secondary electrons: the Secondary Electron Imaging (SEI) detector and Lower Electron Imaging (LEI) detector. The secondary electrons are the electrons emitted from the sample as a consequence of the absorption by the sample of the higher energy electrons called primary electrons. The SEI detector is positioned directly in the column of the electron gun and thus collected the electrons that possess relatively high energy and which are therefore emitted close to the surface of the sample. As a result, little contrast between elements or different crystallographic orientations can be observed. The LEI detector is situated on the side of the sample and thus collects electrons with lower energy that are deflected with the voltage applied by this detector. The LEI images present high topological contrast due to the detector position inside the SEM. The probability that an electron issued from the sample can be deflected and collected by this detector is higher for a feature that faces the detector. Thus, for instance, a facet of a pyramid that faces the detector appears brighter than the facet that is opposite to the detector because a higher number of secondary electrons are collected.

Figure 2.9 presents a comparison between an image taken with the LEI detector and an image taken with the SEI detector. The sample is a flat light-light scattering substrate as discussed in chapter 6 and consists of ZnO embedded in a matrix of a-Si:H. The a-Si:H appears darker in both images. In both images it is possible to distinguish between both materials. However, SEI imaging does not show the substrate roughness while the LEI imaging clearly reveals that asperities are present at the sample surface. As it was of most importance for this kind of substrate to know whether they contained asperities, this comparison shows the importance

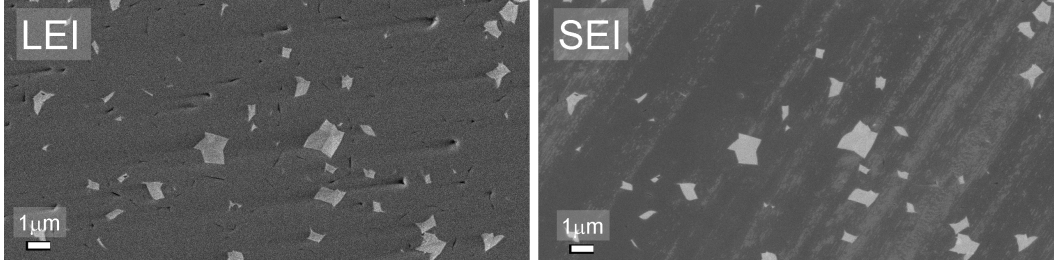


Figure 2.9: *Comparison of SEM images using LEI or SEI detectors.*

of being critical when analysing SEM images.

Atomic force microscopy

Atomic force microscopy (AFM) was used to perform substrate morphological analysis using a Digital Instruments Nanoscope 300. The majority of the images that are shown in this thesis were performed by M. Leboeuf from the Swiss Center for Electronic and Microtechnology (CSEM) and a few of them was performed by the author. Depending on the substrate feature sizes, the probed surfaces were of $10 \cdot 10 \mu\text{m}^2$ or $5 \cdot 5 \mu\text{m}^2$ with a resolution of $512 \cdot 512$ pixels. Image manipulation was done using the free software presented in Horcas et al. [Horcas 07] and several parameters were extracted using in-house softwares that were developed on Matlab by Dr. J. Escarré in order to quantify the surface features with figures of merit. The root mean square roughness (σ_{rms}), the correlation length (L), the mean angle and the ratio between the scanned area and the projected flat surface (A_{flat}/A_{scan}) were extracted to compare the surface features. σ_{rms} gives information about the vertical size of the roughness and was directly extracted with the software WSxM. L represents the lateral size distribution of the surface texture, and it is defined as the radius of the disc obtained by cutting the autocorrelation peak of the AFM image at $1/e$ of its maximum. Note that σ_{rms} and L represent the commonly used approximations of the surface height distribution and the autocorrelation function, respectively, by Gaussian distributions [Davies 54]. When the autocorrelation functions extracted from the AFM images are not perfectly Gaussian, the cut used to determine L is slightly elliptic. In this case L was approximated as the radius of a disc having the area of the elliptic cut. The mean angle was determined as the average angle between the surface normal and the local inclination evaluated for every point of the surface of the AFM image giving both vertical and lateral information.

2.4.2 Solar cell characterisations

This section describes the two main measurement tools which were used to characterise solar cells. The external quantum efficiency (EQE) measurement is used to determine the optical performance of a device, while an I-V measurement is used to evaluate its electrical

performance. All solar cells characterisation were performed by the author except the one shown in chapters 3 and for the I-V measurement of the cell discussed in chapter 4.

External quantum efficiency

The EQE is a measurement of the probability of collecting a photo-generated electron-hole pair per photon of each wavelength that is shined on a device in short-circuit condition. This measurement was often used in this thesis to compare light trapping in solar cells which were co-deposited on different substrates. Roughly, the EQE can be divided into two zones: Below 500 nm the EQE is mainly influenced by the absorption occurring in the front TCO and the p -doped layer, and by the anti-reflection properties due to the surface morphology of the front contact. Above 500 nm the light begins to interact with the back reflector and the EQE is thus also influenced by the quality of the light trapping and by the parasitic absorption that takes place in the n -doped layer and in the back reflector. This measurement was used to calculate the J_{sc} of the solar cells by integrating the convolution of the EQE and the AM1.5G spectrum.

The setup used for the measurement of single-junction devices is described below. The setup for measuring multi-junction devices is the same as for single junction devices but, additionally, a set of bias lights are needed to resolve the EQE of each sub-cell [Burdick 86]. The different possible bias lights are shown in figure 2.10 where the bias lights that are obtained from using a halogen lamp in combination with different types of filters are shown as solid lines, and additional blue and red LEDs that can be used are shown in dashed lines. The

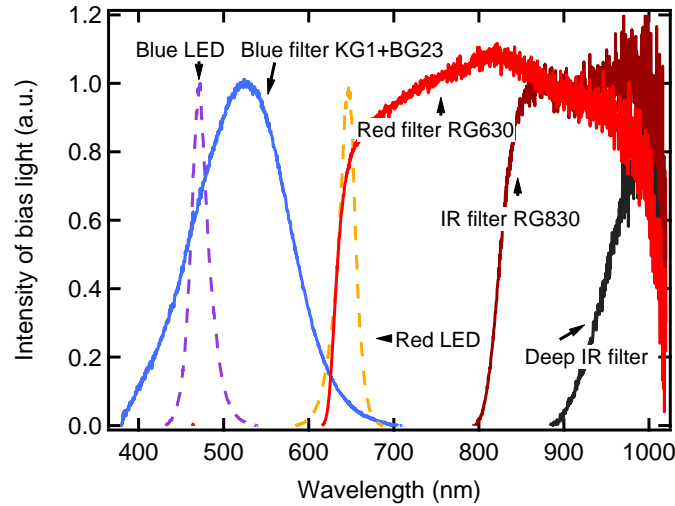


Figure 2.10: Bias lights that are available on the EQE measurement setup. In dashed lines are shown the red and blue LED emission peaks and in solid lines are shown the transmission of different filters that can be used in front of the halogen lamp.

measurement conditions which were used for the characterisation of multi-junctions devices are described in detail below because it is not trivial to measure them accurately. Indeed, the

EQE measurement of each sub-cell in a multi-junction device requires the saturation of the other sub-cells with light; as a consequence, the sub-cells which are saturated with light apply a negative voltage to the cell under measurement which help the carrier collection and can lead to an over-estimation of the EQE [Burdick 86]. In order to best reproduce the short-circuit conditions for the sub-cell under measurement, a positive bias voltage was applied. As the negative bias voltages that are applied by the sub-cells which are saturated with light depend on the current matching of the cell and on the intensity of the probe and bias lights, it is difficult to know exactly the positive voltage that should be added to obtain the most accurate measurement. Hence, the bias light and the voltage bias that were used in this thesis are given below for each type of device.

The EQE is useful in itself for solar cell analysis, but one can go further, as the sum of the EQE, the parasitic absorption A_p and the TR is equal to unity if there is no light transmitted through the device (i.e. $TR+TA=1$ implies that $TR+EQE+A_p=1$, where TA is the total absorbance). Additional information can thus be obtained from the measurement of the EQE and TA of the solar cell. A_p can be compared using the internal quantum efficiency (IQE) which is defined as $IQE=EQE/TA$. If $TA=EQE$, which corresponds to the ideal case where $A_p=0$, the IQE reaches its maximum value of unity. It is thus a measure which does not depend on the light trapping properties of substrates and is the probability that an absorbed photon creates an electron-hole pair which is collected.

Single-junction solar cell measurement:

The EQE setup which was built at IMT is made of a monochromator which is used to scan the wavelengths of the probe beam issued from a Xenon lamp. The probe beam is chopped at a frequency of 230 Hz and then separated in two to illuminate both the solar cell (spot of $\approx 1 \text{ mm}^2$ when focused) and a reference photodetector. A lock-in is used to amplify the signal delivered by the cell, which has the defined frequency of 230 Hz. In order to best estimate the EQE under an AM1.5G spectrum, a bias light made of white LEDs is used. In principle, the white light at the position of the measurement should possess the AM1.5G spectrum and intensity and the probe beam intensity should be small compared to the bias light intensity. In this case, the small variation of the measured photocurrent divided by the elementary charge q and the photon flux measured with the reference photodetector allows for the correct determination of the EQE. However, in our system the bias light does not have an intensity of 1000 W/m^2 and the probe beam has a high intensity at particular wavelengths, inducing some measurements error. Nevertheless, after comparison with other EQE setup, it seems that our measurements correlate well with other laboratories (e.g. Utrecht, AIST, Unisolar) and hence the error does not seem to be significant.

Tandem a-Si:H/a-Si:H solar cell measurement:

The measurements of the separate EQEs of the a-Si:H sub-cells which compose a tandem a-Si:H/a-Si:H device were done using a positive bias voltage of 0.5 V for both the top and bottom cells. Figure 2.11 shows the typical EQEs that are obtained. Additionally, the bias light

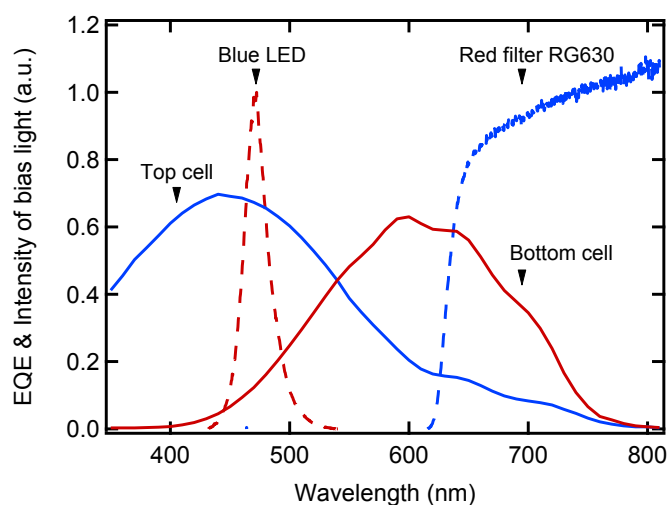


Figure 2.11: Typical conditions for the measurement of $a\text{-Si:H}/a\text{-Si:H}$ devices. The EQEs of the sub-cells are in solid lines and the bias light spectra are in dashed lines.

spectra that were used during the measurement of the sub-cells are shown as dashed lines in figure 2.11. The colors of the dashed lines correspond to the the EQE curves for which the bias lights were used (i.e. the bottom cell EQE measurement requires the saturation of the top cell with the blue LED).

Tandem $a\text{-Si:H}/\mu\text{c-Si:H}$ solar cell measurement:

A positive bias voltage of 0.5 V was applied during the EQE measurement of the top cell of

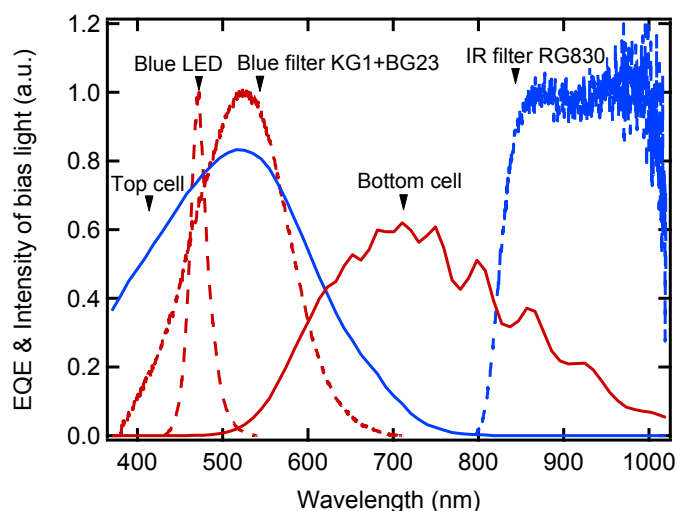


Figure 2.12: Typical conditions for the measurement of $a\text{-Si:H}/\mu\text{c-Si:H}$ devices. The EQEs of the sub-cells are in solid lines and the bias light spectra are in dashed lines.

a-Si:H/ μ c-Si:H devices while 0.7 V was used during the bottom cell measurement. Figure 2.12 shows the typical EQE curves of each sub-cell in solid lines and the bias lights that were used in dashed lines.

Triple-junction a-Si:H/ μ c-Si:H/ μ c-Si:H solar cell measurement:

In the case of triple-junction a-Si:H/ μ c-Si:H/ μ c-Si:H solar cells, a positive bias voltage of 0.7 V

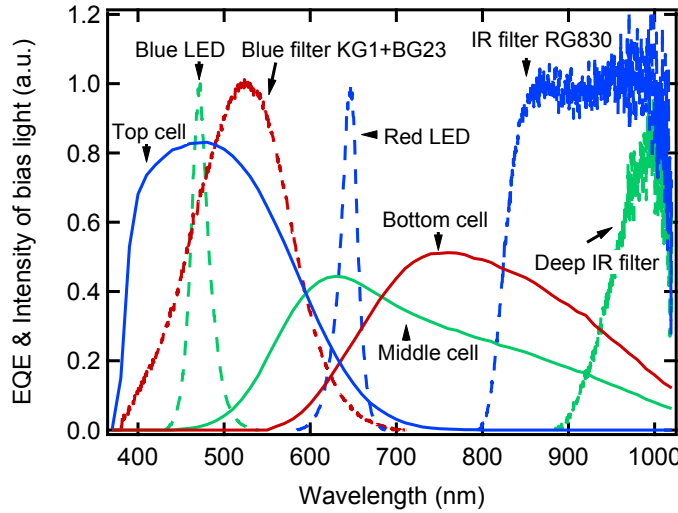


Figure 2.13: Typical conditions for the measurement of a-Si:H/ μ c-Si:H/ μ c-Si:H devices. The EQEs of the sub-cells are in continuous lines and the bias light spectra are in dashed lines.

was used for the top cell measurement while 1 V was used for both the middle and the bottom cell measurements. Figure 2.13 shows the typical EQE curves of each sub-cell in continuous lines and the bias light that were used in dashed lines.

I-V measurements

I-V measurements were performed using a steady-state dual-beam sun simulator from Wacom (WXS-220S-L2). The light intensity was set at 1000 W/m^2 with a spectrum that was regularly checked and calibrated to be as close as possible to the AM1.5G spectrum. I-V curves were obtained by a four-probe voltage sweep on cells and were used to derive the V_{oc} and FF of the cells. The J_{sc} was determined from EQE measurement as explained above because J_{sc} extraction from an I-V curve requires the exact determination of the solar cell area. The incertitude in the measurements of the cells presented in this thesis are mainly due to three sources. First, inexact determination of the cell temperature during measurements can lead to an under- or over-estimation of the V_{oc} . In some experiments such as the measurement of triple-junction *n-i-p* solar cells shown in section 7.6 a cooling table was used in order to maintain the temperature between 22°C and 25°C for all substrates. Second, an over-estimation of the FF can occur when four-probe measurements are done on a solar cell which combines

resistive contacts and high J_{sc} values. However, this should not be important for the $n-i-p$ solar cells shown in this thesis because of the low resistance of the silver back contact and ZnO:B front contact. When ITO was used as a front contact, a silver paste was added and hence there should not be over-estimation of the presented FF values. The third and last major issue that can influence the precision of the FF measurements of a multi-junction device is an incorrect calibration of the I-V lamps. As the current matching conditions dramatically influence the device FF [Burdick 86], the incorrect reproduction of the AM1.5G solar spectrum leads to differences in the sub-cells J_{sc} which leads to an under- or over-estimation of the real FF . As we use a class AAA sun simulator this latter issue should not be important.

3 UV nano-imprint lithography

This chapter presents the replication fidelity that can be obtained by using the UV nano-imprint lithography (UV NIL) process as well as the numerous applications for the replicas in different type of devices and in different positions in devices. First, the replication fidelity depending on the stamp material is discussed in section 3.2. The use of the soft PDMS stamp allows smoothening aggressive textures, rendering the post-deposition plasma treatment of LP-CVD ZnO avoidable, while use of solid stamp allows the replication of nano-textures with a high level of fidelity such that the master and replica are indistinguishable by AFM, SEM or optical characterisation. It is then shown that the UV NIL process not only allows the texturing of back contacts on plastic substrates in the *n-i-p* configuration (section 3.3) but also can work for texturing front contacts in the *p-i-n* configuration (section 3.4). Efficiencies similar to those on standard electrodes are obtained in both configurations. A tandem a-Si:H/a-Si:H device in the *n-i-p* configuration with an 8.1% stable efficiency is obtained on a plastic substrate textured with UV-NIL, and a micromorph solar cell in the *p-i-n* configuration exhibited a 12% initial efficiency. In both cases, UV NIL promises further efficiency increases by allowing the implementation of novel photonic textures for improved light management. This is particularly useful for *p-i-n* devices, which have for a long time been limited by the shapes of the textured electrodes. It is shown in section 3.4.2 that by introducing a multi-scale electrode via nano-imprinting, a record initial efficiency above 14% was obtained for a micromorph device. Section 3.5 presents results of the novel nanomoulding tool used to shape LP-CVD ZnO surfaces, which allows for independent optimisation of the texture and the electrical properties. High-fidelity replication is demonstrated and devices grown on these new electrodes exhibit similar efficiencies to those grown on standard electrodes. Finally, UV NIL replicas placed at the front of devices can also further enhance solar cell efficiencies by acting as an anti-reflective coating, and a boost in J_{sc} of more than 4% is demonstrated in section 3.6. All these results demonstrate that the versatility and flexibility of the UV NIL technique opens novel routes to further improve solar cell efficiencies. As well, it is an extremely useful experimental tool for research as it allows the design of substrates specifically for the requirements of a particular experiment. In this thesis, substrates made by UV NIL are used in all the following chapters with the exception of chapter 6.

3.1 Introduction

In general, the interface texture used for light scattering in thin-film silicon solar cells is given primarily by the contact layer onto which the solar cell is deposited. Therefore, most of the feature shapes are based on the self-developing texture that forms during the growth of the contact. Because the electrode on which the solar cell is deposited is required to be transparent in the *p-i-n* configuration, the textures are commonly made of SnO₂:F [Iida 83, Mizuhashi 88] and ZnO:B [Faÿ 05] which are known to develop a pyramidal texture for a certain range of depositions parameters, and flat sputtered ZnO:Al which develops a crater-like texture after acid etching [Kluth 99]. In addition to these textures, the *n-i-p* configuration allows the use of opaque textures such as those that develop due to grain growth when silver or aluminium are sputtered onto a substrate held at high temperature [Thornton 86]. However, when *n-i-p* solar cells are deposited on plastic substrates, texturing of the back contact is difficult to implement because of the low thermal resistance of cheap plastic and because of the brittleness of thick ZnO. Therefore, flexible techniques to nano-texture glass and plastic substrates could emancipate thin-film silicon technology from the conventional textures, and integrate optimised textures directly into functional devices.

Contact texturing in thin-film silicon solar cells by the replication of nano- and micro-metric textures using different techniques was demonstrated prior to this thesis. Complex photolithography coupled with reactive etching [Eisele 01, Senoussaoui 04, Stiebig 06b], UV nano-imprint lithography (UV-NIL) [Terrazzoni-Daudrix 03, Bailat 05, Rudigier-Voigt 09] and hot embossing of a substrate [Escarré 05] or a temperature curable sol-gel [Heijna 08, Isabella 08] are technique that had already drawn a certain interest in thin-film silicon solar cells by the beginning of this thesis. From this panel of techniques, UV NIL was chosen and implemented at IMT since 2002 to replicate nano-textures in a transparent UV-sensitive polymer as it possesses several advantages compared to the other mentioned techniques. Photolithography coupled with reactive etching for ZnO texturing is restricted to periodic patterns, is expensive and requires laser illumination. Embossing of polymer is a well-known technique but exhibits in general a lower resolution and requires higher pressure and temperature than UV NIL. Even if NIL is a rather young technique—it was first demonstrated in 1995 by Chou et al. [Chou 95]—, it has attracted tremendous attention over these last fifteen years and has been extensively developed. For these reasons, the UV NIL technique is probably the best choice between the three discussed here to perform replication of nano-textures both at the laboratory scale and in industrial environments.

In a broader view, UV NIL allows the upscaling of textures whose fabrication is limited to small areas, or is time consuming or too expensive, such as those fabricated by e-beam. Furthermore, if done in a transparent polymer, UV NIL is compatible with laser scribing which allows the monolithic series interconnection of cell segments of large-area modules. Recent publications indicate that thin-film silicon solar cell manufacturers are highly interested by this approach: Samsung published a 12.8%-efficient cell on a UV NIL textured glass [Bessonov 11], VHF Technology presented a cell with a stabilised efficiency of 8% on a plastic foil textured by UV

NIL [Couty 11], and Moser Bauer presented a UV NIL textured Gen5 size glass [van Erven 12]. Furthermore, partially because of the excellent results which are shown in this chapter, a European FP7 project called "Fast-Track" is currently running and is aimed at upscaling the technique to the module size.

3.2 Characterisation of the replication quality

The first part of this section presents results of replication using soft stamps made of PDMS as described in section 2.1. Several morphological parameters were extracted from AFM images in order to quantitatively characterise the replication quality. Relationships that exist between the different parameters will be discussed in order to reduce the number of parameters that are needed to characterise each texture. In a second part, the improvement of the replication quality using solid stamps is shown, and a comparison with the quality obtained by using PDMS stamps is given for a standard type of electrode with random features.

3.2.1 Characterisation of replicated texture using soft PDMS stamp

The fidelity of replication was characterised both optically (spectrophotometer and ADF) and morphologically (AFM) as described in section 2.4. Before performing any characterisation, 120 nm of silver was deposited at room temperature on both the master textures and the corresponding replicas (with the exception of the Hot Ag master). The addition of the silver layer had several functions:

1. The scattering properties of substrates without silver layer cannot be directly compared as the index of refraction of the textured materials differs between the masters and the replicas (ZnO, resin or silver).
2. The UV NIL replicas were initially dedicated to *n-i-p* cells, thus the optical properties in reflection were of primary importance.
3. The silver ensured a similar interaction between the AFM tip and the surfaces for both masters and replicas, thus allowing an easier comparison of the AFM scans.

Morphological characterisation

To study the replication fidelity of different morphologies, a Hot Ag and a Z2 were used because they are two standard substrates employed at IMT. Additionally, an inverse texture of Z5 was used (named in this section Z5 for simplicity). These textures are random and possess rounded features, positive pyramids, or negative pyramids for the Hot Ag, Z2 and Z5, respectively.

Figure 3.1 presents AFM scans of master textures and their corresponding UV replicas obtained on glass, and a similar appearance can be seen between the masters and the replicas. In order to quantitatively assess the replication quality, parameters with vertical (σ_{rms}), lateral (L),

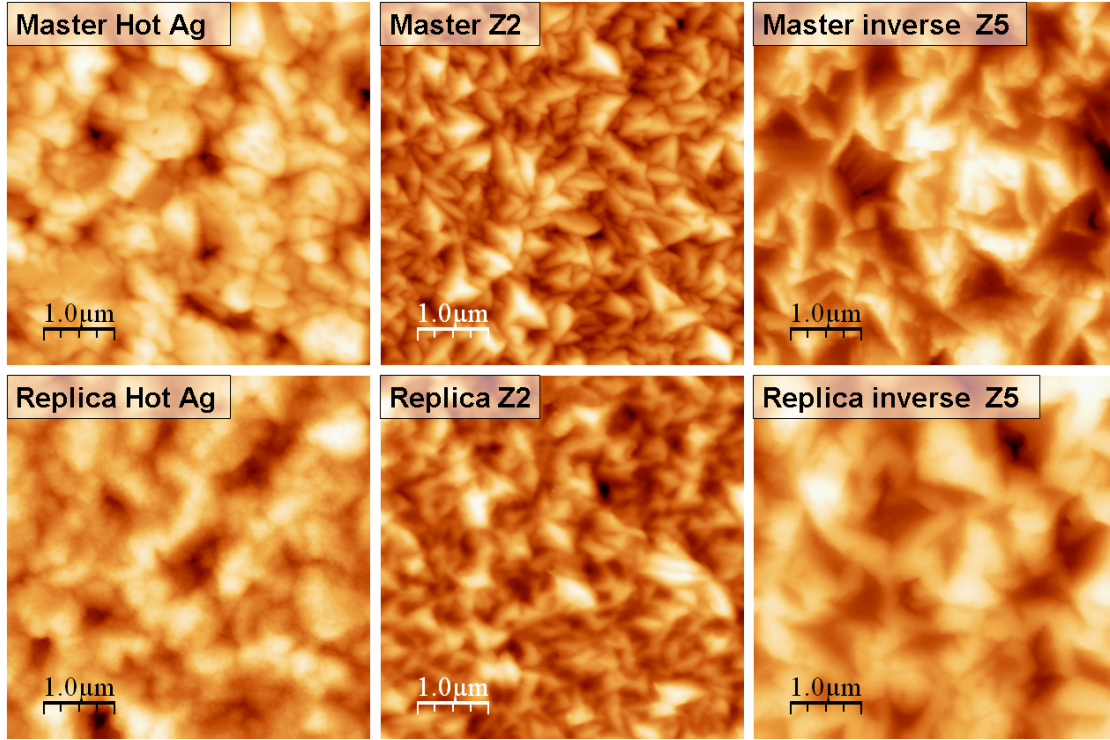


Figure 3.1: AFM images of replicas made by soft PDMS stamps and their corresponding masters.

and both vertical and lateral (mean angle, σ_{rms}/L , A_{flat}/A_{scan}) roughness information were calculated from the AFM scans. These values are reported in table 3.1 and figure 3.2. Figure 3.2a presents correlations between the mean angle, σ_{rms}/L and A_{flat}/A_{scan} .

Correlations between these parameters were observed even for textures that were morphologically very different. We thus reduced the number of figures of merit used to characterise a specific texture. Eventually, σ_{rms} and L were chosen to compare masters and replicas, as they contain vertical and horizontal information, and the ratio σ_{rms}/L provides access to the aspect ratio.

Table 3.1: Summary of the parameters extracted from AFM analysis.

Texture		σ_{rms} (nm)	L (nm)	σ_{rms}/L	Mean angle (°)	A_{flat}/A_{scan}
Hot Ag	Master	46	228	0.20	23	0.89
	Replica	47	280	0.17	20	0.92
Z2	Master	67	167	0.40	38	0.72
	Replica	51	202	0.25	25	0.87
Z5	Master	124	356	0.35	36	0.74
	Replica	99	413	0.24	26	0.85

The replication quality with identical stamping conditions (pre-bake and post-bake time, UV exposure, and pressure) differed for different morphologies: Figure 3.2b shows the relative loss

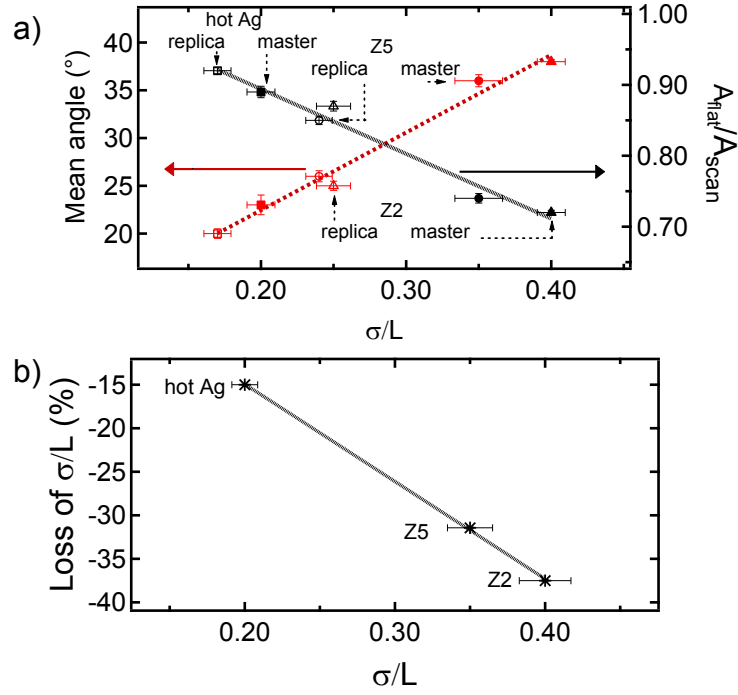


Figure 3.2: Morphological parameters of master and replica Hot Ag, Z2 and Z5 textures: a) mean angle and A_{flat}/A_{scan} as a function of the aspect ratio σ/L , and b) loss of σ/L after replication as a function of the σ/L of the master texture.

in aspect ratio after replicating the original texture. Losses of 15%, 37% and 32% for Hot Ag, Z2 and Z5 replicas were observed, respectively. Table 3.1 shows that the correlation lengths for the replicas were always higher than for their respective masters. As the correlation length is related to the mean horizontal size of the surface features, higher values of L can be explained by the loss of smaller details after replication.

To better quantify the feature sizes that can be reproduced by the technique, a periodic substrate provided by an external partner was used. Figure 3.3 presents a 3D representation of AFM scans performed on both the master and replica of this texture. It can be observed that the period was well reproduced by replication (509 nm for the master and 512 nm for the replica), which demonstrates that features with sizes around 500 nm were not lost during replication. However, the line scan over a typical pyramid reveals that the triangular shape of the tip was not reproduced, showing that feature sizes smaller than 300 nm were lost during the replication. Thus, the poor replication of the smaller features shown here explains the lower mean angle and σ_{rms} , and the higher L , in figure 3.2 and table 3.1 for the replicas of random textures.

The difficulty of reproducing feature sizes below 500 nm using a soft PDMS stamp has already been discussed in the literature and is generally attributed to either a too large stamp soft-

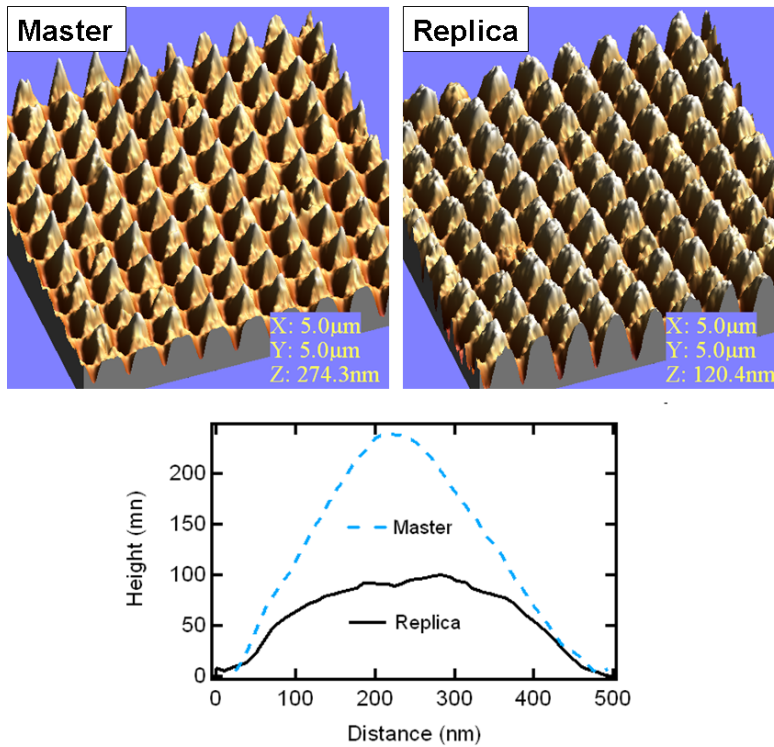


Figure 3.3: The top panel presents 3D representations of AFM images of a periodic master structure and the corresponding replica made by a soft PDMS stamp. The profiles of the pyramids maxima extracted from each images are shown below.

ness [Delamarche 97, Odom 02] or a too large viscosity of the liquid PDMS during the stamp fabrication [Kang 06, Koo 07]. Improved replication fidelity was achieved by modification of the PDMS stamp: Feature sizes below 100 nm were obtained by using a composite stamp that contained a part made of harder a PDMS material [Odom 02]. Resolution below 50 nm was also demonstrated using another approach in which the PDMS was diluted with solvent to increase the wetting of the master texture during stamp fabrication [Kang 06, Koo 07]. Finally, resolution below 50 nm was demonstrated by increasing the hardness of the stamp, e.g. by changing from the conventional PDMS stamp material to a harder polymer material [Gilles 09, Klukowska 09]. In our laboratory, a hard UV resin was chosen for the fabrication of stamps of higher fidelity as it was readily available, c.f. section 3.2.2. Nevertheless, texture smoothing has been demonstrated to be beneficial in some circumstances and it will be shown in section 3.3 that, depending on the original master texture, the smoothing of the surface features observed in this section can improve cell efficiencies.

Optical characterisation

The study of the replication quality with AFM scans allowed a better understanding of which losses can typically be expected. Nevertheless, in this thesis, the replicas were meant to be

inserted in solar cells as light scatterers. Therefore, the optical properties of the replicated substrates are the final benchmarks for qualifying the quality of replication.

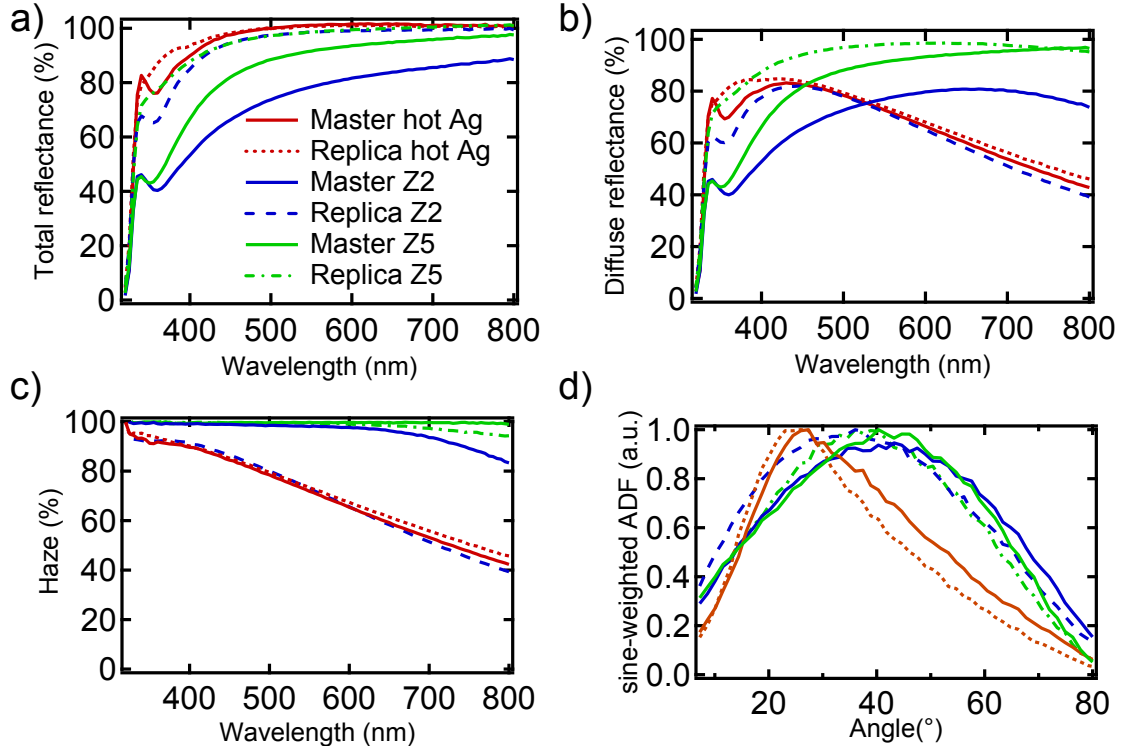


Figure 3.4: *Optical properties of masters and replicas of Hot Ag, Z2 and Z5: a) total reflectance, b) diffuse reflectance, c) haze in reflection and d) sine-weighted angular distribution function of scattered light. The legend in a) applies to all four figures.*

In this section the optical properties of the textures shown in figure 3.1 are discussed. The measurements of TR, DR, haze and ADF are shown in figure 3.4a, b, c and d, respectively, for Hot Ag, Z2 and Z5 textures. In accordance with the morphological parameters discussed previously, it can be observed in figure 3.4 that the Hot Ag replica most faithfully reproduced the optical properties of the master texture. Still, the ADF at high angles ($>30^\circ$) was higher for the master. The discrepancies between the optical properties of the masters and the replicas are much higher for the Z2 and Z5 textures. Both haze and scattering into high angles were higher for the master textures than for the replicas. This is in complete agreement with the morphological parameters found previously.

3.2.2 Comparison of replication between soft and solid stamps: Towards high fidelity replication

In this section, the improvement in fidelity of replication obtained by using a solid stamp as an intermediate mould as described in section 2.1 is discussed. Figure 3.5 presents images obtained from AFM measurements of some examples of replications that were obtained by using a solid stamp. A comparison of the quality of replication is made by analysing replicas of

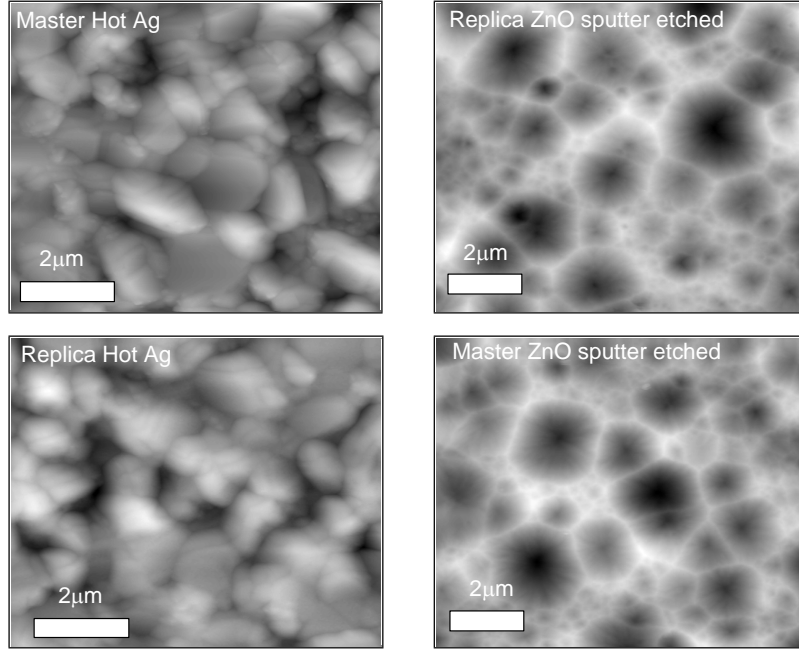


Figure 3.5: *AFM images of examples of replication of Hot Ag and sputter-etched ZnO made using a solid stamp.*

a Z2 texture made with soft or solid stamps. This texture is a perfect template for at least three reasons:

1. It is widely used for high-efficiency single-junction a-Si:H solar cells in our laboratory.
2. It combines the smallest horizontal feature size L and the highest aspect ratio σ_{rms}/L that were reported in table 3.1, and thus the most challenging replication conditions.
3. It was also the texture that was reproduced the least faithfully with PDMS as shown in figure 3.2b.

Finally, to give an approximation of the resolution of the high-fidelity replication process using the solid stamp, an example of the fine details of the Z5 texture which can be reproduced is shown.

Replication of Z2 texture

Figure 3.6 shows SEM images of three substrates that contain the pyramidal texture of the Z2 texture: the master, a replica made by using a solid stamp, and a replica made by using a PDMS stamp. All three samples were covered with a thin silver layer. Qualitatively, no significant differences are observed in the features between the master and the replica made with the solid stamp, while the morphology of the replica made with the soft stamp has much smoother features.

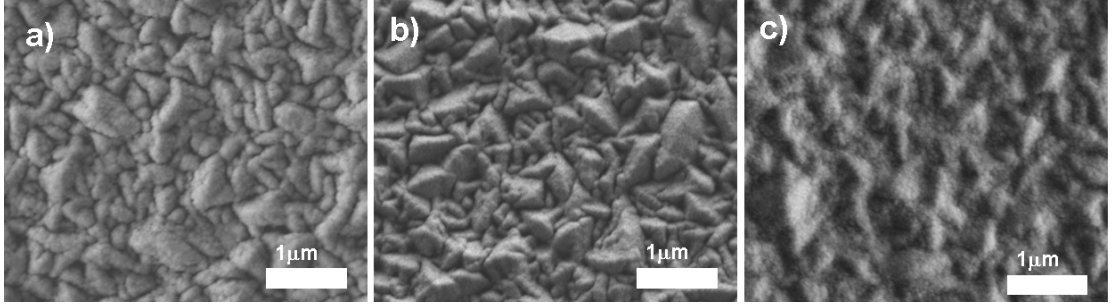


Figure 3.6: SEM images of a) a Z2 master and UV imprinted replicas b) using a solid stamp and c) using a soft PDMS stamp. All samples were covered with 120 nm of silver.

Table 3.2: Parameters extracted from AFM analysis of a master and replicas for a Z2 texture.

	σ_{rms} (nm)	L (nm)	σ_{rms} / L
Master	70	165	0.42
Solid-stamp replica	69	159	0.43
Soft-stamp replica	51	202	0.25

For quantitative comparison, additional information was extracted from AFM images of the master and replicas. Figure 3.7 presents the height histograms, the angle histograms, and the relative change in power spectral density between the master and the replicas. Comparison of the information extracted from the AFM images of the master and the solid-stamp replica in figure 3.7 and table 3.2 reveals no differences between the two. However, as discussed in section 3.2.1, lower quality of replication is evident when the soft PDMS stamp is used. The mean local inclination for the master is approximately 15° steeper than that of the soft-stamp replica. The height histograms shown in figure 3.7b and the σ_{rms} values shown in table 3.2 reveal a narrower distribution of height values for the soft-stamp replica and a lower roughness compared to the master. The correlation length was 22% higher for the soft-stamp replica compared to that of the master. The longer correlation length estimated for this replica suggests a texture consisting of larger lateral features, but is in fact due to the loss of fine surface (sub-micrometer) details as observed in the power spectral density shown in figure 3.7c. For the soft-stamp replica, the combination of both shallow and larger lateral features resulted in a texture with a lower aspect ratio. These results confirm the difficulty of obtaining

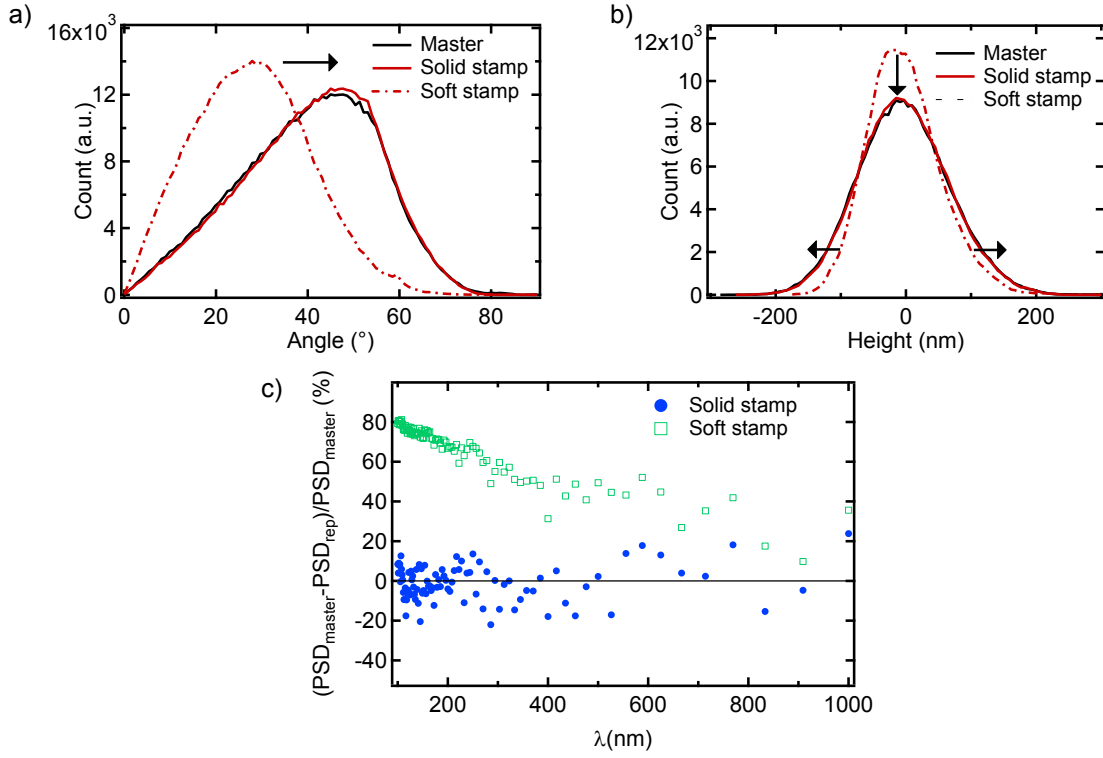


Figure 3.7: *a) Angle and b) height histograms for the master, solid-stamp replica and soft-stamp replica. c) Relative discrepancies in power spectral density between the replicas and the master texture.*

high-quality replicas of these kinds of small textures by UV NIL using an intermediate stamp made from PDMS. Finally, figure 3.8 compares the optical properties of the Z2 master and the

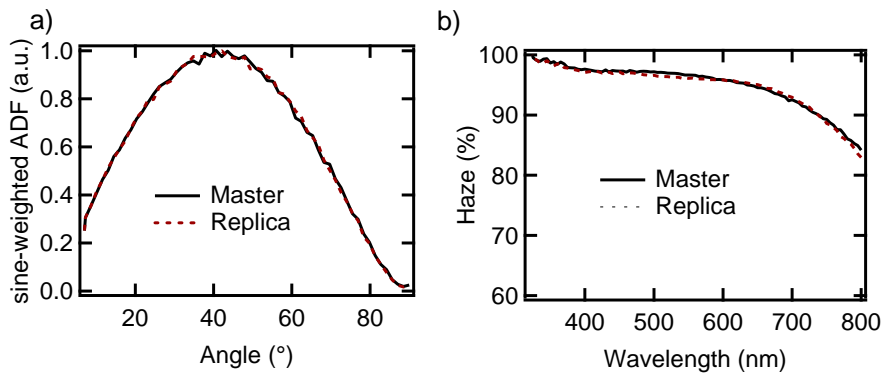


Figure 3.8: *a) ADF and b) haze of the Z2 master and the solid-stamp replica after their covering by 120 nm of silver.*

solid-stamp replica. As expected from the AFM analysis shown in figure 3.7 and table 3.2, the

two substrates behave as similar scatterers after their covering a silver layer. Consequently, it can be concluded that high-fidelity replicas of random structures can be obtained by UV NIL imprinting. Their insertion as back reflectors in solar cells will be discussed in section 3.3. Further details and the analysis of additional replicated textures using the solid stamps can be found in Escarré et al. [Escarré 11, Escarré 12a].

Replication of fine details: Z5 texture

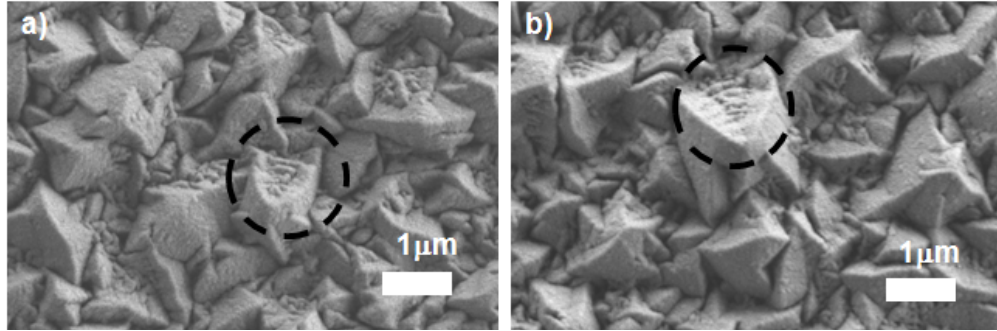


Figure 3.9: SEM images of the a) master and b) replica of Z5. Very small details in the pyramid facets are circled.

The oscillations around 0 in the relative power spectral density of a solid-stamp replica shown in figure 3.7c do not yield a quantitative measure of the smallest sizes that can be reproduced with the high-fidelity replication process. Moreover, a very small 1D grating which is generally used to perform this kind of analysis was not available. Therefore, SEM images of a master and a replicated Z5 texture were used for this specific study.

Figure 3.9 presents SEM images of a master in a) and a replica in b) of Z5. The circles mark very small details in the pyramid facets which are due to competitive growth planes that collide when the LP-CVD ZnO pyramids grow. The size of these "ladder" shapes are estimated to be around 100 nm and were reproduced by the high-fidelity replication process shown in this section. Higher resolution was obtained with similar types of processing [Kang 06, Koo 07, Gilles 09, Klukowska 09] and the resolution depended on the aspect ratio of the texture. In our case, an exact assessment of the lowest feature sizes that can be reproduced was not done. However, figure 3.8 shows that the optical properties of a Z2 texture that contains aggressive small features were reproduced so well that the master and replica were indistinguishable with our characterisation tools.

3.3 Cell results in the $n-i-p$ configuration

The $n-i-p$ solar cells that are presented in this section were deposited in the small-area system E and some details on the cells can be found in section 2.2.2. This section demonstrates that the UV NIL technique is an adequate experimental platform for the testing of novel photonic textures in the $n-i-p$ configuration, and that it is suitable for texturing plastic substrates. First, the effect of the replication quality is studied in single-junction a-Si:H solar cells. Second, the master and replicated substrates that yielded the best single-junction a-Si:H solar cells are applied to a-Si:H/a-Si:H tandem solar cells. The substrates consist of the Hot Ag and the Z2 textures described in section 3.2. It is demonstrated that, via textured PEN substrates, UV NIL allows the growth of devices on flexible substrates with efficiencies as high as state-of-the-art devices on glass.

3.3.1 Single-junction $n-i-p$ a-Si:H solar cells grown on a master substrate and on a solid-stamp replicated substrate

The comparison between cells grown on a master and solid-stamp replicated substrate is quite straightforward since no significant differences between the optical and morphological properties were observed. The Hot Ag texture was used for this experiment since it is suitable for high-efficiency a-Si:H $n-i-p$ solar cells. To be used as a back reflector in the solar cell, the replica was covered by 120 nm of silver and by a thin layer of sputtered ZnO:Al (60 nm) while the master was covered only with the thin ZnO:Al layer. The structures of the single-junction a-Si:H cells that were co-deposited on both substrates and which were completed with ITO front contact are shown in figure 3.10.

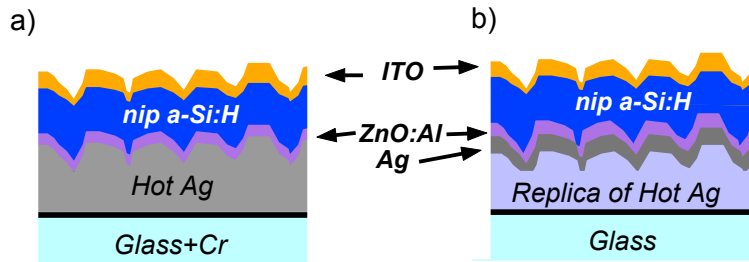


Figure 3.10: Schematics of $n-i-p$ a-Si:H solar cells grown a) on a master Hot Ag texture and b) on a solid-stamp replica of Hot Ag.

Figure 3.11 presents the EQEs and the electrical parameters of the co-deposited single-junction a-Si:H solar cells. The electrical properties are identical, while the EQEs show only a minor loss at 700 nm on the replicated texture. The equal FF and V_{oc} values indicate that the substrates were similarly rough. To conclude, this experiment showed that high-fidelity replicas of the random textures typically used in $n-i-p$ thin-film silicon solar cells can be obtained and used as well in $n-i-p$ solar cells.

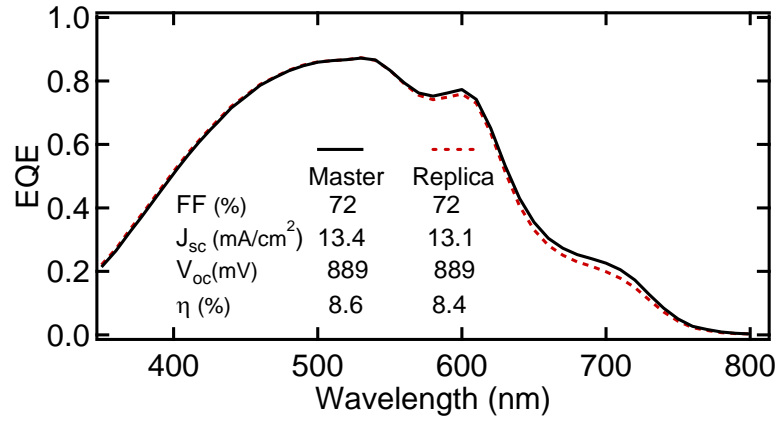


Figure 3.11: EQE and electrical parameters of single-junction *n-i-p* a-Si:H solar cells co-deposited on a Hot Ag master substrate and on a solid-stamp replicated Hot Ag texture on glass.

3.3.2 Single-junction *n-i-p* a-Si:H solar cells grown on master substrate and on a soft-stamp replicated substrate

Hot Ag and Z2 textures were used to study the effect on the solar cell parameters of the differences in morphology induced by soft-stamp replication. A flat reference substrate was also added to quantify the modification in the electrical parameters given by each texture. So as to serve as both a light-scattering back reflector and an electrical contact, all textures, except the Hot Ag master, were covered with a thin Ag layer of 120 nm. Then, a dielectric ZnO:Al buffer layer of 60 nm was deposited on all samples. The structures of the single-junction a-Si:H solar cells are shown in figure 3.12.

Figure 3.13 presents the EQE and the absorption of the best cell on each substrate in the initial state, and the electric parameters are summarised in table 3.3. Compared to the reference cell on a flat substrate, all cells on textured substrates exhibit increased absorption. At short wavelengths, differences are typically related to differences in the μc -Si:H *p*-doped layer whose effective thickness and nucleation can depend on the texture, or to reduced reflection because the roughness zone represents a gradual transition of the refractive index in this wavelength range. With the exception of the cell on the Z2 master, the high V_{oc} and FF values shown in table 3.3 suggest that problems due to thin *p*-layers are unlikely; the enhanced blue response was thus attributable to improved light in-coupling.

At long wavelengths, the four cells differ considerably, but trends between the two types of substrate texture can still be identified. For the Hot Ag texture, a comparison of the EQEs in figure 3.13a shows that the cell on the replica did not reach the level of light trapping that was obtained on the Hot Ag master. This behavior might be attributed to the lower angles of scattered light that were observed in figure 3.4d. For the Z2 replica, the analysis is more complicated. The slightly more pronounced interference fringes due to the cell

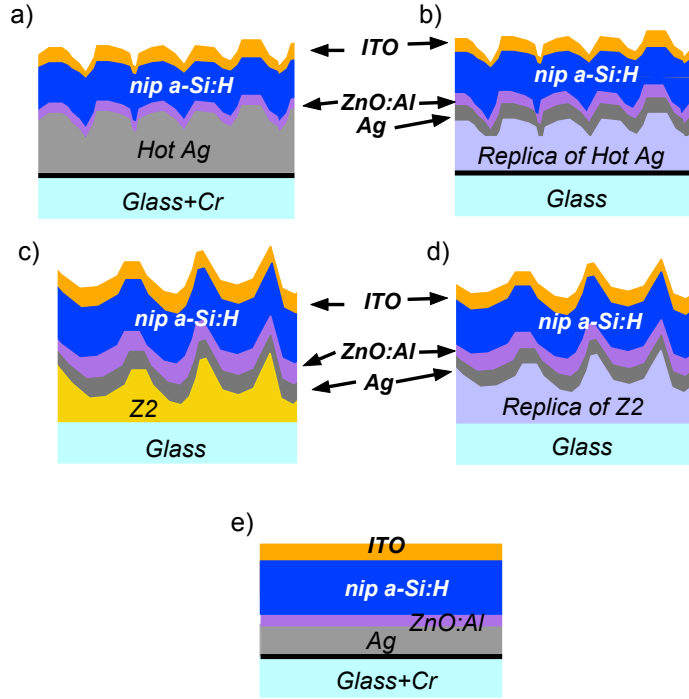


Figure 3.12: Schematics of *n-i-p a-Si:H* solar cells grown a) on a master Hot Ag texture, b) on a replica of Hot Ag made with a soft PDMS stamp, c) on a Z2 master, d) on a replica of Z2 made with a soft PDMS stamp, and e) on a flat Ag layer.

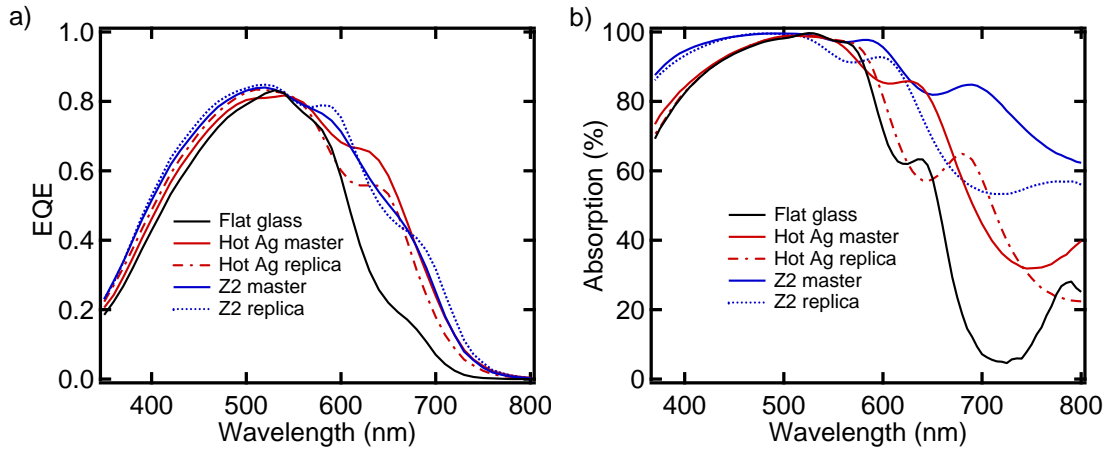


Figure 3.13: a) EQE and b) absorption of single-junction *a-Si:H* solar cells on master and soft-stamp replicated textures.

thickness indicate that the replica is flatter than the master. This accords with the optical and morphological analysis performed on the bare substrates shown in figure 3.4 and table

3.3. Cell results in the *n-i-p* configuration

Table 3.3: *Single-junction a-Si:H solar cell parameters of the best cell on each substrate (initial values).*

Texture		V_{oc} (mV)	FF (%)	J_{sc} (mA/cm ²)	Efficiency (%)
Hot Ag	Master	884	72.7	13.41	8.6
	Replica	881	70.1	12.85	7.9
Z2	Master	847	64.8	13.51	7.4
	Replica	876	70.4	13.84	8.5
Reference cell	Flat glass	888	74.5	10.8	7.1

3.1. However, the loss of aspect ratio is not necessarily detrimental for cell efficiency: The higher V_{oc} and FF of the cell grown on the Z2 replica with respect to the cell on the Z2 master imply that, in this case, the replica had a more favorable surface for the growth of cells. Indeed, the Z2 master has the potential for high J_{sc} , but its deep V-shaped valleys can result in voids and defects in the silicon grown on top [Sakai 90]. Hence, in general this type of substrate is used only after its features have been smoothed with a plasma surface treatment [Bailat 06, Söderström 08a].

The cell on the Z2 replica exhibits a better response than its master between 550 and 800 nm. This is surprising because, in the case of the Hot Ag texture, the loss of small features results in a severe decrease in light trapping in this wavelength range. Since the total absorption in the cell on the replica is lower than for the cell on the master while the J_{sc} on the replica is higher, higher parasitic absorption in the cell on the master seems plausible. This corroborates the strong absorption observed in the reflectance measurements shown in figure 3.4. Note, however, that those measurements were performed on the air/Ag interface and thus cannot be directly linked with the optical behavior in the cells [Haug 09]. A more detailed discussion on parasitic absorption can be found in section 5.4 and in Söderström et al. [Söderström 11b, Söderström 11c].

We conclude that nano-imprinting with soft PDMS does not fully replicate the fine details of the master texture. However, an exaggerated structure like the Z2 master is sufficiently smoothed to suppress detrimental asperities while a high level of light scattering is maintained. Therefore, nano-imprinting with a soft PDMS stamp may eliminate the need for post-fabrication treatments that are generally performed on LP-CVD ZnO before its incorporation as a back reflector in solar cells.

3.3.3 Tandem a-Si:H/a-Si:H cells: Comparison of best master texture and soft-stamp replicated texture

The previous sections showed that the Hot Ag master and the Z2 replica made with the soft PDMS stamp present similar morphological parameters (table 3.1) and that single-junction

a-Si:H solar cells grown on both substrates can achieve comparable efficiencies (table 3.3). To compare their suitability as substrates for high-efficiency tandem *n-i-p* cells and to prove that the texturing process can be applied on flexible plastic sheets without diminishing the yield of good cells, tandem cells were grown on a Hot Ag master and on a soft-stamp replica of the Z2 texture on PEN as shown schematically in figure 3.14.

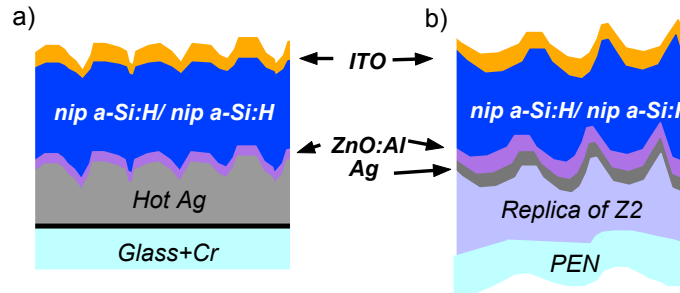


Figure 3.14: Schematic of *n-i-p* a-Si:H/a-Si:H solar cells grown a) on a Hot Ag master texture on glass and b) on a soft-stamp replica of Z2 on PEN.

It should be noted here that the Hot Ag master texture cannot be applied to plastic sheets due to the high deposition temperature of the silver layer. Therefore, other means of texturing are absolutely required to obtain this texture on a plastic substrate.

In order to achieve good current matching, the tandem cell on glass had top- and bottom-cell thicknesses of 70 nm and 300 nm, respectively, and those on PEN had top- and bottom-cell thicknesses of 60 nm and 300 nm, respectively. The adaptation of the top-cell thickness to obtain current matching for the cell grown on the replica of Z2 on PEN comes from better light trapping due to scattering into higher angles compared to the Hot Ag master (figure 3.4d). The effect of the higher angle of scattering was also observed in single-junction a-Si:H cells where a higher J_{sc} was obtained on the Z2 replica compared to the Hot Ag master. It should be noted that the morphological parameters shown in table 3.1 for the Z2 replica on glass are also representative of the morphology of the Z2 replica on PEN because no significant differences were observed between the optical measurements performed on replicas made on both types of substrate when the same stamp was used (not shown).

Table 3.4: Tandem a-Si:H/a-Si:H cell parameters in the initial and stabilised state. Values after degradation are marked in bold.

Substrate	Mean of cells		Best cell	
	V_{oc} (V)	FF (%)	J_{sc} (mA/cm ²)	Efficiency (%)
Hot Ag on Glass	1.73 ± 0.01	71.7 ± 1.8	7.54	9.8
	1.68 ± 0.02	59.6 ± 3.5	7.34	8.3
Z2 on PEN	1.70 ± 0.01	72.8 ± 1.1	7.62	9.5
	1.68 ± 0.01	62.3 ± 1.8	7.35	8.1

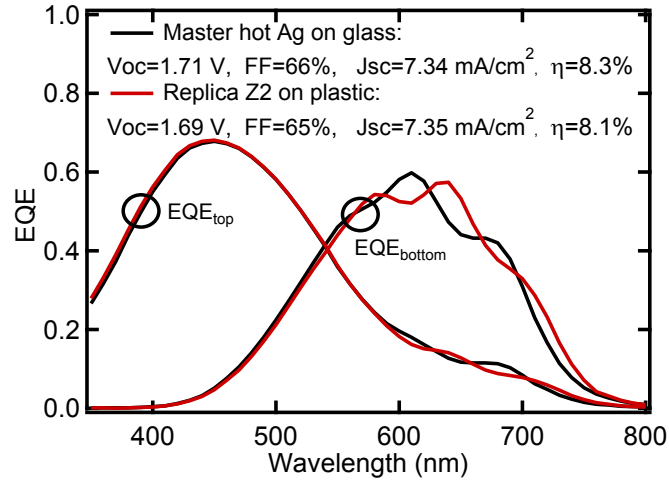


Figure 3.15: EQEs and electrical parameters of stabilised tandem cells on Hot Ag on glass and on soft-stamp replicated Z2 on PEN.

I-V measurements at low illumination were used to assess the suitability of different substrates for solar cell processing; in particular, to check for problems in substrate preparation that often result in shunt paths which decrease parallel resistance. In an I-V measurement under AM1.5G illumination, the parallel resistance can be determined only at large reverse bias, which can damage the cells. Thus, we took the differential resistance at short-circuit conditions, but at a reduced illumination level of 0.4%. Cells with $V_{oc} < 1.2$ V or $FF < 30\%$ under low illumination were considered to be non-functional. Out of the 20 cells deposited on each substrate, this measurement showed a yield of 90% on the PEN substrate, and of 85% on the glass substrate. This nearly equivalent yield of good cells on both substrates proved the ability of the replication process to produce good substrates for PE-CVD-grown a-Si:H even on plastic.

The V_{oc} and FF values shown in table 3.4 are statistical averages from the working cells. The J_{sc} and the efficiency values are given for the best cell of each substrate. The standard deviation of the V_{oc} and FF values was not higher on the nano-imprinted plastic than on the reference texture on glass. Moreover, the light-induced degradation of these parameters was equivalent between the two tandem cells. These two last facts prove that the UV-sensitive resin has no influence on the cell deposition and degradation. Figure 3.15 presents the EQEs and the electrical parameters for the best cell in the stabilised state on each substrate and shows that the best cell efficiency achieved on the nano-imprinted PEN substrate was only slightly lower than that of the best cell obtained on glass. Thus, it can be concluded that the replication process is compatible with PEN substrates and allows growing cells of high quality that are comparable to state-of-art cells grown on glass substrates. It has to be noted that the efficiency of the a-Si:H/a-Si:H device grown on a plastic substrate was further increased beyond the one shown in figure 3.15 by using a more suitable replicated texture and by improving the silver quality. With these modification, a stable efficiency of 9.2% was obtained on PEN by using a nano-imprinted reflector and this result is shown in section 7.4.

3.4 Cell results in the *p-i-n* configuration

This section reports some results that were obtained by using the UV NIL technique to produce front textures for *p-i-n* solar cells. Contrary to in the *n-i-p* configuration, in the *p-i-n* configuration, light passes through the textured resin before entering the cell. The solar cells presented in this section were deposited in large-area reactors (KAI-M for $\mu\text{c-Si:H}$ cells and KAI-S for a-Si:H cells) and some details on the cells can be found in section 2.2.2. The replicas presented in this section were made with solid stamps and therefore exhibited high fidelity of replication.

In section 3.4.1, solar cells grown on UV NIL textured substrates with efficiencies as high as the state-of-the-art cells that use LP-CVD ZnO electrodes will be shown. This experiment demonstrates that the texture and the electronic properties of the front electrode can be independently studied and optimised. Subsequently, in section 3.4.2 multi-scale texturing is presented. We show that a texture that combines the replication of large and wide features with the small features of LP-CVD ZnO may allow cells to reach even higher efficiencies than what can be obtained with standard LP-CVD ZnO textured electrodes. This concept relies on the high transparency of the lacquer. These two sections demonstrate that a new range of photonic textures are made available to the *p-i-n* configuration, presenting new opportunities for the study of the optimal photonic texture directly in complete solar cells.

3.4.1 Proof of concept with micromorph solar cells

Because the transparent resin in which the UV NIL replicas are made is not conductive, an additional TCO layer has to be deposited on top of the replica in order for it to be used as a front contact in the *p-i-n* configuration. Z5 etched by an Ar plasma for 20 minutes was chosen as the master template because it is known to lead to high-efficiency micromorph cells by providing a suitable texture for light trapping as well as good electrical contacts. Because this electrode is so good, it is challenging to produce a replicated electrode with the same optical and electrical properties. Figure 3.16 presents SEM cross sections of micromorph cells co-deposited on a replicated electrode and an LP-CVD ZnO master electrode. As indicated in figure 3.16b light impinges on the cells from the bottom part of these images and has to travel through the replicated electrode. In order to optimise the optical transparency as well as the electrical properties of the replicated electrode, an $\text{In}_2\text{O}_3\text{:H}$ layer was deposited on top of the replica to make the contact as described in section 2.2.1. To protect the $\text{In}_2\text{O}_3\text{:H}$ layer from reduction in the hydrogen-rich plasma used for the deposition of the *p*-doped layer, a 20-nm-thick ZnO:Al was sputtered on top before cell deposition. $\text{In}_2\text{O}_3\text{:H}$ is a remarkable TCO because its low carrier density allows the growth of highly transparent films which keep reasonable sheet resistance via high mobility beyond $100 \text{ cm}^2/\text{V}\cdot\text{s}$ [Koida 07, Koida 10a]. Koida et al. have already introduced these films into thin-film silicon solar cells by using them as front contacts in *n-i-p* solar cells [Koida 10b].

Table 3.5 and figure 3.17a present the electrical and optical properties of the *p-i-n* micromorph solar cells that were co-deposited on the two types of electrodes. Figure 3.17b shows the

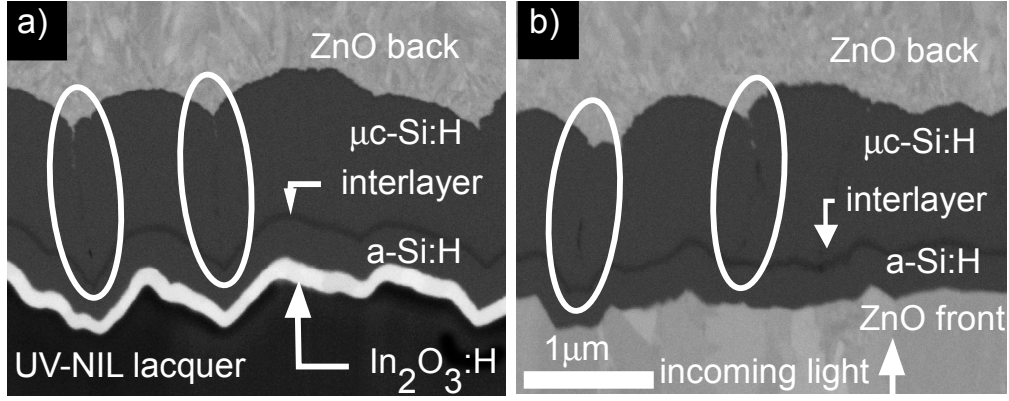


Figure 3.16: FIB cross section imaged by SEM of: a) a cell grown on the UV-NIL replica covered with $\text{In}_2\text{O}_3:\text{H}$, b) a cell grown on the LP-CVD ZnO master. White ellipses indicate the position of texture-induced cracks in the $\mu\text{c-Si:H}$ layer. The FIB cross-sectioning and SEM imaging were done by Dr. D. Alexander in the CIME center of EPFL.

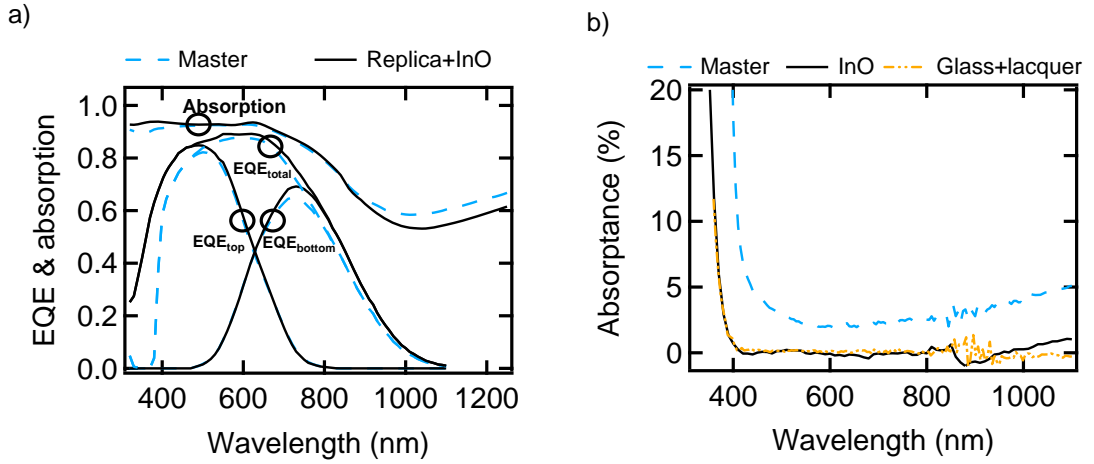


Figure 3.17: a) EQE and absorption spectra of *p-i-n* micromorph cells deposited on different types of front electrodes. b) Absorbance of electrodes and lacquer. The 135-nm-thick $\text{In}_2\text{O}_3:\text{H}$ film was characterised on a flat glass substrate after annealing at 200°C .

absorbance of the front electrodes, revealing that the replicated texture with the $\text{In}_2\text{O}_3:\text{H}$ layer absorbs less than the ZnO electrode. This should lead to a gain in J_{sc} for the cell grown on the textured electrode and, accordingly, a large gain of $1 \text{ mA}/\text{cm}^2$ in J_{sc} was obtained for both the top cell and the bottom cell as shown in figure 3.17a and table 3.5. The gain in the top cell is explained by the higher bandgap of the $\text{In}_2\text{O}_3:\text{H}$ electrode compared to that of the ZnO electrode, which can be observed in figure 3.17b. By contrast, the gain in the bottom cell is attributed to lower parasitic absorption losses due to reduced free-carrier absorption in the $\text{In}_2\text{O}_3:\text{H}$ electrode compared to the ZnO electrode, which is also observed in figure 3.17b. The cell absorption shown in figure 3.17a also indicates higher parasitic losses in the ZnO electrode

above 1100 nm where the silicon is no longer absorbing. These results point out that the highly transparent replica combined with the $\text{In}_2\text{O}_3\text{:H}$ electrode led to a large J_{sc} gain, and thus is promising to lead to efficiency improvement compared to standard electrodes.

Table 3.5: *Electrical parameters of p-i-n micromorph cells grown on different types of front electrodes.*

Substrate	$J_{sc_{tot}}$ (mA/cm ²)	$J_{sc_{top}}$ (mA/cm ²)	$J_{sc_{bot}}$ (mA/cm ²)	V_{oc} (V)	FF (%)	Efficiency (%)
LP-CVD ZnO	24.0	11.9	12.1	1.385	73	12.0
Replica+ $\text{In}_2\text{O}_3\text{:H}$	25.9	12.9	13.0	1.359	69	12.0

Table 3.5 shows that the V_{oc} and FF values are lower on the replicated sample than on the LP-CVD ZnO master electrode. Since both cells are almost matched, the FF difference cannot be explained by the current matching conditions. On the replica, the lower FF can to some extent be explained by the higher resistivity of the $\text{In}_2\text{O}_3\text{:H}$ electrode ($26 \Omega_{\square}$) compared to the ZnO electrode ($8 \Omega_{\square}$) but this cannot explain the V_{oc} difference. It is possible that the V_{oc} and FF losses can be attributed to a slightly higher crack density in the a-Si:H or in the $\mu\text{c-Si:H}$ cell due to a more pinched, V-shaped surface after sputtering the $\text{In}_2\text{O}_3\text{:H}$ layer. The second ellipse, which marks a crack in the cell cross section in figure 3.16a, is drawn on a valley which was more U-shape before the sputtering of the TCO layer. The effect of pinching U-shape textures by sputtering an additional layer on top was also observed for silver sputtering and is shown in figure 5.10.

In conclusion, table 3.5 shows that the solar cells grown on the replicated electrode reach efficiencies as high as on the standard electrode, which validates the UV NIL tool as an adequate experimental platform for *p-i-n* devices. A promising gain of 2 mA/cm² in total J_{sc} was obtained thanks to the high transparency of the resin, but this gain was balanced by losses in V_{oc} and FF . Further details on the experiment presented in this section can be found in Battaglia et al. [Battaglia 11a, Battaglia 11c].

3.4.2 New photonic designs: Multi-scale substrates

This section describes how multi-scale texturing made possible by the replication of large features in the highly transparent resin bring significant improvements to micromorph devices in the *p-i-n* configuration [Boccard 12b]. Experimental contributions [Terrazzoni-Daudrix 06, Taneda 07, Boccard 12d, Boccard 12b] and simulations [Isabella 10] suggested that the combination of small and large feature sizes should be used for efficient light trapping in both sub-cells of micromorph devices. In this case, the large features should allow efficient scattering in the bottom cell and facilitate the growth of high-quality silicon, while smaller features should allow efficient scattering in the top cell [Boccard 12d, Boccard 12b].

As a first trial shown in Boccard et al. [Boccard 12d], multi-scale texturing was achieved

3.4. Cell results in the *p-i-n* configuration

by obtaining the large features from an extremely-thick, highly-treated LP-CVD ZnO and the smaller features were subsequently obtained by adding a thin layer of LP-CVD ZnO:B with small pyramidal features. This approach did confirm that multi-scale texturing could be of high interest. However, because of high parasitic absorption in the thick ZnO layer, it did not result in a cell efficiency improvement compared to a cell grown on a standard electrode. Therefore, replication of the large-scale texture by nano-imprinting using the highly transparent UV-sensitive resin was a route to get rid of this detrimental effect and to take full advantage of the multi-scale texturing.

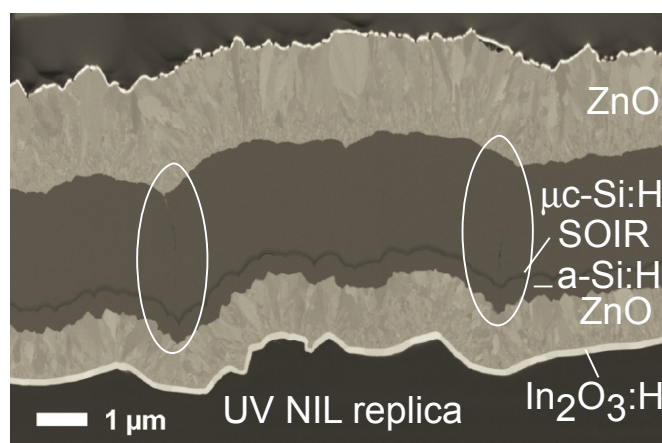


Figure 3.18: FIB cross section imaged by SEM of a cell grown on UV NIL replica covered with $\text{In}_2\text{O}_3\text{:H}$ and LP-CVD ZnO:B with small pyramidal features. White ellipses indicate the position of texture-induced cracks in the $\mu\text{c-Si:H}$ layer. The FIB cross-sectioning and SEM imaging were done by Dr. D. Alexander in the CIME center of EPFL.

Figure 3.18 presents an SEM image of a micromorph cell grown on a substrate made of a replica of an extremely thick highly-treated LP-CVD ZnO on top of which an $\text{In}_2\text{O}_3\text{:H}$ layer was sputtered, after which a thin LP-CVD ZnO:B with small pyramidal features was deposited. The replica with large features ensured high transparency and sufficient scattering of long wavelengths while the stack of $\text{In}_2\text{O}_3\text{:H}$ / thin LP-CVD ZnO:B ensured the carrier collection and efficient light scattering of short wavelengths. On this substrate, a micromorph cell with a record high initial efficiency of over 14% was obtained; a result that could not be obtained with conventional means of texturing at that time. A complete study of this cell can be found in Boccard et al. [Boccard 12b].

The white ellipses which mark the texture-induced cracks in figure 3.18 indicate that further improvements to this cell can still be made. Indeed, it was observed that the deposition of the thin LP-CVD ZnO:B layer on top of the irregular, large-scale features leads to features that are detrimental to the growth of a high-quality $\mu\text{c-Si:H}$ layer. Therefore, the development of a texture with large features that does not cause the thin LP-CVD ZnO:B to develop these V-shapes should lead to further improvements of the cell efficiency.

This experiment demonstrates once again the potential and versatility of UV NIL replication for the implementation of novel textures for light management in high-efficiency devices.

3.5 Nanomoulding of LP-CVD ZnO surfaces

In this section, an innovative method called nanomoulding for the transfer of textures directly into functional materials is shown. The details of the fabrication process, which was derived from an idea of Dr. C. Battaglia are explained in section 2.1.2 and the nanomoulded replicas presented in this section were realised by Dr. J Escarré and the author of this thesis. The aim of this technique was to free the ZnO surface texture from the standard pyramidal or crater shapes that are in general used in *p-i-n* solar cells. To this end, one option was to use a UV NIL textured resin coupled with a thin sputtered TCO layer which is described in section 3.4. However, the latter layer has a drawback because of non-conformal growth of the sputtered TCO layer when features of small size are present. In our laboratory, the growth of LP-CVD ZnO:B and the compromise between its conductivity and transparency are well controlled. For that reason, LP-CVD ZnO:B was chosen as the functional material in which the wanted texture was to be replicated. Further details on the experiment reported in this section can be found in Battaglia et al. [Battaglia 11b, Battaglia 13].

In section 3.5.1 the quality of the nanomoulded substrates will be described by comparing the nanomoulded morphologies obtained from different master textures. Next, section 3.5.2 presents a-Si:H solar cells grown on a master texture and on nanomoulded substrates.

For these studies, master textures fabricated by various techniques were chosen. The first master is a 1D grating texture with sinusoidal shape obtained by interference lithography. The second texture was provided by W. Lee and consists of a quasi-periodic dimple pattern obtained by anodically textured aluminum (ATA). This texture demonstrates the convenience of nanomoulding because this opaque master texture cannot be used as a front electrode in *p-i-n* solar cells, but its replica can. The third texture consists of a typical Z5. The Z5 texture was a perfect template for the following experiments as it leads to efficient solar cells, and we can directly compare solar cells grown on a master of LP-CVD ZnO:B and on a nanomoulded LP-CVD ZnO:B with the same texture and material.

3.5.1 Characterisation of nanomoulded substrates

The three different textures briefly described above were nanomoulded and the replicas were compared with the morphologies of their respective masters by SEM and AFM. Figure 3.19 presents SEM images of the master textures and of the corresponding replicated textures nanomoulded in ZnO. The insets are AFM images which were used to quantitatively assess the replication quality of the nanomoulding process for these substrates. Figure 3.19 shows that the main characteristics of each texture were replicated and that it was difficult to

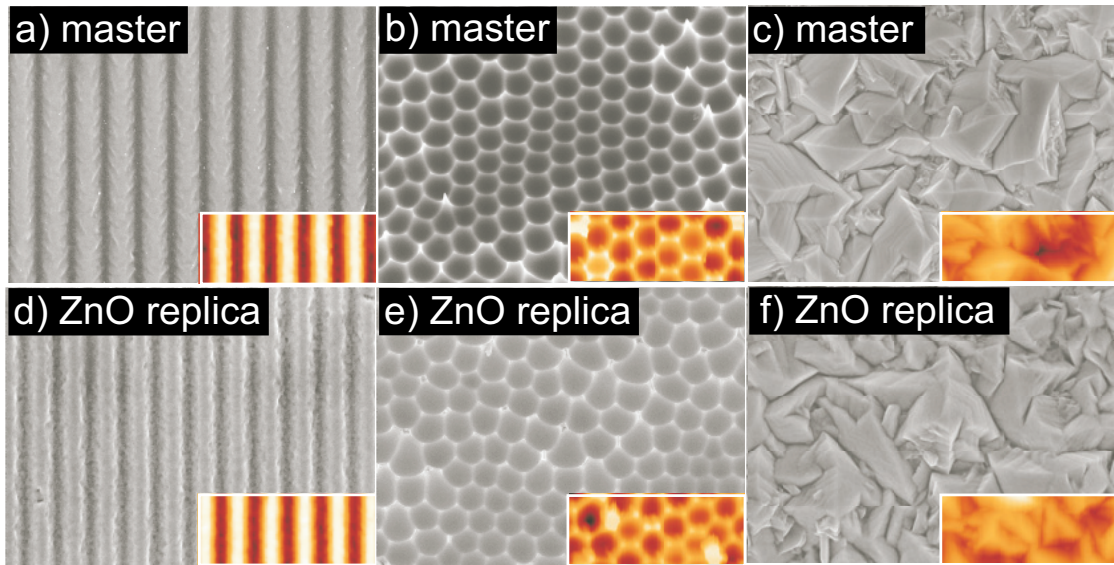


Figure 3.19: SEM images of master test structures and their corresponding nanomoulded ZnO replicas. a) 1D grating, b) ATA, c) Z5. d)–f) present the images of the corresponding nanomoulded replicas. SEM image size: $6.4 \mu\text{m}^2$. Inset: AFM images.

discriminate the master from the nanomoulded texture from the SEM images. Based on these images, only the ATA master can be differentiated from its replica: A close look reveals spikes in the master texture which were only partially reproduced in the nanomoulded replica. The tall spikes appear to be broken in the replicated electrode: They were probably broken during the demoulding of the ZnO and thus are probably still inside the stamp.

For a better assessment of the replication quality, figure 3.20 shows the comparison of the local height and angle histograms which were extracted from the AFM images of the three masters and ZnO replicas. These histograms reveal a remarkable accuracy of the transferred textures. The 1D grating histograms exhibit a slight loss in angle steepness and a slight decrease in amplitude after nanomoulding. Still, the dominant features were well reproduced. The ATA texture suffered from losses similar to those of the 1D grating but again the important features were well reproduced. Finally, the excellent replication of the LP-CVD ZnO:B texture by nanomoulding was striking. The remarkable quality of replication for this texture may be related to the fact that the material used for the nanomoulding naturally had the same facet angles that were imprinted into the mould.

The limiting size resolution of this technique was not analysed in this study, as it would require a dedicated master. However, the SEM image shown in figure 3.19f shows that features due to the collision of competitive planes of LP-CVD ZnO growth are reproduced. These features were also observed in figure 3.9 and have sizes of around one hundred of nanometer. These features could not have been created during the growth of the LP-CVD ZnO:B on the PEN mould as it is the nucleation layer that we observed at the surface of the replicated ZnO sample.

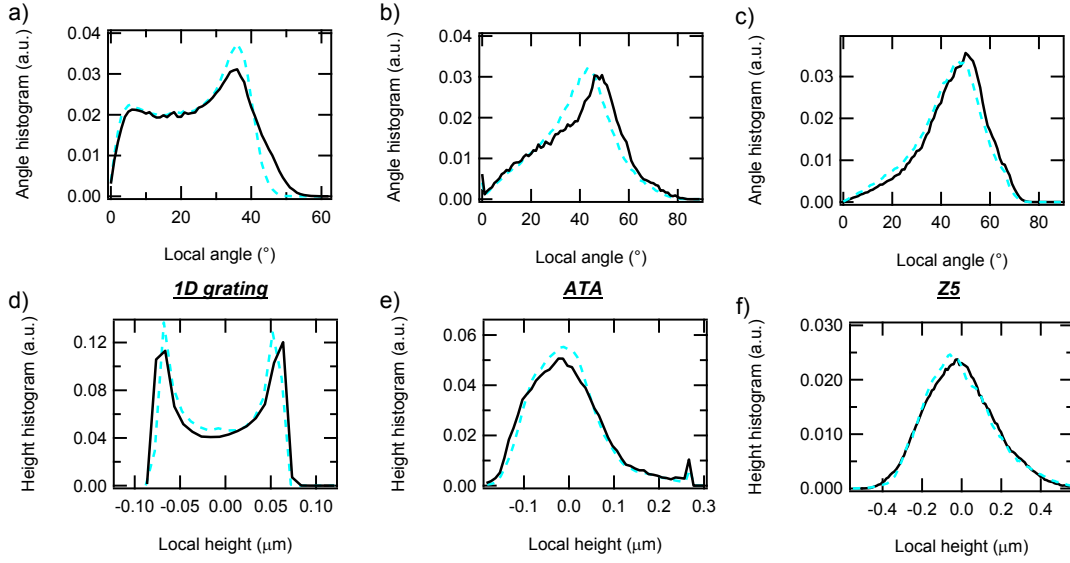


Figure 3.20: Morphological analysis of ZnO nanomoulding: a)–c) local angle and d)–f) height histograms of the three test textures. Master and replica histograms are shown in solid and dashed line, respectively.

Still, the final resolution may be due not only to the mould fidelity, but also to the details of the LP-CVD ZnO:B deposition. We observe that the spikes present in the ATA master texture were not reproduced in the nanomoulded ZnO replica. This can, however, only be positive for the growth of solar cells whose V_{oc} and FF values are likely to suffer from such aggressive features.

3.5.2 a-Si:H *p-i-n* solar cells on nanomoulded substrates

The ATA nanomoulded sample and a Z5 texture etched for 20 minutes in an Ar plasma were chosen specifically for trials in solar cells because the Z5 texture allows the comparison of cells grown on nanomoulded samples with the same shape and material as the master. In addition, the ATA sample demonstrate the potential of this novel technique which can texture the LP-CVD ZnO electrode in a selected shape. In this study, the 1D grating texture was discarded since it is not suited for high-efficiency cells. *p-i-n* a-Si:H solar cells with a 250-nm-thick *i*-layer were co-deposited on the substrates in the KAI-S reactor. Some details on the cells can be found in section 2.2.2.

Figure 3.21 presents cross-section SEM images of the a-Si:H cells which were deposited on the ZnO master, on its corresponding ZnO replica and on the ATA replicated texture. The arrows in these images indicate the direction of the LP-CVD ZnO:B growth. It can be observed that the ZnO nucleation layer is adjacent to the a-Si:H layer for both the front and back contact on the replicated electrodes while the large granular structure of the LP-CVD ZnO:B is in contact with the a-Si:H cell which was grown on the master electrode. As a consequence, it is

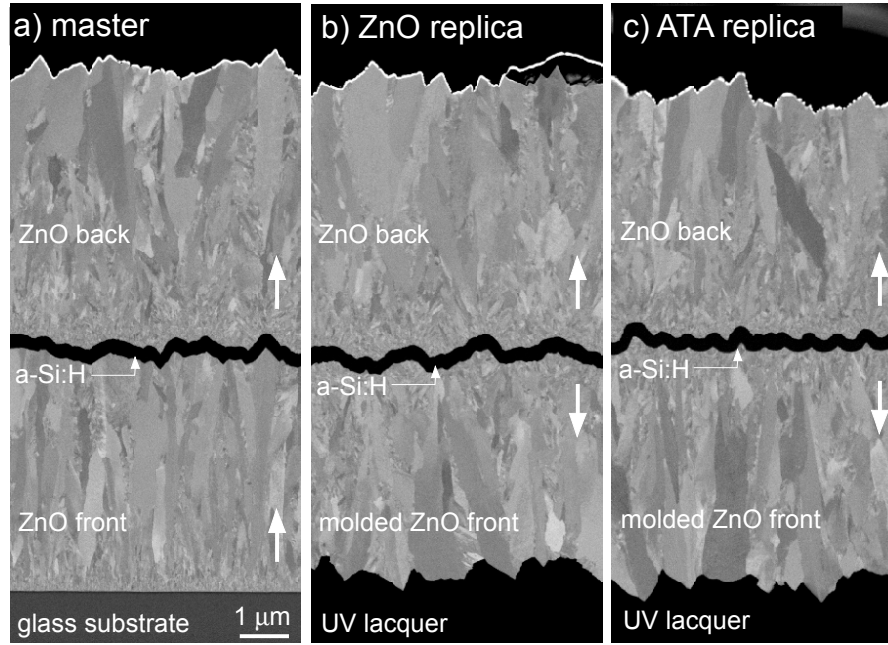


Figure 3.21: FIB cross sections imaged by SEM of *a-Si:H* solar cells on a) the master ZnO, b) the nanomoulded ZnO replica, and c) the nanomoulded ATA replica. The growth direction of the ZnO layers is indicated by white arrows. The FIB cross-sectioning and the SEM imaging were done by Dr. D. Alexander in the CIME center of EPFL.

questionable whether the electrical properties are preserved with the nanomoulded LP-CVD ZnO:B. However, growth on the mould and transfer to glass apparently does not lead to a decrease in the excellent electrical properties of LP-CVD ZnO, as similar electron mobilities were measured by Hall measurements for the replica ($\mu_e=45 \text{ cm}^2/\text{V}\cdot\text{s}$), and the reference LP-CVD ZnO:B which was grown on flat glass ($\mu_e=47 \text{ cm}^2/\text{V}\cdot\text{s}$).

Table 3.6 presents the electrical parameters of the cells shown in figure 3.21. Solar cells with a high initial efficiency of 10.1% were obtained on the Z5 replicated electrode which is as high as the efficiency of the cell grown on the LP-CVD ZnO master electrode. The higher J_{sc} obtained on the ATA sample is due to better light trapping, which shows that it can be interesting to scan a larger distribution of photonic structures than the standard pyramidal and crater-like shapes usually used in *p-i-n* solar cells. Still, the ATA replicated structures may be too aggressive for our cell process that was optimised on the pyramidal features of ZnO. The potential for high current in structures like the ATA will hopefully stimulate the development of new processes and cell designs with better tolerance to more aggressive features. In this case, insertion of an ATA-like structure in the solar cells may lead to efficiency improvements.

Table 3.6: *Electrical parameters of a-Si:H p-i-n solar cells grown on a LP-CVD ZnO master substrate, and LP-CVD ZnO and ATA nanomoulded substrates.*

Substrate	J_{sc} (mA/cm ²)	V_{oc} (mV)	FF (%)	Efficiency (%)
ZnO master	15.2	880	76	10.1
ZnO replica	15.6	879	74	10.1
ATA replica	16.2	871	70	9.9

3.6 Anti-reflective coating

In this section, it is shown that UV NIL replicas of micro-metric features add a broadband anti-reflection effect (ARE) when applied on the front of both *p-i-n* and *n-i-p* devices. Since this replica is added after cell or module fabrication, it can be applied to other PV technologies and on large areas.

Commonly, an ARE is obtained either by anti-reflection coatings made of multi-layers of thin films or by nano-textures that provide a gradual change in the effective index of refraction, the latter being inspired from natural moth eye textures [Bernhard 67]. Another approach to obtain an ARE —investigated here and widely used in wafer-based silicon technology— is the use of geometric textures that introduce multiple rebounds for impinging light. These textures are in general obtained by anisotropic etching of a (100)-oriented crystalline silicon wafer using a diluted potassium hydroxide solution (KOH). For low-cost crystalline solar cells, random pyramids are used while additional photolithography steps are performed to obtain more complicated —and more expensive— designs like the inverted pyramidal structures used in the high-efficiency PERL device [Wang 90].

Because features that can be replicated by nano-imprint lithography are not limited to pyramidal features that naturally develop with the etching of the (100) silicon surface, a wide range of textures that produce an ARE can be investigated. The best design, which should be effective over a broad range of wavelengths and have little sensitivity to the angle of incident light, is still to be found. Recently, a promising design made of retro reflectors was proposed by the company SolarExcel. They reproduce this texture in a polymer foil that can be applied to the front of modules after their fabrication, and they have shown remarkable J_{sc} increase for this specific asymmetric texture [Ulbrich 12]. This approach is similar to nano-imprinting a texture directly onto a cell, which is investigated here.

In this section, a broadband ARE is demonstrated in *p-i-n* devices using the random pyramidal textures that are used for light trapping in crystalline silicon solar cells. Figure 3.22 presents SEM images of a silicon master and a replica made by PDMS, and does not reveal striking differences. The replica appears to have larger feature sizes but this is probably due to non-uniform etching of the master wafer which contained regions with larger and smaller pyramids. Morphological characterisation could not be performed by AFM due to too large feature heights. However, the angles of the facets were derived from angular resolved scattering

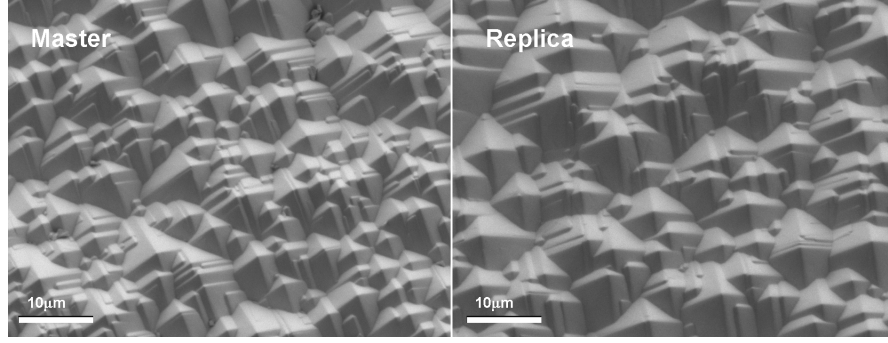


Figure 3.22: SEM images of master and replica textures with macro-metric pyramids obtained after KOH etching of (100) silicon wafers. Both substrates were covered with a thin Ag layer.

measurements, for which the maxima are directly related to the angle of the facets by the double rebound effect. Therefore, a thin silver layer was used to cover the substrates before performing these measurements in reflection mode (not shown). The facet angle of the replica was around 49° which was a few degrees lower than for the master texture (54°). Still, the replicated structure preserved the relevant double rebound characteristics and was therefore tested at the front of *p-i-n* devices.

Table 3.7: Micromorph solar cell electrical parameters measured before and after imprinting the anti-reflective layer on the front surface of the glass substrate.

Front	$J_{sc_{tot}}$ (mA/cm ²)	$J_{sc_{top}}$ (mA/cm ²)	$J_{sc_{bot}}$ (mA/cm ²)	Voc (V)	FF (%)	Efficiency (%)
Without pyramids	24.9	12.4	12.5	1.38	73	12.4
With pyramids	26.3	13.3	12.9	1.38	73	13

Table 3.7 and figure 3.23 describe the characteristics of the same micromorph cell before and after imprinting the anti-reflective texture described above. This micromorph cell is made of a 260-nm-thick *p-i-n* a-Si:H top cell that was deposited in the KAI-S reactor and a 1.2- μ m-thick μ c-Si:H bottom cell that was deposited in the KAI-M reactor.

The additional light in-coupling thanks to the double rebound can be clearly observed in the EQEs shown in figure 3.23, which were measured before and after the imprinting of the pyramids. The total J_{sc} was boosted by more than 5% as shown in table 3.7. However, the efficiency was not increased by the same factor because of interplay between intermediate reflector and the double rebound effect. A redistribution of the current which was more beneficial for the top cell was observed here and transformed this particular micromorph cell from being top limited to bottom limited after the addition of the pyramids. It is likely that the J_{sc} gain and its redistribution between the sub-cells also depends on the front glass thickness, the texture of the front electrode and the thickness and index of refraction of the intermediate reflector layer. Therefore, no rule of thumb concerning the J_{sc} gain in multi-

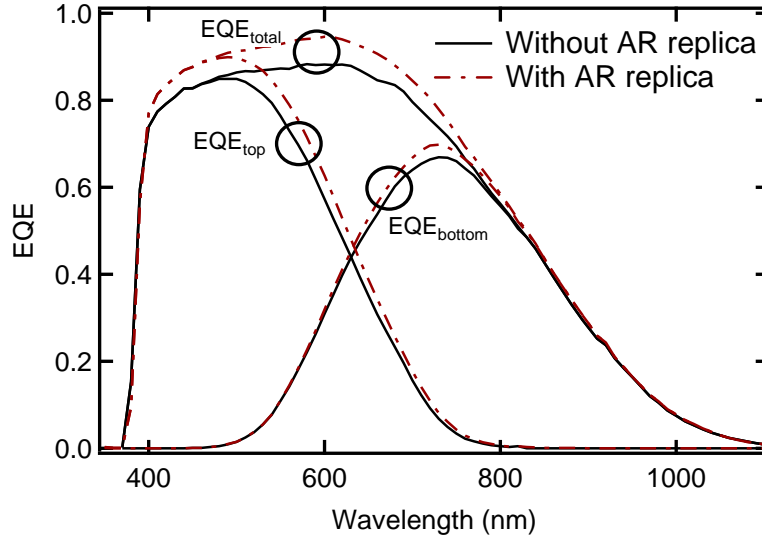


Figure 3.23: EQEs of a micromorph cell measured before and after imprinting the anti-reflective layer.

junction cell can be given on the basis of this experiment, but the beneficial effect has been clearly demonstrated.

It is also remarkable that the enhancement in J_{sc} was observed up to 900 nm. This may be due to a positive light-trapping gain resulting from a lower out-coupling of the solar cells [Campbell 87]. Finally, it should also be noted that the NIL process which involved heating and exposing the cell to UV light for a short time evidently did not damage the cell as the V_{oc} and FF were the same before and after imprinting. However, the post-bake of the replica was slightly modified and done at 120 °C and not at the usual 150 °C .

The replication of texture at the front of $n-i-p$ devices also led to a J_{sc} increase even though, in the $n-i-p$ case, the front of the device is made of textured LP-CVD ZnO which provides an ARE by the gradual change in the index of refraction. Figure 3.24 presents the EQEs of triple-junction solar cells in the $n-i-p$ configuration measured before and after imprinting an anti-reflective layer made by UV NIL. This triple-junction cell is similar to the one described in section 7.6. The broadband ARE is also clear in this figure, and from the J_{sc} values that are reported in table 3.8, a boost of 4% in total current is observed. This is slightly less than in the $p-i-n$ case where the texture is placed at a flat interface between air and glass. Nevertheless, this J_{sc} boost is significant and has contributed to the cell with a stable efficiency of 13% which is shown in section 7.6.

An extended study of the ARE produced by the nano-imprinted pyramids can be found in Escarré et al. [Escarré 12c]. In this study, which is not reproduced completely in this thesis, the ARE provided by large pyramids was found to be more efficient than either a standard anti-reflective coating made a multi-layer of TiO_2 and SiO_2 or the diffusive pyramidal texture

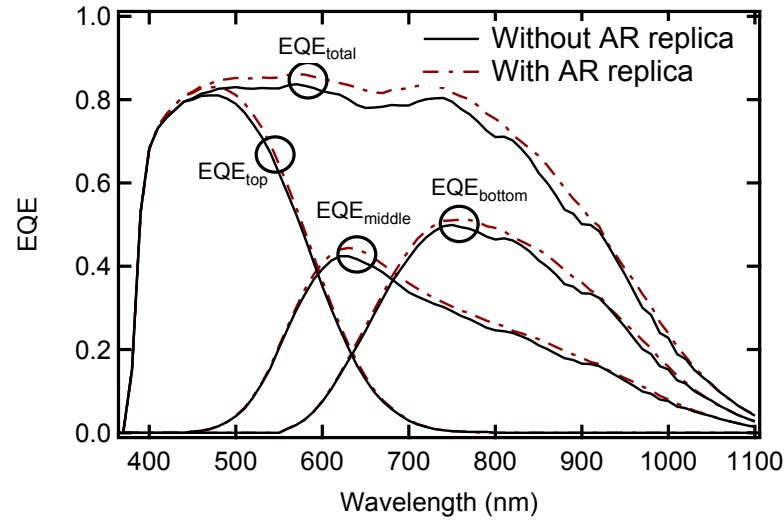


Figure 3.24: EQEs of a triple-junction solar cell in the $n-i-p$ configuration measured before and after the imprinting of an anti-reflective layer at the front of the device made by UV NIL.

Table 3.8: J_{sc} of a triple-junction solar cell in the $n-i-p$ configuration measured before and after the imprinting of an anti-reflective layer at the front of the device made by UV NIL.

Front	$J_{sc_{tot}}$ (mA/cm ²)	$J_{sc_{top}}$ (mA/cm ²)	$J_{sc_{mid}}$ (mA/cm ²)	$J_{sc_{bot}}$ (mA/cm ²)
Without pyramids	27.2	9.4	8.5	9.3
With pyramids	28.3	9.7	8.9	9.7

of Z5.

To conclude, it was shown that the UV NIL technique can also be applied in a post-process step in $p-i-n$ and $n-i-p$ devices to increase J_{sc} . This may help in reducing the costs of thin-film silicon solar cell technology by allowing thinner intrinsic layers. In particular, the beneficial redistribution in current for the top cell in micromorph $p-i-n$ design as shown in this section could allow for further reduction of the a-Si:H i -layer thickness which can potentially reduce light-induced degradation.

3.7 Conclusions

This chapter demonstrated the versatility of the UV NIL process. The quality of replication was shown to be remarkably high for replicas made with solid stamps while it was lower when soft PDMS stamps were used. These two sorts of stamps allowed for the production of textures on rigid glass substrates as well as flexible polymer sheets, the latter establishing a texturing process that is suitable for roll-to-roll processing on substrates other than temperature-resistant

metal foils or polyimide sheets [Ahn 08].

It was shown that novel textures, that prior to this work could not be used on plastic substrates, can be implemented and that a tandem a-Si:H/a-Si:H solar cell grown on a UV NIL textured plastic substrate exhibited a similar efficiency as state-of-the-art cells deposited on glass substrates. A further efficiency increase for this type of device will be shown in section 7.4.2 which reports that a record stable efficiency of 9.2% was obtained on a UV-NIL-textured plastic substrate using less than half a micron of a-Si:H. In the *p-i-n* configuration, the high transparency of the resin allowed the implementation of novel multi-scaled electrodes contributing to a micromorph a-Si:H/ μ c-Si:H device with a record initial efficiency of over 14% [Boccard 12b]. Besides these results, the shaping of LP-CVD ZnO surface layers with nano-scale precision was demonstrated allowing the decoupling of the light-scattering properties from the electrical properties. Finally, it was demonstrated that a replica of micro-metric features placed at the front of *p-i-n* and *n-i-p* devices acts as a broadband anti-reflective coating boosting the J_{sc} of micromorph and triple-junction devices by more than 4%.

To conclude, the incorporation of UV NIL replicated textures in different positions in solar cells led to significant improvements in their efficiencies and opened new perspectives for the technology. In this thesis, the solar cells that are investigated are not very tolerant of the substrate roughness and further improvements should be made to the deposition conditions and to the cell design to overcome this issue. If solar cells can be deposited on more aggressive structures, further efficiency enhancement can be expected by implementing novel photonic structures via nano-imprinting or nanomoulding. For instance, it was discussed that, even though the typical pyramidal features of LP-CVD ZnO are known to efficiently increase the light path in solar cells [Rockstuhl 10], even taller pyramids would allow for Lambertian scattering into silicon which could further increase light trapping [Battaglia 12a]. Also, if it were possible to maintain high V_{oc} and FF values for cells grown on nano-pillars, it would definitely be of high interest to incorporate these high-aspect ratio textures. The literature on nano-imprinting nano-pillars is vast, and the replication of high-aspect ratio textures were already demonstrated using UV NIL and PDMS stamps [Zhang 10, Kang 11]. If it is necessary to obtain a dense array of features with an extremely high-aspect ratio, nano-imprinting can be combined with deep reactive ion etching [Morton 08] but this technique would be more expensive than simple nano-imprinting which can probably produce most of the textures suitable for photovoltaic applications. The UV NIL replication of features is also a very valuable tool for experimental research. This is shown in the rest of this thesis (chapter 4, section 5.4 and section 5.5) where UV NIL replicas are used for specific dedicated tests for which special textures were required.

4 Experimental observation of guided mode excitation in a-Si:H solar cells

A metallic back reflector containing the texture of a 1D grating was prepared by using the nano-imprint lithography process discussed in chapter 3. The EQE of a single-junction a-Si:H *n-i-p* solar cell deposited on it shows clearly defined peaks of enhanced photocurrent in the weakly absorbing region. The resolution of the EQE in angle and in polarisation is used to explain these absorption phenomena. Calculation using an equivalent flat multilayer system relates the experimental angular variation of these peaks to theoretical values of guided modes. This demonstrates that light management can be viewed as the excitation via grating coupling of the guided modes that are supported by the silicon layers.

4.1 Introduction

Light propagation in a-Si:H solar cells cannot be interpreted by geometrical optics and far-field measurements as the surface textures used for light scattering have feature sizes close to the wavelength that is scattered. Also, layer thicknesses of a few hundreds of nanometers are not sufficient to break the light coherence and near-field phenomena should be taken into account. To model the electromagnetic field in this optical system, several options are possible. First, high-resolution computer simulations that rigorously solve the Maxwell equations [Bittkau 07, Rockstuhl 07, Rockstuhl 10, Ferry 09, Ferry 10, Ferry 11, Paetzold 11a, Paetzold 11b] explain the experimental observations but require time-consuming calculations and do not provide an intuitive understanding of the light-trapping mechanism. A second modeling solution is the scalar scattering theory [Poruba 00, Krč 02, Jäger 09, Dominé 10, Bittkau 11, Schulte 11, Lin 11, Bittkau 12] which show good agreement with the experiments. Still, this is an empirical approach using questionable approximations.

In this chapter, a simple explanation of light trapping provided by textured interface is given. Since the silicon layer is embedded between two media having lower refractive indices, this layer can be considered as an absorbing wave-guiding medium. Figure 4.1 presents a sketch of a typical flat device with an ITO front contact. Incoming light can enter the silicon layer by coupling to radiation modes according to Snell's law. The light trapping is not very efficient

in this case because of the weak path enhancement and because the light couples out of as easily as it couples into the silicon layer. Other modes which are better confined exist in the silicon layer: Guided modes propagate parallel to the interfaces and remain trapped in the wave-guiding layer which leads to much better absorption in case the wave-guiding medium is absorbing. Still, there is no access to these guided modes for light impinging on a flat device and therefore a surface corrugation is necessary to allow in-coupling with the drawback that it will also allow out-coupling.

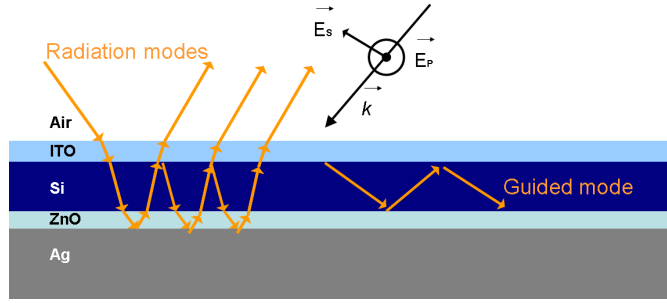


Figure 4.1: Schematic of the investigated device which consists of a stack of Ag/ZnO/Si/ITO/Air. S- and P-polarisation are defined for light impinging with a wave vector \vec{k} .

To experimentally observe the excitation of guided modes in solar cells, a periodic structure is used in this chapter. Light trapping promoted by grating textures was experimentally observed for a long time by other groups [Heine 95, Eisele 01, Senoussaoui 04, Söderström 09c, Ferry 09] and simulations have also suggested that the light trapping provided by a grating structure was related to the excitation of guided modes [Lee 08]. In 2010, three groups experimentally demonstrated the existence of guided modes in a-Si:H devices: First, the study which is reported in this section [Söderström 10c] and Ferry et al. [Ferry 10] used angular resolved EQE of cells grown on periodic structures. The work of Ferry et al. was realised on a 2D structure while our work was done on a 1D structure which allowed us to resolve polarisation as well but the results of both experiments are similar. A different approach was used by Bittkau and Beckers [Bittkau 10], who validated the accuracy of their high-resolution simulation code by using near-field scanning optical microscopy which is one of the few experimental methods which provides access to optical near-field phenomena. They showed then with simulation that the main absorption enhancement in a thin a-Si:H solar cell is provided by the excitation of guided modes via surface corrugations and only a minor enhancement is due to the excitation of radiation modes. Certainly, these three studies which were made in parallel using different methods showed that the light trapping in a-Si:H solar cells can be viewed as guided mode excitation by periodic structures [Söderström 10c, Ferry 10] or by random structures [Bittkau 10].

In the following, the model that we used is presented as well as experimental evidence of guided mode excitation. First, section 4.2 gives a review of the nature of wave guiding and presents the equations that were used to simulate the wave guides dispersion curves of a

flat device. Remarkably, the simulation requires as input only the individual thicknesses of the layers and their refractive index dispersions. Section 4.3 describes how light couples to the waveguide modes via grating coupling. The validation of the waveguide model for describing a thin-film silicon solar cell is then shown in section 4.4; the guided modes and their dispersion curves are experimentally observed using a solar cell grown on a 1D grating by relating localised absorption phenomena in the weakly absorbing region of the EQE spectra to the theoretical calculation described in section 4.2.

4.2 Flat interface waveguide model

For an intuitive understanding of propagating waves in a waveguide, it is convenient to first discuss the simplest waveguide design, which consists of an infinite dielectric slab of thickness d embedded between two perfect metallic walls (i.e. lossless mirrors). Figure 4.2a presents such a waveguide; the rotational symmetry along the z axis allows defining the wave vector of the electromagnetic field in such a structure as $\vec{k} = (k_{\parallel}, k_z)$ with $k_{\parallel}^2 = k_x^2 + k_y^2$.

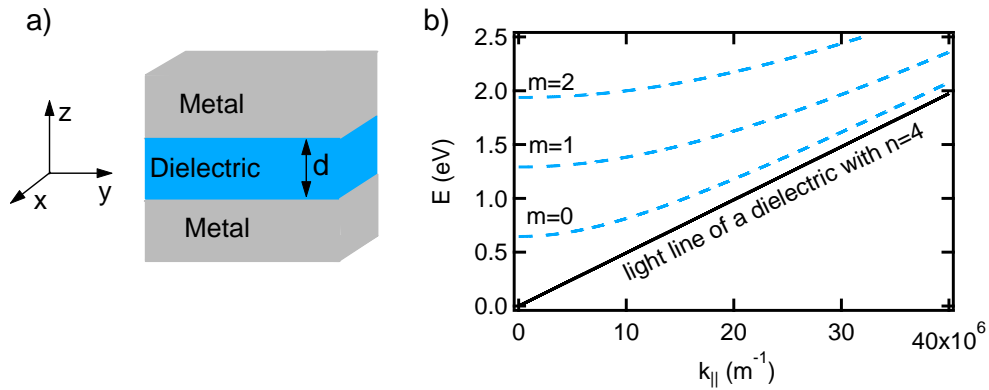


Figure 4.2: a) Schematic of a slab waveguide consisting of an infinite dielectric slab of thickness d embedded between two perfect metallic walls. b) Dispersion curves of waveguide modes existing in 240-nm-thick dielectric material embedded in two lossless metallic walls. A refractive index of 4 without dispersion was assumed for the dielectric layer.

As d tends toward infinity, the free dielectric space supports a continuous spectrum of possible modes that lie between the ordinate axis of figure 4.2b—the ordinate axis line corresponds to a field whose wave vector component is along the z axis only—and the light line of the dielectric, which has a slope equal to $\hbar c/n$ and which corresponds to an electromagnetic field with a wave vector that lies in the xy plane only. Here \hbar is the reduced Planck constant and c the speed of light in vacuum. As the thickness d is reduced, the electromagnetic field is still free in the xy plane but the z component of the electric field is quantised as it should vanish inside the metal, thus restricting the possible existing wave vectors in the dielectric to the form

$\vec{k} = (k_{\parallel}, q\pi/d)$ where $q=1, 2, 3\ldots$. Hence, the dispersion relations can be written:

$$E = \hbar c k = \frac{\hbar c}{n} \sqrt{k_{\parallel}^2 + \left(\frac{q\pi}{d}\right)^2}$$

The dispersion relations are plotted as dashed lines in figure 4.2b for $q=1, 2$ and 3 for the example of a 240-nm-thick dielectric slab with a wavelength-independent refractive index of $n=4$. In figure 4.2b they are labeled with $m=q-1$ as is common in the literature; m refers to the number of nodes of the electric field profile inside the dielectric layer. The dispersion curves are plotted only for positive k_{\parallel} (i.e forward propagating waves). Mirroring the diagram across the ordinate yields the backward propagating waves with negative k_{\parallel} .

Intuitively, a guided mode that propagates with a wave vector k_{\parallel} can be seen as the result of the interference of a plane wave which propagates with an angle α in the slab, and its reflections at the metallic walls. The interference pattern creates an electric and magnetic field distribution that does not vary along the direction of propagation of the guided mode $k_{\parallel} = nk \cos \alpha$.

The examination of the extremes of the dispersion curves in figure 4.2b (i.e. $k_{\parallel} \rightarrow 0$ and $k_{\parallel} \rightarrow \infty$) is helpful to understand the dispersion curves and how an electromagnetic field propagates in this waveguide. For $k_{\parallel} \rightarrow 0$ it can be observed that none of the guided modes propagate as their group velocities are equal to zero. Hence, these points represent standing waves that bounce back and forth in the z direction against the metallic walls without propagating in the xy plane. They thus feel strongly the confinement provided by the metallic walls. On the contrary, as $k_{\parallel} \rightarrow \infty$ the dispersion relations of the modes approach a wave that propagates freely in the xy plane in a dielectric slab of infinite thickness d . Thus, when k_{\parallel} increases, it signifies that the electromagnetic field of a particular mode feels less and less the confinement due to the metallic walls.

The description of the perfect slab waveguide helps to explain the mechanism behind wave guiding but, in the case of solar cells, an asymmetric dielectric waveguide should be considered. The wave guiding in a dielectric waveguide is due to total internal reflection and the S and P modes (see figure 4.1 for the definition of the polarisation directions) are not degenerate as in the case of the lossless mirror symmetric waveguide, because the phase shift at each total internal reflection is different for S and P waves. For asymmetric waveguides the calculation of the guided mode dispersion curves must be carried out numerically. This was done using a routine implemented in Mathematica which calculates the poles of the reflection coefficient of a multi-layer stack. This is based on the model described by Shakir and Turner [Shakir 82] who argue that these singularities (i.e. the poles of the reflection coefficients) correspond to energies where specific resonances take place, such as plasmonic or guided modes which propagate along the interfaces in one of the layers of the system. This calculation was applied to a solar cell stack to study plasmonic absorption occurring in the back reflectors [Haug 08, Haug 09]. The reflection coefficients at an interface between two media, for the two directions

of polarisations, are written :

$$r_{12}^S = \frac{\epsilon_2 S_1 - \epsilon_1 S_2}{\epsilon_2 S_1 + \epsilon_1 S_2}$$

$$r_{12}^P = \frac{S_2 - S_1}{S_1 + S_2}$$

with ϵ_j the complex dielectric constant in the j^{th} medium and S_j defined as:

$$S_j = \sqrt{k_j^2 - k_{\parallel}^2} = i k_j \sqrt{\frac{k_j^2}{k_{\parallel}^2} - \epsilon_j}$$

For a stack of layers with more than two media, the reflection coefficient is calculated recursively and should take into account the phase shift of the fields propagating in each layer. For a stack of five layers:

$$r_{12345} = \frac{r_{12} + r_{2345} \exp(2i \cdot S_2 d_2)}{1 + r_{12} \cdot r_{2345} \exp(2i \cdot S_2 d_2)} = \frac{r_{12} + \frac{r_{23} + r_{345} \exp(2i \cdot S_3 d_3)}{1 + r_{23} \cdot r_{345} \exp(2i \cdot S_3 d_3)} \exp(2i \cdot S_2 d_2)}{1 + r_{12} \cdot \frac{r_{23} + r_{345} \exp(2i \cdot S_3 d_3)}{1 + r_{23} \cdot r_{345} \exp(2i \cdot S_3 d_3)} \exp(2i \cdot S_2 d_2)}$$

$$= \frac{r_{12} + \frac{r_{23} + \frac{r_{34} + r_{45} \exp(2i \cdot S_4 d_4)}{1 + r_{34} \cdot r_{45} \exp(2i \cdot S_4 d_4)} \exp(2i \cdot S_3 d_3)}{1 + r_{23} \cdot \frac{r_{34} + r_{45} \exp(2i \cdot S_4 d_4)}{1 + r_{34} \cdot r_{45} \exp(2i \cdot S_4 d_4)} \exp(2i \cdot S_3 d_3)} \exp(2i \cdot S_2 d_2)}{1 + r_{12} \cdot \frac{r_{23} + \frac{r_{34} + r_{45} \exp(2i \cdot S_4 d_4)}{1 + r_{34} \cdot r_{45} \exp(2i \cdot S_4 d_4)} \exp(2i \cdot S_3 d_3)}{1 + r_{23} \cdot \frac{r_{34} + r_{45} \exp(2i \cdot S_4 d_4)}{1 + r_{34} \cdot r_{45} \exp(2i \cdot S_4 d_4)} \exp(2i \cdot S_3 d_3)} \exp(2i \cdot S_2 d_2)}$$

It should be observed that this calculation requires as input only the individual thicknesses of the layers and their refractive index dispersions. This model already showed good agreement with experimental data when used to study plasmonic absorption in solar cell back reflectors [Haug 08]. Similarly, this model was applied to a stack of Ag/ZnO:Al/Si/air and showed that the ZnO:Al buffer layer used in a solar cell on top of a silver reflector not only serves to prevent the diffusion of silver atoms in the silicon layer, but also converts the plasmonic mode into a guided mode, thus limiting parasitic absorption in the silver layer [Haug 09]. In the present chapter, the aim was to compare electrical measurements of a complete solar cell with theoretical predictions to validate the use of the flat waveguide model. Including the ITO front contact, the reflection coefficients r_{12345} must be applied to the stack shown in figure 4.1 (i.e. a stack of Ag/ZnO:Al/Si/ITO/air).

A typical diagram of dispersion curves calculated for a flat solar cell with the Ag (semi-infinite)/ZnO:Al (60 nm)/Si (240 nm)/ITO (65 nm)/air (semi-infinite) structure is shown in figure 4.3 for the energy range of interest for light confinement in a-Si:H solar cells. Again, only the forward propagating waves are shown but the same curves exist for the backward propagating waves. The refractive indices were characterised by using ellipsometry for the ZnO, a-Si:H and ITO layers while the silver data were taken from published values [Johnson 72].

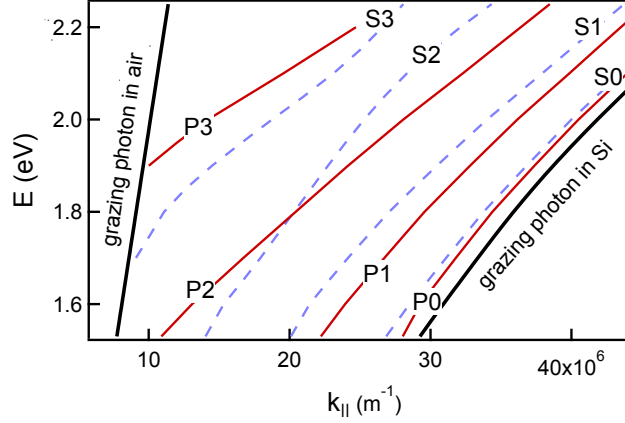


Figure 4.3: Dispersion curves of a flat Ag (semi-infinite)/ZnO:Al (60 nm)/Si (240 nm)/ITO (65 nm)/air (semi-infinite) waveguide for the wavelength range of interest for light trapping in a-Si:H solar cells. Note the discrete nature mode in the silicon layer. Dashed and solid lines are guided modes for S- and P-polarisation, respectively.

4.3 Coupling of incident light

Section 4.2 described how the dispersion curves were obtained. However, in a flat solar cell, light impinging on the device cannot couple to the guided modes of the silicon layer because their dispersion curves lie below the line of the grazing photon in air as figure 4.3 shows. The mechanism behind the excitation of guided modes via grating coupling is described in this section. The particular case of a device that is corrugated with a grating structure allows a simple description of the coupling mechanism by the diffraction orders and the Brillouin zones. It has to be noted that the dispersion curves shown in figure 4.3 are valid for a flat device but can still be used to describe the corrugated device as long as the texture can be considered as a perturbation.

A photon impinging on a grating structure can gain or lose momentum proportional to a multiple of the reciprocal lattice vector, which yields a multitude of equivalent wave vectors \vec{k}' given by

$$\vec{k}' = \vec{k}_{\parallel}^i + m\vec{G} = \sin\theta^i \vec{k}^i + m\vec{G}$$

where \vec{k}^i , \vec{k}_{\parallel}^i and θ^i are the incident wave vector, parallel wave vector and angle in air, respectively. \vec{G} is a vector of the reciprocal lattice of the grating and m can be any integer. For 1D grating with period a it is sufficient to describe the reciprocal lattice vector by its norm $\|\vec{G}\| = \frac{2\pi}{a}$. In this case, the periodicity from the grating can be described in Brillouin zones which can be introduced into the dispersion diagrams in two ways. First, the dispersion curves can be folded into the first Brillouin zone and the dispersion diagram should be plotted

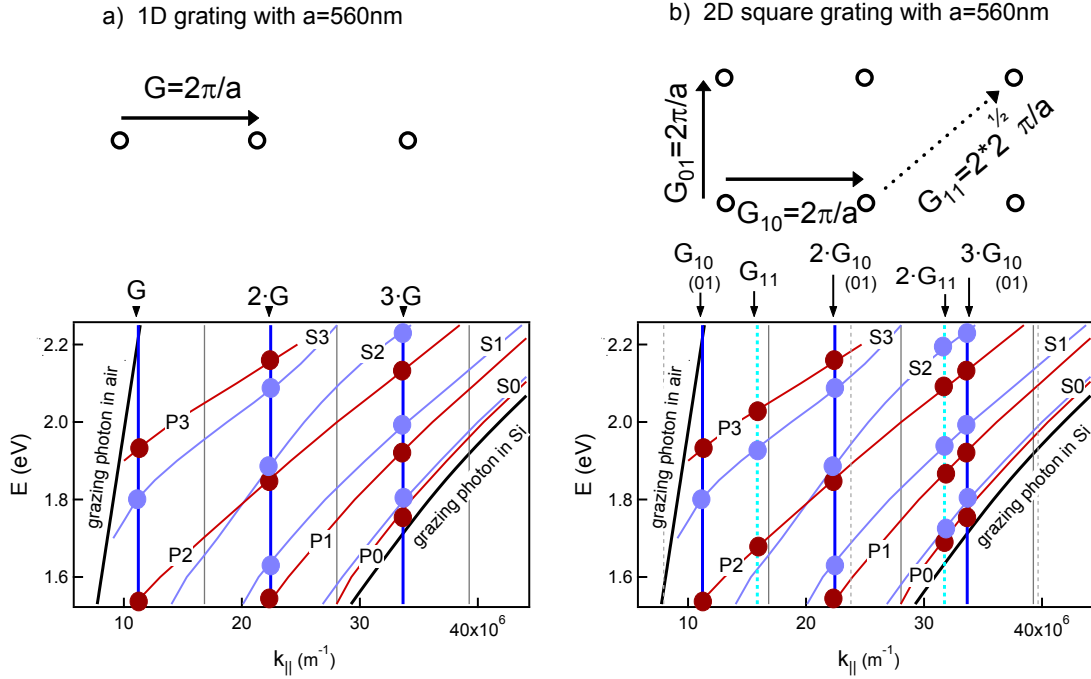


Figure 4.4: Coupling to guided modes by diffraction for a) a 1D grating and b) a 2D square grating with a period of 560 nm. Upper panels represent the reciprocal lattices with the corresponding coupling wave vectors G . The dispersion diagrams of a flat waveguide of Ag (semi-infinite)/ZnO (60 nm)/Si (240 nm)/ITO (65 nm)/air (semi-infinite) are shown in the lower panels. The vertical thin lines are the borders of the Brillouin zones (solid lines for $G=2\pi/a$ and dashed lines for $G=2\sqrt{2}\pi/a$). Coupling may occur when the diffracted light (thick vertical lines are examples for light with perpendicular incidence, the dashed and continuous lines refer to $G=2\pi/a$ and dashed lines for $G=2\sqrt{2}\pi/a$, respectively) intersects with a guided mode; the latter intersections are marked with circles.

only between its borders which are given by $k_{\parallel}^i = \pm \frac{\pi}{a}$. Second, the dispersion diagram can be extended to higher-order Brillouin zones. We chose to use the second procedure as it also allows observation of the number m of vectors \vec{G} that should be added for the coupling (i.e. the diffraction order). Figure 4.4a shows the reciprocal lattice and the dispersion diagram (same stack as in figure 4.3) including the Brillouin zones given by a 1D grating with $a = 560$ nm. The thin vertical lines represent the borders of the 2nd, 3rd and 4th Brillouin zones. The thick vertical lines are multiples of the reciprocal vector \vec{G} which correspond to the 1st, 2nd and 3rd diffraction orders for perpendicularly incident light. Excitation of guided modes may occur whenever the momentum k_{\parallel} is conserved, i.e. when a diffraction order crosses the dispersion curve of a mode. The possible excitations for perpendicularly incident light are marked with circles in figure 4.4a. For non-perpendicularly incident light, the vertical lines corresponding to diffraction orders would have a slope equal to $\hbar \frac{c}{n} \sin \theta^i$ (sum of dispersion curve of non-perpendicularly incident light and reciprocal vector \vec{G}) which in turn shifts the resonant energy. Therefore, an angle dependence of the coupling energy should be observed

if guided modes are excited by the grating diffraction orders. This will be experimentally observed in section 4.4.

Figure 4.4b presents coupling possibilities due to a 2D square grating with the same period $a = 560$ nm. The same coupling can occur thanks to the vector $\|\vec{G}\| = \frac{2\pi}{a}$ but whereas on a 1D grating there are only two possible diffraction orders ($\pm\vec{G}$), four possible diffractions may occur in the case of a 2D grating ($\pm\vec{G}_{10}$ and $\pm\vec{G}_{01}$). Additionally, diffraction can take place with slightly longer reciprocal vector of which $\|\vec{G}_{11}\| = \frac{\sqrt{2} \cdot 2\pi}{a}$ is an example. It is therefore clear that the light confinement provided by a 2D grating is higher than for a 1D structure and that its geometry (e.g. square, triangular, hexagonal lattice) has an influence by modifying the number and the modulus of the reciprocal lattice vectors.

4.4 Experimental observation of guided mode excitation via grating coupling in a-Si:H solar cells

In this section, experimental validation of the waveguide model is shown. Using EQE measurements resolved in angle and in polarisation, it is shown that localised absorption phenomena in the weakly absorbing region can be related to the excitation of guided modes whose dispersion curves were calculated using the flat interface model described in section 4.2.

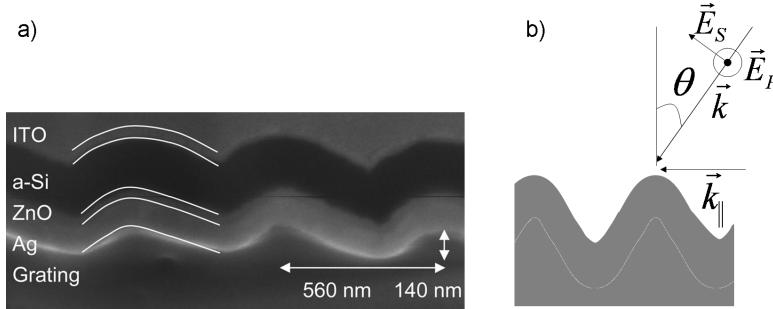


Figure 4.5: *a) SEM image of a cell cross section performed by C. Calderone in CIME of EPFL. b) Experimental configuration for the EQE measurements.*

The investigated device was a single-junction $n-i-p$ a-Si:H solar cell grown on a 1D grating that served as textured back reflector. Figure 4.5a shows an SEM image of the device cross section and figure 4.5b defines the polarisation directions S and P. A thin a-Si:H cell on a 1D grating allows an easier attribution of experimental localised absorption as:

1. The a-Si:H solar cell structure supports only a limited number of modes in the wavelength region of interest as shown in figure 4.3.
2. The number of possible couplings is reduced compared to a 2D grating as seen in figure 4.4.
3. The 1D structure allows for discrimination between the polarisation directions as shown

4.4. Experimental observation of guided mode excitation via grating coupling in a-Si:H solar cells

in figure 4.5b.

The grating substrate had a period $a=560$ nm and, an amplitude $h=70$ nm (half the peak to valley depth) and was made using the nano-imprint technique described in chapter 3, using a commercial master. The structure was covered with a standard back reflector made of 120 nm of silver and 60 nm of ZnO:Al. The cells were deposited in system E and were grown with a total silicon thickness of approximately 240 nm. The front contact was made of 65 nm of ITO. In addition to standard characterisation of the solar cell, P- and S-polarisation were distinguished in the EQE measurements by using a broadband wire polariser (Proflux PPL05C, Moxtek).

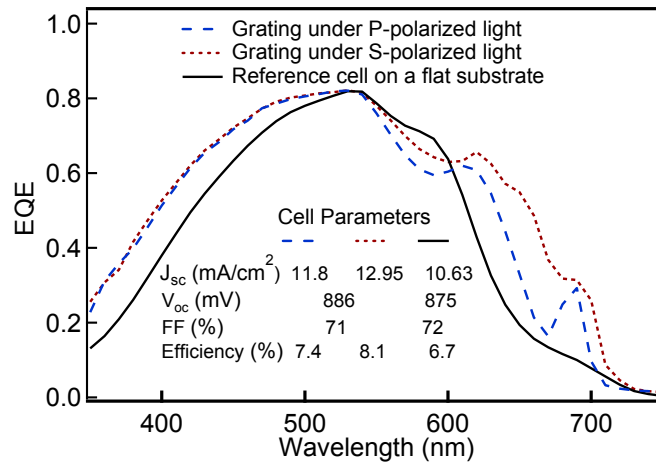


Figure 4.6: EQE measured under normal incidence for a reference cell grown on a flat substrate and for a cell grown on the 1D grating substrate.

Figure 4.6 presents the EQE and the electrical parameters of a flat reference cell and of a cell grown on the grating substrate for both polarisation directions, using perpendicular incidence. The total current enhancement produced by the grating structure is apparent and is approximately 10% and 20% for P- and S-polarisation, respectively. For this particular structure, S-polarised light is preferential for light trapping under small angles as shown in figure 4.6, but for large angles P-polarised incident light produces higher photocurrent as shown in figure 4.7. This effect can be attributed to the angle dependance of light coupling to the guided modes and on the efficiency of coupling which is not provided by our model.

In figure 4.6, a strong localised absorption peak at a wavelength of 690 nm is obvious for the EQE of the solar cell grown on the grating substrate measured under P-polarisation. To understand the phenomenon behind this strong photocurrent enhancement, P- and S-polarised angle-resolved EQEs were measured on this cell, varying the angle of incidence in 5° steps between -50° and 55°. The angle was measured with respect to the surface normal and the rotational axis was parallel to the grooves of the grating as illustrated in figure 4.5b. For a symmetric grating, the same information is expected for negative and positive angles while

a blazed grating should induce differences in coupling strength for forward and backward traveling waves due to the different intensities of positive and negative diffracted orders. The grating that was investigated here had a slight blazed angle but the effect of the blazing on the efficiency of coupling was not clearly observed in this experiment. Hence the measurement from -50° to 55° solely permits us to estimate the uncertainty when extracting k_{\parallel}^i from the experimental data. The raw data are presented in figure 4.7a for S-polarisation and figure 4.7b for P-polarisation; the upper panels show a 3D representation of this experiment and the systematic changes of the absorption signatures in the weakly absorbing region between 600 nm and 750 nm are clear. The lower panel presents 2D plots of the EQEs in a more standard view; the solid lines point out the position of a constructive interference fringe due to the silicon thickness and the signatures of mode excitation are underlined with dashed arrows of different colors.

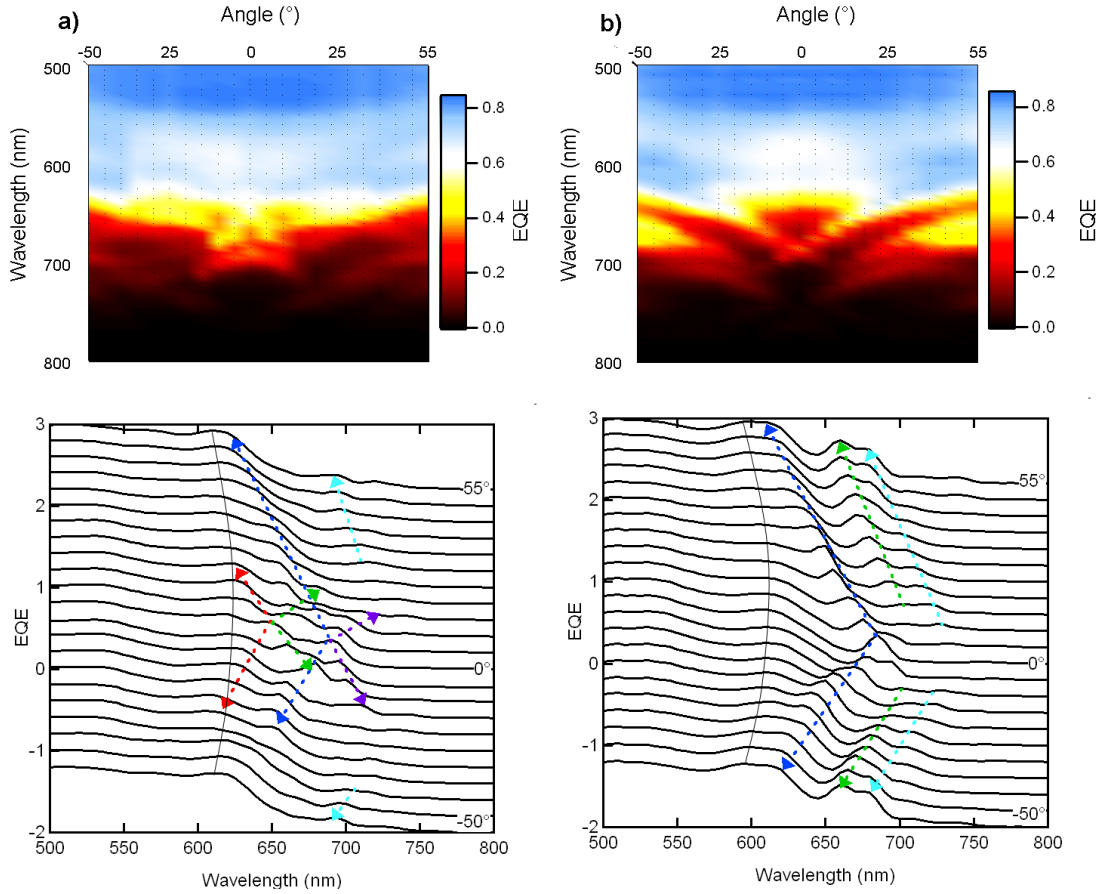


Figure 4.7: Angular-resolved EQE measurements in a) S-polarisation and b) P-polarisation. The graphics in the upper panels are 3D representations while the lower panels represent a more standard view of the EQEs which are offset vertically for clarity. The arrows in the lower panels show the experimental modes that were extracted for each polarisation.

4.4. Experimental observation of guided mode excitation via grating coupling in a-Si:H solar cells

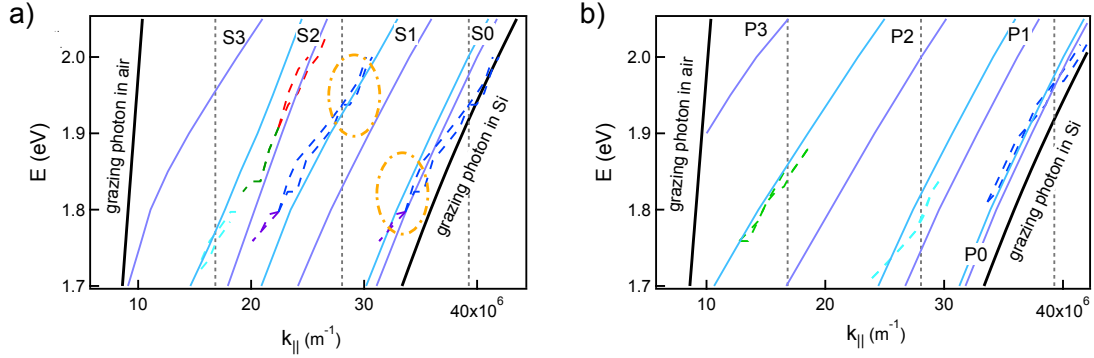


Figure 4.8: Attribution of the a) S-polarised and b) P-polarised modes that were experimentally observed in figure 4.7 using the dispersion curves of a flat waveguide of Ag (semi-infinite)/ZnO:Al (60 nm)/Si (200 nm in light blue, 240 nm in purple)/ITO (65 nm)/air (semi-infinite). Vertical dashed lines represent the borders of the 2nd, 3rd and 4th Brillouin zones for $a=560\text{nm}$. The experimental modes are shown as dashed lines and their colors correspond to those in the lower panels of figure 4.7. The circles in a) show that the dark blue experimental S-polarised mode should be separated into two different modes for better matching with theory.

As explained in section 4.3, the absorption phenomena were interpreted as grating coupling between the incident wave vector component parallel to the surface k_{\parallel}^i and guided modes of the structure. Hence, using the angular range shown in figure 4.7, the propagating modes in the structure were experimentally extracted to form a set of (E, k_{\parallel}^i) (arrows in figure 4.7). As explained previously, a photon impinging on a grating structure can gain or lose momentum proportional to a multiple of the reciprocal lattice vector, which yields a multitude of equivalent wave vectors k' given by

$$k' = k_{\parallel}^i + m \frac{2\pi}{a} = \sin\theta^i \frac{2\pi}{\lambda^i} + m \frac{2\pi}{a}$$

where k_{\parallel}^i , θ^i and, λ^i are the incident parallel wave vectors, angles and wavelengths in air, respectively, m can be any integer, and a is the period of the grating. At a given energy, excitation of guided modes propagating in the silicon layer occurs whenever the wave vectors of the guided mode are equal to k' . Thus, a comparison between the k -vector calculation of the guided modes in the structure and the experimental values of the impinging k_{\parallel}^i vector was made, adding multiples of the reciprocal grating vector. This is plotted in figure 4.8 for both polarisation directions. The dispersion curves were calculated for two silicon layer thicknesses of 200 and 240 nm to account for thickness variations ($\pm 10\%$ across the substrate). For illustration, the experimental values in figure 4.8 use the same colors as in figure 4.7. Figure 4.8 shows good correspondence between the experimental values and the calculated dispersion curves. The dashed circles in figure 4.8a show that the dark blue measured data, which were initially interpreted as the signature of a single mode, better match the theoretical dispersion curves if they are separated into two modes: A set of (E, k_{\parallel}^i) with high energies that

should be attributed to the S1 mode, and a set of (E, k_{\parallel}^i) with lower energies that, along with the purple data better match with the S0 theoretical mode.

The successful attribution of the experimental data to the dispersion diagram of guided modes calculated for an equivalent five-layer flat device demonstrates that photocurrent enhancement in the weakly absorbing region of silicon, commonly called light trapping, can be viewed as the excitation of guided modes within the silicon layer via grating coupling. As the J_{sc} enhancement is large with a texture that contains only a single spatial frequency, we conclude that the majority of photocurrent enhancement induced by textured surfaces is due to the excitation of guided modes, consistent with the conclusions of Bittkau and Beckers [Bittkau 10].

4.5 Conclusions

In the study presented in this chapter, the 1D grating was a valuable tool; particularly its selectivity to polarisation directions was useful for understanding the light trapping process. For application in a device, a 1D grating structure is clearly not the ideal substrate because the resulting absorption enhancement is limited to specific wavelengths and is sensitive to the light polarisation. The ideal periodic substrate for thin-film solar cell would combine multiple frequencies in 2D to avoid polarisation effects and to yield more resonances in the weakly absorbing region. Also, by extending our modeling approach to multi-scaled substrates it might be possible to understand the light trapping provided by widely used random textures in terms of an expansion into Fourier components as expressed in the power spectral density of random surface morphologies.

It was recently shown that light coupling promoted by a periodic texture into the guided modes of a stack of layers similar to thin-film silicon devices could be predicted by using an analytical model based on a Rayleigh expansion [Haug 12b]. The simple model described in this chapter allows for the prediction of the energies at which the resonances take place and the number of them for each spatial frequency and for each type of device. Hence, by combining this model with the work shown by Haug et al. [Haug 12b] it should be possible to simulate and design the texture for ideal light trapping. The calculation of the guided mode dispersion curves shows that the ideal texture depends on the optical constants and thicknesses—especially of the silicon thickness—of each layer. An analytical simulation tool with a lower computational time than a simulation that rigorously solves Maxwell's equations, could allow for a quick simulation of the light trapping promoted by numerous texture designs. Its accuracy might be lower than that of a more rigorous simulation tool but it could provide the basic features of the ideal texture and thereby reduce the space of parameters that should be used as input for exact simulation. Simulation tools should be combined to find the ideal texture as each methods have positive and negative aspects.

Finally, the experiments in this chapter have validated the use of the waveguide framework and have formed the basis for theoretical considerations on the upper limits of enhancement

in real devices [Haug 11b, Haug 11a, Naqavi 11]. These experiments were also used as input for rigorous computer modeling which revealed the importance of correctly mapping the changes of the interface geometries because of film growth [Naqavi 11], something which was also recently discussed by Solntsev et al. [Solntsev 13]. In combination with the nano-imprint technique presented in chapter 3, our approach has contributed to experimental and theoretical discussion of the light-trapping potential provided by periodic and random texturing in *p-i-n* devices [Battaglia 12b].

5 Back reflector materials in a-Si:H solar cells

This chapter discusses back reflectors consisting of a rough metallic layer combined with a thin dielectric buffer layer of ZnO:Al. It is shown that the ZnO:Al layer can help to mitigate parasitic absorption in the metallic back reflector and also in the n -doped layer. It is then shown that, independent of the ZnO:Al buffer layer thickness, silver back reflectors perform better than aluminium reflectors and that relative J_{sc} gains between 5.5% and 8.2% are obtained by using silver. Subsequently, it is shown that the growth of silver on rough nano-textures leads to a decrease in the silver reflectance which decreases the efficiency of the solar cell grown on top. A thermal annealing of the silver layer at low temperature is shown to increase the silver grain size up to 40% and at the same time increase the silver reflectance from 80% to 98% at a wavelength of 500 nm. Because of reduced parasitic absorption, this results in an absolute efficiency gain up to 1% for solar cells grown on annealed back reflectors compared to non-annealed back reflectors. Finally, rough random scattering textures made in a plasmonic material and in a dielectric material are compared. It is shown that the light management provided by the two materials is similar but that the plasmonic back reflector provides higher total absorption which does not translate into higher photocurrent but into more pronounced parasitic losses. Therefore, it is likely that textures made in rough dielectric layers combined with a flat silver reflector can perform better than reflectors containing a rough silver layer which allows the light to couple to plasmonic resonances that parasitically absorb part of the light.

5.1 Introduction

Remarkable efficiency improvements can be obtained in thin-film silicon solar cells by engineering light management in the solar cells. The quality of the back reflector and the materials that compose it are of particular importance as light with long wavelengths interacts with it. This chapter concentrates on back reflectors that are compatible with the UV nano-imprint process that allows the texturing of substrates for $n-i-p$ a-Si:H solar cells and which was shown in chapter 3. Hence, the focus in this chapter is drawn to rough metallic back reflectors which are in general covered with a thin buffer layer of dielectric material like ZnO:Al.

Section 5.2 discusses the influence of the ZnO:Al buffer layer thickness on the light management provided by a silver back reflector. It is shown that a thin layer of approximately 60 nm is necessary to reduce the parasitic absorption due to surface plasmon polaritons and that a further increase of the ZnO:Al thickness leads to an oscillating behaviour of J_{sc} values with an optimum obtained experimentally for 120 nm of ZnO:Al. The improved light management for a thickness of 120 nm is explained by a minimum of absorption in the n -doped layer by comparing the experimental data with simulation done via the transfer matrix method (TMM).

Back reflectors made of aluminium could be of higher interest than silver for industrial purposes because aluminium is a more abundant material and thus less expensive than silver. Therefore, section 5.3 discusses the differences in light trapping that are provided by the two metals and the experimental evidence shows that aluminium reflectors lead to higher parasitic absorption, probably due to intra- and inter-band transitions. This is in accordance with previous experimental studies [Banerjee 91, Springer 05, Yang 09b, Söderström 09a, Palanchoke 12], although theoretical studies diverge on this point, with some favoring aluminium [Ferry 11] and others favoring silver [Springer 05, Palanchoke 12]. As section 5.2 shows that the ZnO:Al buffer layer can significantly modify the J_{sc} of the solar cells, section 5.3 presents a variation of the ZnO:Al buffer layer thickness from 30 nm to 200 nm. This study confirms that aluminium reflectors do not outperform silver reflectors.

Section 5.4 demonstrates that a high reflectance of the nanotextured silver layer is important for light management. When the silver layer is deposited on a textured surface, it is not straightforward to obtain sufficient reflectance as observed previously by other groups [Springer 05, Sainju 06, Yan 12a]. Here, a thermal annealing step at low temperature which is compatible with the use of plastic substrates is proposed to improve the reflectance of bare silver films as well as the efficiencies of solar cells grown on silver films. The effect of annealing on the films is evaluated by SEM, AFM and XRD and a comparison of solar cells grown on annealed and as-grown silver layers shows that an absolute efficiency gain up to 1% can be obtained on the annealed silver layer.

Finally, section 5.5 presents a discussion of the differences in J_{sc} enhancement that can be achieved if the same scattering texture is made in a rough dielectric back reflector or a rough silver back reflector. Based on experimental evidence, it is found that there is no clear advantage for either type of back reflector since the metallic back reflector leads to higher parasitic absorption but not to higher photocurrent. Still, as a rough silver layer is bound to induce the excitation of plasmonic resonances which parasitically absorb part of the light, it could be of higher interest to use a back reflector design made of a flat silver layer combined with a rough dielectric layer.

5.2 ZnO:Al buffer layer

This section investigates the effect on the optical response of cells of the thickness of the ZnO:Al buffer layer which lies between a silver reflector and the silicon layers as shown in the schematic of a typical *n-i-p* solar cell depicted in figure 5.1. Since 1991 [Kothandaraman 91, Banerjee 91] it has been observed that the addition of a ZnO:Al buffer layer on top of a metallic reflector improves the J_{sc} values of the cells grown on it compared to cells grown on bare metallic layers. It was then recently shown that this was due to a reduction of parasitic absorption losses arising from the excitation of plasmonic resonances at the surface of the metal in thin-film silicon solar cells [Haug 09, Lal 12] as well as in thick wafer-based heterojunction solar cells [Holman 13a, Holman 13b]. In the following, it is experimentally shown that, as expected, this layer helps to mitigate parasitic absorption in the silver layer. It is also observed that this is not the only role of this layer and that it can modify the intensity of the electric field in the *n*-doped layer and therefore minimise parasitic absorption losses in this layer as well.

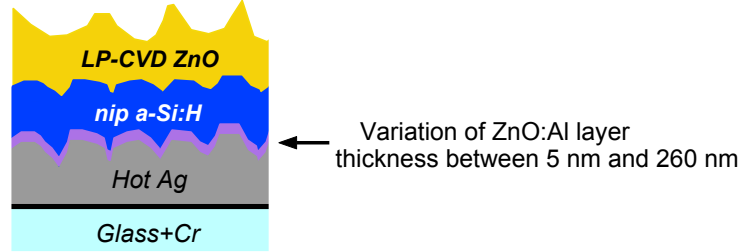


Figure 5.1: Schematic of experiments 1 and 2: The cells are co-deposited on identical silver textured back reflectors for which the thicknesses of the ZnO:Al buffer layer was varied between 5 nm and 260 nm.

The substrates used for this experiment were made of Hot Ag suitable for the growth of a-Si:H solar cells. On top of the silver textured layers different thicknesses of ZnO:Al buffer layers in the range of 5 nm to 260 nm were deposited. a-Si:H solar cells with total silicon thicknesses of 300 nm were deposited in a *n-i-p* sequence in the large-area Kai-M reactor (a few details on this cell can be found in section 2.2.2) and the front contact was made of a lowly doped 2- μm -thick LP-CVD ZnO layer. The cells were made in two co-depositions: Experiment 1 used substrates with 5 nm, 20 nm, 40 nm, 60 nm, 80 nm, 100 nm, 120 nm, 140 nm, 160 nm, 180 nm and 200 nm of ZnO:Al and Experiment 2 used the same cell recipe on two substrates with ZnO:Al layer thicknesses of 200 nm and 260 nm. A small J_{sc} discrepancy of 0.1 mA/cm² could be found between the two depositions which was probably due to a slightly thicker *p*-layer in Experiment 2.

In order to understand better the effect of the thickness variation of the ZnO:Al layer, TMM was used to simulate a flat cell with a total silicon thickness of 300 nm (28 nm, 257 nm and 15 nm of *n*-, *i*- and *p*-layer, respectively) and a front contact made of ITO. The fact that the front contact is different in the simulation than in the experiments should have only little impact on

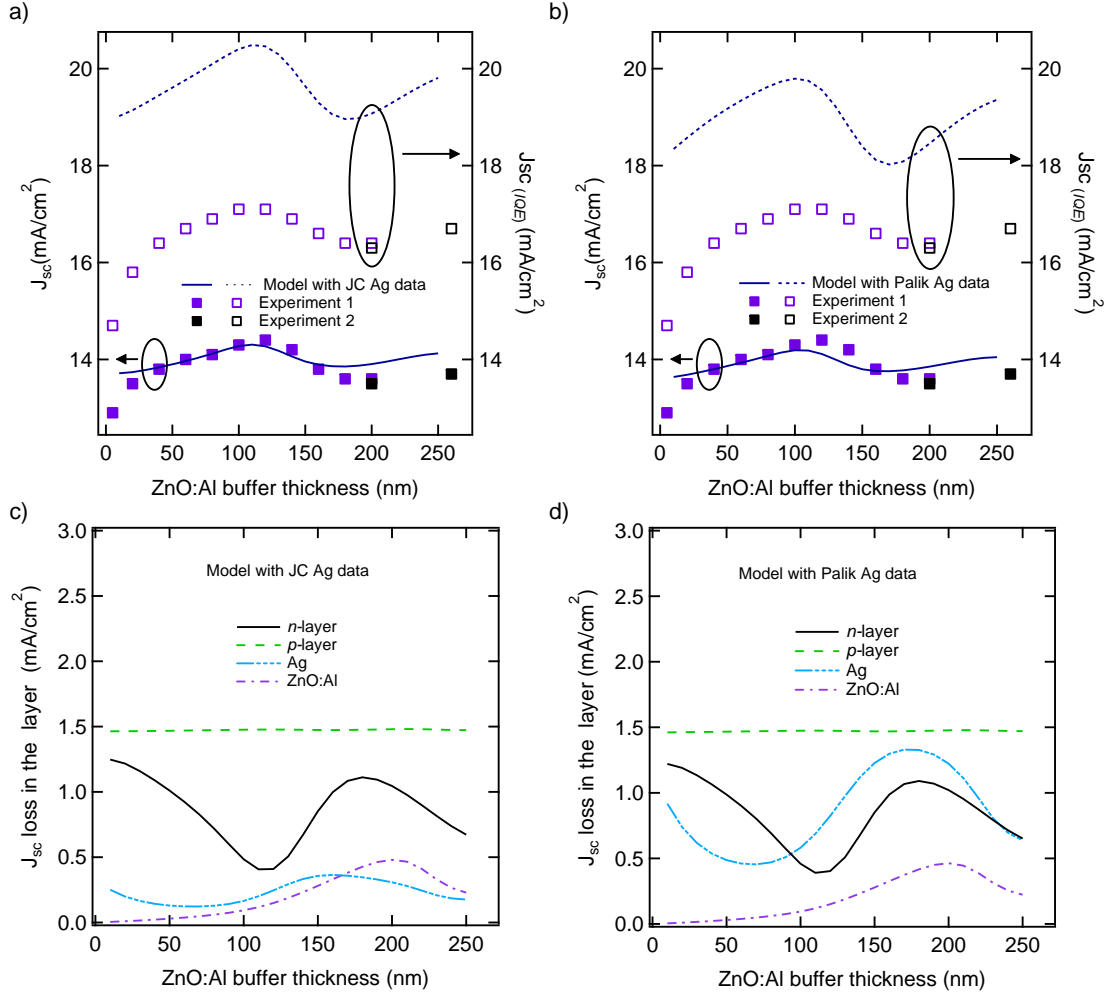


Figure 5.2: *a) and b) present the experimental and TMM-calculated J_{sc} and $J_{sc(IQE)}$. c) and d) present the J_{sc} losses that were simulated in each layer. The silver optical constants of JC were taken in the model used in a) and c) and the one of Palik were used in b) and d).*

the mechanisms behind absorption at the back of the cell. The simulations were performed by A. Naqavi and the layers' optical data were extracted by ellipsometry for the ZnO:Al, ITO, n -, p - and i -layers. For the optical constants of the silver layer, two sets of published data were considered, one from Johnson and Christy (JC) [Johnson 72] and the other from Palik [Palik 98]. The data from JC have a permittivity with a lower imaginary part than those of Palik and therefore describe a metal of better quality with lower intrinsic absorption.

Figures 5.2a and b present the experimental J_{sc} and $J_{sc(IQE)}$ as well as those calculated from TMM simulations. $J_{sc(IQE)}$ was calculated by integrating the convolution of the IQE and the AM1.5G solar spectrum and describes the J_{sc} that could be obtained if there were no light escaping the device. Figures 5.2c) and d) present the J_{sc} losses that were simulated in each layer. These J_{sc} values were calculated by integrating the convolution of the absorption in

each layer and the AM1.5G spectrum. The silver optical constants of JC were used in figures 5.2a and c and the one of Palik were used in figures 5.2b and d.

It can be observed in figures 5.2a and b that both the simulated sets of J_{sc} and $J_{sc (IQE)}$ and the experimental sets of J_{sc} and $J_{sc (IQE)}$ present an oscillating behaviour with respect to the ZnO:Al layer thickness and that an optimum can be found for a ZnO:Al thickness of 120 nm. From the simulated J_{sc} losses shown in figures 5.2c and d, the optimum appears to correspond to a thickness for which there is a minimum of absorption in the n -doped layer and does not seem to be strongly affected by the silver quality. Indeed, only a minor change in the simulated J_{sc} can be observed when the data of a more lossy silver is used as in figure 5.2b. Here, the effect of using an silver layer with higher absorption is seen to influence predominantly the simulated $J_{sc (IQE)}$. This might however not correspond to reality as the simulations were realised using a flat device and, if there were an efficient light trapping, the effect of the metal could be more important as the light interacts more with it. Also the optical constants taken from Palik may still underestimate the real absorption of the deposited silver and hence the impact on J_{sc} due to absorption in the silver layer can be more important than that of the n -doped layer. However, the IQE spectra that are shown in figure 5.3 seem to indicate as well that the oscillating behaviour of the J_{sc} for ZnO:Al layers between 60 nm and 260 nm is probably due to a reduction of the absorption in the n -doped layer as explained below.

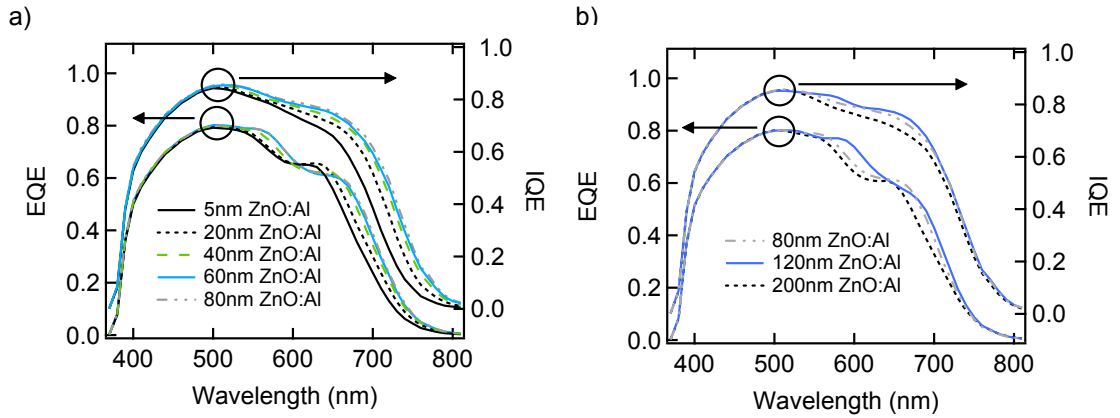


Figure 5.3: a) EQE and IQE of solar cells with ZnO:Al buffer layer thicknesses between 5 nm and 80 nm showing parasitic absorption due to surface plasmon polariton resonances for the two thinnest ZnO:Al layers. b) EQE and IQE of solar cells with ZnO:Al buffer layer thicknesses of 80 nm, 120 nm and 200 nm which exhibits differences in n -doped layer parasitic absorption.

For values of ZnO:Al thicknesses below 60 nm it appears from figure 5.2a and b that there is a stronger decrease of J_{sc} and $J_{sc (IQE)}$ in the Experimental data than in the simulated data. This is not surprising because the model of a flat device cannot account for the parasitic losses due to coupling of light to surface plasmon polaritons which occur for thin ZnO:Al buffer layers on rough substrates [Haug 09]. Figures 5.3a and b, which present the EQE and the IQE of the solar cells of Experiment 1 for particular values of ZnO:Al layer thicknesses, provide further evidence for this assumption. The EQEs exhibit different interference fringes due to different optical

thicknesses of the devices which depend on the ZnO:Al thickness. Hence, parasitic absorption should be discussed by comparing the IQEs. For thin ZnO:Al layers of 5 nm and 20 nm, there are strong absorption losses over the whole wavelength range between 500 nm and 800 nm for which the light interacts with the back reflector. There are only minor differences between the IQEs of the cells grown on the substrates with ZnO:Al thicknesses of 40 nm, 60 nm, and 80 nm over the same wavelength range. Interestingly, for the thicker ZnO:Al layers that are shown in figure 5.3b, the behaviour is very different and there are discrepancies between these IQEs only between 500 nm and 700 nm. Because of this very different behaviour the absorptions that occur on the full wavelength range of 500 nm to 800 nm for the two thinnest layer of ZnO:Al are attributed to parasitic losses due to surface plasmon resonances, while for the thicker layers of ZnO:Al the discrepancies between the IQE between 500 nm and 700 nm are attributed as explained above to different absorptions in the n -doped layer. Indeed, this type of difference in IQE between 500 nm and 700 nm are also typically observed when there is some problem of collection due to contamination near the n/i interface but measurements under reverse bias voltage did not reveal collection issues.

Table 5.1: *Characteristics of $n-i-p$ a-Si:H solar cells co-deposited on identical silver textured back reflectors for which the ZnO:Al buffer layer thickness was varied between 5 nm and 260 nm. The best cell for which the ZnO:Al thickness is optimal is marked in bold.*

ZnO:Al thickness	J_{sc} (mA/cm ²)	V_{oc} (mV)	FF (%)	Efficiency (%)
5 nm	12.9	924	70	8.3
20 nm	13.5	927	69	8.6
40 nm	13.8	929	70	9.0
60 nm	14.0	929	70	9.1
80 nm	14.1	929	69	9.0
100 nm	14.3	932	70	9.3
120 nm	14.4	931	70	9.4
140 nm	14.2	932	70	9.2
160 nm	13.8	932	70	9.0
180 nm	13.6	921	67	8.4
200 nm	13.6	920	68	8.5

To conclude, table 5.1 presents the electrical parameters of cells co-deposited in Experiment 1. It shows that relative differences in J_{sc} of more than 11% can be obtained by varying the ZnO:Al layer thickness without hampering the other electrical properties. The effect of the ZnO:Al buffer layer can be separated in two: First, an increase of the thickness of ZnO:Al layer up to 60 nm helps to mitigate parasitic absorption due to surface plasmon excitation. Second, for ZnO:Al layer thicknesses above 60 nm there is an optimal thickness for which the electrical field inside the n -doped layer is lower and hence the parasitic losses in this layer are lower.

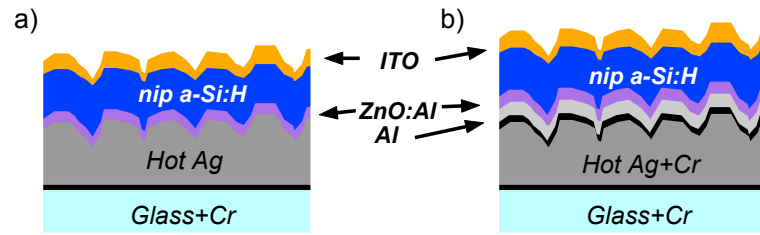


Figure 5.4: Schematic of the experiment. The cells are co-deposited on the same texture but a) half have a silver reflector and b) half an aluminium reflector. The thickness of the ZnO:Al buffer layer was varied in each case between 30 nm and 200 nm.

5.3 Aluminium vs silver as metallic back reflector

The aim of this section is to provide an experimental comparison of the light management provided by metallic back reflectors made of aluminium and silver. All experimental comparisons made so far have shown that silver behaves better than aluminium when used as a back reflector in thin-film silicon solar cells [Banerjee 91, Springer 05, Yang 09b, Söderström 09a, Palanchoke 12]. Nevertheless, it was suggested that aluminium could be of higher interest than silver as its surface plasmon resonance takes place at a lower wavelength range and hence parasitic plasmonic losses could be lower when aluminium is used. Unfortunately, in aluminium layers there is absorption due to intra-band and inter-band transitions which take place in a wavelength range which is detrimental for light management in solar cells [Benett 63]. The differences between the theoretical study that shows an advantage of aluminium over silver [Ferry 11] and those that show the contrary [Springer 05, Palanchoke 12] can probably be attributed to differences in the optical constants used to model the metallic layers.

In the following, a-Si:H single-junction solar cells which were co-deposited on back reflectors made either of aluminium or of silver are investigated. In order to have a fair comparison the scattering texture is similar as shown by optical characterisation of the bare substrates. To complete this study, the thickness of the dielectric buffer ZnO:Al layer which lies between the metal and the silicon layers was varied. Indeed, as shown for silver back reflectors in section 5.2, the ZnO:Al buffer layer has an influence on the optical response of a cell by modifying the absorption losses. As the optimum thickness for this layer could be different when used with silver and aluminium reflectors, a broad range of ZnO:Al thicknesses from 30 nm to 200 nm was investigated.

The structures of the a-Si:H cells studied in this chapter are shown in figure 5.4. The substrates are made of Hot Ag suitable for a-Si:H cell deposition. The aluminium reflectors were obtained by covering half of the Hot Ag substrates with a thin sputtered Cr layer and 130 nm of evaporated aluminium. The optical characterisation of the bare substrates are reported in figure 5.5. It can be observed that the aluminium reflector has a lower total reflectance than

the silver reflector in the whole wavelength range of interest while the haze is similar on both substrates. Hence, the fraction of scattered light provided by both substrates is similar but the parasitic absorption in the metallic layers is different as measured in air. A set of ZnO:Al buffer layers of 30 nm, 60 nm, 90 nm, 120 nm, 160 nm and 200 nm were deposited on each metallic layer and a-Si:H solar cells with a total silicon thickness of 310 nm were co-deposited on these in a Kai-M industrial reactor (some details on the cell can be found in chapter 2.2.2). The front contact was made of 65 nm of sputtered ITO. The EQE spectra of the solar cells were extracted and to complete the study, their total reflectance spectra were also measured in order to extract the IQE.

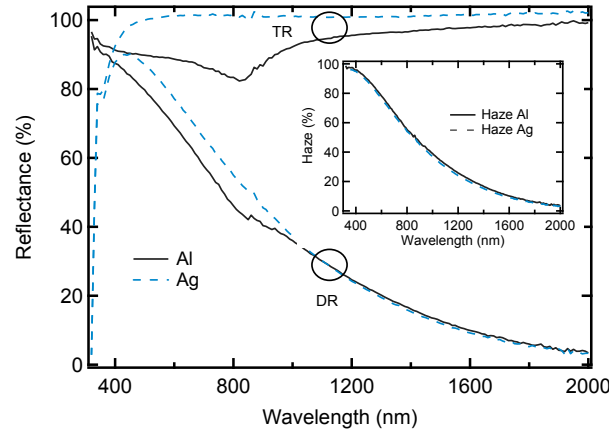


Figure 5.5: *Optical characterisation of the bare metallic layers used as substrates for single-junction a-Si:H solar cells. The DR and TR are reported and the inset presents the corresponding haze values.*

Figure 5.6a the dependence of the measured J_{sc} and $J_{sc} (IQE)$ as a function of the ZnO:Al buffer layer thickness, for silver and aluminium back reflectors. For both types of metallic back reflector, the J_{sc} and $J_{sc} (IQE)$ trends as a function of the ZnO:Al buffer layer thickness are the same as observed in section 5.2. The larger difference between J_{sc} and $J_{sc} (IQE)$ on silver (around 17%) than on aluminium (around 11%) shows that cells grown on aluminium reflectors exhibit higher parasitic absorption in the metallic layer than cells grown on silver. This can also be seen in figure 5.6b which presents examples of EQE and IQE curves for thicknesses of ZnO:Al of 160 nm and 120 nm for silver and aluminium back reflectors: The IQEs of the cells grown on aluminium reflectors are lower than the IQEs of the cells grown on silver reflectors over the whole wavelength range between 500 nm and 800 nm for which the light interacts with the back reflector, showing the higher parasitic absorption losses. It is interesting to note the different effects that variation of the ZnO:Al thickness has on the IQE of cells with aluminium and silver reflectors. With silver reflectors, the use of 120 nm of ZnO:Al compared to 160 nm leads to a decrease in the absorption losses between 500 nm and 670 nm and this is probably related to a minimum of absorption in the n -doped layer as explained in section 5.2. On the contrary, with aluminium reflectors the IQEs diverge over the whole wavelength

5.4. Improvement of silver by thermal annealing at low temperature

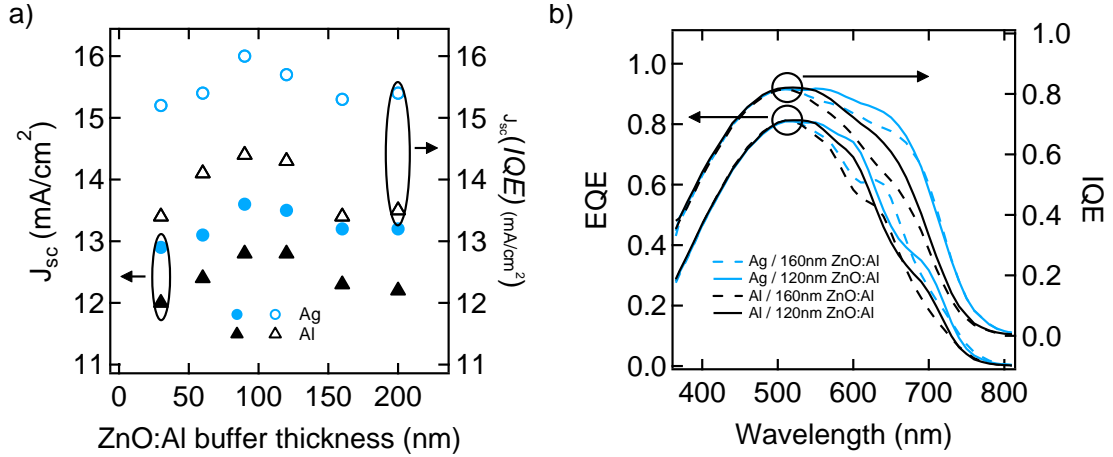


Figure 5.6: a) Dependence of the measured J_{sc} and the calculated J_{sc} (IQE) as a function of the buffer layer ZnO:Al thickness, both for silver and aluminium back reflectors. b) EQE and IQE curves for ZnO:Al thicknesses of 160 nm and 120 nm for silver and aluminium back reflectors.

range between 500 nm and 800 nm. This indicates that, when a more lossy material such as aluminium is used, optimisation of the ZnO:Al layers also helps to minimise absorption in the metal and not only in the n -doped layer.

To conclude, this section has shown that, independent of the ZnO:Al buffer layer thickness, the aluminium reflector does not perform better than the silver reflector. In section 5.4 it will be shown that the reflectance of the silver back reflector depends on its material quality, which depends on the type of texture it is deposited on. Hence, it is possible that the aluminium reflectance can be similarly increased. Nevertheless, during this thesis, the highest TR obtained for a flat aluminium film was only marginally (4%) higher than the one shown in figure 5.5 and it is extremely doubtful that the parasitic losses due to inter- and intra-band transitions can be significantly reduced.

5.4 Improvement of silver by thermal annealing at low temperature

Silver is an almost perfect reflector throughout the visible and infrared range of wavelengths and absorption effects other than free carriers absorption in the UV are limited to particular configurations. It was however discovered that strong losses due to parasitic absorption were occurring in our textured metallic back reflectors based on a simple experiment. Figure 5.7 shows that contrary to previous studies [Söderström 08a, Söderström 08b, Boccard 11], decreasing the substrate roughness by using plasma treatment leads to an increase in J_{sc} if the LP-CVD ZnO is covered with a Ag/ZnO:Al back reflector before the cell deposition. Figure 5.7 shows two sets of cells which were co-deposited on three Z2 substrates which were treated for different times. In figure 5.7a a detached flat silver back reflector was used during the EQE measurement, and, as expected, the EQE decreases with higher treatment time. In 5.7b

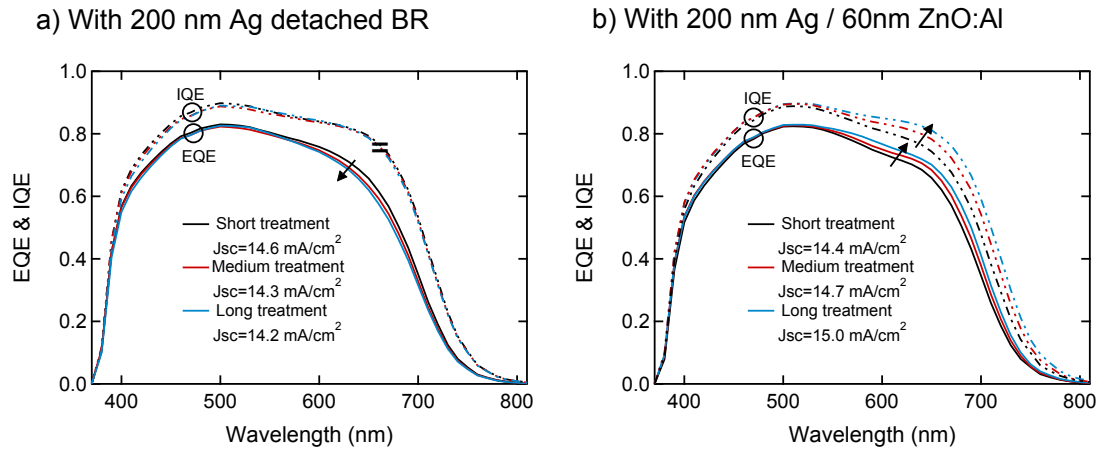


Figure 5.7: EQE spectra of co-deposited a-Si:H solar cells on a) LP-CVD ZnO treated for different times with a detached flat silver back reflector added behind the glass substrate and b) LP-CVD ZnO treated for different times covered with a Ag/ZnO:Al sputtered back reflector before the cell growth.

the silver back reflector was deposited on the textured ZnO and the J_{sc} increases with higher treatment times. This is attributed to parasitic absorption in figure 5.7b as the IQEs show. Hence, in the following, the impact of the lower reflectance of textured silver is discussed and a means to improve the silver reflectance by using a low-temperature thermal annealing step compatible with plastic substrates is shown.

Absorption effects in silver layers are widely covered in the literature and mainly attributed to resonances of surface plasmon polaritons or localised plasmon polaritons. For flat silver films deposited at low temperature the localised plasmon resonance was observed to disappear when the films were heated to room temperature because of microstructure modification of the silver layer [Hunderi 80, McBreen 83]. The surface plasmon polaritons and localised plasmon polaritons resonances were also optically observed long ago on silver deposited at room temperature on rough surfaces [Ritchie 57, Tokarsky 76]. The deposition of silver and the behaviour of silver after deposition have been widely studied: The grain growth during annealing of films was studied with X-rays [Light 66, Hurt 85] and electron microscopy [Light 66, Hurt 85, Sharma 80, Dannenberg 00a, Dannenberg 00b]. Properties of silver films such as their crystalline orientations and optical and electrical properties were also studied as a function of the sputtering conditions [Parmigiani 86, Jung 04], and the morphology of films was related to deposition conditions in the zone model of Thornton et al. [Thornton 86].

In this section, it is shown that thermal annealing at 150 °C improves the reflectance of silver films deposited by sputtering at room temperature on nano-textured substrates. The annealing provokes two interlinked effects: A rearrangement of the silver layer with a modification of its morphology, and an increase of up to 42% in the grain size of the polycrystalline film for the preferential orientation as measured by X-ray diffraction. The main consequence of

5.4. Improvement of silver by thermal annealing at low temperature

these two mechanisms is a large increase in the reflectance of the silver when measured in air. This reflectance increase is also noticeable in devices: a-Si:H solar cells grown on annealed silver films yield higher IQEs and EQEs compared to cells grown on as-deposited silver. The morphology modification also smoothens the substrate which leads to a clear increase of the V_{oc} and FF of the cells grown on annealed silver reflectors. Finally, as the additional annealing step in the back reflector fabrication may be difficult to industrialise, sputtering of thinner silver films onto substrates heated to 150 °C is investigated; the resulting films exhibit equivalent diffuse reflection, but a slightly lower total reflection compared to similar silver films annealed after their deposition at room temperature. In both cases the studied temperatures are compatible with plastic substrates like PEN.

5.4.1 Experimental details

The substrate templates consisted of the pyramidal surface texture of Z2. Two different configurations were used to observe the annealing effect, as shown in figure 5.8.

In the first experiment, to observe the effect of annealing on the optical properties and within

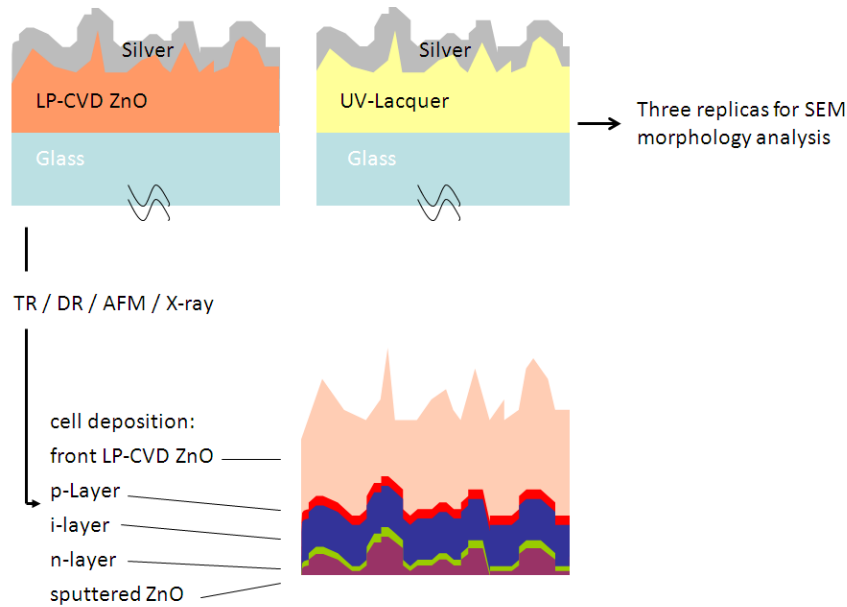


Figure 5.8: *Schematics of the samples and the corresponding measurements and experiments performed on each.*

the cells, two Ar plasma treatments were made on as-grown Z2: Type A refers to samples that were treated for a shorter time than samples of type B, and they are hence rougher. Then, 300-nm-thick silver layers were co-deposited on these samples by sputtering at room temperature. Half of each type of substrate was subjected to thermal annealing in air atmosphere at 150 °C for 50 minutes. The silver layers on these substrates were characterised optically

by TR and DR, morphologically by AFM and SEM cross-section imaging and also by X-ray analysis in a $\theta/2\theta$ configuration (PANalytical X'Pert PRO MPD diffractometer using $\text{CuK}\alpha$ radiation) which allowed the determination of the crystallographic orientations of the silver. The Scherrer formula [Jones 38] was used to estimate the average grain size of coherent domains of the preferential crystallographic orientation after correction of the peak width from the instrument contribution (LaB6 was used). Also, these four types of substrates with annealed silver (A_{ann} , B_{ann}) or as-deposited silver (A_{as-dep} , B_{as-dep}) were inserted as back reflectors into solar cells to observe the effect of annealing directly in the cell. To this end, the silver layers were covered with 70 nm of ZnO:Al to finish the back reflectors. The a-Si:H cells with 200-nm-thick intrinsic layers were co-deposited on these four substrates in system E and were front contacted using a 5- μm -thick lightly doped LP-CVD ZnO:B. For a better understanding of the absorption, TR of the cells was measured to calculate the IQE.

In the second experiment, to observe qualitatively the morphological modification with annealing, the structure of untreated Z2 was replicated three times. To reveal the morphological changes due to the deposition of silver and its annealing, SEM images were recorded on the same features on the three different substrates. The first one was covered with 50 nm of silver which acted as a conductive layer for imaging purposes. The second image was taken of a substrate covered with 300 nm of silver. The third image was taken of a substrate covered with 300 nm of silver that was annealed after its deposition.

In the last experiment, the industrial application of the processes is investigated. For this purpose, LP-CVD ZnO similar to type A presented above was used. First, two thicknesses of silver were deposited at room temperature (120 nm and 300 nm) and compared optically after annealing. In a second step, a 120-nm-thick silver layer deposited onto a substrate kept at approximately 150 °C was characterised optically.

5.4.2 Optical properties and morphology analysis of bare substrates

The effect of thermal annealing is observed in the optical properties of the substrates which are shown in figure 5.9. Both annealed samples approach TR around 100% for the whole spectral range of interest (360 nm to 1100 nm) while the substrates with as-deposited silver layers show strong absorption in this wavelength range. The roughness σ_{rms} of the substrate as extracted from 5.5 μm^2 AFM images is reported in figure 5.9, revealing a smoothening of the substrates with annealing. This is also observed qualitatively with SEM imaging of cross sections of type A samples before and after annealing (figure 5.10). Figure 5.10 also shows that an original U-shaped valley of ZnO may transform into a V-shaped valley after the silver layer deposition which may be detrimental for the electrical properties of a cell grown on this kind of substrate. In a separate experiment (not shown here) it was observed that the haze value at 1000 nm of a Z2 substrate increased from 41% when covered with a 100-nm-thick silver layer to 50% and 54% for 200- and 300-nm-thick silver layers, respectively, suggesting that the substrate becomes rougher when a thicker silver layer is deposited by sputtering. Clearly, figure 5.10 shows that not only does the σ_{rms} decrease with subsequent annealing but more importantly the V-shaped valleys are smoothened.

5.4. Improvement of silver by thermal annealing at low temperature

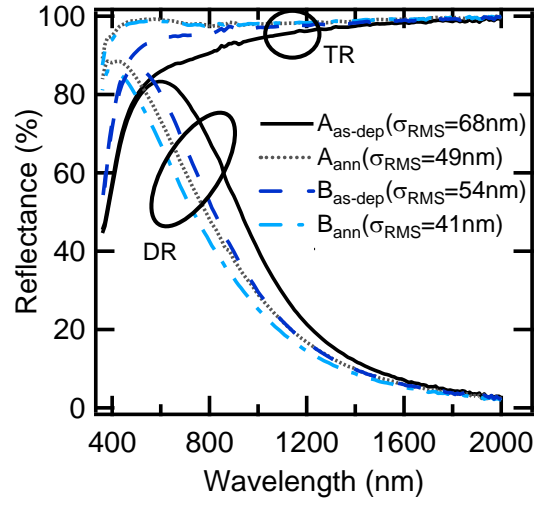


Figure 5.9: *TR and DR of type A and B substrates covered with 300 nm of silver before and after annealing. The σ_{rms} values extracted from AFM is presented.*

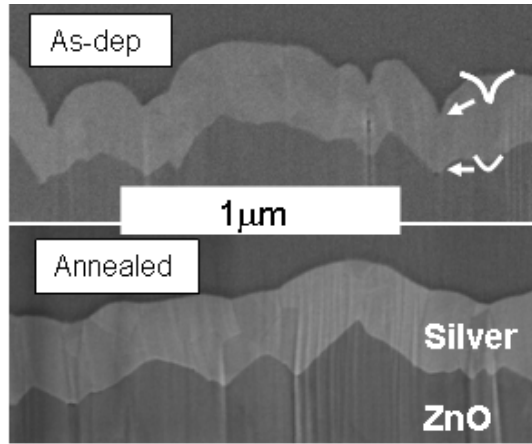


Figure 5.10: *SEM images of cross sections of a type A sample before and after annealing. The sections and the images were made by Dr. M. Duchamp from the Center for Electron Nanoscopy of the Technical University of Denmark.*

For further investigation of the morphological changes, figure 5.11 presents SEM images taken on the same features on three identical replicas of LP-CVD ZnO. White circle segments and crosses mark the same position on all three samples. A comparison of figures 5.11a and 5.11b shows that silver films with thicknesses of 50 and 300 nm essentially reproduce the pyramidal surface features of the LP-CVD ZnO surfaces. Closer inspection of figure 5.11b reveals the development of a fine granular structure superimposed onto the facets. After annealing, the triangular facets are no longer visible and silver grain growth yields more rounded shapes. The dashed circles in figure 5.11c identify zones where the valleys between pyramids have been

replaced by large grains that show internal contrast due to domains with different orientations, as can be induced by twin grain boundaries.

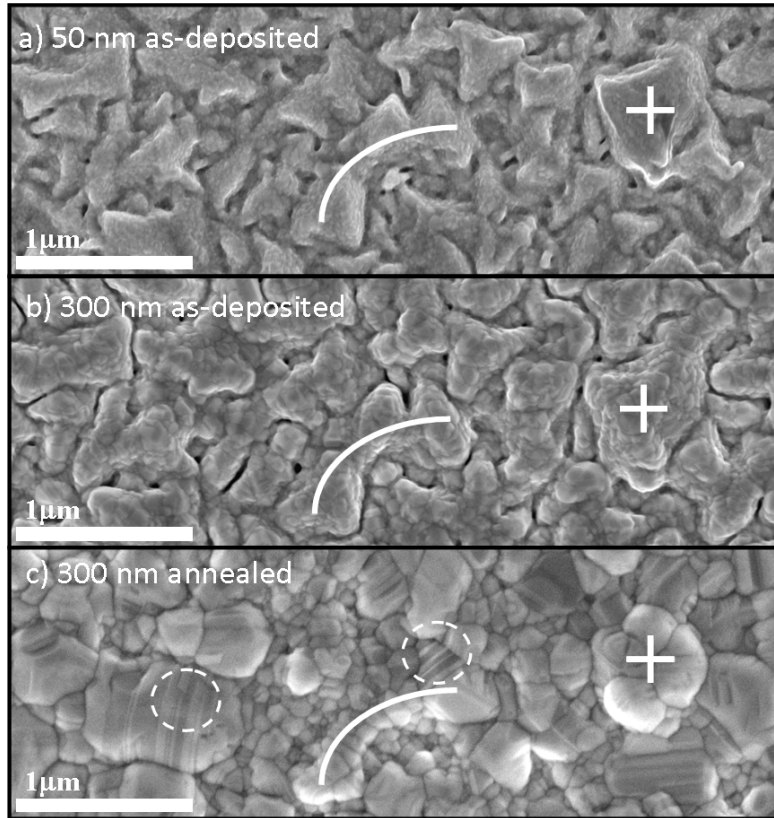


Figure 5.11: SEM images of identical pyramids covered with a) 50 nm of silver, b) 300 nm of silver and c) 300 nm of silver after annealing. White circle segments and crosses mark the same features on the substrates.

The SEM images of figure 5.11 show that large grains are formed by the annealing. This was further studied by an XRD analysis whose results are presented in table 5.2 and figure 5.12. Figure 5.12 presents the spectra of a silver powder sample with no preferential orientation, and as-deposited and annealed 300-nm-thick silver films grown on a replica of untreated LP-CVD ZnO:B, ZnO samples of type A and B.

On the polymer substrate shown in figure 5.12b the diffraction pattern is very similar to the powder sample shown in a, suggesting that there is no preferential orientation. On the contrary, on the ZnO samples of type A and B, there is a strong 220 orientation for the silver grains. Therefore, it can be concluded that the silver growth is modified on the LP-CVD ZnO:B sample due to the ZnO:B crystallographic orientation which induce a local epitaxial growth of the silver. Indeed, the LP-CVD ZnO:B layers which develop the pyramidal features are known to have a 110 orientation [Nicolay 09], and the latter peak is observed in figure 5.12c and d.

The grain sizes determined from the preferential 220 line on samples of type A and B increased

5.4. Improvement of silver by thermal annealing at low temperature

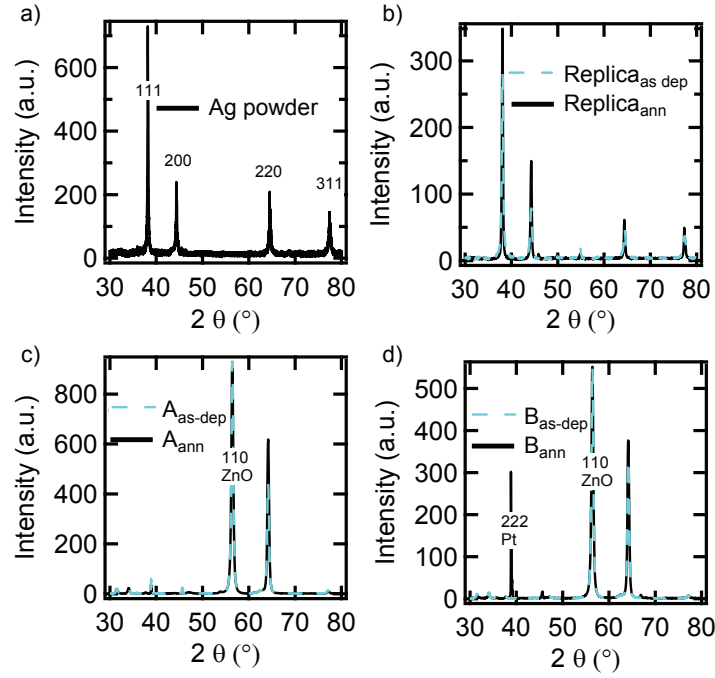


Figure 5.12: XRD spectra of a) silver powder (reference taken from RRUFFTM project database), and 300-nm-thick silver films on b) a Z2 replica, c) a type A substrate, and d) a type B substrate. Dashed and full lines denote spectra of as-deposited and annealed samples, respectively.

Table 5.2: Results of XRD analysis: preferential orientation, average grain size of the 220 peak and increase of grain size with annealing.

Type	Orientation	Grain size (nm)	Increase in size (%)
A_{as-dep}	220	55	42
A_{ann}	220	78	
B_{as-dep}	220	62	13
B_{ann}	220	78	

strongly with annealing as shown in table 5.2. This may explain the large reflectance increase with annealing because the grain boundaries are known to decrease the reflectance in polycrystalline films [Sotelo 03]. This is also supported by the fact that the reflectance as well as the grain size is larger in B_{as-dep} than in A_{as-dep} . The grain growth during annealing at this low temperature is attributed to surface diffusion of the silver atoms. Grain boundary diffusion, which is an alternative process for grain growth, is unlikely; it is typically reported for temperatures above 400 °C [Dannenberg 00a, Dannenberg 00b]. The absence of grain boundary diffusion is also corroborated by the observation that the reflection of silver layers did not improve if they were covered with a ZnO:Al layer of 5 nm before annealing (not shown). It appears that the annealing of the silver back reflector for solar cell applications has to be carried out before the deposition of the ZnO:Al buffer layer and the experiment shown in

the next section will confirm this observation. The modification and stabilisation of silver films subjected to annealing when capped with a barrier layer was also previously reported [Smith 77].

5.4.3 Cell results

Figure 5.13 and table 5.3 present the results of a-Si:H solar cells made on the four types of back reflectors (A_{as-dep} , A_{ann} , B_{as-dep} and B_{ann}). Figure 5.13a and b present the EQE, absorption and IQE of the cells while table 5.3 shows their corresponding J_{sc} , V_{oc} , FF , and efficiency values. In all the curves shown in figure 5.13a differences between the cells grown on as-deposited and annealed silver samples are seen for wavelengths greater than 500 nm where the incident light begins to impinge upon the back reflectors. The cells grown on as-deposited silver demonstrate higher absorption than cells grown on annealed silver while it is the opposite for the EQEs. This indicates that stronger parasitic absorption is present in the cells grown on as-deposited silver. As the silver layer is the only part of the cells that differs, it can be concluded that losses occur in this layer. This is even clearer in the IQE curves; the IQE of cells grown on as-deposited silver is lower than the IQE of the cells grown on annealed silver which demonstrates the better use of the light that enters the cells after annealing. It is interesting to note that the optical measurements shown in figure 5.9 are performed in an air environment which does not reflect what happens in the cells. However, as EQE and IQE analysis shows, the higher reflectance on the bare substrates also leads to lower parasitic absorption in cells, and consequently to higher EQE. It can also be seen that the difference between the EQE, IQE, and absorption of cells grown on B_{as-dep} and B_{ann} is lower than the difference between the cells grown on A_{as-dep} and A_{ann} . This is in line with the smaller difference in the TR between B_{as-dep} and B_{ann} compared to the difference in TR between A_{as-dep} and A_{ann} (see figure 5.9). Finally, the possibility that the observed EQE differences can be due to collection problems on the rougher substrates is excluded, since the EQE measurements performed under a bias of -1 V were close to the EQE measured without bias for all solar cells (not shown).

Table 5.3: Characteristics of *n-i-p* a-Si:H solar cells fabricated with silver-covered ZnO substrates.

Type	J_{sc} (mA/cm ²)	V_{oc} (mV)	FF (%)	Efficiency (%)
A_{as-dep}	14.0	900	63	7.9
A_{ann}	14.7	930	64	8.8
B_{as-dep}	14.4	930	65	8.7
B_{ann}	14.6	950	66	9.2

Table 5.3 shows that annealing leads to an increase in all solar cell parameters. This is in accordance with the optical and microscopy measurements, from which it is expected that the annealed samples are advantageous for cell growth as the AFM and SEM images reveal a lower roughness and a decrease of the V-shaped structures between pyramids (see area with

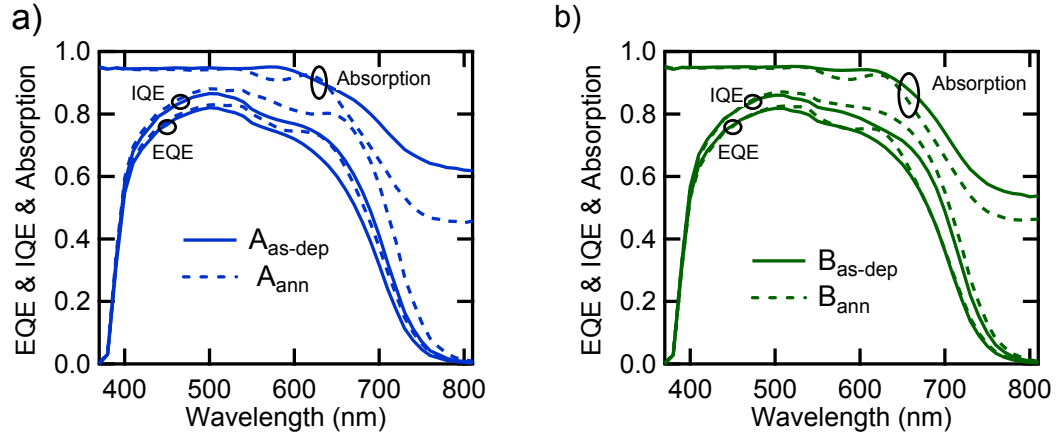


Figure 5.13: EQE, IQE, and absorption of cells grown on the four types of back reflectors.

dark contrast in figure 5.11b and figure 5.10) that are detrimental to V_{oc} and FF . However, in terms of light trapping, annealing appears to be disadvantageous because the diffuse reflectance in figure 5.9 shows that annealed samples scatter light less efficiently. Nevertheless, the possible loss in light trapping is more than compensated by the reduction of the silver parasitic absorption, as seen in the J_{sc} comparison. Finally, table 5.3 shows an increase in absolute efficiency of almost 1% (0.5%) for the type A (B) substrate after annealing due to an increase in all three parameters (J_{sc} , V_{oc} and FF). The comparison in table 5.3 shows that sample A_{ann} yielded to the highest current; however, this texture also shows losses of V_{oc} and FF compared to the less severe texture of type B. Thus, for the silicon layers shown here, the gain in current obtained on a rougher substrate like type A is not sufficient to compensate the losses in V_{oc} and FF . The trade-off that is required on the roughness of the substrate for the growth of a-Si:H solar cell with high efficiency will be further discussed in section 7.2.

5.4.4 Towards industrialisation

In the previous sections it was shown that a high reflectance of the silver reflector is of high importance for cell efficiency. Unfortunately, it was also shown that an additional step, which has to take place just after silver deposition on rough surfaces, was necessary. The results of the co-deposited cells shown previously clearly indicate that the heating of the silver layers during cell deposition does not increase the quality of the back reflector, since it is usually covered with a ZnO:Al buffer layer that suppresses surface diffusion. The work presented here is not directly transferable to the industry for several reasons: First, large thicknesses of silver were used to obtain a suitable signal-to-noise ratio for the X-ray experiments. Obviously, for an industrial process such thick layers will be too expensive. However, figure 5.14 shows that a thin layer (120 nm) deposited at room temperature and annealed at 150 °C, which would be of interest for industrial purposes, exhibits similar total reflection as an annealed layer of 300 nm deposited at room temperature. Before silver deposition, all the textured samples

presented in figure 5.14 were made of LP-CVD ZnO with a short plasma treatment similar to the type A samples presented previously. The second issue arising with the annealing process presented above is the addition of a step in the production sequence and the air break in between the silver deposition and the sputtering of the thin ZnO buffer layer. The additional step increases the time of module processing and the air break can allow contaminants to accumulate on the silver layer which may lead to adhesion problems with subsequent layers. A way to reduce the contaminants would be to perform the annealing under vacuum. Toward further reduced processing time, we investigated the deposition onto heated substrates, using the same temperature of 150 °C which is compatible with plastic substrates. Figure 5.14 also presents the result of a thin sputtered silver layer of 120 nm using a substrate holder that was heated to a temperature of approximately 150 °C. It is clear that the total reflectance is high and comparable to the reflectance of the 120-nm-thick silver layer annealed after deposition at room temperature. The thicker silver film with post-deposition annealing exhibits higher TR but the high reflectance obtained on the thin silver film deposited at the moderate temperature of 150 °C gets very close and is more industrially relevant.

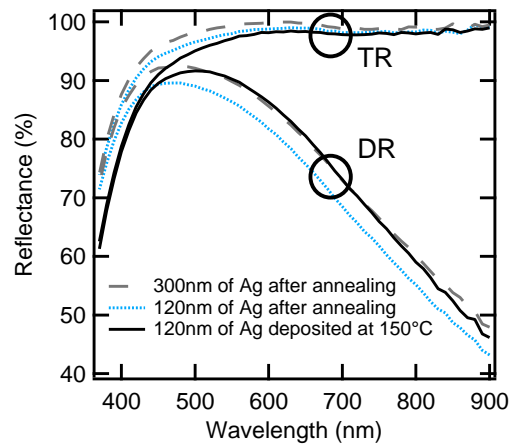


Figure 5.14: Reflectance of LP-CVD ZnO covered with 300 nm of silver annealed after deposition, 120 nm of silver annealed after deposition, and 120 nm of silver deposited on a moderately heated substrate.

5.5 Comparison of rough random textures in plasmonic or dielectric materials

This section discusses differences in J_{sc} enhancement when a given light-trapping texture is made either from a metallic or from a dielectric material. Because of the free-electron plasma present in metals, scattering provided by metals is sometimes referred to as plasmonic scattering. However, it seems reasonable to separate the light trapping that can be promoted by a textured metallic reflector into three different mechanisms:

1. The excitation of surface plasmon polaritons that travel at the interface between a dielectric layer and a metallic layer localises the electromagnetic field to within a few tenths of nanometers around that interface. This is promising for fabricating extremely thin solar cells because the electromagnetic field can be spatially concentrated via the excitation of these resonances. Unfortunately, because of the lower absorption coefficient of silicon compared to silver for wavelengths around 600 nm, it appears that the resulting absorption enhancement from the excitation of surface plasmon polaritons at the Ag/Si interface will occur predominantly in the silver layer [Atwater 10, Schiff 11, Haug 11c]. Hence, this mechanism to enhance light trapping is not adapted to thin-film silicon devices but remains very promising for other technologies for which the absorption coefficient of the active material is high, as is the case for some organic solar cells.
2. Light path enhancement by the excitation of guided modes using metallic textured surfaces was already discussed in chapter 4. A textured interface between media with different indices of refraction induces scattering at precise angles for a periodic texture or over a distributed range of angles for a randomly textured interface. In reflection, the angle of scattering from a metallic textured layer is the same than as provided by a textured dielectric layer, but the efficiency of scattering may be higher in the metallic case. When the textured surface is metallic there are, in addition to standard scattering, plasmonic effects that can occur: First, surface plasmon polaritons can be excited but, as discussed above, these are not very promising for light trapping in thin-film silicon solar cells. Therefore, to prevent their existence, a thin dielectric buffer layer is generally added between the metallic layer and the cell as shown by Haug et al. [Haug 09] and as discussed in section 5.2. Second, in regions of strong curvature, textured metals also support localised surface plasmons but it appears that, as for the case of surface plasmon excitations, the low absorption coefficient of silicon renders the use of these localised surface plasmons not very promising [Lal 12]. In the literature several contributions have shown increased light trapping properties on metallic 2D gratings compared to random metallic back reflectors [Ferry 10, Bhattacharya 11] and random dielectric back reflectors [Paetzold 11a], claiming a higher light trapping thanks to plasmonic effects. However, in these cases, the morphologies that provide the light scattering are extremely different and the coupling and out-coupling equilibrium that is provided by one single spatial frequency as in the case of the grating or by a broad-range of spacial frequency as in the random case may not be compared. Therefore, comparison should be made between materials that support plasmonic resonances and those that do not if their texture is the same (i.e same spatial frequencies for coupling and same depth for the intensity of coupling). To conclude, metallic rough textures are promising for efficient light scattering but parasitic absorption losses are inherent to the use of rough metals.
3. The light trapping promoted by field enhancement and light scattering at high angles from the excitation of localised surface plasmon resonances in nanoparticles was already investigated in numerous of studies and it was shown to be efficient in thin-film silicon solar cells [Catchpole 06, Derkacs 06, Matheu 08, Moulin 08, Beck 09, Santbergen 10,

Eminian 11, Ouyang 11, Tan 12, Chen 12]. Enhancement in J_{sc} was observed compared to flat devices but it still has to be determined whether scattering from localised surface plasmons can be more efficient than the mechanism of scattering by rough textures discussed above. Pahud et al. [Pahud 13] have recently attempted to answer this question by comparing a back reflector made of independent silver nanoparticles separated from a flat silver layer by a ZnO:Al spacer layer and with another back reflector in which these nanoparticles were deposited directly on the flat silver layer. The silver features in both back reflectors shown in this study have the same height and pitch and are therefore comparable. In the first case, scattering occurs by localised plasmon polaritons while in the second case diffraction occurs by grating scattering. Their experimental results suggest that light management provided by the grating scattering is more efficient; modeling results in the same article showed the opposite. The authors attribute this finding to a lower quality of the isolated silver nanoparticles deposited on the ZnO:Al layer compared to the silver particles deposited directly on the flat silver layer which provides suitable nucleation sites. Further studies are necessary to conclude whether localised surface plasmon resonances can be used efficiently for light trapping in thin-film silicon solar cells.

Among the three mechanisms discussed above, the most promising for light path enhancement in thin-film silicon solar cells is probably scattering induced by a rough texture because absorption losses are inherent to the excitation of plasmon resonances discussed in 1) and 3). Nevertheless, light scattering from a rough silver layer will also induce unavoidable parasitic plasmonic absorption which was experimentally observed in sections 5.2 and 5.4 and also in different contributions [Springer 04, Haug 08, Paetzold 10, Palanchoke 12]. Still, compared to dielectric back reflectors, the efficiency of scattering in reflection is higher when light impinges on a metallic layer. It should thus be discussed whether the better scattering from metals can counterbalance the inherent absorption losses that occur. Hence, the purpose of this section is to compare the scattering provided by the same morphology made out of different materials, either plasmonic or dielectric. This is a perfect application for nano-imprinting since it permits the decoupling of a given texture from the material the texture is made of. Hence, the nano-imprint process was used to reproduce the texture of a rough silver layer in a dielectric material and compare the scattering performance of a plasmonic and a dielectric back reflector directly in solar cells.

The two optical systems that are compared are schematically described in figure 5.15. Figure 5.15a presents the plasmonic back reflector which consists of a rough Z2 texture treated for 10 minutes by plasma treatment and then covered by a high-quality silver layer (the TR of this sample is similar to that of sample B_{ann} shown in figure 5.9). Figure 5.15b presents the other type of back reflector which avoids or at least reduces the plasmonic resonances: It consists of a flat silver reflector onto which the texture of the rough silver back reflector shown in figure 5.15a is reproduced by nano-imprinting. An ITO layer of 60 nm was co-sputtered on the two textured substrates for different reasons. It reduces the plasmonic absorption in the silver

5.5. Comparison of rough random textures in plasmonic or dielectric materials

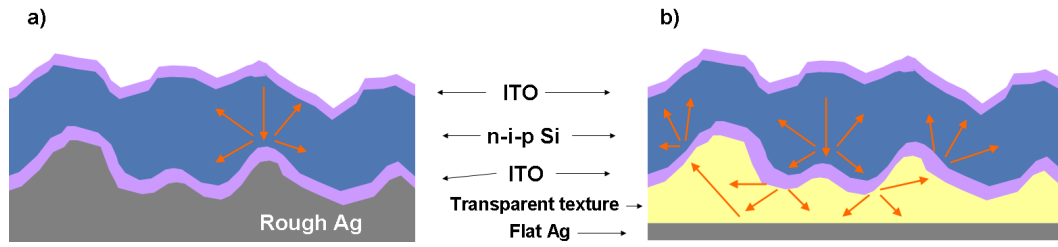


Figure 5.15: Schematic of the optical system studied in this section: a) a plasmonic random rough back reflector, and b) a dielectric random rough texture on a flat silver reflector.

layer as shown in section 5.2 for the rough plasmonic back reflector and it serves as the back contact in the dielectric back reflector.

Optical and morphological measurements were performed after the rough dielectric back reflector was covered with 180 nm of silver. The haze and sine-weighted ADF measured in reflection are shown in figure 5.16a and b, respectively, and SEM images are reported in figure 5.16c. This figure indicates that the silver features were not replicated perfectly in the dielectric material as slightly lower haze and angles of scattered light are observed for the dielectric structure covered with a silver layer. Nevertheless, the discrepancies are small and the SEM images show that the typical feature shapes are similar, even though the replicated texture is slightly less rough. In terms of light trapping, if both textures were made out of the same lossless material, the rougher non-replicated texture would probably give a slight advantage (if any) for J_{sc} enhancement.

As the morphologies are similar between both back reflectors, the optical properties of the a-Si:H solar cells that were co-deposited on these can be compared. The solar cells were grown with a total silicon thickness of 270 nm in system E and a sputtered ITO layer of 60 nm was used as the front contact. Figure 5.17 presents the EQEs, IQEs and absorption spectra of the solar cells grown on the two types of back reflectors. Table 5.4 reports J_{sc} and $J_{sc (IQE)}$ which were calculated by the convolution of the EQEs and the IQEs that are shown in figure 5.17 with the AM1.5G spectrum, respectively. The J_{sc} is the figure of merit here as it is the current which is actually delivered by the cell. There is no striking difference between the two back reflectors in this regard and hence no optical design can be preferred based on the EQE comparison. The main difference that can be observed in the EQEs is the presence of stronger interference fringes in the plasmonic back reflector. This can be explained by the difference in optical thickness of the two designs. In the dielectric back reflector the light travels a longer path and hence more light coherence is lost: In this case, the light is not only reflected at the Si/ITO interface but a part is also transmitted through the resin and reflected by the silver layer re-entering once more in the silicon layer as shown schematically in figure 5.15.

Further insights can be gained by comparing the IQEs and the $J_{sc (IQE)}$ which reveal the differences in parasitic absorptions for the cells grown on the different back reflectors. Since

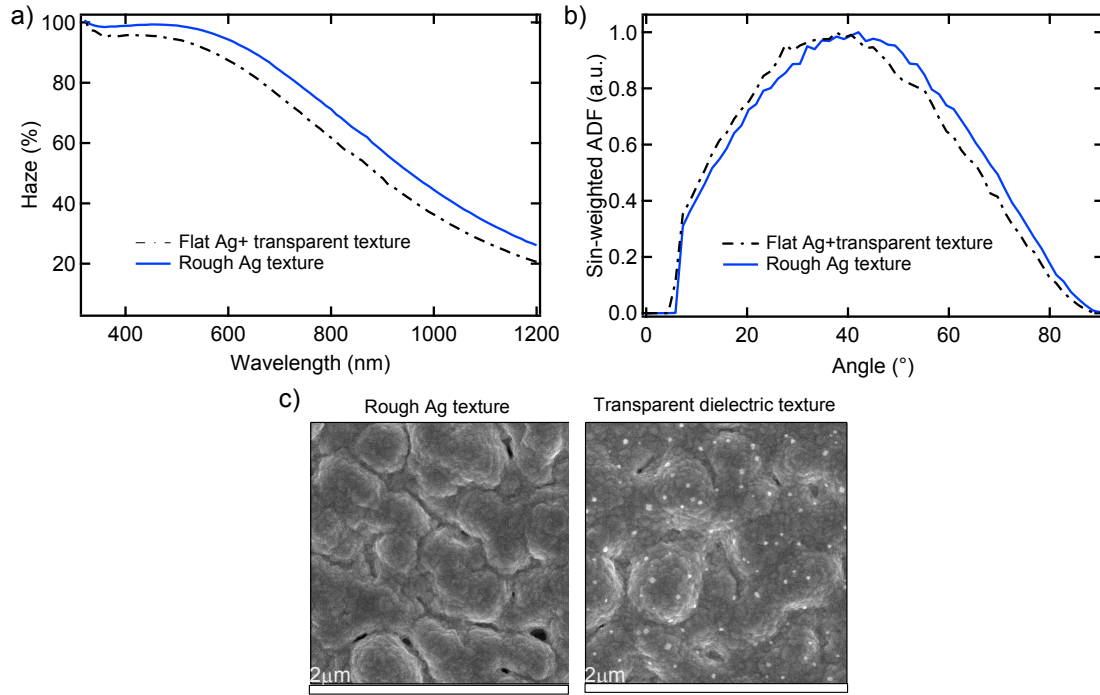


Figure 5.16: *Optical and morphological comparisons of the back reflectors. For this purpose the dielectric transparent texture was covered with 180 nm of silver. a) Haze, b) sine-weighted ADF, and c) SEM images of the two back reflectors (sizes of $2 \cdot 2 \mu\text{m}^2$).*

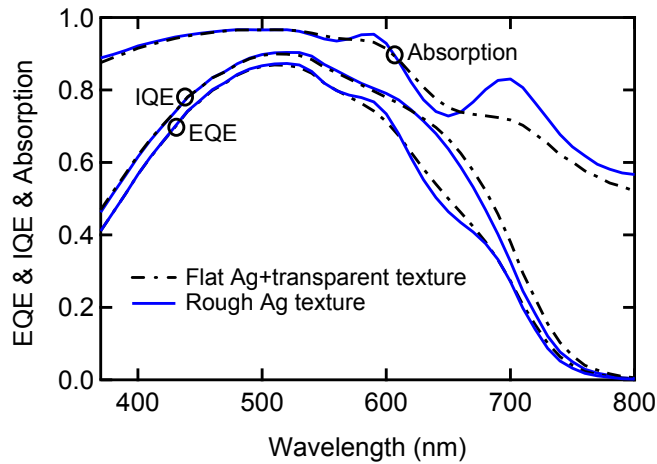


Figure 5.17: *EQE, IQE and absorption of co-deposited cells on the two back reflectors.*

the IQE is lower for the plasmonic back reflector, it appears that the plasmonic resonance gives rise to absorption which is less pronounced in a flat silver layer. It can thus be concluded that there is a better use of the light in the dielectric back reflector which leads to a higher J_{sc} (IQE). This was also shown in simulation even with the dielectric constant of very high-quality silver

Table 5.4: J_{sc} and $J_{sc\ IQE}$ of solar cells grown on plasmonic and dielectric rough textures.

Type	J_{sc} (mA/cm ²)	$J_{sc\ IQE}$ (mA/cm ²)
Dielectric rough texture	14	15.5
Plasmonic rough Ag	13.9	15.2

as in [Nam 12].

To conclude, two rough optical designs using plasmonic or dielectric materials for light scattering were compared. The resulting J_{sc} values were similar and hence neither back reflector outperform the other even if the plasmonic back reflector led to higher total absorption. It was shown that, unfortunately, parasitic absorption is inherent to plasmonic resonances and, therefore, the dielectric back reflector leads to the best use of light. The texture that was used for this study was smooth in order to compare a silver layer of good quality with a dielectric texture. For a more aggressive texture that is desirable for light trapping, it was shown in section 5.4 that the silver layer becomes highly absorbing. This is therefore a further advantage of the dielectric texture which could be made rougher without increasing parasitic absorption. This could however be different if one succeeded at growing rough silver layers with high reflectance.

5.6 Conclusions

This chapter has discussed the different back reflector materials that are generally used in the $n-i-p$ configuration. The considerations thus apply to back reflector configurations that are easily compatible with the texturing process introduced in chapter 3; i.e. rough metallic back reflectors that are covered with a thin buffer layer of sputtered ZnO:Al.

In section 5.2, the effect of the ZnO:Al buffer layer on a-Si:H solar cell performance was discussed. As in the literature [Kothandraraman 91, Haug 09], it was found that a certain thickness of ZnO:Al is necessary to reduce plasmonic absorption in the back reflector. A further increase of the buffer layer thickness was seen to induce an oscillating behaviour of J_{sc} with the thickness of the ZnO:Al layer. This behaviour was explained by a variation of the field intensity in the n -doped layer. A maximum in J_{sc} was obtained for a thickness of ZnO:Al of 120 nm.

Section 5.3 showed that a rough silver layer leads to higher J_{sc} enhancement than an aluminium reflector with the same texture by lowering the parasitic absorption in the metallic layer independent of the thickness of ZnO:Al buffer layer used. Some theoretical studies suggest the more favorable energy of the surface plasmonic excitation of aluminium should erode J_{sc} less than silver. However, all experiments as shown here and by others [Banerjee 91, Springer 05, Yang 09b, Söderström 09a, Palanchoke 12] demonstrate that silver back reflectors lead to better performance than their aluminium counterparts probably be-

cause of the inter- and intra-band transitions that occur in aluminium layers which induce parasitic absorption.

Section 5.4 discussed the annealing of thin sputtered silver films grown on textured substrates at moderate temperatures (150 °C, plastic compatible process). A strong increase in TR and a decrease in the surface roughness was observed after annealing. The large reflectance increase is attributed to better quality and larger grain size in the annealed silver, as shown by SEM and XRD analysis. Solar cells grown on the annealed silver-covered substrates show an increased J_{sc} compared to those on as-deposited silver reflectors, even though the smoothening of the substrates decreases their light-scattering properties. This points out the importance of high back reflector reflectance. As the V_{oc} and FF values also increase thanks to the smoothening of the annealed substrates, an absolute efficiency gain up to 1% is obtained.

Finally, section 5.5 discussed the advantages and drawbacks of back reflectors made in plasmonic and dielectric materials by comparing the light trapping provided by the same random texture, made either from silver or from a transparent dielectric material. It was shown that, for the texture used in this experiment, neither back reflector material provides a clear advantage. Closer inspection showed that the plasmonic metallic back reflector leads to higher parasitic absorption.

The next chapter discusses substrates that are fundamentally different than the one discussed in this chapter. When comparing different substrates in section 5.4, table 5.3 shows that the solar cell with the highest efficiency was not the one exhibiting the highest J_{sc} . This is attributed to a lower quality of the silicon layer which has limited the V_{oc} and FF of this solar cell which was grown on a rougher substrate than the solar cell exhibiting the highest efficiency. In order to allow the growth of silicon with low defect density while having efficient light scattering, novel substrates that decouples the light-scattering interface from the growth surface are investigated in chapter 6.

6 Experimental study of flat light-scattering back reflectors in thick $\mu\text{c-Si:H}$ solar cells

In this chapter, a novel type of substrate that is fundamentally different from the rough metallic substrates discussed in chapter 5 is studied. The substrate has the advantage of being physically flat to allow the growth of solar cells with excellent silicon material quality leading to high V_{oc} and FF while being optically rough for enhanced light trapping that leads to high J_{sc} . This novel approach is highly promising as it demonstrates that the morphology trade-off usually used to reach high efficiencies can be overcome through the use of a single flat light-scattering substrate. The substrate is made of rough ZnO which is grown on a flat silver reflector, minimising parasitic absorption in the metal layer. The ZnO is then covered with a-Si:H, and the stack is polished to expose the tips of the pyramidal ZnO surface. The ZnO embedded in the amorphous matrix provides the desired scattering of light while the surface onto which the cell is deposited is flat and allows for the growth of material with low defect density. This chapter presents results of a 4- μm -thick $\mu\text{c-Si:H}$ solar cell prepared on such substrates that exhibits high V_{oc} of 520 mV. A large relative efficiency gain of 10% is demonstrated compared to a state-of-the-art cell which is grown directly on a textured substrate. This substrate performs best in thick multi-junction solar cells such as the triple-junction a-Si:H/ $\mu\text{c-Si:H}$ / $\mu\text{c-Si:H}$ solar cell with a record stable efficiency of 13% that will be shown in section 7.6.

6.1 Introduction

To reconcile the opposing requirements of layer growth and light scattering, which need flat and rough interfaces, respectively, separating the light-scattering interface from the growth surface has been proposed [Ballif 09, Sai 11a, Lee 11, Grandidier 12, Massiot 12, Isabella 12]. In 2009, IMT patented one method to integrate a flat light-scattering back reflector substrate into a solar cell [Ballif 09]. In this approach, light scattering is promoted by a textured layer with a low index of refraction filled with a material with a higher refractive index. This stack is then polished to obtain a flat substrate. As schematically shown in figure 6.1 a silicon layer with a low

Chapter 6. Experimental study of flat light-scattering back reflectors in thick $\mu\text{c-Si:H}$ solar cells

defect density can be grown on the flat substrate, while porous areas forms in a $\mu\text{c-Si:H}$ layer grown on a standard rough texture as demonstrated by Python et al. and Hänni et al. with high-resolution microscopy [Python 08a, Hänni 13a]. The defective growth of layers on rough substrates was seen to limit the V_{oc} and FF of solar cells compared to solar cells grown on smoother surfaces [Sakai 90, Nasuno 01, Bailat 06, Söderström 08b, Python 08a, Hänni 13a]. Chapter 7 will show that the solar cells used in this thesis also require smooth texture to maintain high V_{oc} and FF . Therefore, the type of substrate investigated in this chapter, which allows the growth of high-quality $\mu\text{c-Si:H}$ as well as enhances light trapping, is an extremely promising substrate to push further the efficiencies of current solar cells. This was demonstrated in simulation recently by Isabella et al. [Isabella 12] as well as experimentally with the 13% stable efficiency shown in section 7.6.

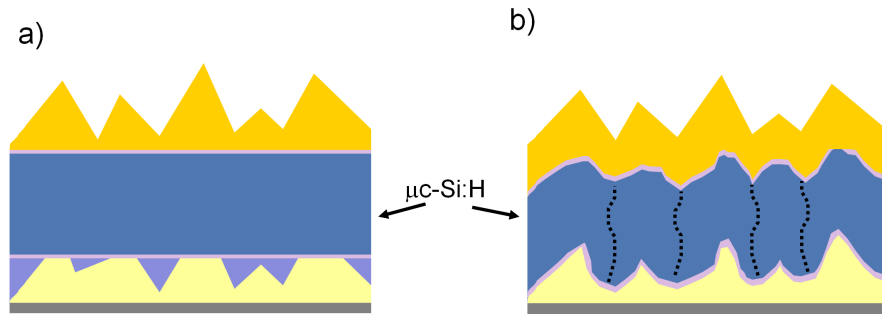


Figure 6.1: Schematics of $\mu\text{c-Si:H}$ solar cells grown on a) a flat light-scattering substrate with a defect-free $\mu\text{c-Si:H}$ layer, and b) a standard solar cell grown on a textured substrate which results in a $\mu\text{c-Si:H}$ layer that contains a lot of cracks.

The choice of materials for this flat light-scattering substrate is crucial for several reasons. First, the difference between their refractive indices should be large enough for efficient scattering into high angles. Second, the filling material should have a refractive index similar to the one of the cell grown on top. In this case, light that is scattered at the scattering interface can re-enter the active layer of the solar cell at the growth interface under high angles without being refracted towards the surface normal. Third, the filling material is an inactive part of the cell and should be non-absorbing. In order to best fulfill these requirements, LP-CVD ZnO was chosen as the material with low index of refraction ($n_{\text{ZnO}}=2$), as its pyramidal shape is known for its excellent light-trapping properties [Rockstuhl 10, Rockstuhl 11]. This ZnO layer was deposited without doping to reduce parasitic free-carrier absorption. It was grown on a flat silver layer which has high reflection and ensures a good conductivity of the Ag/ZnO back contact stack. In order to prevent roughening of the silver layer during the LP-CVD ZnO deposition which is performed at high temperature ($>150^\circ\text{C}$), a thin sputtered ZnO:Al film of 20 nm was deposited on top of the flat silver layer prior to the LP-CVD ZnO deposition. Intrinsic a-Si:H was chosen as the filling material because its index of refraction is similar to that of the $\mu\text{c-Si:H}$ cells in the wavelength range of interest and because it does not absorb light above 800 nm. However, a significant amount of light below this wavelength should

be absorbed in a single pass through the active layer, else part of it would be lost in this "dummy" inactive filler layer. Therefore, it is believed that these substrates will be best used in multi-junction thin-film silicon solar cells such as triple-junction a-Si:H/a-SiGe:H/ μ c-Si:H or a-Si:H/ μ c-Si:H/ μ c-Si:H devices. In this case, the optical thickness is large for a single light pass through the solar cell for light below 800 nm, while longer wavelengths benefit from the light scattering given by the back reflector. In this thesis, these back reflectors were successfully integrated in triple-junction a-Si:H/ μ c-Si:H/ μ c-Si:H solar cells but this will be discussed in section 7.6.

In order to mimic thick triple-junction solar cells, this chapter presents these substrates in thick single-junction μ c-Si:H solar cells ($\approx 3.8 \mu\text{m}$ of intrinsic layer). This allowed us to investigate the potential total current that can be obtained with these substrates and the light-trapping properties compared to a state-of-the-art reference cell grown on a textured substrate. This experiment also revealed the effect of polishing on the FF of the cell, which can be difficult to interpret in multi-junction solar cells as the FF depends on the current matching between the sub-cells. Using the thick single-junction cells, it is shown that a large relative efficiency gain is obtained for the solar cell on the polished substrate compared to a reference cell when both cells are optimised independently for each substrate. A high V_{oc} of 520 mV was obtained for a cell grown on the polished substrate, while only 490 mV was achieved for the reference cell grown on a textured surface with features that were smoothened by plasma treatment for good cell growth.

6.2 Experimental details

Figure 6.2 shows SEM images for both types of substrates as well as schematic drawings of the typical cell structures studied in this chapter. The starting point for both flattened and reference textured substrates was a stack of Cr (10 nm)/Ag (180 nm)/ZnO:Al (20 nm) that was deposited by sputtering at room temperature on flat glass. Two different thicknesses (sample A with thickness $t_A = 2 \mu\text{m}$, sample B with thickness $t_B = 5 \mu\text{m}$) of LP-CVD ZnO were then deposited.

The left side of figure 6.2 presents the flattened substrates. Dummy a-Si:H layers were deposited to entirely cover the ZnO pyramids. This stack was then flattened by using a chemical mechanical polishing process which is described in section 2.3.2. Stronger polishing removes more material from the sample, which increases the area of ZnO contact because of its underlying pyramidal shape. The right side of figure 6.2 shows the reference textured substrate made by treating sample B with a plasma to smoothen the sharp ZnO features.

On top of these substrates, p - i - n μ c-Si:H solar cells were deposited in a Kai-M reactor described in section 2.2.2. They consisted of a 35-nm-thick microcrystalline p -doped layer (p - μ c-Si:H), an intrinsic layer of $3.8 \mu\text{m}$, and a 50-nm-thick silicon oxide n -doped layer (n -SiO_x:H). As a front electrode, a lightly boron-doped LP-CVD ZnO layer of $5 \mu\text{m}$ was deposited. Each cell had an area of approximately 0.25 cm^2 . Standard measurements were performed on the cells to

Chapter 6. Experimental study of flat light-scattering back reflectors in thick $\mu\text{c-Si:H}$ solar cells

yield FF , V_{oc} , J_{sc} and total absorption (TA).

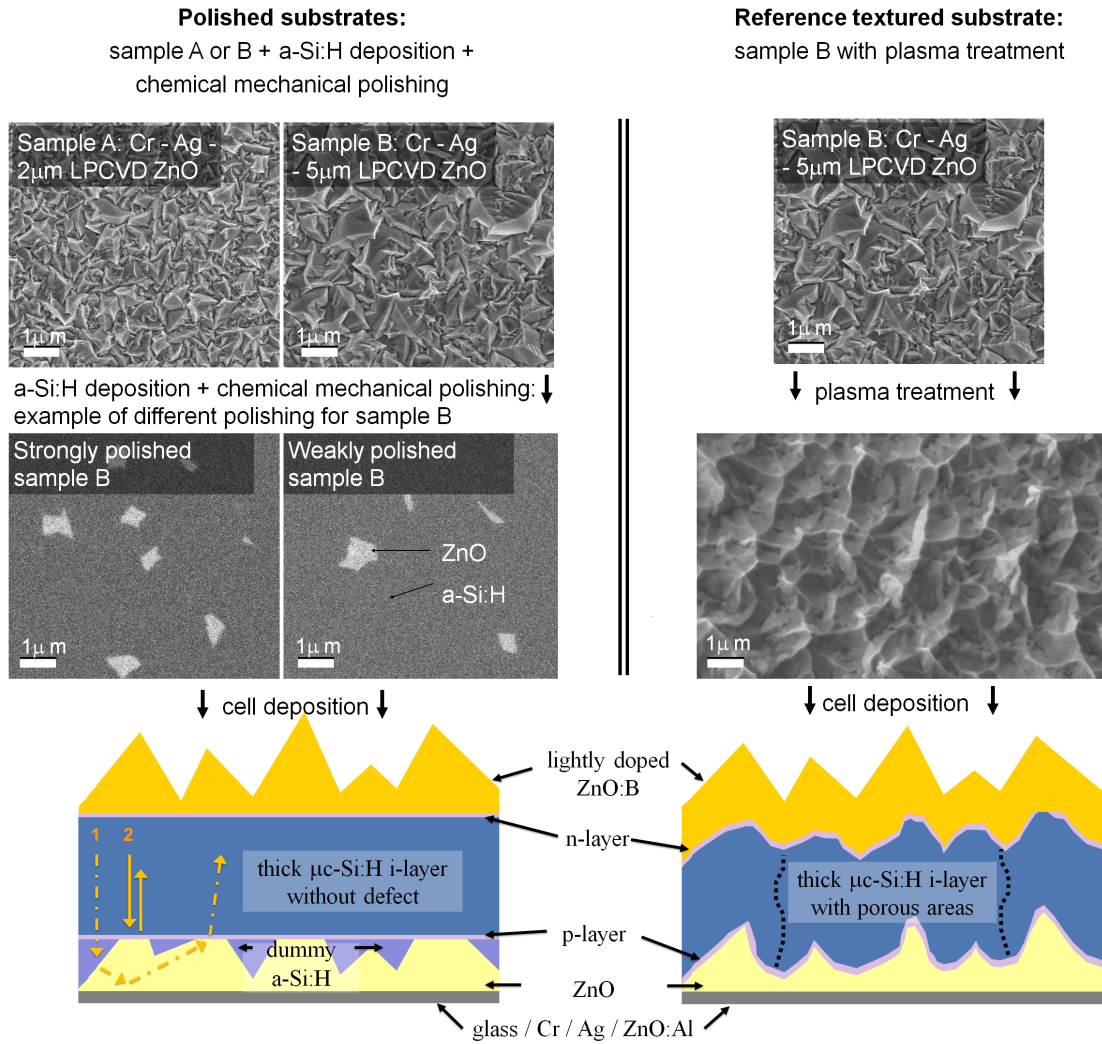


Figure 6.2: SEM images of (left) polished substrates and (right) reference textured substrate during fabrication. Schematic drawings of cells grown on both types of substrates appear below. The colored arrows in the lower left panel illustrate loss in light trapping due to the flat ZnO/Si zones. The dashed lines in the lower right panel illustrate porous areas due to defective $\mu\text{c-Si:H}$ growth.

6.3 Effect of dummy a-Si:H layer and its polishing

Figure 6.3 presents cell results (EQE, TA and electrical parameters) measured on flattened sample A and B substrates with the polishing state that yielded the most efficient cells. The EQEs of cells on both substrates exhibit a drop between 600 nm and 800 nm. This is ascribed to the fact that, at these wavelengths, light is not fully absorbed in a single pass and gets absorbed

in the a-Si:H dummy layer instead. The drop becomes less significant towards 800 nm where the a-Si:H intrinsic dummy layer becomes transparent. Two main differences can be observed between the two polished substrates. The drop due to the a-Si:H parasitic absorption is more pronounced in the flattened sample B. This is ascribed to the thicker dummy layer that was needed on sample B to completely fill the pyramidal features that are larger than those of sample A. However, the loss in J_{sc} is counterbalanced by a gain in the long wavelength range which is related to more efficient light scattering on substrates with larger feature sizes, as was observed by Boccard et al. [Boccard 10]. The total currents as well as the electrical parameters are similar for both substrates.

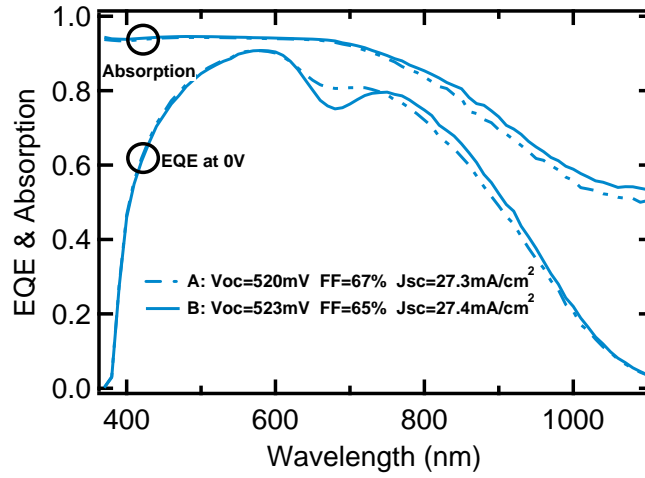


Figure 6.3: EQE and TA of cells deposited on polished sample A and B.

The effect of polishing intensity is shown in figure 6.4 for flattened samples of type A. WP stands for weak polishing, MP for medium or intermediate polishing and SP for strong polishing. The EQE is affected by the polishing in two ways: First, the drop due to parasitic absorption in the dummy a-Si:H layer tends to be smaller with increased polishing because a larger part of this layer is removed. More interestingly, the EQE and the TA between 750 nm and 1100 nm for MP and WP substrates are similar.

Figure 6.4 is helpful to understand why there is almost no change in light trapping between WP and MP substrates. It presents a SEM image of MP sample A after removing all silicon layers by $\text{SF}_6\text{-O}_2$ plasma etching. It is observed that only the big pyramids are trimmed by this polishing state, allowing all the other smaller pyramids to continue to efficiently scatter the light, as in WP sample A. In contrast, figure 6.4 also shows that a loss of light trapping in the solar cell occurs for SP. This loss in light trapping can be explained by the increased flat area of the ZnO/Si interface when too many pyramids are trimmed. There are two major paths of losses in light trapping due to the flat ZnO/Si zones which are illustrated by the colored arrows in figure 6.2: The first path (1) shows that light which goes through the back reflector stack and is efficiently scattered into a high angle will be refracted toward the normal when impinging

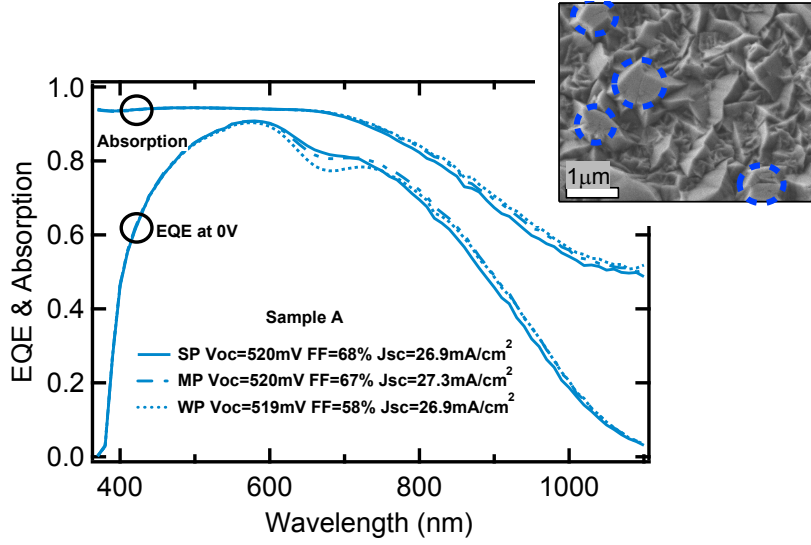


Figure 6.4: EQE and TA of cells with different polishing intensities on flattened sample A (WP stands for weak polishing, MP for medium polishing and SP for strong polishing). The inset presents an SEM image of MP sample A after removing all silicon layers. Circles mark polished pyramids.

on a flat ZnO/Si zone. The second path (2) shows that a significant part of the light will be directly reflected when impinging on a flat ZnO/Si zone after a single pass through the active layer.

The effect of polishing intensity on FF is opposite that on J_{sc} . When substrate A is less polished (WP), a low FF is observed. A high FF is recovered for higher polishing (MP), but further polishing (SP) does not improve FF any more. On this kind of substrate, the FF trend is obviously not related to roughness but can be explained by the serial resistance, which decreases as more points of contact are opened between the cell $p\text{-}\mu\text{c-Si:H}$ contact layer and the ZnO with increased polishing. Therefore, the carriers have a smaller distance to travel laterally through the p -layer before being collected by the ZnO back contact, leading to lower resistive losses. The V_{oc} is affected mainly by material quality and surface recombination. In this set of experiments the V_{oc} is stable because of the similarly low roughness of the substrates. In this case, the material quality is the same as the cells are co-deposited, and the surface recombination should also be similar.

It has to be emphasised that the dependencies of V_{oc} and FF on the polishing intensity strongly depend on the type of p -layer used for the cell. Indeed, a $p\text{-SiO}_x\text{:H}$ doped layer which has been proven to drastically enhance cell performance on rough substrates [Despeisse 10] will be highly detrimental to the FF of a cell grown on a polished substrate because of its low lateral conductivity. In addition, such a $p\text{-SiO}_x\text{:H}$ doped layer has a significantly different refractive index from an oxygen-free silicon layer, which would introduce undesired refraction at the

flat interfaces. Thus the optimum state of polishing for V_{oc} , FF and J_{sc} depends on the device architecture.

In a third experiment, the effect of a doped dummy layer on the EQE is compared to an intrinsic dummy layer for substrates of type A. Figure 6.5 shows that doping in the dummy layer affects the EQE at long wavelengths and decreases the J_{sc} by 1.3 mA/cm^2 . It is concluded that there is larger parasitic absorption (compared to the undoped case) due to the dopant. However, the addition of dopant in the dummy layer could allow for better transport of the carriers and therefore improve the cell FF . Still, we believe that it is more beneficial for the cell efficiency to carefully tune the ZnO areas of contact and the mean distance between them, while using a highly conductive p -layer with an undoped dummy layer, than to design a cell with a doped dummy layer and a thinner conductive layer on top. Indeed, from the results of different polishing states for sample A shown in figure 6.4, it was observed that a good FF can be reached without current losses with medium polishing. By increasing the density of contact points (stronger polishing SP) the FF did not improve significantly (only 1%). Thus, we suppose that the FF of 67-68% obtained in this experiment is the highest achievable for such thick cells.

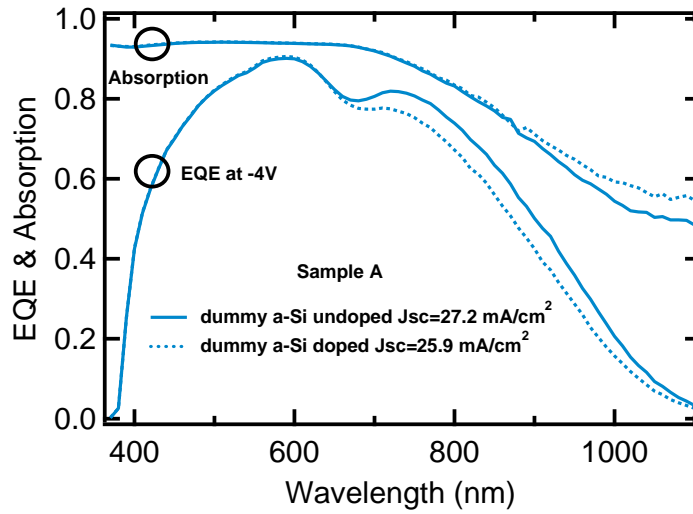


Figure 6.5: EQE and TA of cells deposited on flattened sample A filled with doped or intrinsic a-Si:H dummy layers.

Of course this discussion on the addition of dopant depends on the thickness of the dummy layer that is needed to cover the ZnO features. If shallow features are sufficient for efficient light confinement, and if a dummy layer thinner than 100 nm is sufficient to fill the ZnO, then a doped material may not significantly deteriorate the cell EQE. In the case of MP sample A used in this experiment, several hundreds of nanometers of a-Si:H dummy layer remained on the substrates after polishing, substantially reducing the cell EQE.

6.4 Potential of polished substrates: Comparison with a reference textured cell

In this section, the potential and issues of the polished substrates are studied. First, to compare light trapping, the cell with the highest J_{sc} grown on a polished substrate is compared to a cell grown on a textured reference substrate. Second, the reference cell and the best cell on a polished substrate are compared in terms of V_{oc} , FF and overall efficiency. The reference cell is grown on a state-of-the-art textured substrate designed for $\mu\text{c-Si:H}$ solar cells with high efficiencies. As shown in figure 6.2 it consists of a type B sample with plasma-treated ZnO to render its surface smoother, leading to high V_{oc} and FF [Bailat 06]. However, the plasma treatment is known to decrease the light-trapping properties of the LP-CVD ZnO pyramidal shape [Python 08b, Li 08, Söderström 08a]. Here, the length of the plasma treatment is adapted to obtain a substrate that optimises the cell efficiency by making a trade-off between the V_{oc} , FF and J_{sc} values. With the chosen plasma treatment of 50 minutes, the quality of $\mu\text{c-Si:H}$ deposited on the rough ZnO is good but it will be observed that the polished substrates lead to $\mu\text{c-Si:H}$ material with higher quality.

6.4.1 Light-trapping performance of the polished substrates

The highest current at long wavelength (800 nm to 1100 nm) on a polished substrate was obtained on a flattened type B sample with weak polishing. This is expected, as (1) the feature size of sample B is better adapted for light trapping in $\mu\text{c-Si:H}$ cells than the feature size of sample A [Boccard 10]; (2) the weak polishing ensures the smallest flat ZnO/Si area; and (3) the thick layer of a-Si:H deposited on sample B to bury its features does not affect the EQE above 800 nm. In figure 6.6, the EQE and TA of WP flattened sample B are compared with those of the reference cell grown on the textured substrate. When comparing the EQE curves with a bias of -4 V and without bias, no difference is observed below 550 nm for the polished substrate, whereas the textured substrate shows a gap between these two curves (not shown). Thus, the EQE difference in the blue region is attributed to collection losses in the reference cell. This difference does not affect the light-trapping properties in the long wavelength range. The drop in the EQE curve around 700 nm for the polished substrate was already explained as being due to absorption in the dummy layer. However, above 800 nm the dummy a-Si:H layer does not absorb, and light trapping can be compared for these two substrates.

Higher light-trapping capabilities with the weakly polished substrate are to be expected. Indeed, its textured buried interface corresponds to an untreated LP-CVD ZnO sample, except for a few trimmed pyramids as the SEM image in figure 6.6 shows. The textured substrate has feature sizes similar to those of the polished substrate but is highly smoothened by the plasma treatment (see SEM images in figure 6.6), which is known to significantly decrease light trapping compared to an untreated sample [Python 08b, Boccard 11, Rockstuhl 11, Boccard 10]. Thus, the result shown in figure 6.6, where both EQE and TA are similar between 800 nm and 1100 nm, was not anticipated. Indeed, a slight advantage in light trapping is observed for the

6.4. Potential of polished substrates: Comparison with a reference textured cell

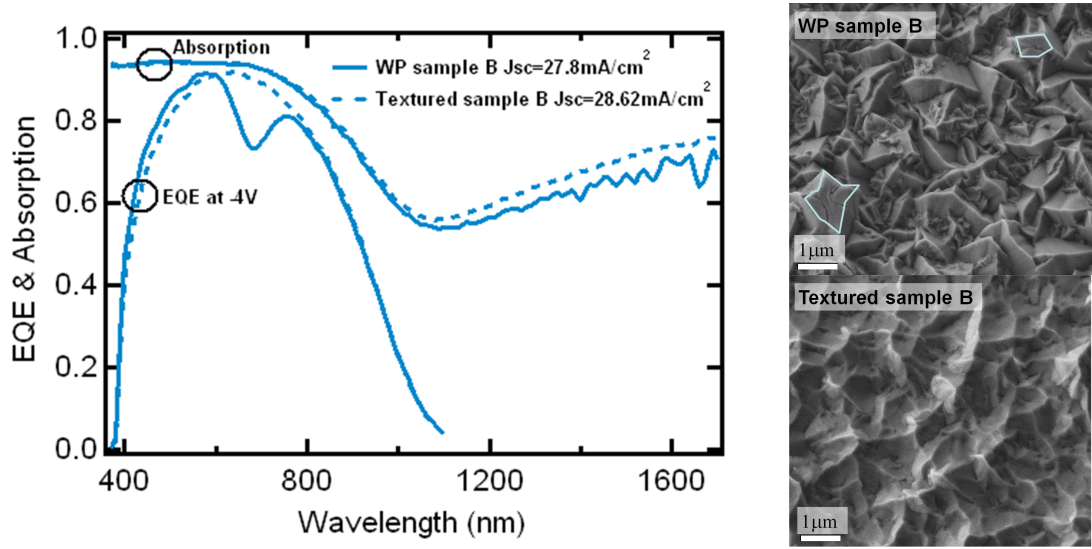


Figure 6.6: *Left) EQE and TA of cells grown on a flattened sample B with weak polishing and on a reference textured cell on sample B treated by plasma. The indicated J_{sc} were calculated from the EQE measured at -4 V. Right) SEM images of both substrates after removal of all silicon layers. The outlines drawn in WP sample B mark polished pyramids.*

cell grown on the textured reference substrate.

The slightly lower light trapping of the polished substrate is attributed to the flat ZnO/ μ c-Si:H areas created by the polishing process. This is corroborated by oscillation fringes in the polished cell absorption curve above 1200 nm shown in figure 6.6. These oscillations are attributed to interference fringes due to flat interfaces and are not observed in the absorption curve of the textured cell. Furthermore, the higher absorption of the textured cell above 1100 nm also indicates better light confinement for these wavelengths. To conclude, this experiment shows that flat interfaces remain optically visible even in WP samples with limited flat ZnO/Si areas, and are detrimental to light trapping.

6.4.2 Cell electrical performance on polished substrates

The results of the preceding section showed that light scattering of polished substrates is not as good as anticipated. Yet, at long wavelengths the light confinement is comparable to the textured substrate which is already efficient. The potential of these substrates to lead to high-efficiency cells via improved V_{oc} and FF thanks to the growth of high-quality μ c-Si:H on the physically flat interface is presented below.

Table 6.1 presents the parameters of solar cells made in two independent depositions. The first two rows correspond to co-deposited cells on our best polished substrate and the reference textured substrate, made using a p - μ c-Si:H doped layer that is optimised for the architecture

Chapter 6. Experimental study of flat light-scattering back reflectors in thick $\mu\text{c-Si:H}$ solar cells

Table 6.1: *Results for two co-deposited cells with a $p\text{-}\mu\text{c-Si:H}$ doped layer optimised for polished substrates, and for a cell with a p -doped layer optimised for textured substrates.*

Type of substrate / p -doped layer	FF (%)	V_{oc} (mV)	J_{sc} (mA/cm ²)	Efficiency (%)
Textured / $p\text{-}\mu\text{c-Si:H}$	58	494	28	8
MP sample A / $p\text{-}\mu\text{c-Si:H}$	67	520	27.3	9.5
Textured / $p\text{-SiO}_x\text{:H}$	62	491	28.3	8.6

of the polished substrate. The third row corresponds to an identical cell, but with a $p\text{-SiO}_x\text{:H}$ doped layer that is optimised for textured substrates. This allows a fair comparison between the polished and the textured substrates, since this cell is not hampered by layers that are designed for other cell architectures.

The improvement of cell performance thanks to the polished substrate is clear in the co-deposited cells with a $p\text{-}\mu\text{c-Si:H}$ doped layer. As the cells are co-deposited, the higher FF and V_{oc} values obtained on the polished substrate are directly attributable to the improved quality of the $\mu\text{c-Si:H}$ material grown on the flat interface. The lower current is due to absorption in the dummy layer and to lower light trapping as explained previously. However this loss is more than compensated by the improved FF and V_{oc} values. Finally, an overall relative efficiency gain of almost 20% is realised by using the polished substrate. This result is also interesting because $p\text{-}\mu\text{c-Si:H}$ doped layers are commonly used and can be implemented in the simplest cell designs.

As discussed previously, the effect of electronically poor material grown on textured surfaces can be mitigated by using well-designed cell architectures. The use of a $p\text{-SiO}_x\text{:H}$ doped layer helps the cell to be less sensitive to locally porous material, which leads to an increase of the reference cell FF , as expected. Nevertheless, the cell on the polished substrate with a $p\text{-}\mu\text{c-Si:H}$ doped layer outperforms the reference cell in V_{oc} and FF . The efficiency of the cell grown on the polished substrate with an ordinary $p\text{-}\mu\text{c-Si:H}$ doped layer exhibits a 10% relative gain compared to the cell grown on the textured substrate with an optimised $p\text{-SiO}_x\text{:H}$ doped layer.

6.5 Perspectives

Efficiencies greater than 10% can be obtained on textured substrates with a cell thickness of 1.8 μm , whereas here the 4- μm -thick cell shown in table 6.1 reached only 8.6%. This indicates that a 4- μm -thick single-junction $\mu\text{c-Si:H}$ cell is not an optimal structure. Thick $\mu\text{c-Si:H}$ cells were used here to mimic absorption in an optically thick cell, allowing the assessment of the substrate's potential with regard to J_{sc} as well as V_{oc} and FF . As the dummy layer absorbs below 800 nm, the incorporation of these substrates into triple-junction cells ($a\text{-Si:H}/a\text{-SiGe:H}/\mu\text{c-Si:H}$), which absorb a substantial amount of light in a single pass through the cell, is a promising route to high efficiencies. The incorporation of these substrates in

triple-junction a-Si:H/ μ c-Si:H/ μ c-Si:H cells will be further discussed in section 7.6.

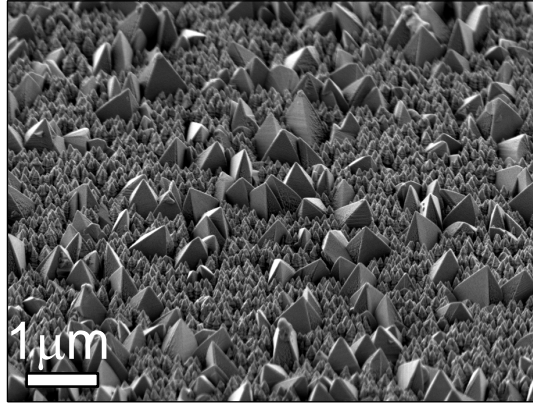


Figure 6.7: SEM image of an adapted ZnO morphology for further improving the polished back reflector substrates presented in this chapter.

In addition, better control of the mean distance between the polished ZnO areas that act as contacts is desirable. In this regard, the approach of Sai et al. [Sai 11b, Sai 11a] to use periodic arrays may be promising. Another improvement would be an optimised ZnO texture for enhanced light trapping. It was shown that a wide range of different ZnO morphologies can be obtained by modifying the LP-CVD deposition conditions of ZnO [Nicolay 09, Nicolay 11]. A promising texture to provide both better control of the density of contacts and better light trapping would have features with multiple scales, as shown in figure 6.7. The ZnO in this figure consists of large, tall pyramids surrounded by smaller ones. The growth conditions allow the tuning of the tall-pyramid density which determines the density of electrical contact points after polishing. The smaller pyramids would remain untouched by polishing and their size should be optimised for light trapping.

Further improvement would be to address absorption in the dummy layer material. Alloying with oxygen or carbon, for example, increases the silicon bandgap, hence reducing absorption losses close to 800 nm. However, such alloying is accompanied by a lowering of the refractive index, which would lead to stronger undesirable refraction at the interface between the filler material and the μ c-Si:H cell. It will thus require a careful trade-off between these two effects (less parasitic absorption vs. more reflection losses) to boost cell efficiency. From previous unpublished studies, this approach does not appear to be very promising.

6.6 Conclusions

A concept for physically flat back reflectors that ensure the deposition of good material quality, but that are optically rough for enhanced J_{sc} , was discussed. LP-CVD ZnO with pyramidal texture was covered with a dummy a-Si:H layer which was then polished to reveal the ZnO contact and to obtain a flat substrate. Scattering occurs at the interface between the ZnO pyramidal texture and the a-Si:H dummy layer and provides impressive light confinement. The flat substrate surface allows the growth of $\mu\text{c-Si:H}$ material with few structural defects as indicated by the high V_{oc} (520 mV) and FF (67%) of the cells grown on top. The effect of polishing on light trapping as well as on V_{oc} and FF was discussed. Finally, the efficiency of the best cell obtained on the polished substrate with a $p\text{-}\mu\text{c-Si:H}$ doped layer was compared with an optimised $\mu\text{c-Si:H}$ reference cell with a $p\text{-SiO}_x\text{:H}$ doped layer on an optimised textured substrate. A 10% relative efficiency gain was observed, showing that polished substrates have the potential to be successfully applied in high-efficiency multi-junction solar cells. This will be studied in section 7.6 and we will demonstrate that these substrates are highly promising. A record stable efficiency of 13% will be achieved which is the highest stable efficiency demonstrated yet for thin-film silicon solar cells by our laboratory and which is close to the current world record of 13.4% reported in 2012 by LG Solar.

7 Texture optimisation: Towards high efficiencies in the $n-i-p$ configuration

This chapter presents the substrate optimisation for each type of device studied in this thesis and the highest efficiencies that were achieved, for which a summary is reported in table 7.1. As well, some perspectives and possible roads for further improvements are described. Because of the better understanding of back-reflector requirements acquired during this thesis, several remarkable achievements were obtained in multi-junction devices: By combining the improvement of silver reflectance discussed in section 5.4 with texturing of PEN substrates by UV nano-imprinting shown in chapter 3, a tandem a-Si:H/a-Si:H device exhibiting a stable efficiency of 9.2% was obtained with less than half a micron of a-Si:H. This efficiency is, to the author's knowledge, the highest reported to date for a-Si:H material on a PEN substrate. With the same goal of demonstrating efficiencies high enough for industrialisation of thin-film silicon solar cells on PEN, an a-Si:H/ μ c-Si:H solar cell with a stable efficiency above 10% was fabricated with processes fully compatible with PEN substrates. Finally, by using the innovative flat light-scattering substrate described in chapter 6 and an anti-reflective coating made by UV nano-imprinting as shown in section 3.6, a triple-junction a-Si:H/ μ c-Si:H/ μ c-Si:H solar cell with a record stable efficiency of 13% was achieved. This is the highest stable efficiency reported so far for thin-film silicon devices in our laboratory, and it is an efficiency very close to the current world record of 13.4% recently shown by LG Solar.

Table 7.1: *Highest efficiencies obtained for each type of device after substrate optimisation.*

Device	Substrate	Thickness (μ m)	Initial η (%)	Stable η (%)
a-Si:H	Hot Ag 200 °C	0.25	10.4	8.1
μ c-Si:H	Hot Ag 300 °C	1.7	10.1	-
a-Si:H/a-Si:H	Replica of Z2 treated 8' nano-imprinted on PEN, covered with warm Ag/ZnO:Al	0.07/0.37	11.1	9.2
a-Si:H/ μ c-Si:H	Hot Ag	0.31/1	11.7	10.4
a-Si:H/ μ c-Si:H/ μ c-Si:H	Flat light-scattering	0.27/1.8/3.5	>13.7	13

7.1 Introduction

Throughout this thesis, multiple photonic structures were investigated and integrated into both single-junction and multi-junction devices. For the state-of-art silicon material quality, we identified the most promising optical systems that led to the growth of cells with the highest efficiencies yet achievable, and the corresponding conclusions are reported in this chapter.

First, the optimisation of textures in single-junction solar cells is presented. An extended study on textures suitable for single-junction a-Si:H solar cells was carried out and the main conclusions are reported in section 7.2. Likewise, textures suitable for single-junction $\mu\text{c-Si:H}$ solar cells were studied and the conclusions are reported in section 7.3. In both cases, texture optimisation was performed on devices with LP-CVD ZnO:B front contacts and therefore these studies are dedicated to applications on glass substrates. For both type of devices, these experiments allowed us to identify the compromises that have to be made on the feature size and shape of the photonic textures used for light management in order to obtain highly efficient cells with our state-of-the-art deposition conditions. It appears that, in order to reach high efficiencies, the focus should mainly be directed to the optimisation of smooth textures that allow for the growth of good-quality material and thus high V_{oc} and FF .

Second, thin-film silicon processes on plastic substrates was investigated. In order to take advantage of *n-i-p* devices that can be deposited on opaque substrates, the optimisation of textures suitable for either tandem a-Si:H/a-Si:H solar cells (section 7.4) or micromorph a-Si:H/ $\mu\text{c-Si:H}$ solar cells with thin $\mu\text{c-Si:H}$ layers (section 7.5) were studied. The textures and the corresponding devices were optimised using a sputtered ITO front contact which is compatible with the process flow of thin-film silicon solar cells on flexible substrates. Both types of devices have advantages for industrial production. The deposition of a-Si:H is well mastered, and good uniformity can be obtained for high deposition rate. This favours the a-Si:H/a-Si:H device compared to the a-Si:H/ $\mu\text{c-Si:H}$ device which suffers from the low deposition rate of the $\mu\text{c-Si:H}$ layer. However, the a-Si:H/ $\mu\text{c-Si:H}$ device possesses a large advantage in terms of stabilised efficiency, as the $\mu\text{c-Si:H}$ cell contributes one-third of the device output power and suffers only little from light-induced degradation [Meier 94]. Furthermore, the objective was to keep the $\mu\text{c-Si:H}$ layer as thin as possible in order to reduce the process time dedicated to the $\mu\text{c-Si:H}$ layer deposition and subsequent reactor cleaning. The efficiencies reported in these two sections are not as high as for devices deposited on glass substrates but the other benefits of flexible modules compared to rigid modules (i.e. roll-to-roll deposition, lower installation costs, roofs with textured surfaces can be easily covered, niche market for portable applications) could nevertheless allow market penetration of these types of technologies. At this stage, it appears that large-scale PV electricity production will not be reached with these flexible modules because of their lower efficiencies compared to their rigid counterparts and also because the encapsulants currently used in flexible modules are more expensive than glass.

Finally, section 7.6 reports work targeted at obtaining a device with the highest achievable stable efficiency with state-of-the-art solar cells. It therefore means that there were no limitations on the materials, on the layer thicknesses, or on the back reflector texture. To achieve high-efficiency, triple-junction a-Si:H/ μ c-Si:H/ μ c-Si:H solar cells were chosen since they have the advantage that approximately half of the output power is produced by the two μ c-Si:H cells which suffer little from light-induced degradation. Different types of back reflectors are discussed with a focus on the one which has the highest potential, i.e. the flat light-scattering substrate described in chapter 6. A high-efficiency device with a 13% stable efficiency is obtained on the flat light-scattering substrate by adding an anti-reflective coating made by UV nano-imprinting at the front of the a-Si:H/ μ c-Si:H/ μ c-Si:H *n-i-p* device. This high stable efficiency demonstrates that the flat light-scattering substrate has the potential to improve upon the current solar cell efficiencies.

7.2 Single-junction a-Si:H solar cells

The solar cells presented in this section were deposited in the small-area system E and details on the cell design can be found in section 2.2.2.

First, section 7.2.1 presents a study which shows that light scattering into the silicon provided by a textured silver layer is much higher than what can be measured in air. It is demonstrated that, compared to a cell grown on a flat substrate, up to 13% relative J_{sc} enhancement is achievable without significant losses in V_{oc} and FF with a substrate that has a roughness of only 19 nm and for which less than 30% of diffuse reflectance is measured in air at a wavelength of 400 nm.

Second, section 7.2.2 discusses the use of rougher back reflectors. As is widely known, it is shown that substrates with higher roughness may lead to higher J_{sc} enhancement but, in general, have the drawback of growing silicon material of lower quality and thus lead to devices with lower V_{oc} and FF . At the same time, it is found that roughness can help to mitigate shunts which may occur in solar cells grown on very smooth substrates. Finally, it is shown that significantly different J_{sc} enhancements are obtained in solar cells grown on back reflectors that have similar optical properties as measured in air. This emphasizes that the feature sizes of rough textures are highly important and that optical characterisation of substrates in air can be misleading.

Section 7.2.3 presents an optimised single-junction a-Si:H cell with 8.1% stable efficiency. It was deposited on a substrate with medium roughness to allow for a good J_{sc} , V_{oc} and FF trade-off.

7.2.1 Study of various back reflectors with low roughnesses

The four single-junction a-Si:H solar cells presented in this section were co-deposited on substrates with very low roughnesses (figure 7.1). The substrates were made of sputtered silver, and AFM measurements were used to extract the roughness σ_{rms} of each substrate. One flat silver reflector approximately 150 nm thick was sputtered at room temperature ($\sigma_{rms} = 3$ nm). The other three back reflectors were made by sputtering silver layers of different thicknesses on glass substrates held at 150 °C. When thickened, the surface of the silver layers is rougher and the corresponding σ_{rms} were 9 nm, 13 nm and 19 nm for 150-nm-, 300-nm- and 450-nm-thick silver layers, respectively. All substrates were subsequently covered by 60 nm of sputtered ZnO:Al when used as substrates for the growth of solar cells, though the optical properties were characterised on the bare silver layers.

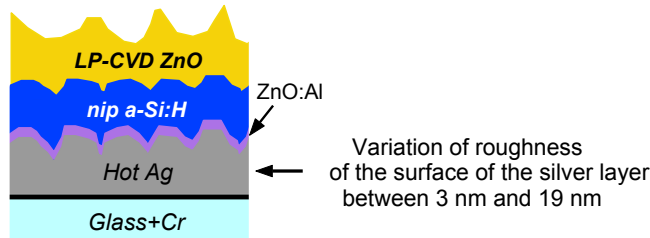


Figure 7.1: Schematic of the experiment. Single-junction *n-i-p* a-Si:H solar cells were co-deposited on silver reflectors whose surfaces exhibit roughnesses between 3 nm and 19 nm.

Figure 7.2 presents the optical properties of the four different back reflectors and the EQE spectra of the solar cells that were co-deposited on them. The low DR values shown in figure 7.2a indicate that these substrates were of low roughness which corroborates the low σ_{rms} that were extracted from AFM data. Despite the low DR measured in air, the three substrates with $\sigma_{rms} > 3$ nm show a remarkable increase in the EQE of the solar cells grown on them compared to the solar cell grown on the flat substrate, as figure 7.2d shows. Table 7.2 shows that these low roughnesses did not affect the solar cell V_{oc} and decreased the FF by only 1% for the two rougher substrates compared to the cell grown on the flat substrate. The remarkable J_{sc} increase (up to 13% relative) is attributed to two effects: First, as shown in figure 7.2b, the three rougher substrates scatter the light into high angles, very close (in air) to the sine-weighted ADF curve of Lambertian scattering. Second, the haze is much higher at the Ag/Si interface in the solar cell than that measured in air. Figure 7.2c presents in thick lines experimental measurements of haze in air, and in thin lines the haze for scattering into air and into silicon calculated from the AFM data based on the scalar scattering theory developed by Dominé et al. [Dominé 10]. Although the calculated values exhibit remarkable correlation with measurements performed in air in the transmission configuration, it can be observed that the reflection haze curves in air calculated from the AFM data grossly underestimate the experimental values. In spite of this, as qualitatively shown in figure 7.2c, it is clear that due to the higher index of refraction of silicon compared to air, the haze of these substrates for

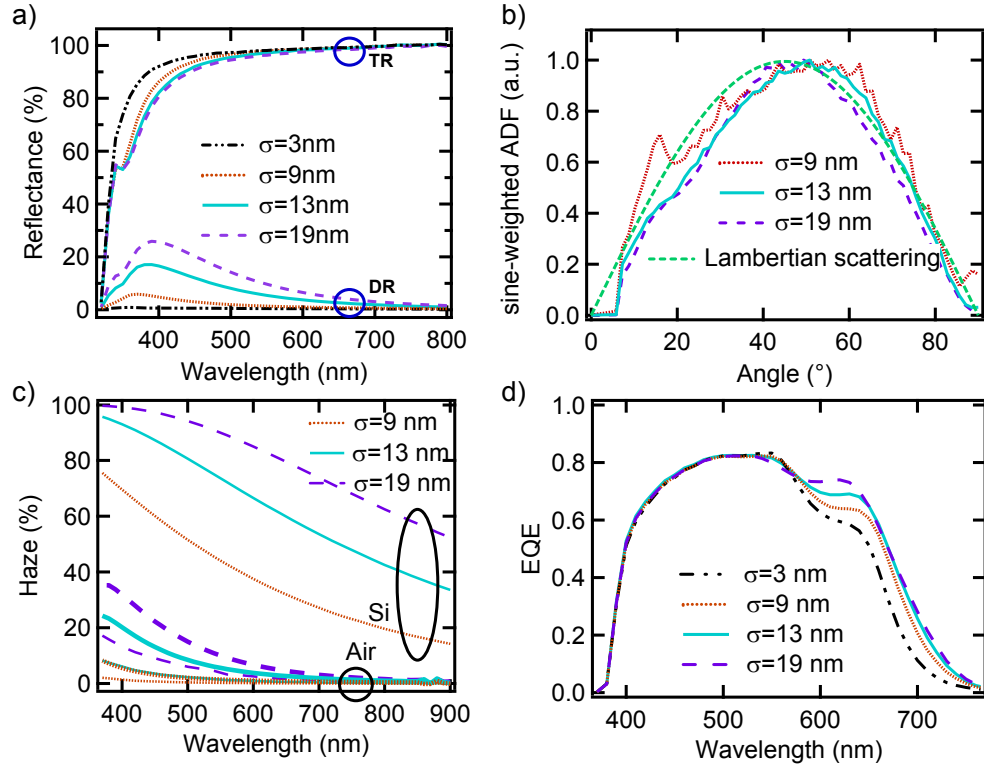


Figure 7.2: Comparison of smooth silver reflectors and their effects on the EQE spectra of a-Si:H solar cells when used as substrates for the cell growth. a) TR and DR measured in air, b) sine-weighted ADF of scattered light measured at a wavelength of 543 nm (the sine-weighted ADF of Lambertian scattering was added for comparison), c) haze, and d) EQE spectra of co-deposited a-Si:H solar cells on the various back reflectors. In c) experimental data are marked in thick line whereas the haze in air and in silicon simulated based on AFM data are marked in thin lines.

scattering into silicon is much higher than into air.

Table 7.2: Initial electrical parameters of co-deposited single-junction a-Si:H solar cells grown on four different smooth silver reflectors.

Substrate roughness	V_{oc} (mV)	FF (%)	J_{sc} (mA/cm ²)	Efficiency (%)
$\sigma_{rms} = 3$ nm	960	76	12.5	9.1
$\sigma_{rms} = 9$ nm	960	76	13.4	9.7
$\sigma_{rms} = 13$ nm	960	75	13.9	10.0
$\sigma_{rms} = 19$ nm	960	75	14.1	10.1

This demonstrates that the use of substrates with very low roughness can lead to a large increase in J_{sc} while maintaining the FF and V_{oc} of a device grown on a flat substrate. It thus shows that high haze values as measured in air should not necessarily be high and that the

angles of scattering are of main importance to obtain high light trapping.

7.2.2 Study of various back reflectors with larger roughnesses

Section 7.2.1 has shown that remarkable J_{sc} enhancement can be provided by substrates of very low roughness with only minor FF losses compared to a flat substrate. In this section, substrates with larger roughness are investigated and the effect of this roughness on the electrical parameters of solar cells grown on them is discussed. Two different depositions that were done on different back reflectors are discussed in this section in separate paragraphs because they provide distinct insights into the requirements of the back reflector texture for the growth of solar cells with high efficiencies.

The first study shows that substrates with higher roughnesses than in section 7.2.1 can be beneficial to obtain solar cells with higher J_{sc} but, as is widely known, are detrimental to the V_{oc} and FF . More interestingly, this study also shows that the use of a substrate with a roughness of $40\text{ nm} > \sigma_{rms} > 30\text{ nm}$ can reduce shunts that are observed in solar cells grown on flat substrates and whose origin is probably due to stress accumulated during the silicon growth.

In a second experiment, we compare solar cells grown on substrates with large roughness (i.e. $\sigma_{rms} > 50\text{ nm}$) that have similar sine-weighted ADFs of scattered light as measured in air. It is observed that the highest J_{sc} enhancement is obtained for the solar cell grown on the substrate that exhibits the lowest measured haze. This illustrates that optical measurements performed in air do not provide enough information about the surface texture to assess a substrate's light-trapping potential when used in a solar cell, and that the feature sizes of the substrate texture are of primary importance.

Enhanced J_{sc} and shunt reduction with substrate of larger roughness

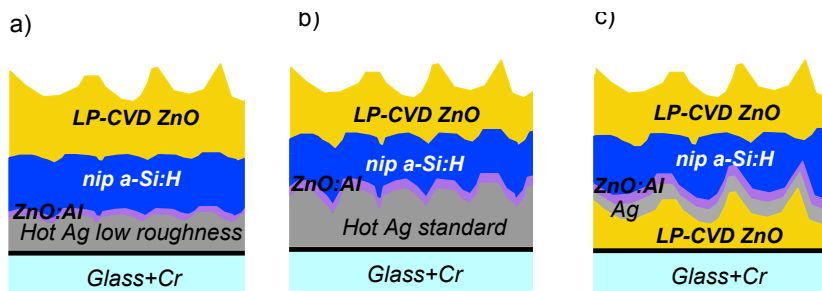


Figure 7.3: Schematic of the experiment. Single-junction *n-i-p* *a-Si:H* solar cells were co-deposited on three silver reflectors. a) A silver reflector made of Hot Ag with a low roughness of 20 nm. b) A standard Hot Ag reflector with a roughness of 35 nm. c) The roughest reflector with a roughness of 50 nm made of a silver layer deposited on a rough 2- μm -thick LP-CVD ZnO layer treated for a short time.

Single-junction a-Si:H solar cells were co-deposited on three different substrates shown schematically in figure 7.3 to identify which provide higher J_{sc} enhancement than shown in section 7.2.1. The substrate shown in figure 7.3a is called Hot Ag_{low roughness}, and serves as a reference as it is similar to the rougher substrate presented in section 7.2.1. The substrate in figure 7.3b is called Hot Ag_{standard}, and it is the standard Hot Ag substrate deposited at a temperature of 200 °C suitable for a-Si:H solar cells used in the whole thesis. The substrate shown in figure 7.3c is the roughest of the three, and it is made of Z2 etched by plasma for 6 minutes and subsequently covered with a 200-nm-thick silver layer. The silver layer was deposited on the LP-CVD ZnO at 150 °C in order to improve its reflectance as discussed in section 5.4. The first substrate is, as seen in section 7.2.1, of low roughness with $\sigma_{rms} = 20$ nm. The other two substrates are rougher with $\sigma_{rms} = 35$ nm and 50 nm for the Hot Ag_{standard} and the LP-CVD ZnO/Ag substrate, respectively. All substrates were covered by 60 nm of sputtered ZnO:Al when used as substrates for the growth of solar cells, though the optical properties were characterised on the bare silver layers.

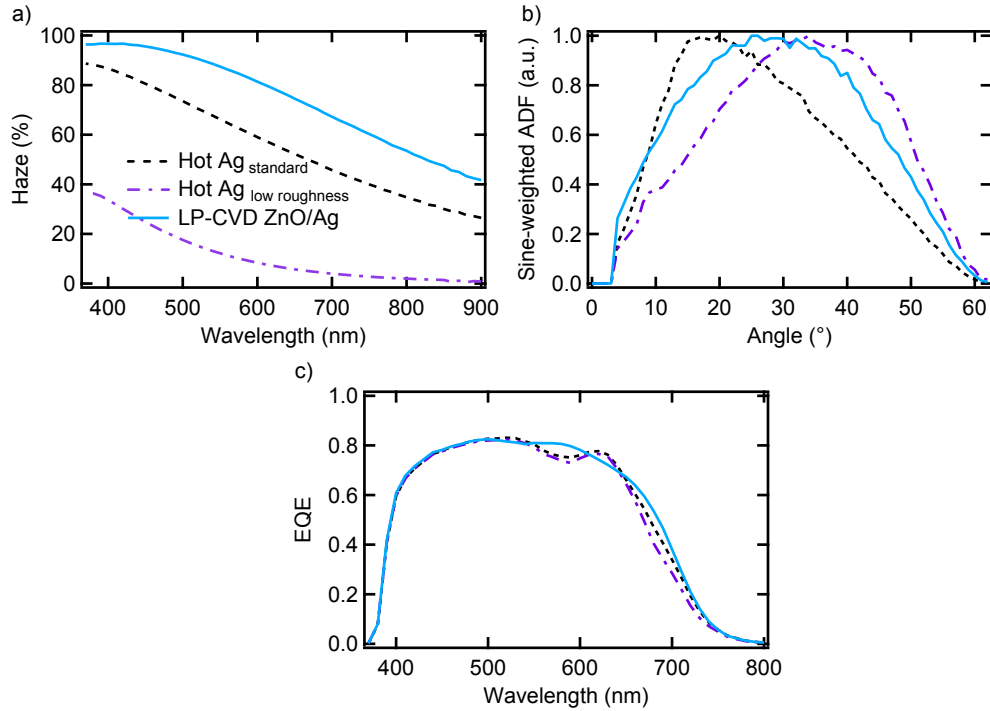


Figure 7.4: *a) Experimental haze, b) sine-weighted ADF measured at a wavelength of 543 nm, and c) EQE spectra of co-deposited solar cells on the various types of back reflector. The legend in a), which indicates the type of back reflector, applies to all graphics.*

Figure 7.4 presents the optical characterisation of the three different back reflectors and the EQE spectra of the solar cells that were co-deposited on them, while table 7.3 provides the electrical properties of the solar cells and morphological parameters of the back reflector textures extracted from AFM measurements. The optical properties of the back reflectors that are shown in figures 7.4a and 7.4b show that the substrates possess very different scattering

properties. The Hot Ag_{low roughness} exhibits—unsurprisingly—the lowest haze and it scatters the light at the highest angles. The Hot Ag_{standard} exhibits higher haze but scatters the light at the lowest angles. Finally, the LP-CVD ZnO/Ag exhibits the highest haze and scatters light at high angles, although at slightly lower angles than the Hot Ag_{low roughness}. These experimental curves qualitatively describe the substrates and they may not be directly correlated with their potential for light confinement in devices. Therefore, the EQE spectra of solar cells grown on these substrates are a better indicator of the effect of the different substrate shapes and roughnesses on light management.

Table 7.3: *Initial electrical parameters of single-junction a-Si:H solar cells co-deposited on various back reflectors.*

Substrate	V_{oc} (mV)	FF (%)	J_{sc} (mA/cm ²)	Efficiency (%)
ZnO/Ag	920	62	15.0	8.6
Hot Ag _{standard}	950	72	14.7	10.1
Hot Ag _{low roughness}	960	68	14.3	9.3

The lower J_{sc} obtained on the Hot Ag_{low roughness} compared to the Hot Ag_{standard} substrate demonstrates that high angles of scattering are not sufficient for high J_{sc} enhancement. Higher haze than that provided by the Hot Ag_{low roughness} is desirable, even though, as observed in section 7.2.1, this small roughness already provides remarkable J_{sc} enhancement compared to a flat substrate. Intuitively, higher haze and a maxima of the sine-weighted ADF at higher angles than the Hot Ag_{standard} should provide higher J_{sc} . These are indeed obtained with the rougher LP-CVD ZnO/Ag substrate. Nevertheless, as higher haze value combined with a sine-weighted ADF that peaks at high angles does not always bring additional J_{sc} enhancement, a discussion is provided in the next section on this subject.

Several empirical insights were obtained by comparing the EQE spectra of the solar cells grown on these different substrates. Yet, our main interest is the solar cell efficiency and not only its J_{sc} . Table 7.3 presents the electrical properties of the cells whose EQE spectra are reported in figure 7.4c. Even though the LP-CVD ZnO/Ag substrate provides a higher J_{sc} compared to the other substrates, the V_{oc} and FF losses are too large to lead to cells with high efficiencies. Clearly, the scattering of light at high angles can be related in this case to the higher haze (higher roughness) and probably to the sharp angles of the texture. Therefore, cracks are likely to appear during the growth of the silicon layers, creating shunt paths [Sakai 90] which strongly limit the V_{oc} and FF of the solar cell grown on the LP-CVD ZnO/Ag substrate.

The lower FF value that is obtained for the solar cell grown on the Hot Ag_{low roughness} compared to the one grown on the Hot Ag_{standard} is more surprising. Indeed, in section 7.2.1, a high FF of 75% was obtained for a solar cell grown on the Hot Ag_{low roughness}, which was only an absolute decrease of 1% compared to the solar cell grown on the flat substrate. For the deposition shown in this section, the low FF is ascribed to shunts arising from stresses that build up during the growth of the silicon layers on the smooth substrate. Here, a flat

silver reflector was also added for comparison but the solar cells were highly shunted and the FF values were even lower than on the Hot Ag_{low roughness}, with the consequence that the EQE spectrum could not be measured correctly. It was observed that, depending on the history of the reactor used for the silicon deposition, the yield of the solar cells deposited on flat substrates could be very different. In the small-area system E, the reactor walls were not cleaned after each cell deposition and only intrinsic coating layers were used between cell depositions. It is thus likely that the intrinsic properties of the deposited silicon layers drift with the number of cells that are deposited, and it was observed that the yield of solar cells deposited on a flat substrate was likely to be low after a prolonged use of the reactor. It is therefore possible that a small roughness like that provided by the Hot Ag_{standard} can help to decrease shunts as already observed by Deckman [Deckman 83]. The Hot Ag_{low roughness} has a high potential for the growth of high-efficiency solar cells because solar cells with high V_{oc} and FF can be grown as shown in section 7.2.1, but there is the risk to grow shunted cells as shown in this paragraph.

To conclude it was demonstrated that solar cells grown on substrates with larger roughnesses than that of the Hot Ag_{low roughness} can lead to solar cells with higher J_{sc} but that the use of a too rough substrate like the LP-CVD ZnO/Ag leads to a large decrease in the V_{oc} and FF of the solar cell. Also, the use of a too smooth substrate such as the Hot Ag_{low roughness} may lead to the creation of shunts in the cell which reduces its FF . Thus, the standard Hot Ag substrate is probably the best substrate for state-of-the-art cells because it provides a good V_{oc} , FF and J_{sc} trade-off and it also ensures that the solar cells are not shunted because of a too low roughness of the substrate.

Lack of J_{sc} enhancement with increased roughness

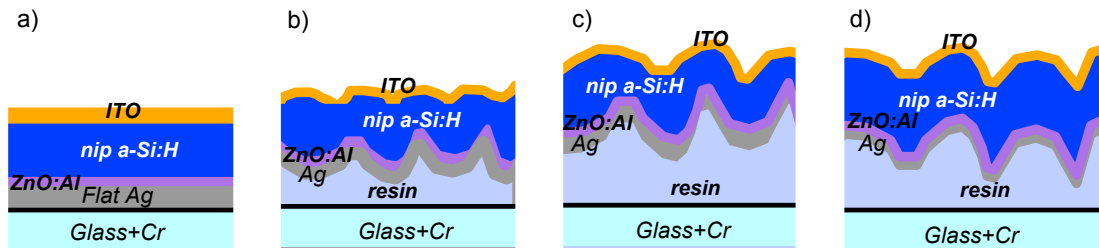


Figure 7.5: Schematic of the experiment. Single-junction $n-i-p$ a-Si:H solar cells were co-deposited on four silver reflectors. a) A flat silver reflector and b), c) and d) substrates called respectively A, B_{positive} and B_{negative}. These three last substrates were made of replicas of different LP-CVD ZnO layers covered with silver reflectors.

Optical characterisation of substrates in air, such as haze and sine-weighted ADE, can be misleading for the assessment of a substrate's potential to provide good light scattering for light trapping in solar cells. As schematically shown in figure 7.5 solar cells were co-deposited on four different back reflectors and ITO was used as the front contact. A flat silver reflector

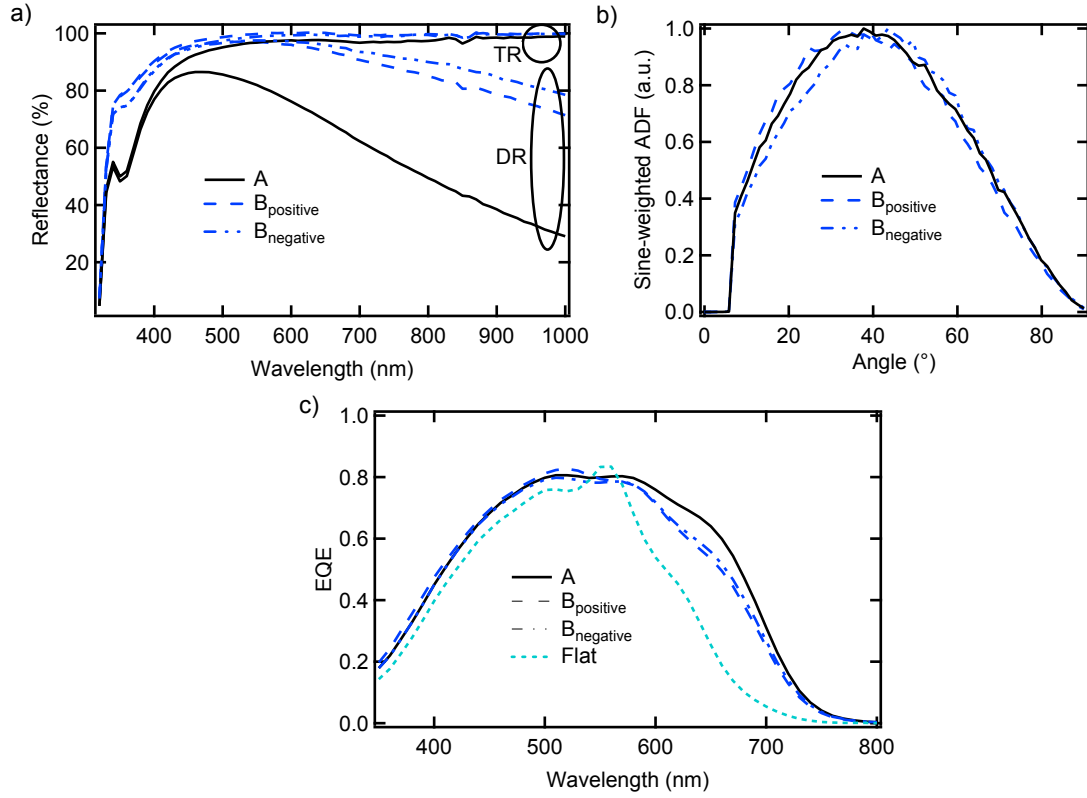


Figure 7.6: *a) Experimental haze, b) sine-weighted ADF measured at a wavelength of 543 nm, and c) EQE of co-deposited solar cells.*

was used to serve as a benchmark for the J_{sc} enhancement that is provided by the three rough reflectors. The rough reflectors were made of nano-imprinted resin layers on top of which a 200-nm-thick silver layer was deposited. The original master substrates for the rough reflectors were a Z2 texture etched by Ar plasma for 10 minutes for substrate A, and a Z5 texture which was treated for 60 min by Ar plasma. From the highly treated Z5, two different textures were extracted and inserted as substrates for the solar cells: $B_{positive}$ contained the positive pyramids of LP-CVD ZnO and $B_{negative}$ contained the inverse pyramids. Optical and morphological characterisation was performed on the replicas covered with silver and, as usual, 60 nm of sputtered ZnO:Al was added to the substrates when they were used as back reflectors for the deposition of the solar cells.

Figure 7.6 presents the optical characterisation of substrates A, $B_{positive}$, and $B_{negative}$ after they were covered with silver, and the EQE spectra of solar cells co-deposited on these substrates and of a cell grown on a reference flat substrate. Table 7.4 presents the electrical parameters of the cells whose EQE spectra are shown in figure 7.6c and, additionally, the morphological parameters that were extracted from AFM measurements of the rough reflectors. Comparison of the optical properties shows that the ADF values of the three substrates

Table 7.4: *Initial electrical parameters of single-junction a-Si:H solar cells grown on various back reflectors. Morphological parameters that characterise the back reflector texture and which were extracted from AFM analysis are also reported.*

Substrate	V_{oc} (mV)	FF (%)	J_{sc} (mA/cm ²)	Efficiency (%)	σ_{rms} (nm)	L (nm)	σ_{rms} / L
A	920	69	14.1	8.9	56	215	0.26
$B_{positive}$	920	72	13.4	8.9	80	355	0.22
$B_{negative}$	900	71	13.4	8.6	92	400	0.23
Flat	910	71	10.6	6.7			

are similar, while substrates $B_{positive}$ and $B_{negative}$ have higher DR and TR (hence higher haze and lower parasitic absorption in the silver layer). Therefore, higher J_{sc} enhancement is expected on substrates $B_{positive}$ and $B_{negative}$ compared to substrate A. Nevertheless, the opposite is observed in figure 7.6c and table 7.4. This is probably related to the lateral feature sizes of the texture that are reported in table 7.4. For substrates $B_{positive}$ and $B_{negative}$, the correlation length is larger than in substrate A, and thus the efficiency of scattering in the silicon layer may be reduced for substrates of type B even if this is not observed in air. Further insights may be gained by measuring the sine-weighted ADF curves for different wavelengths as shown by Jäger et al. and Dewald et al. [Jäger 10, Dewald 11]. To conclude, it was shown that not only the optical properties are important for J_{sc} enhancement, but that the lateral feature sizes are of high importance too, as already discussed by Terrazzoni-Daudrix et al. [Terrazzoni-Daudrix 06].

7.2.3 Optimised cell on glass substrate: 10.4% initial efficiency, 8.1% after degradation

Figure 7.7 presents the single-junction a-Si:H solar cell with the highest stable efficiency (8.1%) achieved during this thesis, as well as a schematic of the cell design. This solar cell is similar to those presented in the two previous sections except for a slightly thicker p -layer which increased the V_{oc} and FF . The substrate was made of a standard Hot Ag.

The choice of substrate was based on our previous experiments: The Hot Ag substrate is an adequate compromise between sufficient roughness for respectable light confinement sufficient smoothness to grow of silicon material with few zones of structural defects, thus maintaining high V_{oc} and FF . It was observed in section 7.2.2 that even lower roughnesses could be interesting but they risk growing shunted cells.

This solar cell is one of the bricks on which the multi-junction solar cells shown in sections 7.4, 7.5 and 7.6 are based. However, in multi-junction devices it may be appropriate to decrease the p -layer thickness in order to increase the J_{sc} of each sub-cell. In this case, the loss in V_{oc} and FF can be largely compensated by a J_{sc} enhancement whereas, in single-junction a-Si:H solar

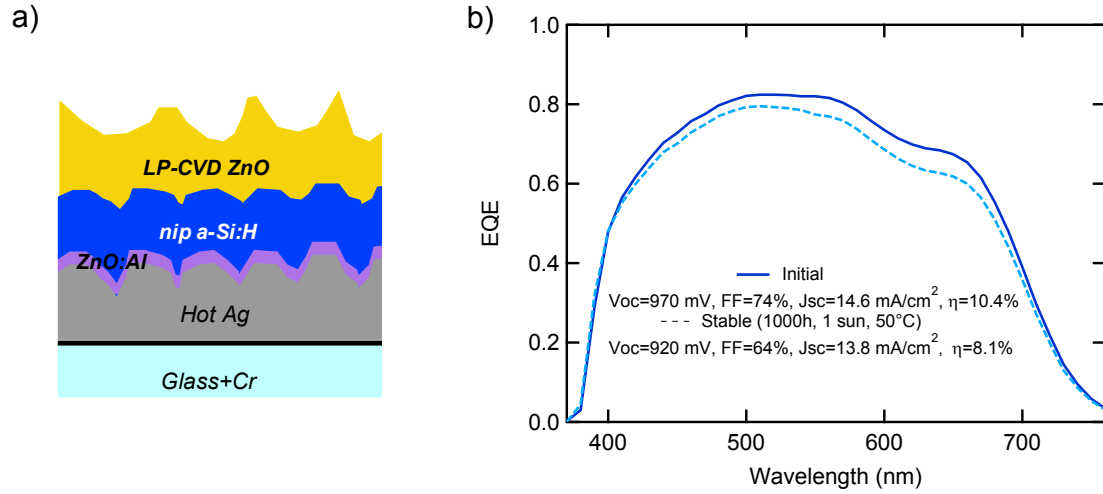


Figure 7.7: a) Schematic of the cell design, and b) EQE spectra and electrical parameters of the single-junction *n-i-p* a-Si:H solar cell with the highest stable efficiency achieved during this thesis.

cells, the J_{sc} vs. V_{oc} and FF trade-off due to the *p*-doped layer thickness is often visible in the initial efficiency while the stable efficiency is similar even for very different *p*-layer thicknesses.

Some routes for further improvements of the stable efficiency of this a-Si:H cell are given below.

1. A higher deposition temperature for the *i*-layer was seen to lead to lower degradation but it also decreased the bandgap of the material, thus increasing the J_{sc} but also decreasing the V_{oc} . This should be kept in mind in multi-junction devices. Also, if the cell is deposited on a plastic substrate, the deposition temperature cannot be increased to a large extent.
2. With the state-of-art solar cells, the use of rough substrates is prohibited because of a too large decrease of the V_{oc} and FF of solar cells grown on them. In principle, solar cells that are more tolerant of textured substrates can be realised by the modification of the doped layers [Despeisse 10] or by the modification of the deposition regimes [Bugnon 12]. Thus, higher J_{sc} values are in principle achievable and, if the V_{oc} and FF decrease less on a rough substrate, higher efficiency is within range. Because of large parasitic absorption that may occur in highly textured silver (see section 5.4) other optical schemes like "flat Ag/LP-CVD ZnO" or "flat Ag/replica/In₂O₃:H" are preferred to design substrates with higher roughnesses without detrimental parasitic absorption.
3. The transparency of the doped layers can be improved by depositing them at a lower temperature (i.e. 150 °C). This should increase the J_{sc} , but the effect on the V_{oc} and FF values should be studied further.
4. The J_{sc} can be increased by reducing parasitic absorption in the *n*-layer and in the silver

layer by using a thicker ZnO:Al buffer layer of 120 nm as shown in section 5.2.

To conclude, the substrate that was used here for the optimisation of the a-Si:H single-junction solar cell is not very rough because of the high losses in V_{oc} and FF that occur when the solar cell is grown on rougher substrates. Still, further improvements are within range and they should predominantly aim at the deposition of cells with electrical parameters that are more tolerant to substrates with aggressive features to allow for increased J_{sc} .

7.3 Single-junction $\mu\text{c-Si:H}$ solar cells

The solar cells that are presented in this section were deposited in the large-area KAI-M industrial reactor and some details on the cells are given in section 2.2.2.

Section 7.3.1 discusses different types of back reflector substrates with particular characteristics that allow the drawing of two main conclusions:

1. The importance of a smooth growth interface to obtain solar cells with high V_{oc} and FF with the state-of-art deposition conditions.
2. The importance of adding a buried, optically rough interface when the cell is grown on a smooth texture to increase light trapping.

In section 7.3.2, a single-junction $\mu\text{c-Si:H}$ solar cell with a high efficiency of 10.1% is shown, and roads for further improvements are given.

7.3.1 Study of various back reflectors

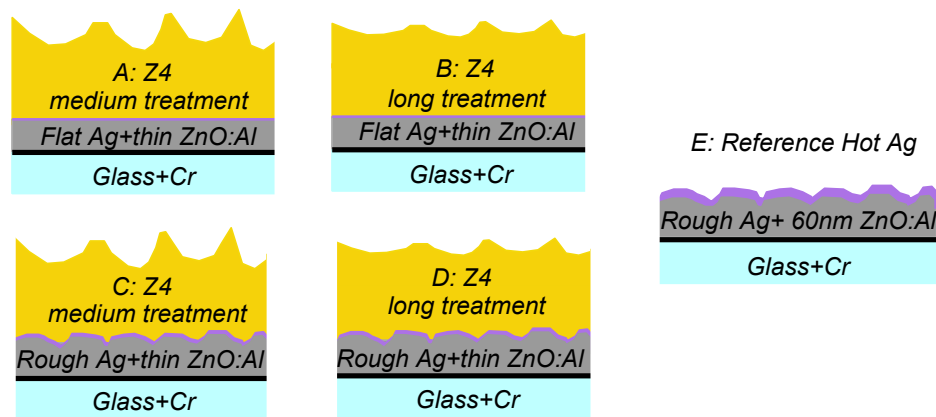


Figure 7.8: Schematics of the different substrates used as back reflectors in single-junction $\mu\text{c-Si:H}$ n-i-p solar cells.

Chapter 7. Texture optimisation: Towards high efficiencies in the *n-i-p* configuration

The single-junction $\mu\text{c-Si:H}$ solar cells presented in this section were co-deposited with a total silicon thickness of $1.36\ \mu\text{m}$ on five different substrates that are shown schematically in figure 7.8. The solar cells had a $2.5\text{-}\mu\text{m}$ -thick LP-CVD ZnO:B front contact. Substrates A–D consist of a silver layer (flat silver in A and B and rough silver in C and D) which plays the role of a buried back reflector. A thin layer of ZnO:Al was sputtered on the silver layers to prevent their roughening during the higher-temperature subsequent deposition of $4\text{-}\mu\text{m}$ -thick (Z4) non intentionally doped LP-CVD ZnO. Two plasma surface treatment times [Bailat 06, Python 08b, Boccard 12e] were applied to the LP-CVD ZnO to smoothen the pyramidal features: Substrates A and C were treated for a shorter time (35 minutes) than substrates B and D (90 minutes) and are therefore rougher. Substrate E is a Hot Ag reference substrate which consists of a rough Ag back reflector sputtered onto a substrate held at approximately $300\ ^\circ\text{C}$, which was then further covered by $60\ \text{nm}$ of ZnO:Al. It should be noted that the rough silver layers in substrates C and D were sputtered at the same temperature as the Hot Ag reference.

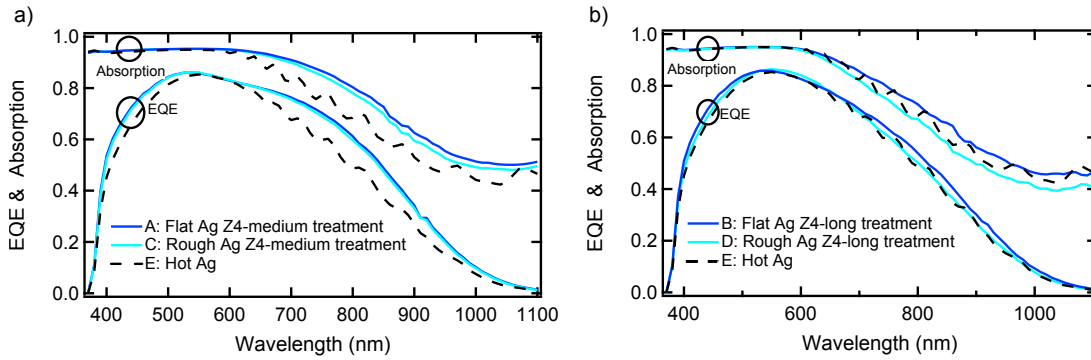


Figure 7.9: *a) and b) EQE and absorption spectra of co-deposited single-junction $\mu\text{c-Si:H}$ solar cells grown on various substrates.*

Table 7.5: *Electrical parameters of co-deposited single-junction $\mu\text{c-Si:H}$ solar cells grown on various substrates.*

Substrate	V_{oc} (mV)	FF (%)	J_{sc} (mA/cm^2)	Efficiency (%)
A: Flat Ag Z4-medium treatment	530	70	24.3	9.0
B: Flat Ag Z4-long treatment	560	77	22.7	9.8
C: Rough Ag Z4-medium treatment	520	70	24.6	9.0
D: Rough Ag Z4-long treatment	550	77	23.3	9.8
E: Hot Ag	560	78	22.3	9.7

Figure 7.9 and table 7.5 present the results of the single-junction $\mu\text{c-Si:H}$ solar cells grown on substrates A–E. The similar EQE and absorption spectra of cells grown on substrates A and C (figure 7.9a) indicate that the buried, optically rough silver interface yields only a marginal J_{sc} enhancement since the surface of the LP-CVD ZnO is rough enough to efficiently scatter the incoming light. However, when this LP-CVD ZnO surface is smoother, as is the case for substrates B and D, it is beneficial for light that is transmitted through the ZnO to be scattered

on a rough buried silver layer. This results in higher EQE and absorption spectra for the cell grown on substrate *D* compared to the cell grown on substrate *B* as figure 7.9b shows. Still, the J_{sc} of substrate *D* is lower than those given by the roughest substrates (*A* and *C*) as table 7.5 reveals. This can be attributed to a larger primary reflection at the LP-CVD ZnO surface in substrates *B* and *D*. Nevertheless, the real figure of merit is the cell efficiency and is shown in table 7.5. Despite the fact that SiO_x doped layers were used, the V_{oc} and FF exhibit a large decrease for the rougher substrates *A* and *C*. These losses are not counterbalanced by the increase in J_{sc} given by the rough LP-CVD ZnO surface. A relative efficiency increase of 9% is hence obtained by using the smoother substrates *B* and *D*. Furthermore, an even higher FF can be obtained by using the smoothest substrate of this series, i.e. the reference Hot Ag substrate *E*. The high V_{oc} of 560 mV and FF of 78% show that $\mu\text{c-Si:H}$ grown on this substrate is of very high quality with few structural defects. These $n-i-p$ cells show that a smooth interface for $\mu\text{c-Si:H}$ cell growth is of first and foremost importance for the cell efficiency. This will have consequences on the insertion of the $\mu\text{c-Si:H}$ cells in multi-junction devices which will be discussed in sections 7.5 and 7.6.

7.3.2 Optimised cell on glass substrate: 10.1% initial efficiency

This section presents the best efficiency which was achieved during this thesis for a single-junction $\mu\text{c-Si:H}$ solar cell. The Hot Ag reference substrate was chosen for optimisation as, based on section 7.3.1, it appears to be difficult to grow solar cells with high efficiencies on rougher substrates with state-of-art deposition conditions. Figure 7.10 presents the single-junction $\mu\text{c-Si:H}$ cell with the highest efficiency (10.1%) achieved during this thesis as well as a schematic of the cell design. The cell was deposited with a total thickness of $1.86\ \mu\text{m}$ and had a $2.5\text{-}\mu\text{m}$ -thick LP-CVD ZnO:B front contact. This cell is the other brick on which the

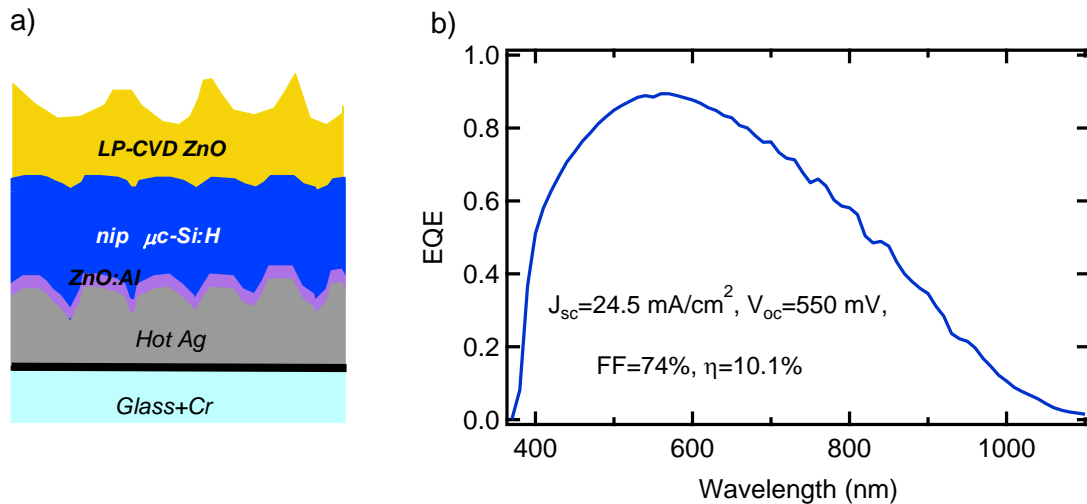


Figure 7.10: a) Schematic of the cell design and b) EQE spectrum and electrical parameters for our best single-junction $n-i-p\ \mu\text{c-Si:H}$ solar cell.

multi-junction devices shown in sections 7.5 and 7.6 are based. Even if an efficiency of 10% is satisfactory for the insertion of this cell in tandem a-Si:H/ μ c-Si:H and in triple-junction a-Si:H/ μ c-Si:H/ μ c-Si:H solar cells, further improvements are within range and thus several directions are given below.

1. Under reverse bias, a loss in collection between 600 nm and 750 nm was observed in the EQE. This collection loss was seen to come from contamination at the *n/i* interface. This contamination could be due either to phosphorous diffusion from the *n*-layer into the *i*-layer [Yan 12b] or to residual oxygen from the reactor which is incorporated in the *i*-layer during its deposition as observed by Yue et al. [Yue 12a, Yue 12b]. The phosphorous contamination could be solved or at least decreased by reducing the amount of dopant in the *n*-doped layer or by the incorporation of a buffer layer at the *n/i* interface which could act as a barrier for phosphorous diffusion as discussed by Yan et al. [Yan 12b]. Oxygen contamination could possibly be mitigated by boron micro-doping as was done successfully by Yue et al. [Yue 12a, Yue 12b].
2. The strong decrease in the V_{oc} and FF values when the cell is grown on rough substrates (see section 7.3.1) could be reduced by growing a seed layer deposited after the *n*-doped layer. If the seed is more amorphous than the rest of the *i*-layer, a more dense material is grown at the *n/i* interface, which decreases the growth of porous material on rough substrates as observed in other studies [Söderström 08b, Yan 12b]. It could hence allow us to maintain high V_{oc} and FF values on rough substrates while increasing the J_{sc} by benefiting from better light trapping.
3. An appropriate buffer at the *i/p* interface was seen to improve both the FF and V_{oc} values by decreasing the dark recombination current generated at this interface [Yue 08, Yan 12b]. This effect was seen to be more pronounced for thin cells and this could help to grow thinner cells than the 1.8 μ m used here. As well the use of thin cells can also lead to an impressive V_{oc} as demonstrated recently by Hänni et al. [Hänni 13b] who grew a single-junction μ c-Si:H *p-i-n* solar cell with a V_{oc} above 600 mV.
4. The deposition temperature of the doped layers can be further optimised to improve their transparency. Clearly, the EQE response of 51% at 400 nm shown in figure 7.10 is not high enough. All the doped layers can be improved by adjusting their crystallinity, oxygen content, deposition temperatures and thickness.
5. The J_{sc} could be increased by reducing parasitic absorption in the *n*-layer and in the silver layer by using a thicker ZnO:Al buffer layer of 120 nm as shown in section 5.2.

In summary, an efficiency above 10% was reached with a single-junction *n-i-p* μ c-Si:H cell. This solar cell paves the way for excellent multi-junction devices as will be shown in sections 7.5 and 7.6, but further improvements are within reach. The direction for the cell optimisation depends on the type of devices into which the μ c-Si:H cell is incorporated.

7.4 Tandem a-Si:H/a-Si:H solar cells

The solar cells that are presented in this section were deposited in the small-area system E reactor. Details on the a-Si:H sub-cells can be found in sections 2.2.2 and 7.2 and details on the EQE measurements can be found in section 2.4.2.

The aim of the work presented here was to obtain a flexible solar cell with a stable efficiency above 9% by using only a-Si:H and a thin flexible front contact such as ITO. However, to observe the potential provided by different front contacts, ITO and LP-CVD ZnO front contacts are first compared in section 7.4.1. Section 7.4.2 then presents an optimised tandem a-Si:H/a-Si:H solar cell grown on a PEN substrate that exhibits a stabilised efficiency of 9.2% using a thin sputtered ITO front contact.

7.4.1 Comparison of front contacts: Sputtered ITO vs LP-CVD ZnO:B

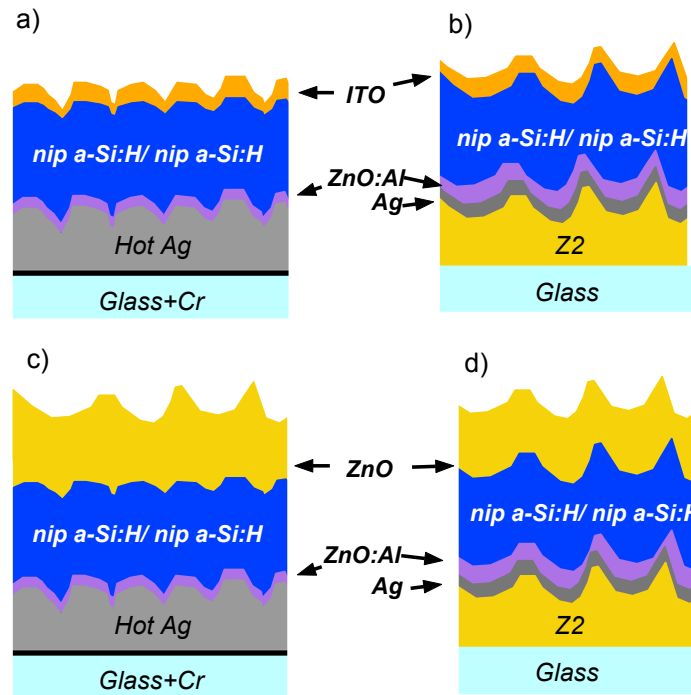


Figure 7.11: Schematic of the experiment: Four solar cells were co-deposited on two types of substrates: a) and c) a Hot Ag substrate, and b) and d) an LP-CVD ZnO Z2 substrate covered with a silver layer. Two types of front contact were investigated: a) and b) a thin layer of 65 nm of ITO, c) and d) a 2.5- μm -thick LP-CVD ZnO:B layer.

Figure 7.11 presents a schematic of the experiment shown in this section. A set of co-deposited tandem a-Si:H/a-Si:H solar cells grown on two types of substrates and with two different types of TCO front contacts is presented. The top- and bottom-cell *i*-layer thicknesses are 65 nm and 320 nm, respectively. The substrates that are compared are a Hot Ag of low roughness and

a 2- μm -thick LP-CVD ZnO:B treated for 8 minutes by Ar plasma and subsequently covered by a standard stack of Ag (200 nm)/ZnO:Al (60 nm). The optical properties of the Hot Ag of low roughness are shown in figure 7.4. The Z2 substrate is slightly smoother than the ZnO/Ag whose optical properties are shown in the same figure. When inserted into single-junction a-Si:H solar cells, the rougher ZnO/Ag substrate was seen to provide a higher J_{sc} than the Hot Ag substrate, but because of the high V_{oc} and FF that can be obtained on smooth substrates the solar cell efficiency was seen to be higher on the Hot Ag substrate. In the case of tandem a-Si:H/a-Si:H solar cells, this might be different because the efficiency is limited predominantly by the total J_{sc} that can be achieved.

Figure 7.12 presents a comparison of the EQEs of solar cells grown on the two textures with each type of front TCO (i.e. 2.5- μm -thick LP-CVD ZnO:B and 65 nm of sputtered ITO), and table 7.6 presents the corresponding electrical parameters.

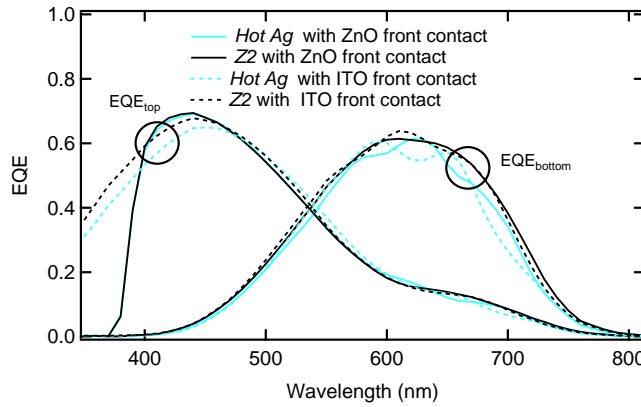


Figure 7.12: *EQE spectra of tandem a-Si:H/a-Si:H solar cells co-deposited on two types of substrates and with two different types of front contact.*

Table 7.6: *Initial electrical parameters of co-deposited a-Si:H/a-Si:H cells on two different substrates and with two different TCO front contacts. The limiting J_{sc} is marked in bold.*

Substrate	front TCO	J_{sc} [top/bottom] (mA/cm ²)	J_{sc} [total] (mA/cm ²)	V_{oc} (V)	FF (%)	Efficiency (%)
Hot Ag	ITO	7.2 /7.7	14.9	1.83	75	9.9
Z2	ITO	7.4 /8.4	15.8	1.85	74	10.1
Hot Ag	ZnO:B	6.9 /7.8	14.7	1.89	76	9.9
Z2	ZnO:B	7 /8.4	15.4	1.88	76	9.9

Table 7.6 shows that both substrates and both front TCOs can lead to solar cells with similar efficiencies, but in different ways. Devices with LP-CVD ZnO:B front contacts exhibit higher V_{oc} and FF than devices with ITO. At the same time, devices with LP-CVD ZnO:B exhibit a lower J_{sc} because of the lower bandgap of this TCO, which limits the J_{sc} of the top cell as can

be observed in the EQE spectra shown in figure 7.12. Yet, the higher V_{oc} and FF values of the devices with LP-CVD ZnO:B indicate that the use of this front contact can potentially lead to cells with higher efficiencies because the J_{sc} value can be tuned with the thickness and the dilution of the bottom- and top-cell i -layers. However, an increase in the thicknesses of the i -layers or a modification of their dilutions will influence the device V_{oc} and FF and thus no definitive conclusion can be drawn here.

Let's now focus on the ITO front contact for plastic applications, and study which back reflector (the smooth Hot Ag or the rougher ZnO/Ag) is the most suitable for the growth of an a-Si:H/a-Si:H device with high efficiency. The use of the rougher substrate increases the total J_{sc} by 0.9 mA/cm² due to an increase in the top-cell J_{sc} via an anti-reflective effect and the bottom-cell J_{sc} via better light confinement. Besides, the V_{oc} and FF are not very different between the two substrates and hence, contrary to what was observed in single-junction a-Si:H solar cells with LP-CVD ZnO:B front contacts (section 7.2), a rough substrate has a higher potential for the growth of a high-efficiency tandem a-Si:H/a-Si:H solar cell because of the higher total J_{sc} .

7.4.2 Optimised cell on plastic substrate: 11.1% initial efficiency, 9.2% after degradation

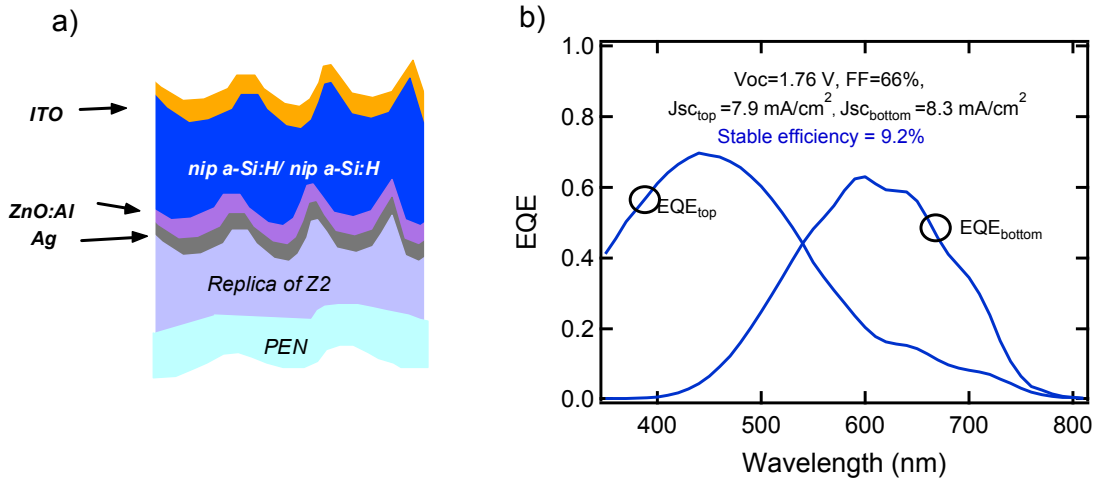


Figure 7.13: a) Schematic and b) stable EQE spectrum and electrical parameters of the tandem a-Si:H/a-Si:H solar cell grown on a PEN substrate textured by UV nano-imprinting that exhibits a high efficiency of 9.2%.

Because of the high total J_{sc} that can be obtained for a tandem a-Si:H/a-Si:H device grown on a Z2 texture covered with a Ag/ZnO:Al reflector, this texture was chosen for further optimisation of the device on a PEN substrate. A Z2 treated for 8 minutes by plasma was replicated on a PEN substrate according to the process described in chapter 3. This replica was covered with a 200-nm-thick silver layer which was annealed to increase its reflectance before the subsequent

deposition of 60 nm of ZnO:Al. To improve the current matching compared to the cells shown in the previous section, the *i*-layer thicknesses were increased to 75 nm and 360 nm for the top and bottom cells respectively. Subsequently, an ITO front contact was sputtered with a thickness of 65 nm.

Figure 7.13 presents a schematic of the best tandem a-Si:H/a-Si:H solar cell grown on a plastic substrate during this thesis, as well as its stable EQE spectrum and electrical parameter. The EQE spectrum of this cell was not measured in the initial state, but the initial efficiency could be calculated based on the J_{sc} obtained from the I-V measurement. The efficiencies in the initial state and after degradation are given in table 7.7.

Table 7.7: *Electrical parameters of the best tandem a-Si:H/a-Si:H device grown on a PEN substrate with a sputtered ITO front contact in the initial and stabilised state.*

	V_{oc} (V)	FF (%)	J_{sc} (mA/cm ²)	Efficiency (%)
Initial	1.84	74	8.2	11.1
Stable	1.76	66	7.9	9.2

These efficiencies are, to the author's knowledge, higher than other devices on plastic substrates which were produced with a-Si:H (e.g. 8% in Couty et al. [Couty 11] and 7% in Gonz  lez Lazo et al. [Gonz  lez Lazo 12], both with a-Si:H/a-Si:H *n-i-p* devices in the stabilised state and 6.4% initial efficiency with an a-Si:H *p-i-n* single-junction device in de Jong et al. [de Jong 12]). However, improvements are within range and some routes are given below.

1. The *i*-layer dilutions of the top and bottom cells are the same in the device shown in figure 7.13, but a tuning of these dilutions as done in Couty et al. [Couty 11] could be used to decrease the bottom-cell thickness, which could reduce the light-induced degradation of the device.
2. The deposition temperature of each layer could be modified. The bottom-cell bandgap could be reduced by increasing the temperature of its *i*-layer deposition but this unfortunately conflicts with the use of the PEN substrate. Still, a decrease of the temperature for the top-cell *i*-layer could be used to increase its bandgap, and deposition of the doped layers at 150 °C could lead to higher transparencies and enhanced J_{sc} .
3. Section 7.4.1 showed that the use of an ITO front contact leads to lower V_{oc} than if an LP-CVD ZnO:B front contact is used. As it is clear that the use of ITO is compatible with high V_{oc} values (single-junction a-Si:H solar cells with V_{oc} of 1 V were already demonstrated by United Solar [Yang 09a]), the V_{oc} loss should be studied in more detail and higher efficiencies could be obtained if this loss were reduced. In fact, higher V_{oc} can be expected when ITO is used because its higher work function, compared to LP-CVD ZnO:B [Minami 05], should favor higher V_{oc} [Haug 12a]. Hence, the loss in V_{oc} by using ITO can be ascribed either to sputtering damage to the *p*-layer of the top cell or the *i/p* interface because sputtering-induced damage to a-Si:H were previously observed

7.5. Thin micromorph a-Si:H/ μ c-Si:H solar cells with fabrication processes compatible with plastic substrates

[Street 79, Demareux 12]. Or, the V_{oc} loss could also be due to non-optimised contact between the p -layer and the ITO.

4. Finally, section 5.2 demonstrated that the use of a 120-nm-thick ZnO:Al layer on top of the silver contact at the back helps to increase the J_{sc} of the device.

To conclude this section, a stable efficiency above 9% was achieved on flexible plastic substrates with an ITO front contact and using less than half a micron of a-Si:H. Further improvements are within range and higher efficiencies can be expected for an optimised device.

7.5 Thin micromorph a-Si:H/ μ c-Si:H solar cells with fabrication processes compatible with plastic substrates

The solar cells presented in this section were deposited in the small-area system E (a-Si:H top cell) and in the large-area KAI-M reactor (μ c-Si:H bottom cell). Details on a-Si:H single-junction solar cells can be found in sections 2.2.2 and 7.2 and details on μ c-Si:H single-junction solar cell can be found in sections 2.2.2 and 7.3. Also, details on EQE measurements can be found in section 2.4.2.

The aim of the section was to produce a thin micromorph a-Si:H/ μ c-Si:H device with a stable efficiency above 10% with a process compatible with plastic substrates. Section 7.5.1 describes a co-deposition of thin a-Si:H/ μ c-Si:H devices on different back reflectors. This study showed that the use of a smooth substrate is the most promising back reflector for device optimisation. An optimised cell with a stable efficiency of 10.4% is then shown in section 7.5.2.

7.5.1 Study of various back reflectors

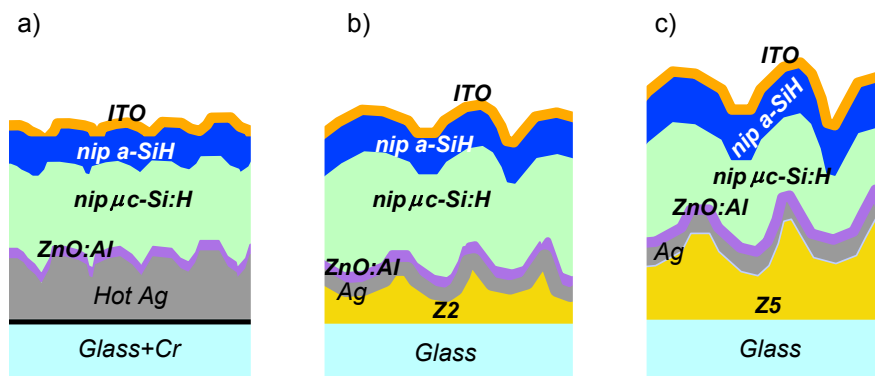


Figure 7.14: Schematic of the experiment in which thin a-Si:H/ μ c-Si:H devices were co-deposited on three different substrates: a) a Hot Ag, b) a 2- μ m-thick LP-CVD ZnO treated for a short time and subsequently covered with a Ag/ZnO:Al reflector, and c) a 5- μ m-thick LP-CVD ZnO treated for a long time and subsequently covered with a Ag/ZnO:Al reflector.

Chapter 7. Texture optimisation: Towards high efficiencies in the *n-i-p* configuration

Figure 7.14 shows schematically the experiment in which thin a-Si:H/ μ c-Si:H devices were co-deposited on three different back reflectors to study the influence of the substrate texture on the device efficiency. The three substrates are a standard Hot Ag sputtered at 300 °C and two rougher substrates labeled Z2 and Z5. The Z2 is a 2- μ m-thick LP-CVD ZnO:B treated for 7 minutes by an Ar plasma and the Z5 is a 5- μ m-thick LP-CVD ZnO:B treated for 50 minutes by an Ar plasma. Both LP-CVD ZnO textures were covered with silver (200 nm) and ZnO:Al (60 nm), and the Hot Ag substrate was also covered with 60 nm of ZnO:Al. Generally, Z2 substrates are used for a-Si:H single-junction solar cells while the Hot Ag and Z5 substrates are used for single-junction μ c-Si:H solar cells. All these textures can be reproduced on plastic substrate with the replication process described in chapter 3 which is also compatible with the use of an ITO front contact. In this section, thin a-Si:H/ μ c-Si:H devices were co-deposited on these three substrates with total silicon thicknesses of 900 nm and 300 nm for the μ c-Si:H and a-Si:H cells, respectively, and the ITO front contact had a thickness of 65 nm.

Table 7.8: *Initial electrical parameters of thin a-Si:H/ μ c-Si:H cells co-deposited on various substrates. The limiting J_{sc} is marked in bold.*

Substrate	V_{oc} (V)	FF (%)	J_{sc} [top/bottom] (mA/cm ²)	Efficiency (%)
Hot Ag	1.46	77	11/ 9.2	10.3
Z2	1.38	65	11.3/ 11	9.9
Z5	1.39	64	11.1 /11.4	9.9

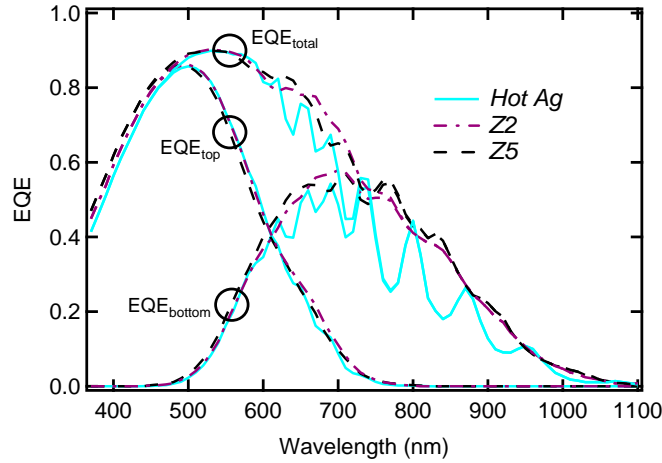


Figure 7.15: *EQE spectra of thin a-Si:H/ μ c-Si:H cells co-deposited on various substrates.*

Figure 7.15 and table 7.8 show the initial EQE spectra and electrical parameters, respectively, of the co-deposited a-Si:H/ μ c-Si:H devices. It is observed that the light trapping provided by the Z2 and Z5 substrates is much higher than that provided by the Hot Ag. On the other hand, the V_{oc} and FF are much lower for the devices grown on the two rougher substrates and the highest efficiency is obtained on the Hot Ag substrate. The lower V_{oc} values on the Z2 and Z5 rough substrates can certainly be correlated with the V_{oc} losses that were observed on

7.5. Thin micromorph a-Si:H/ μ c-Si:H solar cells with fabrication processes compatible with plastic substrates

rough substrates both in single-junction a-Si:H (section 7.2) and μ c-Si:H (section 7.3) solar cells. Indeed, the Hot Ag substrate allows the growth of high-quality μ c-Si:H as demonstrated in section 7.3 and, as schematically shown in figure 7.14, the morphology obtained after the growth of the μ c-Si:H layer is more amenable to the growth of the a-Si:H top cell than for the rough substrates. The FF analysis is not as straightforward as the V_{oc} analysis because the J_{sc} dematching artificially increases the FF of the device grown on the Hot Ag substrate. Still, the low initial FF values on the Z2 and Z5 substrates, which are certainly attributable to shunted cells, suggest that these substrates are not highly promising for the growth of a-Si:H/ μ c-Si:H devices with high efficiencies. This is different if an asymmetric reflector is used between the sub-cells as discussed by Biron et al. [Biron 13]. In this case the reflector can be used to create the desired smooth features needed for a top cell with high performance even if the substrate on which the bottom cell is grown is much rougher. In this thesis, to fulfill the requirement of a process compatible with plastic substrates, the use of an asymmetric reflector, which is generally made of brittle LP-CVD ZnO, was avoided.

7.5.2 Optimised cell on a glass substrate with a process fully compatible with plastic substrates: 11.7% initial efficiency, 10.4% after degradation

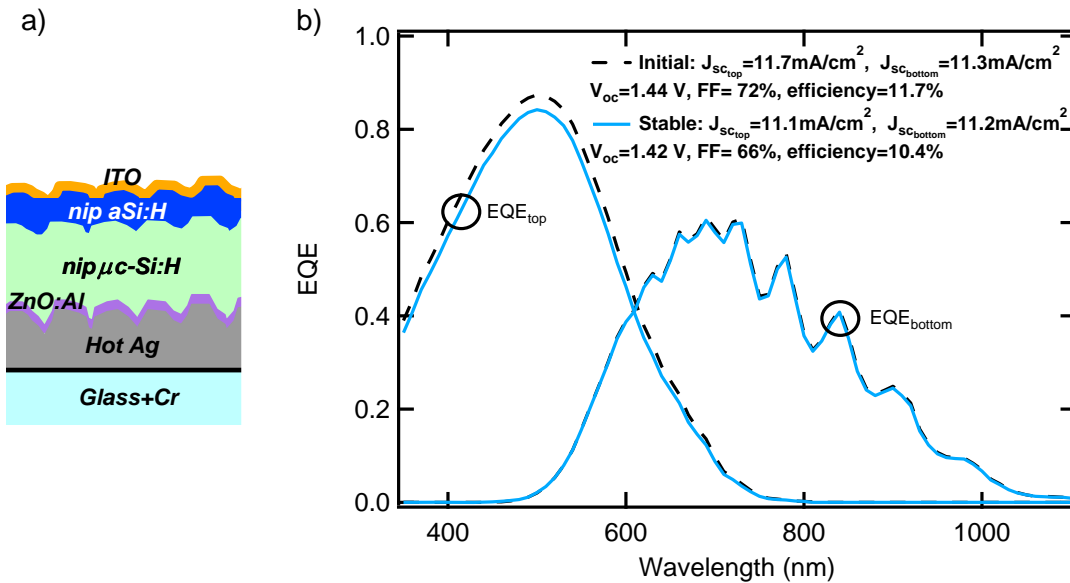


Figure 7.16: a) Schematic of the thin a-Si:H/ μ c-Si:H device fabricated with a process compatible with plastic substrates and b) its EQE spectra and electrical parameters in the initial and degraded states.

Figure 7.16 presents the cell design and electrical parameters of the thin a-Si:H/ μ c-Si:H device that exhibits the highest efficiencies in the initial and in stabilised states achieved during this thesis. It shows that a stable efficiency above 10% can be obtained using a process that is fully compatible with plastic substrates.

The efficiency was increased with respect to that given in section 7.5.1 using the following modifications:

1. The thickness of the $\mu\text{c-Si:H}$ bottom cell was increased to $1\ \mu\text{m}$ to increase the bottom-cell J_{sc} .
2. The ITO thickness was slightly increased to 70 nm. This also increased the bottom-cell J_{sc} by slightly shifting the minimum of reflection in the red.
3. To obtain higher top-cell J_{sc} for good current matching after degradation, the top-cell *i*-layer thickness was increased slightly by 10–15 nm, and the top-cell *p*-doped layer thickness was reduced by 15% to increase its transparency. This was necessary because the thicker bottom cell and the thicker ITO decrease the J_{sc} of the top cell. The thinner *p*-layer may be responsible for the lower initial V_{oc} value obtained here compared to that in table 7.8 on the Hot Ag substrate. Nevertheless, in this multi-junction device it is mostly a higher current that was required to reach higher efficiencies.

The potential improvements that can still be made to this cell are similar as those discussed for both single-junction a-Si:H and $\mu\text{c-Si:H}$ devices. The main challenge is to decrease the sensitivity of the V_{oc} and FF to the roughness of the substrate. If this were possible, it would allow for the use of rougher substrates such as Z2 and Z5 that were shown in section 7.5.1. Because of the better light trapping provided by such substrates, this would lead to a drastic reduction of the process time of the $\mu\text{c-Si:H}$ sub-cell because a thinner cell could be used. As seen in section 7.4, the negative impact of the ITO front contact on the V_{oc} value must still be solved. Nevertheless, the goal of achieving more than 10% efficiency with a thin a-Si:H/ $\mu\text{c-Si:H}$ device with a fabrication process that is fully compatible with flexible substrates has been achieved.

7.6 Triple-junction a-Si:H/ $\mu\text{c-Si:H}$ / $\mu\text{c-Si:H}$ solar cells

The solar cells presented in this section were deposited in the small-area system E (a-Si:H top cell) and in the large-area KAI-M reactor ($\mu\text{c-Si:H}$ bottom and middle cells). Details on a-Si:H single-junction cells can be found in sections 2.2.2 and 7.2 and details on $\mu\text{c-Si:H}$ single-junction cells can be found in sections 2.2.2 and 7.3. Also, details on the EQE measurements can be found in section 2.4.2.

The aim of this section was to fully utilise the potential of the substrates which were developed in chapter 6. Hence, it was chosen to work with triple-junction a-Si:H/ $\mu\text{c-Si:H}$ / $\mu\text{c-Si:H}$ cells to reduce the influence of parasitic absorption due to the dummy a-Si:H layer in the back reflector as explained in chapter 6. Also, in production, triple-junction solar cells are not the choice of manufacturers because the process time for the $\mu\text{c-Si:H}$ layers is too long. But, if a smooth substrate is used, it should be possible to use a fast deposition rate for the $\mu\text{c-Si:H}$ layers without significantly decreasing the electrical parameters of the cell [Bugnon 12]. Hence, these substrates bring novel opportunities for industrial application if the substrate

itself can be fabricated at low cost and with fast processes.

In section 7.6.1, it is demonstrated that the polished substrates developed in chapter 6 are a large improvement compared to other typical substrates like the standard Hot Ag. Then, an optimised cell with high a stable efficiency of 12.5% is shown in section 7.6.2, a result which cannot be achieved at the moment with other standard substrates with state-of-the-art deposition conditions. As well, section 7.6.2 presents the highest stable efficiency obtained for a thin-film silicon solar cell in our laboratory. By adding an anti-reflective coating made by UV nano-imprinting at the front of the device, as explained in section 3.6, a record stable efficiency of 13% was achieved.

In the following sections, the solar cells are made of a 3.5- μ m-thick bottom μ c-Si:H cell which has a μ c-Si:H *n*-doped layer that does not contain oxygen to ensure sufficient lateral conductivity (see chapter 6 for more details) and a standard *p*-doped layer that is alloyed with oxygen to increase its transparency. The μ c-Si:H middle cell has a total silicon thickness of 1.86 μ m and contains standard SiO_x doped layers. The a-Si:H top cell is approximately 270 nm thick and the front contact is a 2.5- μ m-thick LP-CVD ZnO:B layer.

7.6.1 Study of various back reflectors

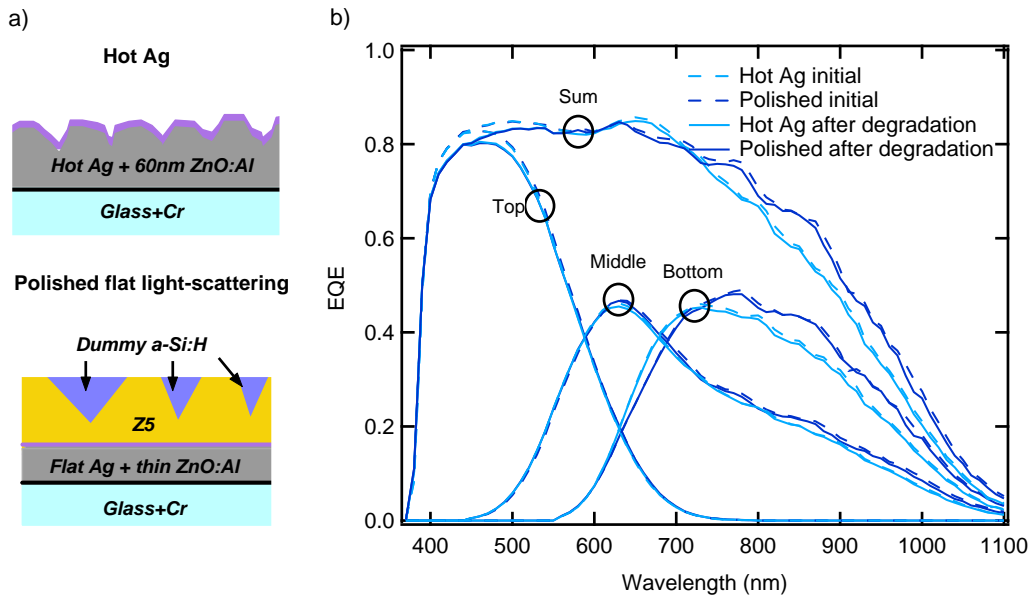


Figure 7.17: a) Schematics of the Hot Ag and polished substrates, and b) comparison of EQE spectra of triple-junction a-Si:H/ μ c-Si:H/ μ c-Si:H solar cells co-deposited on them.

Figure 7.17 presents schematics of the Hot Ag and light-scattering substrates, as well as the EQE spectra of co-deposited triple-junction a-Si:H/ μ c-Si:H/ μ c-Si:H solar cells grown on them.

Table 7.9: *Electrical parameters of triple-junction a-Si:H/ μ c-Si:H/ μ c-Si:H solar cells co-deposited on Hot Ag and polished light-scattering substrates. Degraded values are marked in bold.*

Substrate	V_{oc} (V)	FF (%)	J_{sc} [top/middle/bottom] (mA/cm ²)	Efficiency (%)
Hot silver	1.89	71	9.3/8.7/9	11.7
after degradation	1.84	67	9.1/8.7/8.8	10.7
Polished substrate	1.88	75	9.4/9.1/9.5	12.8
after degradation	1.85	70	9.2/8.9/9.4	11.5

The corresponding electrical parameters are reported in table 7.9, which reveals the gains that are obtained by using the newly developed polished, flat light-scattering substrate.

The polished substrate clearly outperforms the Hot Ag substrate in terms of light management for wavelengths > 700 nm. The efficient light scattering provided by this substrate was also corroborated by an additional experiment in which polished substrates grown on either a flat silver or a rough silver layer were compared. No significant EQE differences (below 1% variation of $J_{sc\ bottom} + J_{sc\ middle}$) were observed (not shown), suggesting that the first "dummy" a-Si:H/ZnO back scattering interface is sufficiently rough that the cell does not benefit from an additional underlying rough Ag layer. This is similar to the observation made by comparing cells grown on substrates *A* and *C* in section 7.3.1.

As demonstrated in single-junction cells (V_{oc} and FF shown in table 7.5), the reference Hot Ag substrate allows the growth of high-quality μ c-Si:H with few structural defects. Similarly, the comparable electrical performances of the triple-junction cells grown on the Hot Ag and polished substrates (table 7.9) show that the latter substrate provides an equivalently good surface for the growth of μ c-Si:H material. As table 7.9 shows, the V_{oc} of the solar cells grown on both substrates is similar, and a slight gain in FF is obtained for the cell grown on the polished substrate. As the difference in current mismatch between both substrates is minor, the higher FF obtained for the cell grown on the polished substrate proves that the material quality is similar, or even slightly better, than that of the material grown on the Hot Ag substrate.

The J_{sc} increase as well as the gains in V_{oc} and FF hence demonstrate that the polished substrate combines efficient light management and an interface suitable for the growth of high-quality silicon layers. This is further supported by the higher initial and post-degradation efficiencies obtained on the polished substrate compared to the reference Hot Ag substrate. Thus the next section presents optimised triple-junctions solar cells made on flat light-scattering substrates.

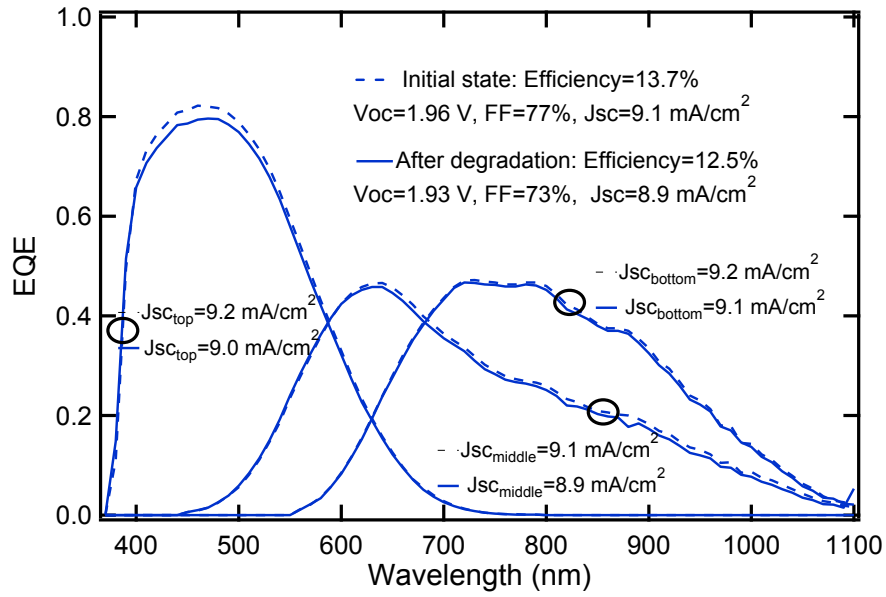


Figure 7.18: EQE and electrical parameters of a triple-junction a-Si:H/ μ c-Si:H/ μ c-Si:H solar cell in the initial state and after degradation.

7.6.2 Optimised cell on flat light-scattering substrate with a 13.0% stable efficiency

Figure 7.18 and table 7.10 presents the EQE and electrical parameters of an optimised triple-junction a-Si:H/ μ c-Si:H/ μ c-Si:H solar cell grown on a polished substrate. This cell differs from the one shown in figure 7.17 in that the top cell, especially its p -layer, was optimised. The doping in the p -layer was increased and as a result, both the V_{oc} and FF improved while a slight loss in J_{sc} can be observed. The substrate was also slightly different as the dummy a-Si:H layer was grown on a Z2.5 compared to a Z5 for the cells shown in section 7.6.1. This cell thus reached an efficiency among the highest reported both in the initial state (13.7%) and after degradation (12.5%) for n - i - p thin-film Si cells without germanium content. The efficiency after degradation is similar to the certified record reported by United Solar for a cell in the n - i - p configuration with ITO as the front contact [Yan 10, Green 12].

Table 7.10: Characteristics of n - i - p triple-junction a-Si:H/ μ c-Si:H/ μ c-Si:H solar cells optimised on the polished substrate. Stable values are marked in bold.

V_{oc} (V)	FF (%)	J_{sc} [top/middle/bottom] (mA/cm ²)	Efficiency (%)
1.96	77	9.2/9.1/9.2	13.7
1.93	73	9.0/8.9/9.1	12.5

Finally, further improvement to this cell was obtained by adding in a post-process step an anti-reflection coating made by UV nano-imprinting as shown in section 3.6. It was not applied on the cell shown in figure 7.18 because this cell had an area smaller than 0.5 cm², and to apply

the anti-reflection coating, a cell with a larger area was preferred. Figure 7.19 presents the EQE and the electrical parameters of a cell for which the anti-reflective coating was added. It exhibits a stable efficiency of 13% which is the highest reported for a thin-film silicon solar cell in our laboratory and is very close to the new stable record efficiency of 13.4% using *p-i-n* triple-junction solar cells presented at the 27th European PV Solar Energy Conference held in Frankfurt in 2012 by LG Solar).

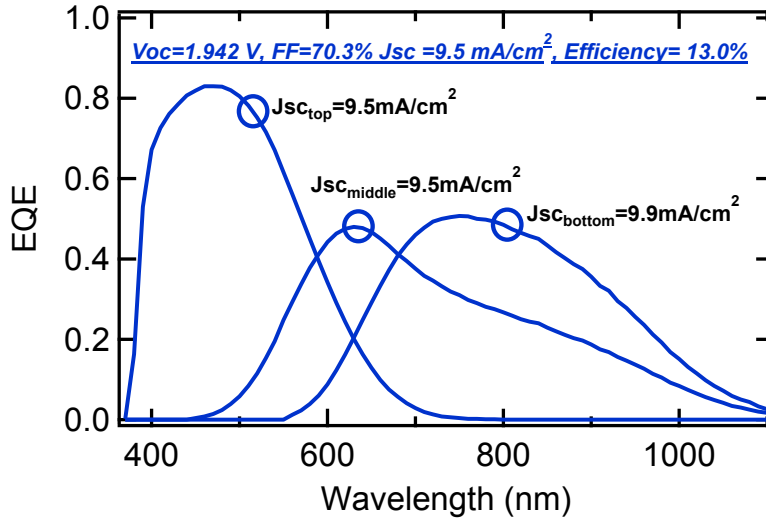


Figure 7.19: EQE spectrum and electrical parameters of a triple-junction *a-Si:H/μc-Si:H/μc-Si:H* solar cell on a flat light-scattering substrate with a UV nano-imprinted anti-reflective coating exhibiting a stable efficiency of 13%.

In this section, thick $\mu\text{c-Si:H}$ layers were used as a proof-of-concept to reach high efficiencies. Future developments should aim at decreasing the layer thicknesses (e.g. by increasing the crystallinity) and decreasing the process time (e.g. by increasing growth rates) for the absorber layers. This is realistic on the flat polished substrates because, when grown on smooth substrates the formation of defective porous areas in the $\mu\text{c-Si:H}$ layer are significantly reduced. This, in turn, avoids losses in FF and V_{oc} which are often observed for high crystallinity or high growth rate [Bugnon 12]. Other routes for process time and layer thickness reduction could be the incorporation of an *a-SiGe:H* middle cell [Yan 10, Yan 11]. Finally, reflection and absorption losses due to the front contact can still be improved, either by reducing the doping in the LP-CVD ZnO:B used in this contribution or by using an ITO or $\text{In}_2\text{O}_3\text{:H}$ front contact coupled with double anti-reflection layers. In both cases, the deposition of a small contact metal grid may become necessary in order to guarantee sufficient conduction of the front contact.

7.7 Conclusions

Various substrates for different solar cell devices were investigated in this chapter. Optimised cells were grown on the most promising back reflectors for each type of device.

For both a-Si:H and μ c-Si:H single-junction solar cells it was found that the growth on rough substrates leads to a large decrease of the V_{oc} and FF values which cannot be compensated by a J_{sc} increase to obtain high efficiencies with our state-of-the-art deposition conditions. Hence, the cells were optimised for smooth substrates and a stable efficiency of 8.1% was obtained for single-junction a-Si:H solar cells and 10.1% for single-junction μ c-Si:H solar cells. These two cells were the basis on which multi-junction devices were subsequently built.

For application on plastic substrates, a-Si:H/a-Si:H devices and thin a-Si:H/ μ c-Si:H devices were investigated using an ITO front contact. An a-Si:H/a-Si:H device with an initial and stable efficiency of 11.1% and 9.2% respectively was obtained on a plastic substrate using a nano-imprinted PEN substrate. The thin a-Si:H/ μ c-Si:H device was not realised on a plastic substrate but was made with processes compatible with such a substrate, and an initial and stable efficiency of 11.7% and 10.4% respectively, were obtained. These high efficiencies show that optimised processes can lead to cells with efficiencies which, in principle, should allow for their industrialisation on plastic foils.

Finally, the full potential of the substrates developed in chapter 6 were used in triple-junction a-Si:H/ μ c-Si:H/ μ c-Si:H solar cells. It was shown that the standard substrate may not allow for the growth of triple-junction solar cells of as high quality as the polished substrate and a 13% stable efficiency was demonstrated on a polished flat light-scattering substrate. This result is among the highest efficiencies demonstrated in thin-film silicon devices and the highest reported so far by our laboratory. The study of this type of substrate is only at its beginning and, because the contradicting requirements of an optically rough substrate for light scattering and a flat surface for the growth of high-quality silicon layers are fulfilled in a single substrate, it is a very promising template to push further the efficiencies of thin-film silicon solar cells.

8 Conclusions and perspectives

The general conclusions and achievements of this thesis are first drawn in section 8.1. Section 8.2 presents the general perspectives that aim at opening roads for further improvements.

8.1 General conclusions

8.1.1 Applications of the nano-imprint lithography technique

During this thesis, the development of a process for obtaining high-fidelity replicas using a UV nano-imprinting technique was continued in collaboration with Dr. J. Escarré. Although the development of UV nano-imprinting at IMT has been underway since 2002, it gained visibility through the work performed during this thesis. The impact of this work on the thin-film silicon field will be further discussed in section 8.2.1.

Details of the process were given in section 2.1 to allow for its reproduction by newcomers to this field. Chapter 3 presented the manifold applications in devices for which the nano-imprint process brought efficiency improvements.

It was first demonstrated in section 3.3 that nano-imprinting allows for the texturing of plastic substrates for use in flexible *n-i-p* solar cells, which was previously not feasible. Consequently, devices with efficiencies comparable to those of state-of-the-art cells on glass substrates can be obtained. Combined with other developments, the texturing of a plastic substrate by nano-imprinting led to the growth of a flexible tandem a-Si:H/a-Si:H device that exhibited a high stable efficiency of 9.2% using less than half a micron of silicon as discussed in section 7.4.2 and in Söderström et al. [Söderström 12b].

It was shown in section 3.4 that the transparency of the imprinted replicas allows for the texturing of In₂O₃:H front electrodes for *p-i-n* solar cells on glass substrates using photonic textures that were not accessible prior to the use of the nano-imprinting technique. The replication of large micro-metric features facilitated the development of a multi-scale electrode with low parasitic absorption that helped to obtain a micromorph a-Si:H/ μ c-Si:H *p-i-n* device with an initial efficiency above 14% as discussed in Boccard et al. [Boccard 12b].

Section 3.5 showed, as a third application of UV NIL, that the surface of LP-CVD ZnO can be selectively shape by using a process similar to the one used to replicate textures in the UV-sensitive resin. With this technique, the texture of the LP-CVD ZnO surface is no longer restricted to pyramidal shapes and its electrical properties can be tuned independently of the desired surface texture.

Finally, section 3.6 presented further improvements provided by nano-imprint replicas of micro-metric features at the front of $p-i-n$ and $n-i-p$ solar cells, which provided an anti-reflection effect that significantly boosted the J_{sc} by more than 4% and the efficiency of the device.

8.1.2 Experimental evidence of light trapping by guided mode excitation

In chapter 4, new insights were gained on the mechanism responsible for the enhancement of photocurrent by textured interfaces in thin-film silicon solar cells. It was shown experimentally from EQE measurements that the mechanism is related to guided mode excitation. First, the simulation of a flat device was used to find the dispersion curves of the guided modes that are supported in the silicon layers of a single-junction a-Si:H solar cell. Second, an experimental template was realised by replicating a one-dimensional periodic grating structure by nano-imprinting. The one-dimensional periodic texture allows the experimental resolution of polarisation effects and simplifies the problem because the texture couples with only a single spatial frequency. Third, by performing angular-resolved EQE measurements of an a-Si:H cell grown on the one-dimensional periodic texture, the angular variation of peaks in the EQE was related to the calculated dispersion curves of the guided modes. This provided a very intuitive explanation for the light coupling mechanism via surface texturing and new insights into the features required of the texture to obtain efficient light trapping.

8.1.3 Investigation of textured back reflector materials in a-Si:H solar cells

Chapter 5 investigated standard $n-i-p$ back reflectors made of a textured metallic layer which is generally covered, prior to cell deposition, by a thin dielectric layer of low refractive index. It was shown in section 5.2 that the thickness of a ZnO:Al dielectric buffer layer should be optimised to minimise parasitic absorption losses in the metal layer as well as in the n -doped layer which is grown on top of the buffer layer. It was then shown in section 5.3 that an aluminium reflector cannot perform as well as silver even after optimising the ZnO:Al buffer layer. However, it was shown in section 5.4 that the efficiency of a silver reflector can be strongly hampered by parasitic absorption when grown on a rough nano-textured substrate. A low temperature thermal annealing compatible with plastic substrate was shown to increase the reflectance of the silver reflector, and an absolute efficiency gain of up to 1% was observed in devices. Finally, section 5.5 discussed the advantages and drawbacks of a textured metal back reflector. By comparing solar cells grown on the same scattering texture made of either a dielectric material or a high-quality silver layer, it was observed that the metallic rough reflector induces stronger parasitic losses. We concluded that an optimised texture should

probably be integrated into a cell using a rough dielectric material combined with a flat metallic reflector to reduce parasitic losses in the metal.

8.1.4 Study of innovative flat light-scattering substrates

Because efficient light management requires textured interfaces which generally hamper the deposition of high-quality silicon, it was proposed to separate the optically rough interface from the surface on which the cell is grown. Such a substrate was described and realised in chapter 6. It consisted of a flat silver reflector onto which an LP-CVD ZnO layer was grown with its self-developing pyramidal texture which efficiently scatters light. This stack was then covered with an a-Si:H layer to create an optically rough LP-CVD ZnO/a-Si:H interface. Finally, the substrate was completed by creating a morphologically flat surface for the subsequent cell growth with a mechanical polishing step. Note that the use of a flat silver reflector helps to minimise plasmonic parasitic absorption in the metallic layer. Devices grown on this type of substrate showed that remarkable light trapping can be obtained, while the flat growth surface allows for the growth of high-quality silicon. A V_{oc} of 520 mV was achieved for a thick *p-i-n* μ c-Si:H solar cell with an *i*-layer thickness of 3.8 μ m, and a relative efficiency increase of 10% was demonstrated compared to an optimised cell on a textured substrate.

8.1.5 High-efficiency devices

Chapter 7 presented the best devices that were obtained by benefiting from the new insights gained during this thesis. The types of devices that were studied can be separated into two categories. The first uses plastic substrates with rough metallic reflectors that can be transferred using nano-imprinting, keeping the active layers as thin as possible and using a flexible ITO front contact. The second uses glass substrates with the aim of reaching efficiencies as high as possible without limitations on the layer thicknesses.

Devices on plastic substrates

By combining the nano-imprint process with an annealed silver reflector, a flexible a-Si:H/a-Si:H device with initial and stable efficiencies of 11.1% and 9.2%, respectively was achieved, and this result was shown in section 7.4.2. This stable efficiency is, to the knowledge of the author, the highest reported yet for a device based purely on a-Si:H material on a plastic substrate. To further increase the potential efficiency that can be obtained on plastic foil, thin micromorph solar cells grown on glass with processes fully compatible with plastic substrates were studied in section 7.5. An initial efficiency of 11.7% and a stable efficiency of 10.4% were obtained for this type of device. Stable efficiencies of 9.2% and 10.4% are not as high as what can be obtained on glass substrates, but these are remarkably high if obtained for plastic foils. Hence, it is hoped that these results will draw the attention of companies and investors, and that process development of thin-film silicon flexible modules on plastic substrates (such

as was underway at VHF Technology) will be continued because these substrates present advantages over their rigid counterparts.

Record efficiency of 13% on a glass substrate

The studies of different back reflectors in both a-Si:H (section 7.2) and $\mu\text{c-Si:H}$ (section 7.3) single-junction solar cells showed that our state-of-the-art *n-i-p* solar cells require a substrate with a smooth texture to maintain high V_{oc} and FF . Hence, large compromises have to be made on the photonic texture used for light management except if flat light-scattering substrates are used. Section 7.6.2 presented a triple-junction a-Si:H/ $\mu\text{c-Si:H}$ / $\mu\text{c-Si:H}$ *n-i-p* solar cell with a record stable efficiency of 13%. This was made possible by integrating the best knowledge on solar cells and materials available in the laboratory with the innovative flat light-scattering substrate described in chapter 6 and section 8.1.4 and an anti-reflection coating made by nano-imprinting. This result is the best stable efficiency reported so far by our laboratory for thin-film silicon solar cells and is very close to the world record of 13.4% reported in 2012 by the company LG Solar using a device in the *p-i-n* configuration.

8.2 Perspectives

8.2.1 Application of UV nano-imprinting

The replication of textures by UV nano-imprinting is extremely promising to push further solar cell efficiencies by allowing the integration of novel photonic textures for improved light management both at a laboratory scale and in an industrial environment. As shown in this thesis, the technique has applications in a wide range of devices and even at different positions in the device (i.e. back-electrode texturing for *n-i-p* devices on glass and on plastic substrates, and front-electrode texturing for *p-i-n* devices on glass substrates as well as on the front side of *n-i-p* and *p-i-n* devices for an anti-reflection effect). The process can reliably reproduce features with extremely high fidelity at the nano-scale for texturing plastic and glass substrates. The results that were presented in this manuscript have received much interest from other groups and companies. In 2009, the contribution submitted to the Journal Progress in Photovoltaics: Research and Applications [Söderström 11a] was the first study to present high-efficiency solar cells with good yield on textured substrates made by UV nano-imprinting, although several other groups like the Photovoltaics Forschungszentrum of Jülich [Gilles 09] and the company Phillips [Ferry 09] were developing this technique for solar cell applications in parallel. The remarkable results that were then achieved by texturing the front electrodes of *p-i-n* devices [Battaglia 11a, Battaglia 11c, Boccard 12b] have attracted further interest as most of the manufacturers of thin-film silicon modules are depositing in the *p-i-n* configuration. Our work on *p-i-n* devices was one motivation for the development of UV nano-imprinting on large areas which is currently underway in the European FP7 project Fast Track. The remarkable UV nano-imprinting studies that were presented by industry

these last two years should also be mentioned as they show companies' large interest in this topic. Samsung demonstrated in 2011 a micromorph a-Si:H/ μ c-Si:H *p-i-n* solar cell with an initial efficiency of 12.8% [Bessonov 11]. In addition, in 2011, the company VHF Technology demonstrated a flexible tandem a-Si:H/a-Si:H *n-i-p* solar cell with a stable efficiency of 8% on a plastic substrate [Couty 11]. Finally, in 2012 the company Moser Bauer showed that large-scale nano-imprinting of Gen5 size (1.1·1.3 m²) was possible [van Erven 12].

Nano-imprinting of a wide range of textures can be performed, and the replication of high-aspect-ratio textures was already demonstrated [Zhang 10, Kang 11]. This is promising for the production of textures on large areas at low cost, and even extreme textures such as nanopillars that decouple the optical path—which should be elongated as much as possible—from the electrical path—which should be reduced as much as possible—could be realised.

However, at present, the use of novel photonic textures is restricted in thin-film silicon solar cells because of the poor quality of the silicon that is deposited on aggressive textures. Therefore, a major research topic is the deposition of high-quality silicon layers on highly textured substrates. To this end, studies on plasma physics are needed, the major sources of V_{oc} and FF limitation should be identified (e.g. material quality of bulk and interface layers) and, finally, the cell architecture should be made more complex by developing new alloyed materials and buffer layers.

8.2.2 Minimising absorption losses in textured back reflectors

Absorption losses in all optically inactive layers should of course be minimised, but this thesis has shown that, in particular, metallic back reflectors can induce highly detrimental optical losses. This will become an even more serious issue if devices with high V_{oc} and FF can be grown on high-aspect-ratio textures, as the deposition of silver layers on aggressive textures was seen to lead to defective layers that exhibit poor reflectance. Therefore, the deposition of metallic layers with high reflectance should be further studied on all kinds of textured substrates. However, it was also observed that, even for metallic layers of high quality, a rough metal surface is intrinsically bound to induce the excitation of surface plasmon polaritons which in turn dissipate a part of light by parasitic absorption. Therefore, we recommend developing back reflectors made of a highly reflective and flat metallic layer on top of which is deposited a textured dielectric layer with a thickness in the range of a few hundred of nanometers to a few micrometers. This is also compatible with plastic textured by UV nano-imprinting of an insulating resin: Lift-off processes can be used to create holes in the resin to contact the cell on top of the resin to the flat Ag/ZnO:Al reflector below the resin. In this case, a thin TCO layer should be inserted between the resin and the cell to provide lateral electric transport in between the resin openenings to maintain good back-contact electrical properties.

Finally, sections 5.2 and 5.3 showed that the dielectric buffer layer which lies between the metallic reflector and the silicon layers can play a major role in the limitation of parasitic absorption in the metal and *n*-doped layers. Investigating of dielectric materials with different

indices of refraction can help to further decrease the optical losses in these layers.

8.2.3 On the road to the philosopher's stone texture for light management

Exact simulations of the Maxwell's equations can, in principle, be used to find the most adequate texture for light management in each type of device. However, the required simulation time to examine all types of textures prevents their use. Hence, the use of simplified analytical models are preferred at first, even if these may not rigorously provide the correct answer. They could, however, provide the basic features of the ideal texture and thereby reduce the space of parameters that should be used as input for exact simulation.

The work presented in chapter 4 has shown that light trapping is promoted by the excitation of guided modes supported by the silicon layers. It therefore provides a road for finding the most adequate texture for light trapping using analytical simulation, as: 1) for each device configuration the dispersion curves of guided modes can be found; and 2) a given texture contains a range of spatial frequencies that provide possible wave vectors that the incoming light can pick up. The combination of 1) and 2) identifies the number of possible resonances which should be maximised.

This still does not provide the optimised texture as the scattering efficiency of each wave vector and the coupling strength to each possible resonance should be added to the model as well. It seems probable that the efficiency of scattering provided by each spatial frequency is proportional to the intensity of the spatial frequency in the texture power spectral density. Also, it was recently shown that the coupling efficiency could be found for periodic structures using an analytical model based on a Rayleigh expansion [Haug 12b]. Hence, a model which uses the power spectral density as a variable and decomposes the problem into a sum of periodic features with coupling efficiencies to the guided modes that are predicted by the analytical model shown in Haug et al. [Haug 12b] should provide a fast, yet reasonably accurate procedure for assessing light trapping.

8.2.4 Improvement of flat light-scattering substrates

Flat light-scattering substrates were shown to lead to the growth of solar cells with very high efficiencies likely because the flat growth surface promotes the growth of silicon of very high quality. Hence, to improve these back reflectors, one should focus on increasing their light-management properties. One of the weak points of this design is that part of the top surface is made of flat ZnO. Thus, after cell deposition this area has a flat ZnO/ μ c-Si:H interface which specularly reflects a large amount of light. This could be overcome by keeping the tips of the LP-CVD ZnO pyramids by selectively etching the dummy a-Si:H layer only to open contacts. This would create a substrate with U-shaped valleys, that were seen to be less detrimental for cell growth than V-shaped valleys. Nevertheless, the growth of the bottom cell will induce pinching and transform the original U shapes into V shapes. Hence, the surface for the middle cell growth would contain V shapes and the benefit of these substrates would be lost. Therefore,

the areas with flat ZnO/ $\mu\text{c-Si:H}$ interfaces at the back should be accepted and minimised while keeping good electrical contact, as was done in this thesis by optimising the polishing step and the n -doped layer. Hence, the parameters that can still be adjusted are the feature size and shape of the optically rough interface as already discussed in section 6.5. This features can be optimised in part by the modification of the LP-CVD ZnO deposition conditions which provides a wide array of features such as those shown in figure 6.7, where tall features would provide electrical contact and smaller features that are more adapted to light scattering would remain buried under the a-Si:H dummy layer. Also, nano-imprinted resin could be used in combination with a thin TCO layer, giving access to an even wider range of textures.

8.2.5 Towards 15% stable efficiency and higher

From the current result of 13% stable efficiency ($V_{\text{oc}}=1.94$ V, $FF=70\%$ and $J_{\text{sc}}=9.5$ mA/cm²) that was obtained in this thesis in a triple-junction device, it appears that a similar type of device exhibiting 15% stable efficiency is within close range (e.g. $V_{\text{oc}}=2.03$ V, $FF=74\%$ and $J_{\text{sc}}=10$ mA/cm²). When grown on smooth Hot Ag substrates, the single-junction solar cells that were stacked up to obtained the stable efficiency of 13% had initial V_{oc} values of 950 mV, 550 mV and 530 mV, respectively, for the top, middle and bottom cells. If the initial V_{oc} values could be pushed to 1 V, 560 mV and 560 mV, the expected V_{oc} of a triple-junction device made by stacking them would reach a stable value of 2.03 V. The FF value could be improved by the use of a different front TCO, the addition of a metallic grid and a slight current mismatch between the cells. Finally, but perhaps most difficult, J_{sc} could be increased from 9.5 to 10 mA/cm² by optimising the front-contact transparency, minimising all parasitic absorption losses and designing a better scatterer for the back-, optically rough interface as discussed in section 8.2.4. This promising yet realistic stable efficiency should lift the spirits of those who continuously try to improve solar cells based on thin-film silicon processes. Going well over 15% will require moving beyond the traditional $p-i-n$ cell structure and understand better what are limiting the V_{oc} and FF of the standard devices. It was, for instance, recently shown that the introduction of buffer layers at the n/i and i/p interfaces resulted in very high V_{oc} values of 600 mV in single-junction $\mu\text{c-Si:H}$ solar cell [Hänni 13b] and this may be ascribable to the passivation of the interfaces in a similar fashion as a-Si:H layers are used in hetero-junction silicon devices.

Bibliography

- [Addonizio 08] M. L. Addonizio & C. Diletto. *Doping influence on intrinsic stress and carrier mobility of LP-MOCVD-deposited ZnO:B thin films*. Solar Energy Materials and Solar Cells, vol. 92, pages 1488–1494, 2008.
- [Ahn 08] S. H. Ahn & L. J. Guo. *High-speed roll-to-roll nanoimprint lithography on flexible plastic substrates*. Advanced materials, vol. 20, pages 2044–2049, 2008.
- [Arndt 75] R. A. Arndt, J. F. Allison, J. G. Haynes & A. Meulenburg. *Optical properties of the comsat non-reflective cell*. In 11th IEEE Photovoltaic Specialist Conference, New York, pages 40–43, 1975.
- [Atwater 10] H. A. Atwater & A. Polman. *Plasmonics for improved photovoltaic devices*. Nature Materials, vol. 9, pages 205–213, 2010.
- [Bailat 05] J. Bailat, V. Terrazzoni-Daudrix, J. Guillet, F. Freitas, X. Niquille, A. Shah, C. Ballif, T. Scharf, R. Morf, A. Hansen, D. Fischer, Y. Ziegler & A. Closset. *Recent development of solar cells on low-cost plastic substrates*. In Proceedings of the 20th European Photovoltaic Solar Energy Conference and Exhibition, Barcelona, 2005.
- [Bailat 06] J. Bailat, D. Dominé, R. Schlüchter, J. Steinhauser, S. Faÿ, F. Freitas, C. Bücher, L. Feitknecht, X. Niquille, T. Tschärner, A. Shah & C. Ballif. *High efficiency p-i-n microcrystalline and micromorph thin film solar cells deposited on LP-CVD ZnO coated glass substrates*. In Conference Record of the 2006 IEEE 4th World Conference on Photovoltaic Energy Conversion, pages 1533–1536, Hawaiï, 2006.
- [Ballif 09] C. Ballif, F.-J. Haug, S. Sweetnam & T. Söderström. *Patent: Solar Cells and its Production Process*, 2009.
- [Banerjee 91] A. Banerjee & S. Guha. *Study of back reflectors for amorphous silicon alloy solar cell application*. Journal of Applied Physics, vol. 69, pages 1030–1035, 1991.

Bibliography

- [Battaglia 11a] C. Battaglia, L. Erni, M. Boccard, L. Barraud, J. Escarré, K. Söderström, G. Bugnon, A. Billet, L. Ding, M. Despeisse, F.-J. Haug, S. De Wolf & C. Ballif. *Micromorph thin-film silicon solar cells with transparent high-mobility hydrogenated indium oxide front electrodes*. Journal of Applied Physics, vol. 109, page 114501, 2011.
- [Battaglia 11b] C. Battaglia, J. Escarré, K. Söderström, M. Charrière, M. Despeisse, F.-J. Haug & C. Ballif. *Nanomoulding of transparent zinc oxide electrodes for efficient light trapping in solar cells*. Nature: Photonics letters, vol. 5, pages 535–538, 2011.
- [Battaglia 11c] C. Battaglia, J. Escarré, K. Söderström, L. Erni, L. Ding, G. Bugnon, A. Billet, M. Boccard, L. Barraud, S. De Wolf, F.-J. Haug, M. Despeisse & C. Ballif. *Nanoimprint Lithography for High-Efficiency Thin-Film Silicon Solar Cells*. Nano Letters, vol. 11, pages 661–665, 2011.
- [Battaglia 12a] C. Battaglia, M. Boccard, F.-J. Haug & C. Ballif. *Light trapping in solar cells: When does a Lambertian scatterer scatter Lambertianly?* Journal of Applied Physics, vol. 112, pages 094504–6, 2012.
- [Battaglia 12b] C. Battaglia, C.-M. Hsu, K. Söderström, J. Escarré, F.-J. Haug, M. Charrière, M. Boccard, M. Despeisse, D. T. L. Alexander, M. Cantoni, Y. Cui & C. Ballif. *Light Trapping in Solar Cells: Can Periodic Beat Random?* ACS Nano, vol. 6, pages 2790–2797, 2012.
- [Battaglia 13] C. Battaglia, K. Söderström, J. Escarré, F.-J. Haug, M. Despeisse & C. Ballif. *Nanomoulding of Functional Materials, a Versatile Complementary Pattern Replication Method to Nanoimprinting*. Journal of Visual Experiments, vol. 71, page e50177, 2013.
- [Beck 09] F. J. Beck, A. Polman & K. R. Catchpole. *Tunable light trapping for solar cells using localized surface plasmons*. Journal of Applied Physics, vol. 105, page 114310, 2009.
- [Benett 63] H. E. Benett, M. Silver & E. J. Ashley. *Infrared Reflectance of Aluminum Evaporated in Ultra-High Vacuum*. Journal of Optical Society of America, vol. 53, pages 1089–1095, 1963.
- [Berginski 07] M. Berginski, J. Hüpkes, M. Schülte, G. Schöpe, H. Stiebig, B. Rech & M. Wuttig. *The effect of front ZnO:Al surface texture and optical transparency on efficient light trapping in silicon thin-film solar cells*. Journal of Applied Physics, vol. 101, page 074903, 2007.
- [Bernhard 67] C. G. Bernhard. *Structural and functional adaptation in a visual system*. Endeavour, vol. 26, pages 79–84, 1967.

- [Bessonov 11] A. Bessonov, Y. Cho, S.-J. Jung, E.-A. Park, E.-S. Hwang, J.-W. Lee, M. Shin & S. Lee. *Nanoimprint patterning for tunable light trapping in large-area silicon solar cells*. Solar Energy Materials and Solar Cells, vol. 95, pages 2886–2892, 2011.
- [Bhattacharya 11] J. Bhattacharya, N. Chakravarty, S. Pattnaik, W. D. Slafer, R. Biswas & V. L. Dalal. *A photonic-plasmonic structure for enhancing light absorption in thin film solar cells*. Applied Physics Letters, vol. 99, page 131114, 2011.
- [Biron 11] R. Biron, C. Pahud, F.-J. Haug, J. Escarré, K. Söderström & C. Ballif. *Window layer with p doped silicon oxide for high Voc thin-film silicon n-i-p solar cells*. Journal of Applied Physics, vol. 110, page 12451, 2011.
- [Biron 13] R. Biron, S. Hänni, M. Boccard, C. Pahud, G. Bugnon, L. Ding, S. Nicolay, G. Parascandolo, F. Meillaud, M. Despeisse, F.-J. Haug & C. Ballif. *Optimization of the ssymmetric intermediate reflector morphology for high stabilized efficiency thin n-i-p micromorph solar cells*. IEEE Journal of Photovoltaics, vol. 3, no. 1, pages 41–45, 2013.
- [Bittkau 07] K. Bittkau, R. Carius & C. Lienau. *Guided optical modes in randomly textured ZnO thin films imaged by near-field scanning optical microscopy*. Physical Review B, vol. 76, page 035330, 2007.
- [Bittkau 10] K. Bittkau & T. Beckers. *Near-field study of light scattering at rough interfaces of a-Si:H/ μ c-Si:H tandem solar cells*. Physica Status Solidi (a), vol. 207, pages 661–666, 2010.
- [Bittkau 11] K. Bittkau, M. Schulte, M. Klein, T. Beckers & R. Carius. *Modeling of light scattering properties from surface profile in thin-film solar cells by Fourier transform techniques*. Thin Solid Films, vol. 519, pages 6538–6543, 2011.
- [Bittkau 12] K. Bittkau, W. Bottler, M. Ermes, V. Smirnov & F. Finger. *Light scattering at textured back contacts for n-i-p thin-film silicon solar cells*. Journal of Applied Physics, vol. 111, pages 083101–5, 2012.
- [Boccard 10] M. Boccard, P. Cuony, C. Battaglia, M. Despeisse & C. Ballif. *Unlinking absorption and haze in thin film silicon solar cells front electrodes*. Physica Status Solidi, Rapid Research Letters, vol. 4, pages 326–328, 2010.
- [Boccard 11] M. Boccard, P. Cuony, M. Despeisse, D. Dominé, A. Feltrin, N. Wyrsh & C. Ballif. *Substrate dependent stability and interplay between optical and electrical properties in single junction solar cells*. Solar Energy Materials and Solar Cells, vol. 95, pages 195–198, 2011.
- [Boccard 12a] M. Boccard. *Novel Micromorph solar cell structures for efficient light trapping and high-quality absorber layers*. PhD thesis, Ecole Polytechnique Fédérale de Lausanne, 2012.

Bibliography

- [Boccard 12b] M. Boccard, C. Battaglia, S. Hänni, K. Söderström, J. Escarré, S. Nicolay, F. Meillaud, M. Despeisse & C. Ballif. *Multiscale transparent electrode architecture for efficient light management and carrier collection in solar cells*. Nano Letters, vol. 12, pages 1344–1348, 2012.
- [Boccard 12c] M. Boccard, C. Battaglia, F.-J. Haug, M. Despeisse & C. Ballif. *Light trapping in solar cells: Analytical modeling*. Applied Physics Letters, vol. 101, no. 15, page 151105, October 2012.
- [Boccard 12d] M. Boccard, P. Cuony, C. Battaglia, S. Hänni, S. Nicolay, L. Ding, M. Benkhaira, G. Bugnon, A. Billet, M. Charrière, K. Söderström, J. Escarré, F. Sculati-Meillaud, M. Despeisse & C. Ballif. *Nanometer- and micrometer-scale texturing for high-efficiency micromorph thin-film silicon solar cells*. IEEE Journal of Photovoltaics, vol. 2, pages 83–87, 2012.
- [Boccard 12e] M. Boccard, T. Söderström, P. Cuony, C. Battaglia, S. Hänni, S. Nicolay, L. Ding, M. Benkhaira, G. Bugnon, A. Billet, M. Charrière, F. Meillaud, M. Despeisse & C. Ballif. *Optimization of ZnO front electrodes for high-efficiency micromorph thin-film Si solar cells*. IEEE Journal of Photovoltaics, vol. 2, pages 229–235, 2012.
- [Branz 11] H. M. Branz, C. W. Teplin, M. J. Romero, I. T. Martin, Q. Wang, and D. L. Young K. Alberi & P. Stradins. *Hot-wire chemical vapor deposition of epitaxial film crystal silicon for photovoltaics*. Thin Solid Films, vol. 519, pages 4545–4550, 2011.
- [Breyer 13] C. Breyer & A. Gerlach. *Global overview on grid-parity*. Progress in Photovoltaics: Research and Applications, vol. 21, pages 121–136, 2013.
- [Bugnon 12] G. Bugnon, G. Parascandolo, T. Söderström, P. Cuony, M. Despeisse, S. Hänni, J. Holovsky, F. Meillaud & C. Ballif. *A new view of microcrystalline silicon: The role of plasma processing in achieving a dense and stable absorber material for photovoltaic applications*. Advanced Functional Materials, vol. 22, pages 3665–3671, 2012.
- [Burdick 86] J. Burdick & T. Glatfelter. *Spectral response and I-V measurement of tandem amorphous-silicon alloy solar cells*. Solar Cells, vol. 18, pages 301–314, 1986.
- [Campbell 87] P. Campbell & M. A. Green. *Light trapping properties of pyramidally textured surfaces*. Journal of Applied Physics, vol. 62, no. 1, pages 243–249, July 1987.
- [Carlson 76] D. E. Carlson & C. R. Wronski. *Amorphous silicon solar cell*. Applied Physics Letters, vol. 28, pages 671–673, 1976.
- [Catchpole 06] K. R. Catchpole & S. Pillai. *Surface plasmons for enhanced silicon light-emitting diodes and solar cells*. Journal of Luminescence, vol. 121, pages 315–318, 2006.

-
- [Cheek 79] G. Cheek, A. Genis, J. B. DuBow & V. R. Pai Verneker. *Antireflection properties of indium tin oxide (ITO) on silicon for photovoltaic applications*. Applied Physics Letters, vol. 35, pages 495–497, 1979.
- [Chen 12] X. Chen, B. Jia, J. K. Saha, B. Cai, N. Stokes, Q. Qiao, Y. Wang, Z. Shi & M. Gu. *Broadband Enhancement in thin-film amorphous silicon solar cells enabled by nucleated silver nanoparticles*. Nano Letters, vol. 12, pages 2187–2192, 2012.
- [Chevallier 77] J. Chevallier, H. Wieder, A. Onton & C.R. Guarnieri. *Optical properties of amorphous $\text{Si}_x\text{Ge}_{1-x}(\text{H})$ alloys prepared by R.F Glow discharge*. Solid State Communications, vol. 24, pages 867–869, 1977.
- [Chittick 69] R. C. Chittick, J. H. Alexander, & H. F. Sterling. *The Preparation and Properties of Amorphous Silicon*. Journal of The Electrochemical Society, vol. 116, pages 77–81, 1969.
- [Chittick 70] R. C. Chittick. *Properties of glow-discharge deposited amorphous germanium and silicon*. Journal of Non-Crystalline Solids, vol. 3, pages 255–270, 1970.
- [Chou 95] S. Y. Chou, P. R. Krauss & P. J. Renstrom. *Imprint of sub-25 nm vias and trenches in polymers*. Applied Physics Letters, vol. 67, pages 3114–3116, 1995.
- [Chutinan 09] A. Chutinan, N. P. Kherani & S. Zukotynski. *High-efficiency photonic crystal solar cell architecture*. Optics Express, vol. 17, pages 8871–8878, 2009.
- [Couty 11] P. Couty, M. Duchamp, K. Söderström, A. Kovács, R.E. Dunin-Borkowski, L. Sansonnens & Y. Ziegler. *Transmission electron microscopy of amorphous tandem thin-film silicon modules produced by a roll-to-roll process on plastic foil*. In Proceedings of the 26th European Photovoltaic Solar Energy Conference and Exhibition, 3CO.1.4, pages 2395-2398, Hamburg, 2011.
- [Cuony 10] P. Cuony, M. Marending, D. T. L. Alexander, M. Boccard, G. Bugnon, M. Despeisse & C. Ballif. *Mixed-phase p-type silicon oxide containing silicon nanocrystals and its role in thin-film silicon solar cells*. Applied Physics Letters, vol. 97, page 213502, 2010.
- [Cuony 11] P. Cuony. *Optical Layers for Thin-Film Silicon Solar Cells*. PhD thesis, Ecole Polytechnique Fédérale de Lausanne, 2011.
- [Dannenberg 00a] R. Dannenberg, E. Stach, J. R. Groza & B. J. Dresser. *TEM annealing study of normal grain growth in silver thin films*. Thin Solid Films, vol. 379, pages 133–138, 2000.

Bibliography

- [Dannenberg 00b] R. Dannenberg, E. A. Stach, J. R. Groza & B. J. Dresser. *In-situ TEM observations of abnormal grain growth, coarsening, and substrate de-wetting in nanocrystalline Ag thin films*. Thin Solid Films, vol. 370, pages 54–62, 2000.
- [Davies 54] H. Davies. *The reflection of electromagnetic waves from a rough surface*. In Proceedings of the Institute of Electrical Engineers, volume 101, page 209, 1954.
- [de Jong 12] M. M. de Jong, J. K. Rath, R. E. I. Schropp, P. J. Sonneveld, G. L. A. M. Swinkels, H. J. Holterman, J. Baggerman, C. J. M. van Rijn & E. A. G. Hamers. *A novel structured plastic substrate for light confinement in thin film silicon solar cells by a geometric optical effect*. Journal of Non-Crystalline Solids, vol. 358, pages 2308–2312, 2012.
- [Deckman 83] H. W. Deckman, C. R. Wronski, H. Witzke & E. Yablonovitch. *Optically enhanced amorphous silicon solar cells*. Applied Physics Letters, vol. 42, pages 968–970, 1983.
- [Delamarche 97] E. Delamarche, H. Schmid, B. Michel & H. Biebuyck. *Stability of molded polydimethylsiloxane microstructures*. Advanced Materials, vol. 9, pages 741–746, 1997.
- [Delli Veneri 10] P. Delli Veneri, L. V. Mercaldo & I. Usatii. *Silicon oxide based n-doped layer for improved performance of thin film silicon solar cells*. Applied Physics Letters, vol. 97, page 023512, 2010.
- [Demaurex 12] B. Demareux, S. De Wolf, A. Descoeudres, Z. C. Holman & C. Ballif. *Damage at hydrogenated amorphous/crystalline silicon interfaces by indium tin oxide overlayer sputtering*. Applied Physics Letters, vol. 101, page 171604, 2012.
- [Depauw 11] V. Depauw, Y. Qiu, K. Van Nieuwenhuysen, I. Gordon & J. Poortmans. *Epitaxy-free monocrystalline silicon thin film: First steps beyond proof-of-concept solar cells*. Progress in Photovoltaic: Research and Applications, vol. 19, pages 844–850, 2011.
- [Derkacs 06] D. Derkacs, S. H. Lim, P. Matheu, W. Mar & E. T. Yu. *Improved performance of amorphous silicon solar cells via scattering from surface plasmon polaritons in nearby metallic nanoparticles*. Applied Physics Letters, vol. 89, page 093103, 2006.
- [Despeisse 10] M. Despeisse, G. Bugnon, A. Feltrin, M. Stückerberger, P. Cuony, F. Meillaud, A. Billet & C. Ballif. *Resistive interlayer for improved performance of thin film silicon solar cells on highly textured substrate*. Applied Physics Letters, vol. 96, page 073507, 2010.
- [Dewald 11] W. Dewald, V. Sittering, B. Szyszka, D. Wippler, J. Hüpkes, P. Obermeyer, F. Hamelmann, H. Stiebig, F. Säuberlich, D. Severin, S. H. Klein, M. Rhode &

- U. Schmidt. *Evaluation of textured TCOs for a-Si:H/ μ c-Si:H thin film silicon solar cells by angular resolved light scattering measurements*. In Proceedings of the 26th European Photovoltaic Solar Energy Conference and Exhibition, 3AV.2.43, pages 2704–2708, Hamburg, 2011.
- [Dewan 11] R. Dewan, I. Vasilev, V. Jovanov & D. Knipp. *Optical enhancement and losses of pyramid textured thin-film silicon solar cells*. Journal of Applied Physics, vol. 110, page 013101, 2011.
- [Ding 12] L. Ding, M. Boccard, G. Bugnon, M. Benkhaira, S. Nicolay, M. Despeisse, F. Meillaud & C. Ballif. *Highly transparent ZnO bilayers by LP-MOCVD as front electrodes for thin-film micromorph silicon solar cells*. Solar Energy Materials and Solar Cells, vol. 98, pages 331–336, 2012.
- [Dominé 08] D. Dominé. *The role of front electrodes and intermediate reflectors in the optoelectronic properties of high-efficiency micromorph solar cells*. PhD thesis, University of Neuchâtel, 2008.
- [Dominé 10] D. Dominé, F.-J. Haug, C. Battaglia & C. Ballif. *Modeling of light scattering from micro- and nanotextured surfaces*. Journal of Applied Physics, vol. 107, page 044504, 2010.
- [Duché 08] D. Duché, L. Escoubas, J.-J. Simon, P. Torchio, W. Vervisch & F. Flory. *Slow Bloch modes for enhancing the absorption of light in thin films for photovoltaic cells*. Applied Physics Letters, vol. 92, page 193310, 2008.
- [Eisele 01] C. Eisele, C. E. Nebel & M. Stutzmann. *Periodic light coupler gratings in amorphous thin film solar cells*. Journal of Applied Physics, vol. 89, pages 7722–7726, 2001.
- [Eminian 11] C. Eminian, F.-J. Haug, O. Cubero, X. Niquille & C. Ballif. *Photocurrent enhancement in thin film amorphous silicon solar cells with silver nanoparticles*. Progress in Photovoltaics: Research and Applications, vol. 19, pages 260–265, 2011.
- [Escarré 05] J. Escarré, F. Villar, M. Fonrodona, D. Soler, J.M. Asensi, J. Bertomeu & J. Andreu. *Optical analysis of textured plastic substrates to be used in thin silicon solar cells*. Solar Energy Materials and Solar Cells, vol. 87, pages 333–341, 2005.
- [Escarré 11] J. Escarré, K. Söderström, C. Battaglia, F.-J. Haug & C. Ballif. *High fidelity transfer of nanometric random textures by UV embossing for thin film solar cells applications*. Solar Energy Materials and Solar Cells, vol. 95, pages 881–886, 2011.

Bibliography

- [Escarré 12a] J. Escarré, C. Battaglia, K. Söderström, C. Pahud, R. Biron, O. Cubéro, F.-J. Haug & C. Ballif. *UV imprinting for thin film solar cells applications*. Journal of Optics, vol. 14, page 024009, 2012.
- [Escarré 12b] J. Escarré, S. Nicolay, C. Battaglia, M. Boccard, L. Ding, M. Despeisse, F.-J. Haug & C. Ballif. *Nanomoulded front ZnO contacts for thin film solar cell applications*. In Proceedings of the 27th European Photovoltaic Solar Energy Conference and Exhibition, 3DV.2.19, pages 2632–2634, Frankfurt, 2012.
- [Escarré 12c] J. Escarré, K. Söderström, M. Despeisse, S. Nicolay, C. Battaglia, G. Bugnon, L. Ding, F. Meillaud, F.-J. Haug & C. Ballif. *Geometric light trapping for high efficiency thin film silicon solar cells*. Solar Energy Materials and Solar Cells, vol. 98, pages 185–190, 2012.
- [Fahr 11] S. Fahr, T. Kirchartz, C. Rockstuhl & F. Lederer. *Approaching the Lambertian limit in randomly textured thin-film solar cells*. Optics Express, vol. 19, pages A865–A874, 2011.
- [FAO 12] FAO. *The State of Food Insecurity in the World*. 2012.
- [Faÿ 05] S. Faÿ, U. Kroll, C. Bücher, E. Vallat-Sauvain & A. Shah. *Low pressure chemical vapour deposition of ZnO layers for thin-film solar cells: temperature-induced morphological changes*. Solar Energy Materials and Solar Cells, vol. 86, pages 385–397, 2005.
- [Faÿ 07] S. Faÿ, J. Steinhauser, N. Oliveira, E. Vallat-Sauvain & C. Ballif. *Opto-electronic properties of rough LP-CVD ZnO:B for use as TCO in thin-film silicon solar cells*. Thin Solid Films, vol. 515, pages 8558–8561, 2007.
- [Faÿ 10] S. Faÿ, J. Steinhauser, S. Nicolay & C. Ballif. *Polycrystalline ZnO: B grown by LPCVD as TCO for thin film silicon solar cells*. Thin Solid Films, vol. 518, pages 2961–2966, 2010.
- [Ferry 09] V. E. Ferry, M. A. Verschuuren, H. B. T. Li, R. E. I. Schropp, H. A. Atwater & A. Polman. *Improved red-response in thin film a-Si:H solar cells with soft-imprinted plasmonic back reflectors*. Applied Physics Letters, vol. 95, page 183503, 2009.
- [Ferry 10] V. E. Ferry, M. A. Verschuuren, H. B. T. Li, E. Verhagen, R. J. Walters, R. E. I. Schropp, H. A. Atwater & A. Polman. *Light trapping in ultrathin plasmonic solar cells*. Optics Express, vol. 18, pages A237–A245, 2010.
- [Ferry 11] V. E. Ferry, A. Polman & H. A. Atwater. *Modeling Light Trapping in Nanostructured Solar Cells*. ACS Nano, vol. 5, pages 10055–10064, 2011.

- [Franken 07] R. H. Franken, R. L. Stolk, C. H. M. Li H. and. van der Werf, J. K. Rath & R. E. I. Schropp. *Understanding light trapping by light scattering textured back electrodes in thin film n-i-p type silicon solar cells*. Journal of Applied Physics, vol. 102, page 014503, 2007.
- [Fthenakis 11] V. M. Fthenakis & H. C. Kim. *Photovoltaics: Life-cycle analyses*. Solar Energy, vol. 85, pages 1609–1628, 2011.
- [Gall 06] S. Gall, J. Schneider, J. Klein, K. Hübener, M. Muske, B. Rau, E. Conrad, I. Sieber, K. Petter, K. Lips, M. Stöger-Pollach, P. Schattschneider & W. Fuhs. *Large-grained polycrystalline silicon on glass for thin-film solar cells*. Thin Solid Films, vol. 511–512, pages 7–14, 2006.
- [Gall 09] S. Gall, C. Becker, E. Conrad, P. Dogan, F. Fenske, B. Gorka, K.Y. Lee, B. Rau, F. Ruske & B. Rech. *Polycrystalline silicon thin-film solar cells on glass*. Solar Energy Materials and Solar Cells, vol. 93, pages 1004–1008, 2009.
- [Gee 02] J. M. Gee. *Optically enhanced absorption in thin silicon layers using photonic crystals*. In 29th IEEE Photovoltaic Specialists Conference, pages 150–153, New Orleans, 2002.
- [Geiser 10] V. Geiser, Y.-H. Jin, Y. Leterrier & J.-A. E. Manson. *Nanoimprint Lithography with UV-Curable Hyperbranched Polymer Nanocomposites*. Macromolecular Symposia, vol. 296, pages 144–153, 2010.
- [Gilles 09] S. Gilles, M. Meier, M. I. Prömpers, A. van der Hart, C. Kügeler, A. Offenhäusser & D. Mayer. *UV nanoimprint lithography with rigid polymer molds*. Microelectronic Engineering, vol. 86, pages 661 – 664, 2009.
- [Golaz 12] B. Golaz, V. Michaud, Y. Leterrier & J.-A.E. Månson. *UV intensity, temperature and dark-curing effects in cationic photo-polymerization of a cycloaliphatic epoxy resin*. Polymer, vol. 53, pages 2038–2048, 2012.
- [González Lazo 12] M. A. González Lazo, R. Teuscher, Y. Leterrier, J.-A. E. Månson, C. Calderone, A. Hessler-Wyser, P. Couty, Y. Ziegler & D. Fischer. *UV-nanoimprint lithography and large area roll-to-roll texturization with hyperbranched polymer nanocomposites for light-trapping applications*. Solar Energy Materials and Solar Cells, vol. 103, pages 147–156, 2012.
- [Grandidier 12] J. Grandidier, R. A. Weitekamp, M. G. Deceglie, D. M. Callahan, C. Battaglia, C. R. Bukowsky, C. Ballif, R. H. Grubbs & H. A. Atwater. *Solar cell efficiency enhancement via light trapping in printable resonant dielectric nanosphere arrays*. Physica Status Solidi A, pages n/a–n/a, 2012.
- [Green 84] M. A. Green, A. W. Blakers, J. Shi, E. M. Keller & S. R. Wenham. *19.1% efficient silicon solar cell*. Applied Physics Letters, vol. 44, pages 1163–1164, 1984.

Bibliography

- [Green 12] M. A. Green, K. Emery, Y. Hishikawa, W. Warta & E. D. Dunlop. *Solar cell efficiency tables (version 40)*. Progress in Photovoltaic: Research and Applications, vol. 20, pages 606–614, 2012.
- [Guha 81] S. Guha, K. L. Narasimhan & S. M. Pietruszko. *On light induced effect in amorphous hydrogenated silicon*. Journal of Applied Physics, vol. 52, page 859, 1981.
- [Guha 11] S. Guha, J. Yang & B. Yan. Comprehensive semiconductor science and technology. Elsevier, Amsterdam, 2011.
- [Hanak 82] J. J. Hanak & V. Korsun. *Optical stability studies of a-Si:H solar cells*. In Proceedings of the 16th Photovoltaic Specialists Conference, pages 1381–1383, San Diego, 1982.
- [Hänni 13a] S. Hänni, D.T.L. Alexander, L. Ding, G. Bugnon, M. Boccard, C. Battaglia, P. Cuony, J. Escarré, G. Parascandolo, S. Nicolay, M. Cantoni, M. Despeisse, F. Meillaud & C. Ballif. *On the interplay between microstructure and interfaces in high-efficiency microcrystalline silicon solar cells*. Photovoltaics, IEEE Journal of, vol. 3, pages 11–16, 2013.
- [Hänni 13b] S. Hänni & et al. In preparation, 2013.
- [Haug 08] F.-J. Haug, T. Söderström, O. Cubero, V. Terrazzoni-Daudrix & C. Ballif. *Plasmonic absorption in textured silver back reflectors of thin film solar cells*. Journal of Applied Physics, vol. 104, page 064509, 2008.
- [Haug 09] F.-J. Haug, T. Söderström, O. Cubero, V. Terrazzoni-Daudrix & C. Ballif. *Influence of the ZnO buffer on the guided mode structure in Si/ZnO/Ag multilayers*. Journal of Applied Physics, vol. 106, page 044502, 2009.
- [Haug 11a] F.-J. Haug, K. Söderström, A. Naqavi & C. Ballif. *Excitation of guided-mode resonances in thin film silicon solar cells*. In Proceedings of the Material Research Society, 1321, mrss11-1321-a17-12, San Francisco, 2011.
- [Haug 11b] F.-J. Haug, K. Söderström, A. Naqavi & C. Ballif. *Resonances and absorption enhancement in thin film silicon solar cells with periodic interface texture*. Journal of Applied Physics, vol. 109, page 084516, 2011.
- [Haug 11c] F.-J. Haug, K. Söderström, A. Naqavi, C. Battaglia & C. Ballif. *Excitation of plasmon and guided-mode resonances in thin film silicon solar cells*. In In Proceeding of the Material Research Society, vol. 1391, mrsf11-1391-j03-06, Boston, 2011.
- [Haug 12a] F.-J. Haug, R. Biron, G. Kratzer, F. Leresche, J. Besuchet, C. Ballif, M. Dissel, S. Kretschmer, W. Soppe, P. Lippens & K. Leitner. *Improvement of the open circuit voltage by modifying the transparent indium-tin oxide front electrode*

- in amorphous n-i-p solar cells*. Progress in Photovoltaics: Research and Applications, vol. 20, pages 727–734, 2012.
- [Haug 12b] F.-J. Haug, A. Naqavi & C. Ballif. *Diffraction and absorption enhancement from textured back reflectors of thin film solar cells*. Journal of Applied Physics, vol. 112, page 024516, 2012.
- [Heijna 08] M. C. R. Heijna, J. Löffler, B. B. Van Aken, W. J. Soppe, R. van Erven, R. Franken, H. Borg & P. P. G. J. M. Peeters. *Embossing of light trapping patterns in sol-gel coatings for thin film silicon solar cells*. In Proceedings of the Nanoscale Photonic and Cell Technologies for Photovoltaics, volume 7047, pages 704706–9, San Diego, CA, USA, 2008. SPIE.
- [Heine 95] C. Heine & R.H. Morf. *Submicrometer gratings for solar energy applications*. Applied Optics, vol. 34, pages 2476–2482, 1995.
- [Holman 13a] Z. C. Holman, M. Filipič, A. Descoeudres, S. De Wolf, F. Smole, M. Topič & C. Ballif. *Infrared light management in high-efficiency silicon heterojunction and rear-passivated solar cells*. Journal of Applied Physics, vol. 113, page 013107, 2013.
- [Holman 13b] Z. C Holman, S. De Wolf & C. Ballif. *Improving metal reflectors by suppressing surface plasmon polaritons: A priori calculation of the internal reflectance of a solar cell*. N/A, vol. NA, page NA, 2013.
- [Horcas 07] I. Horcas, R. Fernandez, J. M. Gomez-Rodriguez, J. Colchero, J. Gomez-Herrero & A. M. Baro. *WSXM: A software for scanning probe microscopy and a tool for nanotechnology*. Review of Scientific Instruments, vol. 78, page 013705, 2007.
- [Hsu 12] C.-M. Hsu, C. Battaglia, C. Pahud, Z. Ruan, F.-J. Haug, S. Fan, C. Ballif & Y. Cui. *High-Efficiency Amorphous Silicon Solar Cell on a Periodic Nanocone Back Reflector*. Advanced Energy Materials, vol. 2, pages 628–633, 2012.
- [Hunderi 80] O. Hunderi. *Optics of rough surfaces, discontinuous films and heterogeneous materials*. Surface Science, vol. 96, pages 1–31, 1980.
- [Hurt 85] H. H. Hurt & J. M. Bennett. *Relation between optical scattering, microstructure, and topography of thin silver films. 2: Microstructure*. Applied Optics, vol. 24, pages 2712–2720, 1985.
- [Hussain 06] F. Hussain, M. Hojjati, M. Okamoto & R. E. Gorga. *Review article: Polymer-matrix Nanocomposites, Processing, Manufacturing, and Application: An Overview*. Journal of Composite Materials, vol. 40, pages 1511–1575, 2006.
- [IEA 12a] International Energy Agency IEA. *Key World Energy Statistics*. 2012.

Bibliography

- [IEA 12b] International Energy Agency IEA. *World Eneergy Outlook. Executive summary*. 2012.
- [Iida 83] H. Iida, N. Shiba, T. Mishuku, H. Karasawa, A. Ito, M. Yamanaka & Y. Hayashi. *Efficiency of the a-Si:H solar cell and grain size of SnO₂ transparent conductive film*. Electron Device Letters, IEEE, vol. 4, pages 157–159, 1983.
- [IPCC 07] IPCC. *Climate Change 2007: Synthesis Report*. 2007.
- [IPCC 12] IPCC. *Renewable Energy Sources and Climate Change Mitigation*. 2012.
- [IRENA 12] International Renewable Energy Agency IRENA. *Renewable energy technologies: Cost analysis series: Solar Photovoltaics*. 2012.
- [Isabella 08] O. Isabella, A. Campa, M.C.R Heijna, W. Soppe, R. van Erven, R.H. Franken, H. Borg & M. Zeman. *Diffraction gratings for light trapping in thin-film silicon solar cells*. In Proceedings of the 23th European Photovoltaic Solar Energy Conference and Exhibition, 3AV.1.48, pages 2320–2324, Valencia, 2008.
- [Isabella 10] O. Isabella, J. Krč & M. Zeman. *Modulated surface textures for enhanced light trapping in thin-film silicon solar cells*. Applied Physics Letters, vol. 97, page 101106, 2010.
- [Isabella 12] O. Isabella, H. Sai, M. Kondo & M. Zeman. *Full-wave optoelectrical modeling of optimized flattened light-scattering substrate for high efficiency thin-film silicon solar cells*. Progress in Photovoltaics: Research and Applications, pages n/a–n/a, 2012.
- [Jäger 09] K. Jäger & M. Zeman. *A scattering model for surface-textured thin films*. Applied Physics Letters, vol. 95, page 171108, 2009.
- [Jäger 10] K. Jäger, O. Isabella, L. Zhao & M. Zeman. *Light scattering properties of surface-textured substrates*. Physica Status Solidi (c), vol. 7, pages 945–948, 2010.
- [Jia 12] Z. Jia, X. Zhang, Y. Liu, J. Ma, C. Liu & Y. Zhao. *Conductive white back reflector and scatter based on ZnO nanostructure arrays for harvesting solar energy*. Nano Energy, vol. 1, pages 783–788, 2012.
- [Johnson 72] P. B. Johnson & R. W. Christy. *Optical Constants of the Noble Metals*. Physical Review B, vol. 6, pages 4370–4379, 1972.
- [Jones 38] F. W. Jones. *The measurement of particle size by the X-ray method*. In Proceedings of the Royal Society of London. B. Biological Sciences, 1938.

- [Jung 04] Y. S. Jung. *Study on texture evolution and properties of silver thin films prepared by sputtering deposition*. Applied Surface Science, vol. 221, pages 281–287, 2004.
- [Kang 06] H. Kang, J. Lee, J. Park & H. H Lee. *An improved method of preparing composite poly(dimethylsiloxane) moulds*. Nanotechnology, vol. 17, pages 197–200, 2006.
- [Kang 11] Y. Kang, Ma. Okada, Y. Nakai, Y. Haruyama, K. Kanda & S. Matsui. *Mechanical characteristics of imprinted nanostructures fabricated with a poly(dimethylsiloxane) mold*. J. Vac. Sci. Technol. B, vol. 29, pages 06FC10–6, 2011.
- [Klukowska 08] A. Klukowska, M. Vogler, A. Kolander, F. Reuther, G. Grützner, M. Mühlberger, I. Bergmair & R. Schöftner. *Alternative Approach to Transparent Stamps for UV-based Nanoimprint Lithography - Techniques and Materials*. In 24th European Mask and Lithography Conference, 2008.
- [Klukowska 09] A. Klukowska, A. Kolander, I. Bergmair, M. Mühlberger, H. Leichtfried, F. Reuther, G. Grützner & R. Schöftner. *Novel transparent hybrid polymer working stamp for UV-imprinting*. Microelectronic Engineering, vol. 86, pages 697–699, 2009.
- [Kluth 99] O. Kluth, B. Rech, L. Houben, S. Wieder, G. Schöpe, C. Beneking, H. Wagner, A. Löffl & H. W. Schock. *Texture etched ZnO:Al coated glass substrates for silicon based thin film solar cells*. Thin Solid Films, vol. 351, pages 247–253, 1999.
- [Koida 07] T. Koida, H. Fujiwara & M. Kondo. *Hydrogen-doped In_2O_3 as High-mobility Transparent Conductive Oxide*. Japanese Journal of Applied Physics, vol. 46, pages L685–L687, 2007.
- [Koida 10a] T. Koida, M. Kondo, K. Tsutsumi, A. Sakaguchi, M. Suzuki & H. Fujiwara. *Hydrogen-doped In_2O_3 transparent conducting oxide films prepared by solid-phase crystallization method*. Journal of Applied Physics, vol. 107, page 033514, 2010.
- [Koida 10b] T. Koida, H. Sai & M. Kondo. *Application of hydrogen-doped In_2O_3 transparent conductive oxide to thin-film microcrystalline Si solar cells*. Thin Solid Films, vol. 518, pages 2930–2933, 2010.
- [Koo 07] N. Koo, M. Bender, U. Plachetka, A. Fuchs, T. Wahlbrink, J. Bolten & H. Kurz. *Improved mold fabrication for the definition of high quality nanopatterns by Soft UV-Nanoimprint lithography using diluted PDMS material*. Microelectronic Engineering, vol. 84, pages 904–908, 2007.

Bibliography

- [Kothandraraman 91] C. Kothandraraman, T. Tonon, C. huang & A.E. Delahoy. *Improvement of a-Si:H P-I-N devices using zinc oxide based back reflector*. In MRS Proceedings, 219, 1991.
- [Kray 09] D. Kray & K. R. McIntosh. *Analysis of ultrathin high-efficiency silicon solar cells*. Physica status solidi (a), vol. 206, pages 1647–1654, 2009.
- [Krč 02] J. Krč, M. Zeman, F. Smole & M. Topič. *Optical modeling of a-Si:H solar cells deposited on textured glass/SnO₂ substrates*. Journal of Applied Physics, vol. 92, pages 749–755, 2002.
- [Kurdesau 06] F. Kurdesau, G. Khripunov, A.-F. da Cunha, M. Kaelin & A.N. Tiwari. *Comparative study of ITO layers deposited by DC and RF magnetron sputtering at room temperature*. Journal of Non-Crystalline Solids, vol. 352, pages 1466–1470, 2006.
- [Lal 12] N. N. Lal, H. Zhou, M. Hawkeye, J. K. Sinha, P. N. Bartlett, G. A. J. Amaratunga & J. J. Baumberg. *Using spacer layers to control metal and semiconductor absorption in ultrathin solar cells with plasmonic substrates*. Physical Review B, vol. 85, page 245318, 2012.
- [Lee 08] Y.-C. Lee, C.-F. Huang, J.-Y. Chang & M.-L. Wu. *Enhanced light trapping based on guided mode resonance effect for thin-film silicon solar cells with two filling-factor gratings*. Optics Express, vol. 16, pages 7969–7975, 2008.
- [Lee 11] B. G. Lee, P. Stradins, . L. Young, K. Alberi, T.-K. Chuang, J. G. Couillard & H. M. Branz. *Light trapping by a dielectric nanoparticle back reflector in film silicon solar cells*. Applied Physics Letters, vol. 99, pages 064101–3, 2011.
- [Li 08] H. Li, R. Franken, R. L. Stolk, J. K. Rath & R. E. I. Schropp. *Mechanism of shunting of nanocrystalline silicon solar cells deposited on rough Ag/ZnO substrates*. Solid State Phenomena, vol. 131-133, pages 27–32, 2008.
- [Light 66] T. B. Light & C. N. J. Wagner. *X-Ray Diffraction Study of Vacuum-Evaporated Silver Films*. Journal of Vacuum Science and Technology, vol. 3, pages 1–5, 1966.
- [Lin 11] C.-C. Lin, W.-L. Liu & C.-Y. Hsieh. *Scalar scattering model of highly textured transparent conducting oxide*. Journal of Applied Physics, vol. 109, page 014508, 2011.
- [Madzharov 11] D. Madzharov, R. Dewan & D. Knipp. *Influence of front and back grating on light trapping in microcrystalline thin-film silicon solar cells*. Optics Express, vol. 19, pages A95–A107, 2011.
- [Marfaing 79] Y. Marfaing. *Evaluation of multijunction structures using amorphous Si-Ge alloys*. In Proceedings of the 2nd European Photovoltaic Solar Energy Conference, pages 287-294, Berlin, 1979.

- [Massiot 12] I. Massiot, C. Colin, N. Pere-Laperne, P. Roca i Cabarrocas, C. Sauvan, P. Lalanne, J.-L. Pelouard & St. Collin. *Nanopatterned front contact for broadband absorption in ultra-thin amorphous silicon solar cells*. Applied Physics Letters, vol. 101, pages 163901–3, 2012.
- [Matheu 08] P. Matheu, S. H. Lim, D. Derkacs, C. McPheeters & E. T. Yu. *Metal and dielectric nanoparticle scattering for improved optical absorption in photovoltaic devices*. Applied Physics Letters, vol. 93, page 113108, 2008.
- [McBreen 83] P. H. McBreen & M. Moskovits. *Optical properties of silver films deposited at low temperatures*. Journal of Applied Physics, vol. 54, pages 329–335, 1983.
- [Meier 94] J. Meier, R. Fluckiger, H. Keppner & A. Shah. *Complete microcrystalline p-i-n solar cell—Crystalline or amorphous cell behavior?* Applied Physics Letters, vol. 65, pages 860–862, 1994.
- [Meier 96] J. Meier, P. Torres, R. Platz, S. Dubail, U. Kroll, J.A. . Anna Selvan, N. Pellaton Vaucher, Ch. Hof, D. Fisher, R., H. Keppner, A. Shah, K.-D. Ufert, P. Giannoulès & J. Koehler. *On the way towards high efficiency thin film silicon solar cells by the "Micromorph" concept*. In Proceedings of the Material Research Society Symposium, Spring meeting (San Francisco), 1996.
- [Meillaud 06] F. Meillaud, A. Shah, C. Droz, E. Vallat-Sauvain & C. Miazza. *Efficiency limits for single-junction and tandem solar cells*. Solar Energy Materials and Solar Cells, vol. 90, pages 2952–2959, 2006.
- [Meng 11] X. Meng, G. Gomard, O. El Daif, E. Drouard, R. Orobitchouk, A. Kaminski, A. Fave, M. Lemiti, A. Abramov, P. Roca i Cabarrocas & C. Seassal. *Absorbing photonic crystals for silicon thin-film solar cells: Design, fabrication and experimental investigation*. Solar Energy Materials and Solar Cells, vol. 95, Supplement 1, pages S32–S38, 2011.
- [Minami 05] T. Minami. *Transparent conducting oxide semiconductors for transparent electrodes*. Semiconductor Science and Technology, vol. 20, page S35, 2005.
- [Mizuhashi 88] M. Mizuhashi, Y. Gotoh & K. Adachi. *Texture morphology of SnO₂:F films and cell reflectance*. Japanese Journal of Applied Physics, vol. 27, pages 2053–2061, 1988.
- [Mokkapati 12] S. Mokkapati & K.R. Catchpole. *Nanophotonic light trapping in solar cells*. Journal of Applied Physics, vol. 112, page 101101, 2012.
- [Morton 08] K. J. Morton, G.y Nieberg, Sh. Bai & S. Y. Chou. *Wafer-scale patterning of sub-40nm diameter and high aspect ratio (50:1) silicon pillar arrays by nanoimprint and etching*. Nanotechnology, vol. 19, page 345301, 2008.

Bibliography

- [Moulin 08] E. Moulin, J. Sukmanowski, P. Luo, R. Carius, F.X. Royer & H. Stiebig. *Improved light absorption in thin-film silicon solar cells by integration of silver nanoparticles*. Journal of Non-Crystalline Solids, vol. 354, pages 2488–2491, 2008.
- [Mühlberger 09] M. Mühlberger, I. Bergmair, A. Klukowska, A. Kolander, H. Leichtfried, E. Platzgummer, H. Loeschner, Ch. Ebm, G. Grützner & R. Schöftner. *UV-NIL with working stamps made from Ormostamp*. Microelectronic Engineering, vol. 86, pages 691–693, 2009.
- [Müller 04] J. Müller, B. Rech, J. Springer & M. Vaneček. *TCO and light trapping in silicon thin film solar cells*. Solar Energy, vol. 77, pages 917–930, 2004.
- [Nam 12] W. J. Nam, L. Ji, V. V. Varadan & S. J. Fonash. *Exploration of nano-element array architectures for substrate solar cells using an a-Si:H absorber*. Journal of Applied Physics, vol. 111, pages 123103–6, 2012.
- [Naqavi 11] A. Naqavi, K. Söderström, F.-J. Haug, V. Paeder, T. Scharf, H. P. Herzig & C. Ballif. *Understanding of photocurrent enhancement in real thin film solar cells: towards optimal one-dimensional gratings*. Optics Express, vol. 19, pages 128–140, 2011.
- [Naqavi 13] A. Naqavi, , F.-J. Haug, C. Battaglia, H. P. Herzig & C. Ballif. *Light trapping in solar cells at the extreme coupling limit*. Journal Of Optical Society of America B, vol. 30, pages 128–140, 2013.
- [Nasuno 01] Y. Nasuno, M. Kondo & A. Matsuda. *Effects of Substrate Surface Morphology on Microcrystalline Silicon Solar Cells*. Japanese Journal of Applied Physics, vol. 40, pages L303–L305, 2001.
- [Naughton 10] M. J. Naughton, K. Kempa, Z. F. Ren, Y. Gao, J. Rybczynski, N. Argenti, W. Gao, Y. Wang, Y. Peng, J. R. Naughton, G. McMahon, T. Paudel, Y. C. Lan, M. J. Burns, A. Shepard, M. Clary, C. Ballif, F.-J. Haug, T. Söderström, O. Cubero & C. Eminian. *Efficient nanocoax-based solar cells*. physica status solidi (RRL), vol. 4, pages 181–183, 2010.
- [Nicolay 09] S. Nicolay, S. Faÿ & C. Ballif. *Growth model of MOCVD polycrystalline ZnO*. Crystal Growth and Design, vol. 9, pages 4957–4962, 2009.
- [Nicolay 11] S. Nicolay, M. Despeisse, F.-J. Haug & C. Ballif. *Control of LPCVD ZnO growth modes for improved light trapping in thin film silicon solar cells*. Solar Energy Materials and Solar Cells, vol. 95, pages 1031–1034, 2011.
- [Niggemann 04] M. Niggemann, M. Glatthaar, A. Gombert, A. Hinsch & V. Wittwer. *Diffraction gratings and buried nano-electrodes architectures for organic solar cells*. Thin Solid Films, vol. 451–452, pages 619–623, 2004.

- [Odom 02] T. W. Odom, J. C. Love, D. B. Wolfe, E. P. Kateri & G. M. Whitesides. *Improved Pattern Transfer in Soft Lithography Using Composite Stamps*. Langmuir, vol. 18, pages 5314–5320, 2002.
- [Ossenbrink 12] H. Ossenbrink, A. Jäger-Waldau & N. Taylor. *New Opportunities for PV Systems*. In Proceeding of the 27th EUPVSEC, 5DP3.1 pages 3727–3730, Frankfurt, 2012.
- [Ouyang 11] Z. Ouyang, X. Zhao, S. Varlamov, Y. Tao, J. Wong & S. Pillai. *Nanoparticle-enhanced light trapping in thin-film silicon solar cells*. Progress in Photovoltaic: Research and Applications, vol. 19, pages 917–926, 2011.
- [Owen 11] J. I. Owen, J. Hüpkes, H. Zhu, E. Bunte & S. E. Pust. *Novel etch process to tune crater size on magnetron sputtered ZnO:Al*. Physica status solidi (a), vol. 208, pages 109–113, 2011.
- [Paetzold 10] U. W. Paetzold, F. Hallermann, B.E. Pieters, U. Rau, R. Carius & G. von Plessen. *Localized plasmonic losses at metal back contacts of thin-film silicon solar cells*. In Proceeding of the SPIE, vol. 7725, 2010.
- [Paetzold 11a] U. W. Paetzold, E. Moulin, D. Michaelis, W. Bottler, C. Wachter, V. Hagemann, M. Meier, R. Carius & U. Rau. *Plasmonic reflection grating back contacts for microcrystalline silicon solar cells*. Applied Physics Letters, vol. 99, page 181105, 2011.
- [Paetzold 11b] U. W. Paetzold, E. Moulin, B. E. Pieters, R. Carius & U. Rau. *Design of nanostructured plasmonic back contacts for thin-film silicon solar cells*. Optics Express, vol. 19, pages A1219–A1230, 2011.
- [Pahud 13] C. Pahud, A. Naqavi, F.-J. Haug, O. Isabella & C. Ballif. *Impact of material quality on the performance of plasmonic solar cells*. to be decided, 2013.
- [Palanchoke 12] U. Palanchoke, V. Jovanov, H. Kurz, P. Obermeyer, H. Stiebig & D. Knipp. *Plasmonic effects in amorphous silicon thin film solar cells with metal back contacts*. Optics Express, vol. 20, pages 6340–6347, 2012.
- [Palik 98] E. Palik, editeur. Handbook of optical constants of solids. Academic Press, 1998.
- [Parmigiani 86] F. Parmigiani, E. Kay, T. C. Huang, J. Perrin, M. Jurich, Swalen & J. D. *Optical and electrical properties of thin silver films grown under ion bombardment*. Physical Review B, vol. 33, pages 879–888, 1986.
- [Petermann 12] J. H. Petermann, D. Zielke, J. Schmidt, F. Haase, E. Garralaga Rojas & R. Brendel. *19% efficient and 43 μ m thick crystalline Si solar cell from layer transfer using porous silicon*. Progress in Photovoltaic: Research and Applications, vol. 20, pages 1–5, 2012.

Bibliography

- [Pillai 07] S. Pillai, K. R Catchpole, T. Trupke & M. A. Green. *Surface plasmon enhanced silicon solar cells*. Journal of Applied Physics, vol. 101, page 093105, 2007.
- [Poruba 00] A. Poruba, A. Fejfar, Z. Remež, J. Springer, M. Vaněček, J. Kočka, J. Meier, P. Torres & A. Shah. *Optical absorption and light scattering in microcrystalline silicon thin films and solar cells*. Journal of Applied Physics, vol. 88, pages 148–160, 2000.
- [Python 08a] M. Python. *Microcrystalline silicon solar cells: Growth and defects*. PhD thesis, University of neuchâtel, 2008.
- [Python 08b] M. Python, E. Vallat-Sauvain, J. Bailat, D. Dominé, L. Fesquet, A. Shah & C. Ballif. *Relation between substrate surface morphology and microcrystalline silicon solar cell performance*. Journal of Non-Crystalline Solids, vol. 354, pages 2258–2262, 2008.
- [Qin 10] D. Qin, Y. Xia & G. M Whitesides. *Soft lithography for micro- and nanoscale patterning*. Nature Protocols, vol. 5, pages 491–502, 2010.
- [Ritchie 57] R. H. Ritchie. *Plasma Losses by Fast Electrons in Thin Films*. Physical Review B, vol. 106, pages 874–881, 1957.
- [Rockstuhl 07] C. Rockstuhl, F. Lederer, K. Bittkau & R. Carius. *Light localization at randomly textured surfaces for solar-cell applications*. Applied Physics Letters, vol. 91, pages 171104–3, 2007.
- [Rockstuhl 10] C. Rockstuhl, S. Fahr, K. Bittkau, T. Beckers, R. Carius, F.-J. Haug, T. Söderström, C. Ballif & F. Lederer. *Comparison and optimization of randomly textured surfaces in thin-film solar cells*. Optics Express, vol. 18, pages A335–A341, 2010.
- [Rockstuhl 11] C. Rockstuhl, S. Fahr, F. Lederer, F.-J. Haug, T. Söderström, S. Nicolay, M. Despeisse & C. Ballif. *Light absorption in textured thin film silicon solar cells: A simple scalar scattering approach versus rigorous simulation*. Applied Physics Letters, vol. 98, page 051102, 2011.
- [Rudigier-Voigt 09] E. Rudigier-Voigt, M. Bockmeyer, V. Hagemann & S. Bauer. *Sol-gel based structuring of the front electrode in Si-based thin film device*. In 24th European Photovoltaic Solar Energy Conference, Hamburg, Germany, 2009.
- [Sai 09] H. Sai, H. Fujiwara & M. Kondo. *Back surface reflectors with periodic textures fabricated by self-ordering process for light trapping in thin-film microcrystalline silicon solar cells*. Solar Energy Materials and Solar Cells, vol. 93, pages 1087–1090, 2009.
- [Sai 10] H. Sai, H. Jia & M. Kondo. *Impact of front and rear texture of thin-film microcrystalline silicon solar cells on their light trapping properties*. Journal of Applied Physics, vol. 108, page 044505, 2010.

- [Sai 11a] H. Sai, Y. Kanamori & M. Kondo. *Flattened light-scattering substrate in thin film silicon solar cells for improved infrared response*. Applied Physics Letters, vol. 98, page 113502, 2011.
- [Sai 11b] H. Sai, Y. Kanamori & M. Kondo. *Flattened light scattering substrate in thin film silicon solar cells for improved infrared response and photovoltaic performance*. In Proceedings of the 26th European Photovoltaic Solar Energy Conference and Exhibition, 3BO2..4, pages 2336–2339, Hamburg, pages 2336–2339, 2011.
- [Sai 12] H. Sai, K. Saito & M. Kondo. *Enhanced photocurrent and conversion efficiency in thin-film microcrystalline silicon solar cells using periodically textured back reflectors with hexagonal dimple arrays*. Applied Physics Letters, vol. 101, page 173901, 2012.
- [Sainju 06] D. Sainju, P. J. van den Oever, N. J. Podraza, M. Syed, J. A. Stoke, Jie Chen, Xiesen Yang, Xunming Deng & R. W. Collins. *Origin of optical losses in Ag/ZnO back-reflectors for thin film Si photovoltaics*. In 4th IEEE World Conference on Photovoltaic Energy Conversion, volume 2, pages 1732–1735, 2006.
- [Sakai 90] H. Sakai, T. Yoshida, T. Hama & Y. Ichikawa. *Effects of surface morphology of transparent electrode on the open-circuit voltage in a-Si:H solar cells*. Japanese Journal of Applied Physics, vol. 29, pages 630–635, 1990.
- [Sakata 10] H. Sakata, Y. Tsunomura, H. Inoue, S. Taira, T. Baba, H. Kanno, T. Kinoshita, M. Taguchi & E. Maruyama. *R&D progress of next-generation very thin HITtm solar cells*. In Proceedings of the 25th European Photovoltaic Solar Energy Conference and Exhibition, 2DP2.4, pages 1102–1105, Valencia, 2010.
- [Santbergen 10] R. Santbergen, R. Liang, M. Zeman, Q. Wang, B. Yan, S. Higashi, C. Tsai & A. Flewitt. *Amorphous silicon solar cells with silver nanoparticles embedded inside the absorber layer*. In Proceeding of the Material Research Society, vol. 1245, mrss10-1245-A07-20, San Francisco, 2010.
- [Schiff 11] E.A. Schiff. *Thermodynamic limit to photonic-plasmonic light trapping in thin films on metal*. Journal of Applied Physics, vol. 110, page 104501, 2011.
- [Schmidt 07] L. Schmidt, D. Schmäh, Y. Leterrier & J.-A. Manson. *Time-intensity transformation and internal stress in UV-curable hyperbranched acrylates*. Rheologica Acta, vol. 46, pages 693–701, 2007.
- [Schulte 11] M. Schulte, K. Bittkau, K. Jäger, M. Ermes, M. Zeman & B. E. Pieters. *Angular resolved scattering by a nano-textured ZnO/silicon interface*. Applied Physics Letters, vol. 99, page 111107, 2011.

Bibliography

- [Senoussaoui 04] N. Senoussaoui, M. Krause, J. Müller, E. Bunte, T. Brammer & H. Stiebig. *Thin-film solar cells with periodic grating coupler*. Thin Solid Films, vol. 451-452, pages 397–401, 2004.
- [Shakir 82] S. A. Shakir & A. F. Turner. *Method of poles for multilayer thin-film waveguides*. Applied Physics A: Materials Science & Processing, vol. 29, pages 151–155, 1982.
- [Sharma 80] S. K. Sharma & J. Spitz. *Void growth in thin silver films*. Thin Solid Films, vol. 67, pages 109–116, 1980.
- [Sheng 83] P. Sheng, A. N. Bloch & R. S. Stepleman. *Wavelength-selective absorption enhancement in thin-film solar cells*. Applied Physics Letters, vol. 43, pages 579–581, 1983.
- [Smith 77] P. H. Smith & H. Gurev. *Silicon dioxide as a high temperature stabilizer for silver films*. Thin Solid Films, vol. 45, pages 159–168, 1977.
- [Söderström 08a] T. Söderström, F.-J. Haug, V. Terrazzoni-Daudrix & C. Ballif. *Optimization of amorphous silicon thin film solar cells for flexible photovoltaics*. Journal of Applied Physics, vol. 103, page 114509, 2008.
- [Söderström 08b] T. Söderström, F.-J. Haug, V. Terrazzoni-Daudrix, X. Niquille, M. Python & C. Ballif. *NiI buffer layer for substrate microcrystalline thin film silicon solar cell*. Journal of Applied Physics, vol. 104, page 104505, 2008.
- [Söderström 09a] T. Söderström. *Single and multi-junction thin film silicon solar cells for flexible photovoltaics*. PhD thesis, University of Neuchâtel, 2009.
- [Söderström 09b] T. Söderström, F.-J. Haug, X. Niquille & C. Ballif. *TCOs for nip thin film silicon solar cells*. Progress in Photovoltaics: Research and Applications, vol. 17, pages 165–176, 2009.
- [Söderström 09c] T. Söderström, F.-J. Haug, X. Niquille, V. Terrazzoni & C. Ballif. *Asymmetric intermediate reflector for tandem micromorph thin film silicon solar cells*. Applied Physics Letters, vol. 94, page 063501, 2009.
- [Söderström 10a] K. Söderström, J. Escarré, R. Biron, O. Cubéro, C. Eminian, F.-J. Haug & C. Ballif. *Nano-imprint technique for back reflector in high efficiency n-i-p thin film silicon solar cells*. In Proceedings of the 25th European Photovoltaic Solar Energy Conference and Exhibition, 3AV1.8, pages 2899–2903, Valencia, 2010.
- [Söderström 10b] K. Söderström, J. Escarré, O. Cubero, F.-J. Haug & C. Ballif. *Photocurrent increase in thin film solar cells by guided mode excitation*. In Technical digest of OSA meeting: Optical Nanostructures for Photovoltaics, Karlsruhe, paper PTuB6, 2010.

- [Söderström 10c] K. Söderström, F.-J. Haug, J. Escarré, O. Cubero & C. Ballif. *Photocurrent increase in n-i-p thin film silicon solar cells by guided mode excitation via grating coupler*. Applied Physics Letters, vol. 96, page 213508, 2010.
- [Söderström 11a] K. Söderström, J. Escarré, O. Cubero, F.-J. Haug, S. Perregaux & C. Ballif. *UV-nano-imprint lithography technique for the replication of back reflectors for n-i-p thin film silicon solar cells*. Progress in Photovoltaics: Research and Applications, vol. 19, pages 202–210, 2011.
- [Söderström 11b] K. Söderström, F.-J. Haug, J. Escarré, C. Pahud, R. Biron & C. Ballif. *Highly reflective nanotextured sputtered silver back reflector for flexible high-efficiency n-i-p thin-film silicon solar cells*. Solar energy materials and solar cells, vol. 95, pages 3585–3591, 2011.
- [Söderström 11c] K. Söderström, F.-J. Haug, C. Pahud, R. Biron, J. Escarré, M. Duchamp, R. Dunin-Borkowski & C. Ballif. *Reflectance improvement by thermal annealing of sputtered Ag/ZnO back reflectors in a-Si:H thin film silicon solar cells*. In Proceeding of the Material Research Society, vol. 1321, mrss11-1321-a11-05, San Francisco, 2011.
- [Söderström 12a] K. Söderström, G. Bugnon, R. Biron, C. Pahud, F. Meillaud, F.-J. Haug & C. Ballif. *Thin-film silicon triple-junction solar cell with 12.5% stable efficiency on innovative flat light-scattering substrate*. Journal of Applied Physics, vol. 112, page 114503, 2012.
- [Söderström 12b] K. Söderström, G. Bugnon, F.-J. Haug & C. Ballif. *Electrically flat/optically rough substrates for efficiencies above 10% in n-i-p thin film silicon solar cells*. In Proceeding of the Material Research Society, vol. 1426, pages 39–45, San Francisco, 2012.
- [Söderström 12c] K. Söderström, G. Bugnon, F.-J. Haug, S. Nicolay & C. Ballif. *Experimental study of flat light-scattering substrates in thin-film silicon solar cells*. Solar Energy Materials and Solar Cells, vol. 101, pages 193–199, 2012.
- [Solntsev 13] S. Solntsev, O. Isabella, D. Caratelli & Zeman M. *Thin-film silicon solar cells on 1-D periodic gratings with nonconformal layers: optical analysis*. IEEE Journal of photovoltaics, vol. 3, pages 46–52, 2013.
- [Sontheimer 12] T. Sontheimer, E. Rudigier-Voigt, M. Bockmeyer, D. Lockau, C. Klimm, C. Becker & B. Rech. *Light harvesting architectures for electron beam evaporated solid phase crystallized Si thin film solar cells: Statistical and periodic approaches*. Journal of Non-Crystalline Solids, vol. 358, pages 2303–2307, 2012.
- [Sotelo 03] J. Sotelo, J. Ederth & G. Niklasson. *Optical properties of polycrystalline metallic films*. Physical Review B, vol. 67, page 195106, 2003.

Bibliography

- [Spear 75] W. E. Spear & P. G. Le Comber. *Substitutional doping of amorphous silicon*. Solid State Communications, vol. 17, pages 1193–1196, 1975.
- [Springer 04] J. Springer, A. Poruba, L. Mullerova, M. Vaneček, O. Kluth & B. Rech. *Absorption loss at nanorough silver back reflector of thin-film silicon solar cells*. Journal of Applied Physics, vol. 95, pages 1427–1429, 2004.
- [Springer 05] J. Springer, B. Rech, W. Reetz, J. Müller & M. Vaneček. *Light trapping and optical losses in microcrystalline silicon pin solar cells deposited on surface-textured glass/ZnO substrates*. Solar Energy Materials and Solar Cells, vol. 85, pages 1–11, 2005.
- [Staebler 77] D. L. Staebler & C. R. Wronski. *Reversible conductivity changes in discharge-produced amorphous Si*. Applied Physics Letters, vol. 31, pages 292–294, 1977.
- [Steinhauser 07] J. Steinhauser, S. Fay, N. Oliveira, E. Vallat-Sauvain & C. Ballif. *Transition between grain boundary and intragrain scattering transport mechanisms in boron-doped zinc oxide thin films*. Applied Physics Letters, vol. 90, pages 142107–3, 2007.
- [Steinhauser 08] J. Steinhauser. *Low pressure chemical vapor deposited Zinc Oxide for thin film silicon solar cells: Optical and electrical properties*. PhD thesis, University of neuchâtel, 2008.
- [Stiebig 06a] H. Stiebig, C. Haase, C. Zahren, B. Rech & N. Senoussaoui. *Thin-film silicon solar cells with grating couplers - An experimental and numerical study*. Journal of Non-Crystalline Solids, vol. 352, pages 1949–1952, 2006.
- [Stiebig 06b] H. Stiebig, N. Senoussaoui, C. Zahren, C. Haase & J. Müller. *Silicon thin-film solar cells with rectangular-shaped grating couplers*. Progress in Photovoltaic: Research and Applications, vol. 14, pages 13–24, 2006.
- [Street 79] R. Street, D. Biegelsen & J. Stuke. *Defects in bombarded amorphous silicon*. Philosophical Magazine B, vol. 40, pages 451–464, 1979.
- [Stuart 97] H. R. Stuart & D. G. Hall. *Thermodynamic limit to light trapping in thin planar structures*. Journal of the Optical Society of America A, vol. 14, pages 3001–3008, 1997.
- [Tan 12] H. Tan, R. Santbergen, A. H. M. Smets & M. Zeman. *Plasmonic light trapping in thin-film silicon solar cells with improved self-assembled silver nanoparticles*. Nano Letters, vol. 12, pages 4070–4076, 2012.
- [Taneda 07] N. Taneda, T. Oyama & K. Sato. *Light scattering effects of highly textured transparent conductive oxides films*. In Technical Digest of the International PVSEC-17, Fukuoka, Japan, 2007.

- [Terrazzoni-Daudrix 03] V. Terrazzoni-Daudrix, J. Guillet, X. Niquille, A. Shah, R. Morf, A. Tishenko, V. Brioude, O. Parriaux & D. Fisher. *Light trapping in amorphous silicon solar cells on plastic substrates*. In Proceeding of the Material Research Society, vol. 729, mrss03-729-H6.14, 2003.
- [Terrazzoni-Daudrix 06] V. Terrazzoni-Daudrix, J. Guillet, F. Freitas, A. Shah, C. Ballif, P. Winkler, M. Ferreloc, S. Benagli, X. Niquille, D. Fischer & R. Morf. *Characterisation of rough reflecting substrates incorporated into thin-film silicon solar cells*. Progress in Photovoltaics: Research and Applications, vol. 14, pages 485–498, 2006.
- [Thornton 86] J. A. Thornton. *The microstructure of sputter-deposited coatings*. Journal of Vacuum Science & Technology A: Vacuum, Surfaces, and Films, vol. 4, pages 3059–3065, 1986.
- [Tiedje 83] T. Tiedje, B. Abeles, J. M. Cebulka & J. Pelz. *Photoconductivity enhancement by light trapping in rough amorphous silicon*. Applied Physics Letters, vol. 42, pages 712–714, 1983.
- [Tiedje 84] T. Tiedje, E. Yablonovitch, G.D. Cody & B.G. Brooks. *Limiting Efficiency of Silicon Solar Cells*. Electron Devices, IEEE Transactions on, vol. 31, pages 711–716, 1984.
- [Tokarsky 76] R. W. Tokarsky & J. P. Marton. *Double absorptions in aggregate-roughened silver surfaces*. Applied Physics Letters, vol. 28, pages 729–731, 1976.
- [Ulbrich 12] C. Ulbrich, A. Gerber, K. Hermans, A. Lambertz & U. Rau. *Analysis of short circuit current gains by an anti-reflective textured cover on silicon thin film solar cells*. Progress in Photovoltaics: Research and Applications, pages n/a–n/a, 2012.
- [van Erven 12] A.J.M. van Erven, M. Steltenpool, M. Bos, J. Rutten, G. van der Hofstad, J. Muller, H. de Groot, J. de Ruijter, A. Tavakoliyaraki, B. Titulaer & G. Rajeswaran. *Gen5 production tool for light management textures*. In Proceedings of the 38th IEEE Photovoltaic Specialists Conference, pages 000690–000693, 2012.
- [Vaneček 11] M. Vaneček, O. Babchenko, A. Purkrt, J. Holovsky, N. Neykova, A. Poruba, Z. Remes, J.s Meier & U. Kroll. *Nanostructured three-dimensional thin film silicon solar cells with very high efficiency potential*. Applied Physics Letters, vol. 98, page 163503, 2011.
- [Wadia 09] C. Wadia, A. P. Alivisatos & D. M. K. Ammen. *Materials availability expands the opportunity for large-scale photovoltaics deployment*. Environmental Science & technology, vol. 43, pages 2072–2077, 2009.

Bibliography

- [Wang 90] A. Wang, J. Zhao & M.A. Green. *24% efficient silicon solar cells*. Applied Physics Letters, vol. 57, page 602, 1990.
- [Xia 98] Y. Xia & G. M. Whitesides. *Soft Lithography*. Annual Review of Materials Science, vol. 28, pages 153–184, 1998.
- [Yablonovitch 82] E. Yablonovitch & G.D. Cody. *Intensity enhancement in textured optical sheets for solar cells*. Electron Devices, IEEE, vol. 29, pages 300–305, 1982.
- [Yan 10] B. Yan, G. Yue, X. Xu, J. Yang & S. Guha. *High efficiency amorphous and nanocrystalline silicon solar cells*. Physica status solidi A, vol. 207, pages 671–677, 2010.
- [Yan 11] B. Yan, G. Yue, L. Sivec, J. Yang, S. Guha & C.-S. Jiang. *Innovative dual function nc-SiO_x:H layer leading to a > 16% efficient multi-junction thin-film silicon solar cell*. Applied Physics Letters, vol. 99, page 113512, 2011.
- [Yan 12a] B. Yan, G. Yue, L. Sivec, J. Owens-Mawson, J. Yang & S. Guha. *Correlation of texture of Ag/ZnO back reflector and photocurrent in hydrogenated nanocrystalline silicon solar cells*. Solar Energy Materials and Solar Cells, vol. 104, pages 13–17, 2012.
- [Yan 12b] B. Yan, J. Yang & S. Guha. *Amorphous and nanocrystalline silicon thin film photovoltaic technology on flexible substrates*. Journal of Vacuum Science and Technology A, vol. 30, pages 04D108–10, 2012.
- [Yang 09a] J. Yang & S. Guha. *Status and future perspective of a-Si:H, a-SiGe:H, and nc-Si:H thin film photovoltaic technology*. In Proceeding of SPIE Vol. 7409 74090C-1, 2009.
- [Yang 09b] J. Yang, B. Yan, G. Yue & S. Guha. *Light trapping in hydrogenated amorphous and nano-crystalline silicon thin film solar cells*. In Proceedings of the Material Research Society, vol. 1153, mrss09-1143-A13-02, San Fransisco, 2009.
- [Yu 10] Z. Yu, A. Raman & S. Fan. *Fundamental limit of nanophotonic light trapping in solar cells*. Proceedings of the National Academy of Sciences, vol. 107, pages 17491–17496, 2010.
- [Yue 08] G. Yue, B. Yan, C. Teplin, J. Yang & S. Guha. *Optimization and characterization of i/p buffer layer in hydrogenated nanocrystalline silicon solar cells*. Journal of Non-Crystalline Solids, vol. 354, pages 2440–2444, 2008.
- [Yue 12a] G. Yue, B. Yan, L. Sivec, T. Su, Y. Zhou, J. Yang & S. Guha. *Hydrogenated nanocrystalline silicon based solar cell with 13.6% stable efficiency*. In Proceedings of the Material Research Society, vol. 1426, pages 33-38, San Fransisco, 2012.

-
- [Yue 12b] G. Yue, B. Yan, L. Sivec, Y. Zhou, J. Yang & S. Guha. *Effect of impurities on performance of hydrogenated nanocrystalline silicon solar cells*. Solar Energy Materials and Solar Cells, vol. 104, pages 109–112, 2012.
- [Zhang 10] Y. Zhang, C.-T. Lin & S. Yang. *Fabrication of hierarchical pillar arrays from thermoplastic and photosensitive SU-8*. Small, vol. 6, pages 768–775, 2010.
- [Zhu 09] J. Zhu, Z. Yu, G.-F. Burkhard, C.-M. Hsu, S.-T. Connor, Y. Xu, Q. Wang, M. McGehee, S. Fan & Y. Cui. *Optical absorption enhancement in amorphous silicon nanowire and nanocone arrays*. Nano Letters, vol. 9, pages 279–282, 2009.
- [Zhu 10] J. Zhu, C.-M. Hsu, Z. Yu, S. Fan & Y. Cui. *Nanodome solar cells with efficient light management and self-cleaning*. Nano Letters, vol. 10, pages 1979–1984, 2010.
- [Zhu 12] H. Zhu, J. Hükcs, E. Bunte & S.M. Huang. *Study of ZnO:Al films for silicon thin film solar cells*. Applied Surface Science, vol. 261, pages 268–275, 2012.

Acknowledgements

I acknowledge Prof. Christophe Ballif for having provided me with the opportunity to accomplish my thesis in his laboratory. His incentive and enthusiasm are contagious and motivate his colleagues to give their best in every project.

I thank the member of my thesis jury, Prof. Albert Polman, Prof. Ayodaya Tiwari, Dr. Subhendu Guha and Prof. Anna Fontcuberta i Morral for having accepted my invitation and devoted time to the reading of my thesis.

I acknowledge my co-supervisor Dr. Franz-Josef Haug for his availability, the confidence he had in me and my work and, most of all, his willingness to transmit his knowledge.

Then, I thank Jordi, Rémi, Céline and Priscille with whom I shared the office. The office atmosphere was great and we could always count on each other for help. Special thanks to Jordi with whom I spent long hours in the optics clean room and in the office discussing the nano-imprinting process (sometimes luck was required and called).

Having spend a lot of time with the other PhD students, I acknowledge them both for their friendship—and the good time we had around beers and playing "pétanque"—but also for the time we shared in the grey and clean rooms as well as in each other office. I appreciate the many discussions we had during which I learned a lot. Team effort always lead to good work and interesting results and we all know that at PV-Lab. I thus thank Michael, Mathieu B., Laura, Greg, Simon, Jonas, Bénédicte, Ali, Johannes, Peter, Andréa and Yannik.

Of course, I had many fruitful discussions—and beers—with others and I therefore also acknowledge Ségolène, Matthieu R., Adrian, Xavier, Irène, Maximilien, Ricardo, Jérémie, Joel, Matthieu D., Fanny, Corsin, Zak, Nicolas, Linus, Jan-Willem, Mathieu C., Sylvain N., Sylvain D., Mustapha, Antoine, Stefaan, Réto and Cédric. Many thanks to Mary-Claude for her helpful support with administration, Hassan for his support with informatics and Lara for the English proofreading of my thesis.

I'm really grateful to all the PV-Lab people that have contributed in building such a great atmosphere: The constant mutual help and thoughts sharing really made my stay and my work in Neuchâtel a real pleasure.

I eventually thank my family for their support and for the good times we always spend together no matter where we are.

Neuchâtel, March 2013

Karin Söderström

Karin Söderström

*Engineer in Physics from École Polytechnique
Fédérale de Lausanne, Switzerland.*

Rue de l'Eglise, 6
2000 Neuchâtel
Switzerland
Phone : +41 79 508 02 29

karin.soederstroem@epfl.ch
Nationality: Swiss
Age: 26



EDUCATION

- 04/2009 – 03/2013 **École Polytechnique Fédérale de Lausanne:**
PhD candidate in Material Science:
Coupling light into thin silicon layers for high-efficiency solar cells
- 09/2007 – 02/2009 **École Polytechnique Fédérale de Lausanne:**
Master degree in Physics with a grade of 5.78/6.
Master thesis realised in the laboratory of quantum optoelectronics with a grade of 6/6: *Building up a pump and probe experiment to study zero and bi-dimensional polariton*
- 09/2004 – 06/2007 **École Polytechnique Fédérale de Lausanne:**
Bachelor degree in Physics with a grade of 5.21/6
- 08/2001 – 07/2004 **Gymnase du Bugnon:**
Scientific Baccalauréat
Final project obtained with “mention bien”: *Hydrogen fuel cell technology*

Language skills: French (mother tongue), English (fluent), German (basics).

Computer skills: good knowledge of office suite, LaTeX and Igor.

SCIENTIFIC CONTRIBUTIONS

I co-authored twenty scientific peer-reviewed journal contributions, including five as a first author. My last paper published as first author was recognised by appearing in the highlights of Journal of Applied Physics. I also co-authored eleven conference proceedings and four conference technical digests, including three proceedings and one technical digest as a first author. I took part to four international conferences, for which I gave three oral presentations and one poster presentation. For my first participation to an international conference, at the OSA meeting in Karlsruhe in 2010, my paper was selected for an invited oral presentation because of the quality of the scientific work presented.

MISCELLANEOUS

I like playing tennis and I have been taking part in individual and team competitions since 15 years. Besides tennis, I also like running, hiking, skiing, snowboarding and wake surfing.

I am since ever interested in wildlife in general and I am especially amazed to learn about the synergies existing between the different forms of living as well as with their environments.

I am also an avid reader, mostly of English and American Literature.

LIST OF PUBLICATIONS

Journal Contributions as first author

1. K. Söderström, F.-J. Haug, J. Escarré, O. Cubero & C. Ballif. *Photocurrent increase in n-i-p thin film silicon solar cells by guided mode excitation via grating coupler*. Applied Physics Letters, vol. 96, page 213508, 2010.
2. K. Söderström, J. Escarré, O. Cubero, F.-J. Haug, S. Pérregaux & C. Ballif. *UV-nano-imprint lithography technique for the replication of back reflector for n-i-p thin film silicon solar cells*. Progress in Photovoltaics: Research and Applications, Vol. 19, pages 202-210, 2011.
3. K. Söderström, F.-J. Haug, J. Escarré, C. Pahud, R. Biron & C. Ballif. *Highly reflective nanotextured sputtered silver back reflector for flexible high-efficiency n-i-p thin film silicon solar cells*. Solar Energy Materials and Solar Cells, vol. 95, pages 3585–3591, 2011.
4. K. Söderström, G. Bugnon, F.-J. Haug, S. Nicolay & C. Ballif. *Experimental study of flat light-scattering substrates in thin-film silicon solar cells*. Solar Energy Materials and Solar Cells, vol. 101, pages 193–199, 2012.
5. K. Söderström, G. Bugnon, R. Biron, C. Pahud, F. Meillaud, F.-J. Haug & C. Ballif. *Thin-film silicon triple-junction solar cell with 12.5% stable efficiency on innovative flat light-scattering substrate*. Journal of Applied Physics, vol. 112, page 114503, 2012.

Journal Contributions as co-author

1. J. Escarré, K. Söderström, C. Battaglia, F.-J. Haug & C. Ballif. *High fidelity transfer of nanometric random textures by UV embossing for thin film solar cells applications*. Solar Energy Materials and Solar Cells, vol. 95, pages 881–886, 2011.
2. A. Naqavi, K. Söderström, F.-J. Haug, V. Paeder, T. Scharf, H. P. Herzig & C. Ballif. *Understanding of photocurrent enhancement in real thin film solar cells: towards optimal one-dimensional grating*. Optics Express, vol. 19, pages 128–140, 2011.
3. F.-J. Haug, K. Söderström, A. Naqavi & C. Ballif. *Resonances and absorption enhancement in thin film silicon solar cells with periodic interface texture*. Journal of Applied Physics, vol. 109, page 084516, 2011.
4. R. Biron, C. Pahud, F.-J. Haug, J. Escarré, K. Söderström & C. Ballif. *Window layer with p doped silicon oxide for high Voc thin-film silicon n-i-p solar cells*. Journal of Applied Physics, vol. 110, page 124511, 2011.
5. C. Battaglia, K. Söderström, J. Escarré, F.-J. Haug, D. Dominé, P. Cuony, M. Boccard, G. Bugnon, C. Denizot, M. Despeisse, A. Feltrin & C. Ballif. *Efficient light management scheme for thin film silicon solar cells via transparent random nanostructures fabricated by nanoimprinting*. Applied Physics Letters, vol. 96, page 213504, 2010.
6. C. Battaglia, L. Erni, M. Boccard, L. Barraud, J. Escarré, K. Söderström, G. Bugnon, A. Billet, L. Ding, M. Despeisse, F.-J. Haug, S. De Wolf & C. Ballif. *Micromorph thin-film silicon solar cells with transparent high-mobility hydrogenated indium oxide front electrodes*. Journal of Applied Physics, vol. 109, page 114501, 2011.
7. C. Battaglia, J. Escarré, K. Söderström, L. Erni, L. Ding, G. Bugnon, A. Billet, M. Boccard, L. Barraud, S. De Wolf, F.-J. Haug, M. Despeisse & C. Ballif. *Nanoimprint lithography for high-efficiency thin-film silicon solar cells*. Nano Letters, vol. 11, pages 661-665, 2011.
8. C. Battaglia, J. Escarré, K. Söderström, M. Charrière, M. Despeisse, F.-J. Haug & C. Ballif. *Nanomoulding of transparent zinc oxide electrodes for efficient light trapping in solar cells*. Nature: Photonic letters, vol. 5, pages 535-538, 2011.

9. C. Battaglia, J. Escarré, K. Söderström, M. Boccard & C. Ballif. *Experimental evaluation of the light trapping potential of optical nanostructures for thin-film silicon solar cells*. Energy Procedia, Vol. 15, pages 206-211, 2012.
10. C. Battaglia, C.-M. Hsu, K. Söderström, J. Escarré, F.-J. Haug, M. Charrière, M. Boccard, M. Despeisse, D.T.L. Alexander, M. Cantoni, Y. Cui & C. Ballif. *Light trapping in solar cells: Can periodic beat random?* ACS NANO, vol.6, pages 2790-2797, 2012.
11. J. Escarré, C. Battaglia, K. Söderström, C. Pahud, R. Biron, O. Cubéro, F.-J. Haug & C. Ballif. *UV imprinting for thin film solar cells applications*. Journal of Optics, vol. 14, page 024009, 2012.
12. J. Escarré, K. Söderström, M. Despeisse, S. Nicolay, C. Battaglia, G. Bugnon, L. Ding, F. Meillaud, F.-J. Haug & C. Ballif. *Geometric light trapping for high efficiency thin film silicon solar cells*. Solar Energy Materials and Solar Cells, vol. 98, pages 185–190, 2012.
13. M. Boccard, P. Cuony, C. Battaglia, S. Hänni, S. Nicolay, L. Ding, M. Benkhaira, G. Bugnon, A. Billet, M. Charrière, K. Söderström, J. Escarré, F. Sculati-Meillaud, M. Despeisse & C. Ballif. *Nanometer- and micrometer-scale texturing for high-efficiency micromorph thin-film silicon solar cells*. IEEE Journal of Photovoltaics, vol. 2, pages 83–87, 2012.
14. M. Boccard, C. Battaglia, S. Hänni, K. Söderström, J. Escarré, S. Nicolay, F. Meillaud, M. Despeisse & C. Ballif. *Multiscale transparent electrode architecture for efficient light management and carrier collection in solar cells*. Nano Letters, vol. 12, pages 1344–1348, 2012.
15. C. Battaglia, K. Söderström, J. Escarré, F.-J. Haug, M. Despeisse & C. Ballif. *Nanomoulding of functional materials, a versatile complementary pattern replication method to nanoimprinting*. Journal of Visual Experiments, vol. 71, page e50177, 2013.

Conference proceedings as first author

1. K. Söderström, J. Escarré, R. Biron, O. Cubéro, C. Eminian, F.-J. Haug & C. Ballif. *Nano-imprint technique for back reflector in high efficiency n-i-p thin film silicon solar cells*. In Proceeding of the 25th EUPVSEC/ 5th WCPEC-5, 3AV1.8, pages 2899-2903, Valencia, 2010.
2. K. Söderström, F.-J. Haug, C. Pahud, R. Biron, J. Escarré, M. Duchamp, R. Dunin-Borkowski & C. Ballif. *Reflectance improvement by thermal annealing of sputtered Ag/ZnO back reflectors in a-Si:H thin film silicon solar cells*. In Proceeding of the Material Research Society, vol. 1321, mrss11-1321-a11-05, San Francisco, 2011.
3. K. Söderström, G. Bugnon, F.-J. Haug & C. Ballif. *Electrically flat/optically rough substrates for efficiencies above 10% in n-i-p thin film silicon solar cells*. In Proceeding of the Material Research Society, vol. 1426, pages 39-45, San Francisco, 2012.

Conference proceedings as co-author

1. J. Escarré, K. Söderström, O. Cubéro, F.-J. Haug & C. Ballif. *UV-embossed textured back reflector structures for thin film silicon solar cells*. In Proceeding of the Material Research Society, vol. 1245, mrss10-1245-A07-04, San Francisco, 2010.
2. C. Battaglia, J. Escarré, K. Söderström, F.-J. Haug, D. Dominé, A. Feltrin & C. Ballif. *A New approach to light scattering from nanotextured interfaces for thin-film silicon solar cells*. In Proceeding of the Material Research Society, vol. 1245, mrss10-1245-A03-04, San Francisco, 2010.
3. C. Ballif, L. Barraud, C. Battaglia, M. Benkhaira, A. Billet, R. Biron, M. Boccard, G. Bugnon, M. Charrière, P. Cuony, M. Despeisse, L. Ding, J. P. Escarré, F.-J. Haug, S. Hänni, L.

- Löfgren, F. Sculati-Meillaud, S. Nicolay, C. Pahud, G. Parascandolo, B. Perruche, S. De Wolf, K. Söderström & M. Stükelberger. *Novel materials and superstrates for high-efficiency micromorph solar cells*. In Proceedings of the 26th EUPVSEC, 3CO1.1, pages 2384-2391, Hamburg, 2011.
4. M. Duchamp, K. Söderström, Q. Jeangros, C. B. Boothroyd, A. Kovács, T. Kasama, F.-J. Haug, C. Ballif & R.E. Dunin-Borkowski. *Transmission electron microscopy of the textured silver back reflector of a thin film silicon solar cell: From crystallography to optical absorption*. In Proceedings of the 26th EUPVSEC, 3AV.1.38, pages 2554-2557, Hamburg, 2011.
 5. P. Couty, M. Duchamp, K. Söderström, A. Kovács, R.E. Dunin-Borkowski, L. Sansonnens & Y. Ziegler. *Transmission electron microscopy of amorphous tandem thin-film silicon modules produced by a roll-to-roll process on plastic foil*. In Proceedings of the 26th EUPVSEC, 3CO.1.4, pages 2395-2398, Hamburg, 2011.
 6. A. Naqavi, K. Söderström, F.-J. Haug, V. Paeder, T. Scharf, H. P. Herzig & C. Ballif. *Enhanced light trapping in realistic thin film solar cells using one dimensional gratings*. In Proceedings SPIE, vol. 8065, page 80650A, 2011.
 7. F.-J. Haug, K. Söderström, A. Naqavi & C. Ballif. *Excitation of guided-mode resonances in thin film silicon solar cells*. In Proceedings of the Material Research Society, 1321, mrs11-1321-a17-12, San Francisco, 2011.
 8. F.-J. Haug, K. Söderström, A. Naqavi & C. Battaglia & C. Ballif. *Excitation of plasmon and guided-mode resonances in thin film silicon solar cells*. In Proceedings of the Material Research Society, vol. 1391, mrsf11-1391-j03-06, Boston, 2011.

Technical digest as first author

1. K. Söderström, J. Escarré, O. Cubero, F.-J. Haug & C. Ballif. *Photocurrent increase in thin film solar cells by guided mode excitation*. In Technical digest of OSA meeting: Optical Nanostructures for Photovoltaics, Karlsruhe, paper PTuB6, 2010.

Technical digests as co-author

1. A. Naqavi, V. Paeder, T. Scharf, K. Söderström, F.-J. Haug, C. Ballif & H. P. Herzig. *An RCWA Analysis of Solar Cell Back Reflectors: Comparison between modelling and experiment*. In Technical digest of OSA meeting: Optical Nanostructures for Photovoltaics, Karlsruhe, paper PTuC3, 2010.
2. C. Battaglia, L. Barraud, A. Billet, M. Boccard, G. Bugnon, M. Charrière, P. Cuony, M. Despeisse, S. De Wolf, L. Ding, L. Erni, J. Escarré, S. Hänni, F.-J. Haug, L. Löfgren, F.Meillaud, S. Nicolay, G. Parascandolo, K. Söderström, M. Stuckelberger & C. Ballif. *Advanced nanostructured materials for pushing light trapping towards the Yablonovitch limit*. In Technical digest of OSA meeting: Optical Nanostructures and Advanced Materials for Photovoltaics Austin, paper PWC6, 2011.
3. F.-J. Haug, K. Söderström & C. Ballif. *Coupling between radiation and internal modes: light trapping in thin film solar cells with periodic texture*. In Technical digest of OSA meeting: Asia Communications and Photonics Conference, Guangzhou, paper AF3F.1, 2012.